Die approbierte Originalversion dieser Dissertation ist an der Hauptbibliothek der Technischen Universität Wien aufgestellt (http://www.ub.tuwien.ac.at).

The approved original version of this thesis is available at the main library of the Vienna University of Technology (http://www.ub.tuwien.ac.at/englweb/).

D O C T O R A L  T H E S I S

# Investigations on the Serviceability Limit State of Dowel-Type Timber Connections

submitted in satisfaction of the requirements for the degree of
Doctor of Science in Civil Engineering
of the Vienna University of Technology, Faculty of Civil Engineering

---

D I S S E R T A T I O N

# Untersuchungen zum Gebrauchstauglichkeitszustand von Dübelverbindungen im Holzbau

ausgeführt zum Zwecke der Erlangung des akademischen Grades eines
Doktors der technischen Wissenschaften
eingereicht an der Technischen Universität Wien, Fakultät für Bauingenieurwesen

von

Dipl.-Ing. Michael Dorn
Matrikelnummer 9725475
Plenergasse 10/11, A-1180 Wien, Österreich

Gutachter: Associate Prof. Karin de Borst

School of Engineering
University of Glasgow
Rankine Building 703
Glasgow G12 8LT, Scotland

Fakultät für Bauingenieurwesen
Technische Universität Wien
Karlsplatz 13/e202
1040 Wien, Österreich

Gutachter: Prof. Erik Serrano

School of Engineering
Linnæus University
Hus M 3073
351 95 Växjö, Sweden

Wien, im März 2012 .....

# Acknowledgements

This thesis is the outcome of my research activities as an university assistant at the Institute for Mechanics of Materials and Structures (IMWS) at the Vienna University of Technology (TU Wien). Although I take credit for this work, it would not have been possible without the help and support of many people.

First of all, I express my greatest gratitude to Associate Prof. Karin de Borst for her support and guidance as the leader of the wood research group at the IMWS. She was always open for new ideas and, although critically discussing these, very supportive in their realization. I am also deeply thankful for her understanding of private matters.

I would like to thank Prof. Erik Serrano from the Linnæus University, Växjö, Sweden, for serving as co-examiner. I am very grateful for being generous with the deadlines, which I stretched extensively.

I especially thank Ass. Prof. Mehdi Aminbaghai, who first made the proposal for becoming an university assistant at the Institute for Structural Analysis, TU Wien. I enjoyed his creativity to start and his ambitions to finish our jointly developed work. In this context, I would also like to thank Em.O.Univ.-Prof. Helmut Rubin, then head of the institute, as well as Gabriele Ostrowski and René Binder, my former colleagues.

Univ.-Prof. Josef Eberhardsteiner is thanked for the smooth transfer from my former position at the Institute for Structural Analysis and for the warm welcome at the IMWS. Additionally, many thanks for his support in work-related as well as private matters.

I am very thankful to my present and former colleagues of the wood group at the IMWS for both, work-related and private discussions, Thomas Bader, Johannes Eitelberger, Josef Füssl, Stefan Gloimüller, Christoph Hackspiel, Georg Hochreiner, Andreas Jäger, Georg Kandler, Wolfgang Lederer, Markus Lukacevic, Lech Muszyński, Reinhard Stürzenbecher, Leopold Wagner, and Christoph Wikete.

Furthermore, I would like to thank the colleagues at the institute from other research groups, Aram Amouzandeh, Andreas Fritsch, Gerhard Höfinger, Xin Jia, Christoph Kohlhauser, Bernhard Pichler, Thomas Ring, Stefan Scheiner, Mehran Shahidi, and Yiming Zhang. I am confident, that the friendships will continue. I would like to thank the staff at the laboratory, who helped me during the preparation and conduction of the experiments, Wolfgang Dörner, Clemens Engler, Olaf Lahayne, Roland Reihsner, and Matthias Zeiml. In addition, I would like to thank Gabriele Ostrowski, Martina Pöll and Astrid Schuh for their help with various administrative issues.

For supplying me with testing equipment and their generosity I would like to thank O.Univ.Prof. Johann Kolleger, Herbert Pardatscher and Wolfgang Träger from the Institute of Structural Engineering, TU Wien. I would like to thank Lukas Kirchmaier and the other members of the Institute of Transportation, TU Wien, for their help.

Finally, I thank my family, my parents, my brothers, their girlfriends as well as my niece Hannah for their support during the years and especially during the final stage of preparing the thesis. Without their help, support and valuable time, this would not have been possible.

Last, but not at all least, I like to thank my son Moritz. He was very patient in stressful times and reminded me of more important things than work (often not so patiently). I would therefore like to dedicate this work to him, keep being interested, imaginative and curious about as many things as possible!

# Abstract

Dowel-type steel-to-timber connections are commonly used to transfer a large range of loads. Although they are simple to produce and assemble, the load-carrying behavior and the local stress and strain distribution within the connection area are highly complex. In addition to that, wood is a challenging material from an engineering point of view due to its highly anisotropic structure and behavior and due to its natural origin, which results often in inhomogeneities. The failure characteristics of wood are very different in tension and shear and in compression, where brittle failure and plastic-ductile failure modes occur, respectively.

The aim of this thesis is to study the load-carrying behavior of dowel-type steel-to-timber connections in detail. This is achieved by performing experimental tests on single-dowel connections. A large variety of influencing parameters is assessed, which include wood density, connection width, the dowel roughness, and the application of reinforcements in order to prevent brittle behavior. Separate stages in the loading history are identified, starting from an initial consolidation phase, the region of maximum stiffness during load increase, and the point of maximum connection strength. Ductility is of great interest as well as the final failure modes. During the experiments, unloading and reloading cycles are performed, where distinctively higher stiffnesses are observed than during the first loading. The results of the experiments are compared to the design practice in Eurocode 5 for strength and stiffness estimation. Strength prediction is conservative except for slender connections, while stiffness prediction complied with experimental results only for connections of intermediate width.

The initial consolidation phase of the experiments is then investigated further. It is concluded, that the properties of the bore-hole surface, where not a smooth but a rough surface with valleys and rifts is encountered, is responsible for the initially low stiffness. The contact behavior is studied by conducting experiments on wood with varying surface characteristics, which are a result of using different cutting tools. A mathematical model for the soft contact behavior is proposed, which is based on the results of the experimental tests. It also includes the evolution of non-reversible deformations in the surface layer.

Complementing the experiments, a simulation tool suitable for numerically assessing the mechanical behavior of the connections is developed. It allows to perform simulations by means of the Finite Element method on such connections and provides an enhanced insight into the stress and strain distribution in connections compared to the tests. Hereby, a three-dimensional material model for wood is established, which allows to model the anisotropy of wood in the elastic as well as in the plastic domain, based on the theory of small strains and small displacements. The combination of the developed models for the material as well as the contact behavior leads to realistic simulation results, which are verified by comparing model predictions with the experimental results on connections. It is confirmed, that the computed behavior agrees well with the experimental one and that the features observed during the experiments are well reproduced. Due to the limitations of the simulation tool to small deformations, ultimate load and brittle failure modes cannot be predicted. Nevertheless, the influence of various parameters on both can still be estimated.

The modeling approach is suitable for application to more complex situations in the future, such as multi-dowel connections or connection loaded by generalized loads. Especially the contact model, which is a unique feature in the thesis, allows a realistic simulation of the distribution of the forces in such statically indeterminant situations.

# Kurzfassung

Stahl-Holz-Verbindungen mit Stabdübeln sind im Ingenieurholzbau weit verbreitet, um eine große Variation an Lasten zu übertragen. Obwohl sie einfach herzustellen und zusammenzufügen sind, sind die Tragwirkung und die lokalen Spannungs– und Verzerrungsfelder innerhalb des Verbindungsmittelbereichs vergleichsweise komplex. Bedingt durch die Anisotropie in Aufbau und Verhalten und den natürlichen Wuchs, der zu Inhomogenitäten führt, ist Holz aus Sicht des Ingenieurs ein herausfordernder Baustoff. Holz weist sehr unterschiedliche Versagensformen auf, nämlich spröd unter Zug- und Schubbelastungen und plastisch-duktil im Druckbereich.

Das Ziel dieser Arbeit ist es, das Tragverhalten von Stabdübelverbindungen eingehend zu untersuchen. Dazu werden Versuche an Verbindungen mit einem einzelnen Dübel durchgeführt. Dabei wird der Einfluss verschiedener Parameter bestimmt, wie der Holzdichte, der Breite der Verbindung, der Dübelrauigkeit und von Verstärkungen zur Rissvorbeugung. Einzelne Abschnitte im Last-Verschiebungs-Diagramm werden identifiziert, beginnend beim Erstkontakt zwischen Dübel und Holz, über den Abschnitt mit der größten Steifigkeit bei Erstbelastung sowie dem Punkt der Maximallast. Zusätzlich sind die Duktilität und der endgültige Versagensmodus von Interesse. Während der Versuche werden Ent- und Wiederbelastungszyklen durchfahren, die durch deutlich höhere Steifigkeiten als jene bei der Erstbelastung gekennzeichnet sind. Die Versuchsergebnisse werden mit den Ergebnissen nach Eurocode 5 verglichen. Es zeigt sich, dass die Maximallasten konservativ abgeschätzt werden (mit Ausnahme von schmalen Verbindungen), die Vorhersagen für die Steifigkeit sind nur für Verbindungen mittlerer Breite zutreffend.

Der Erstkontakt zwischen Dübel und Holz wird im folgenden genauer betrachtet. Die Oberfläche des Bohrloches ist hierbei für die geringe Steifigkeit zu Beginn verantwortlich, da diese nicht glatt sondern rau und wellig ist. Das Kontaktverhalten wird untersucht, indem Druckversuche an Holzproben mit unterschiedlichen Oberflächenrauigkeiten, erzeugt durch verschiedene Schnittarten, gemacht werden. Basierend auf den Versuchsergebnissen wird ein mathematisches Modell für weichen Kontakt vorgeschlagen, welches auch nicht-reversible Deformationen berücksichtigt.

Ergänzend zu den Versuchen wird ein numerisches Simulationstool entwickelt, das eine Beurteilung des mechanischen Verhaltens von Verbindungen ermöglicht. Dies geschieht mit Hilfe der Finiten Elemente Methode, welche einen verbesserten Einblick in die lokalen Spannungs– und Verzerrungsfelder ermöglicht. Dazu wird ein dreidimensionales Materialmodell für Holz vorgestellt, mit dem das anisotrope Verhalten von Holz sowohl im elastischen als auch im plastischen Bereich innerhalb der Theorie kleiner Verzerrungen und Verschiebungen erfasst wird. Die Kombination der Modelle für das mechanische Verhalten von Holz und für das Kontaktverhalten führt zu realistischen Simulationen, die mit Hilfe der Versuchsergebnisse verifiziert werden. Es zeigt sich, dass das numerisch bestimmte Verhalten mit dem experimentell beobachteten gut übereinstimmt, und dass die oben erwähnten Abschnitte im Last-Verschiebungs-Diagramm gut reproduzierbar sind. Aufgrund der Modellbeschränkung auf kleine Verzerrungen und Verschiebungen können die Traglast und das spröde Versagen nicht vorhergesagt werden. Dennoch ist es möglich, den Einfluss verschiedener Parameter darauf abzuschätzen.

Die Modelle erlauben eine zukünftige Anwendung auf komplexere Gegebenheiten, z.B. in Dübelgruppen oder in Verbindungen mit allgemeiner Belastung. Hierbei ermöglicht vor allem das Kontaktmodell, welches ein wesentlicher originärer Beitrag dieser Arbeit ist, eine realistische Simulation der Kräfteverteilung in statisch unbestimmten Systemen.

# Contents


**1 Introduction** **2**
- 1.1 Motivation . . . 2
- 1.2 Scope and structure . . . 3

**2 Dowel-type timber connections** **5**
- 2.1 Mechanical behavior of sound wood . . . 5
- 2.2 Mechanical behavior of dowel-type steel-to-timber connections . . . 7
- 2.3 Design situation . . . 12
  - 2.3.1 Stiffness determination . . . 12
  - 2.3.2 Strength determination . . . 13
- 2.4 Discussion . . . 15

**3 Tests on single dowel-type timber connections** **17**
- 3.1 Introduction . . . 17
- 3.2 Materials and methods . . . 18
  - 3.2.1 Preparation of wood specimens . . . 18
  - 3.2.2 Test set-up . . . 18
  - 3.2.3 Test series . . . 20
- 3.3 Results . . . 21
  - 3.3.1 Density . . . 21
  - 3.3.2 Width . . . 22
  - 3.3.3 Friction . . . 23
  - 3.3.4 End distance . . . 25
  - 3.3.5 Edge distance . . . 26
  - 3.3.6 Lateral reinforcement . . . 27
- 3.4 Typical loading behavior . . . 28
  - 3.4.1 Initial consolidation . . . 28
  - 3.4.2 First loading . . . 29
  - 3.4.3 Unloading and reloading cycles . . . 29
  - 3.4.4 Decrease of stiffness, yield plateau . . . 30
  - 3.4.5 Failure . . . 30
- 3.5 Discussion . . . 31

**4 Contact tests** **34**
- 4.1 Introduction . . . 34
  - 4.1.1 Aim . . . 35
  - 4.1.2 Basics of roughness determination . . . 35
- 4.2 Preparation of test specimens . . . 37

4.3 Determination of surface texture . . . 41
4.3.1 Measuring system . . . 41
4.3.2 Execution of measurements . . . 42
4.3.3 Evaluation of measurements . . . 44
4.3.4 Comparison of bore-hole surfaces to plane surfaces . . . 45
4.4 Determination of clear wood stiffness . . . 45
4.4.1 Measuring system and data evaluation . . . 45
4.4.2 Results of US-measurements . . . 46
4.5 Compression tests . . . 48
4.5.1 Measuring system . . . 48
4.5.2 Performance of compression tests . . . 48
4.5.3 Loading behavior during compression tests . . . 49
4.5.4 Strength and stiffness determination . . . 51
4.6 Contact stiffness . . . 55
4.6.1 Mechanical model for contact stiffness . . . 55
4.6.2 Mathematical description of the pressure-contact displacement relation . . . 57
4.6.3 Curve fitting . . . 59
4.7 Discussion . . . 62

**5 Contact behavior 64**
5.1 Normal behavior . . . 64
5.1.1 Contact states . . . 65
5.1.2 Algorithmic implementation . . . 66
5.2 Finite Element implementation . . . 67
5.3 Verification examples . . . 68

**6 Elasto-plastic model for wood 71**
6.1 Fields of application . . . 71
6.2 Theory of elasto-plastic material modeling . . . 72
6.2.1 Additive decomposition of strains . . . 72
6.2.2 Free energy potential and the elastic law . . . 72
6.2.3 Yield criterion and yield surface . . . 74
6.2.4 (Associated) Plastic flow rule . . . 77
6.2.5 Loading/Unloading conditions . . . 77
6.2.6 The plastic multiplier . . . 78
6.2.7 Elasto-plastic tangent operator . . . 78
6.3 Algorithmic implementation . . . 79
6.4 Finite Element implementation . . . 80
6.4.1 Input of parameters . . . 80
6.4.2 Results from Finite Element simulations . . . 81
6.5 Verification example . . . 81
6.6 Discussion . . . 84

**7 Structural simulations 86**
7.1 Reference simulation . . . 86
7.1.1 Definition of the reference simulation . . . 86
7.1.2 Results of the reference simulation . . . 91

7.2 Verification of the simulation approach . . . 97
7.2.1 Transversal isotropy . . . 97
7.2.2 Mesh dependency . . . 99
7.3 Parametric study . . . 101
7.3.1 Connection width . . . 102
7.3.2 End distance . . . 104
7.3.3 Edge distance . . . 106
7.3.4 Density variation . . . 107
7.3.5 Dowel material . . . 109
7.3.6 Contact behavior . . . 110
7.3.7 Frictional properties . . . 113
7.3.8 Bore-hole size . . . 116
7.3.9 Compression loading . . . 118
7.3.10 Unloading cycles . . . 120
7.4 Discussion . . . 122

**8 Validation of the Finite Element simulations 125**
8.1 Standard connection . . . 125
8.2 Influence of bore-hole properties . . . 127
8.2.1 Contact stiffness . . . 127
8.2.2 Bore-hole size . . . 129
8.2.3 Friction . . . 130
8.3 Influence of wood density . . . 131
8.4 Influence of geometry . . . 132
8.4.1 Width of specimen . . . 132
8.4.2 End distance . . . 133
8.4.3 Edge distance . . . 134
8.5 Unloading and reloading cycles . . . 135
8.6 Discussion . . . 136

**9 Comparison of experimental results with the design concept of EC5 137**
9.1 Introduction . . . 137
9.2 Stiffness . . . 138
9.3 Strength . . . 140
9.4 Discussion . . . 140

**10 Conclusions 142**

**A Roughness Parameters 146**

**B Results of the roughness measurements 151**

**C Generalized Lamé curve 161**

**D Lamé-parameters for contact properties 163**

**Bibliography 166**

# Introduction

# Chapter 1

# Introduction

## 1.1 Motivation

Despite the fact that wood is presumably one of the oldest building materials, it is currently not widely used as a building material compared to the other main building materials steel and concrete. Nevertheless, in the last decades wood experienced a revival as a structural building material. This is partly due to the fact of wood being a natural resource and due to its ecological importance. On the other hand, the useability has been increased due to a harmonization of the design standards, and there is increased interest of economy and research institutions in the material wood.

In structural timber engineering, joints of the individual members of the structures are of critical interest, since they usually are weaker than the connected parts. It is therefore necessary, to assess load-bearing capacity and stiffness of the connections in an accurate and reliable manner.

This thesis aims at the proper description of the load-bearing behavior of dowel-type steel-to-timber connections. This goal is approached by experiments on single dowel connections, which feature a variation of significant influencing parameters, such as wood density, connection width, and frictional behavior between dowel and wood. From these, individual stages in the loading history are extracted, which are commonly shared for all variations. Additionally, a numerical simulation tool is developed, which is validated successfully by means of the experimental results for the parameters varied. The simulations allow to study the connection behavior in great detail by assessing the internal stress and strain states. In the simulations, focus is placed on the behavior up to the Ultimate Limit State and on prediction of connection stiffness, also during unloading.

## 1.2 Scope and structure

The thesis is divided into several parts, which cover different aspects of the thesis.

**Introduction**
In Chapter 2, the mechanical behavior of wood as building material is briefly described. The characteristics of dowel-type connections are then presented, and the design procedures according to Eurocode 5 (EC5) [24] are recalled.

**Experiments**
A comprehensive test series investigating the load-bearing behavior of single-dowel connections, loaded in tension parallel to the grain direction, is performed (Chapter 3). The specimens are subjected to a large variation of influencing parameters such as connection width and wood density. The distinctive features during the loading process of such connections are highlighted.

The experiments clearly show that contact plays a crucial role in the load-carrying behavior, which motivates to study the behavior of compliant wood surfaces in contact with comparably stiff steel surfaces in detail. The quality of wood surfaces, cut by means of different cutting devices, is determined with an optical, non-destructive test method. Compression tests on the same tests specimens are then performed. From these tests, the contact behavior for the first loading as well as for repeated loading of the surfaces is extracted and a mathematical description derived (Chapter 4).

**Simulations**
A numerical simulation tool is developed in the following chapters, which allows to study the connection behavior in great detail by assessing the internal stress and strain states. The implementation of the contact model in the Finite Element code ABAQUS by means of a user-subroutine is shown first. It is able to imitate the soft contact behavior and the occurrence of non-reversible deformations of the wood surface (Chapter 5).

A three-dimensional material model for wood is presented next (Chapter 6). It is capable of describing the elasto-plastic material behavior in an orthotropic framework, whereby perfect plasticity is assumed. The model is valid within the limits of the theory of small strains and small displacements.

Chapter 7 deals with the simulations of dowel-type connections. The numerical simulations on dowel-type timber connections are explained and displayed in all stages, the material properties are documented, the loading conditions are made clear, and the mesh generation is presented. An extensive parametric study is enclosed, so that the prediction capabilities are revealed. In the conclusions, the possibilities and also the current limitations of the possibilities of the model are pointed out, as well as potential model extensions in the future.

**Discussion**
The validation of the simulation tool is done for all load stages within the scope of the simulation tool by comparison of model predictions with experimental results on

connections and discussed in detail (Chapter 8). Since the model is valid only up to the formation of moderate strains, ultimate strength and fracture behavior is not assessed.

The comparison of the experiments with the design procedures according to EC5 follows in Chapter 9. The design values for strength and stiffness are compared and the differences discussed.

The thesis is finally concluded in Chapter 10.

# Chapter 2

# Dowel-type timber connections

In the following chapter, wood as a building material is described first. This is followed by a description of typically used dowel-type connections and their versatile design possibilities. A short literature review on the current state of research is provided for both sections.

The design rules for dowel-type timber connections according to Eurocode 5 (EC5) [24] are then reviewed. The determination of stiffnesses in the Serviceability Limit State (SLS) as well as in the Ultimate Limit State (ULS) as laid down in EC5 are presented next. This is followed by a description of the design rules for determining the load-carrying capacity in the ULS.

## 2.1 Mechanical behavior of sound wood

The mechanical processes described in the later chapters are based on the assumption of wood being a continuum. This allows the application of the well known principles of continuum mechanics for material properties describing the mechanical behavior.

What makes the use and description of wood rather complicated compared to other building materials are the following features:

- Anisotropy: Due to its annual rings, arranged in layers, wood exhibits distinctive direction-dependence of stiffness and strength. The anisotropy is usually assumed to be of orthotropic manner with the main directions oriented in the $L$-$R$-$T$-system, denoting the longitudinal, radial, and tangential direction in the stem respectively (Figure 2.1).
- Failure mechanisms: Under tension, wood exhibits brittle behavior. Also when loaded under shear, failure is of brittle manner. Brittle behavior is disadvantageous for building purposes as failure occurs without warning signs and often leads to an instantaneous collapse of the structure.

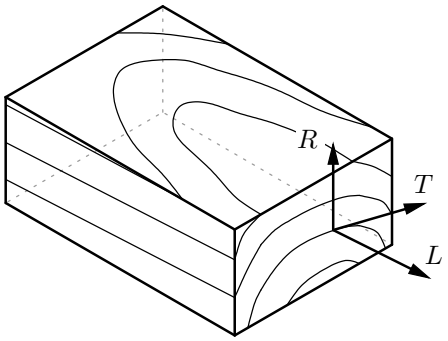


Figure 2.1: Material directions of wood in an orthotropic description.

Under compression, wood reacts distinctively different when loaded up to failure load. The behavior can be described as elasto-plastic, there is no abrupt drop of loads after the peak load, but usually an increase of deformations at more or less constant load. This failure mode is more favorable as there is a warning in advance of possible collapse, e.g. by high, visible deflections of structural members.

In addition, interaction of stresses can have dramatic influence on strength, Figure 2.2 provides an overview of typical failure modes and a possible stress-interaction scenario expressed by a failure surface in the stress space [63] (see Chapter 6.2.3 for a detailed description of the failure surface).

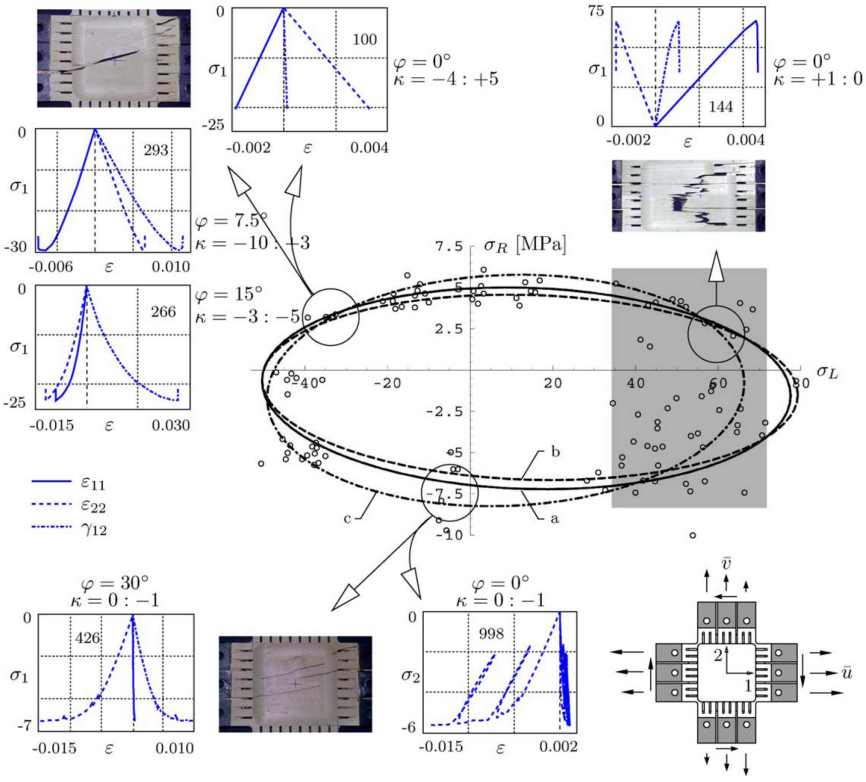


Figure 2.2: Typical failure modes of wood in the $L$-$R$-plane [63].

- Variability: Trees grow over a long time in a natural habitat. The properties of wood reflect the different requirements in young and old trees, also known as juvenile and adult wood. Trees are loaded with different loads (dead load, wind, snow, ...) throughout their life-span, which furthermore influences wood quality. In addition, the habitat has great influence on wood quality [32, 33].
- Wood defects: Due to natural growing and biological needs, wood produces imperfections. These defects are knots, compression (or tension) wood, overgrowth of open wounds, resin pockets, and damage due to rot and insects. In terms of the end-user and from an engineering point of view, these imperfections are considered to be defects, which reduce the wood quality often dramatically [61, 48].
- Time dependent behavior: Because of its origin and composition, wood properties may change due to environmental influences. This is very obvious when wood is subjected to changes in moisture content, which causes swelling and shrinkage and may result in the formation of cracks. Also the biological effects (rot, decay) change the mechanical properties over time. Neither the full consequences of a single influence nor the combined effect of various influences and possible interactions are understood at the moment [35].

**Literature review** The behavior of wood under uniaxial [13, 17, 20], shear [18], or multi-axial loads [21, 34, 43] has been intensively investigated by mechanical testing. Often the influences of particular parameters and loading scenarios are studied, such as the behavior of wood under dynamic loads [2, 74] or the (visco-)plastic behavior due to moisture changes [49]. The formation of cracks and the fracture of wood has also been extensively explored [19, 54, 86, 92].

Complementary to experimental investigations, newly developed approaches such as micromechanical modeling are capable of estimating stiffness [51] and strength properties of wood [5] from corresponding quantities at smaller length scales, which are universal for wood.

On the basis of experimental and numerical parameter indentification, models for structural behavior of wood have been developed and have been used for a large variety of applications [15, 16, 18, 38, 49, 62, 64, 67, 68, 83].

The investigations on wood behavior have shifted from uni-axial loading to bi-axial and in some cases also tri-axial loadings. These findings allow to create suitable models for wood where complex stress and strain-states occur, e.g. locally in dowel-type connections. Still, these interactions are not very easily understood, and the experimental procedures for determining the required parameters are difficult. Also the behavior under shear loads still needs further research. Currently a large variety of failure criteria is applied, which are not always compatible with each other. Standardization would be desirable.

## 2.2 Mechanical behavior of dowel-type steel-to-timber connections

Dowel-type steel-to-timber connections are effective types of connections, which can be applied for a large variety of purposes. The design as well as the manufacturing and

assembly processes are simple, since only a limited number of different items – the timber part, a steel plate, and a steel dowel – are used. Figure 2.3 shows a typical connection with a single dowel.

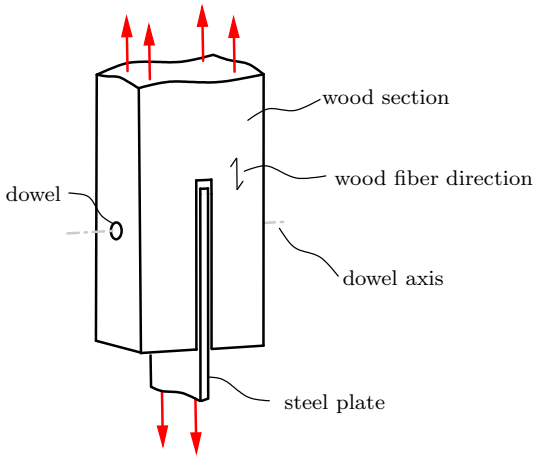


Figure 2.3: Typical dowel-type steel-to-timber connections with a single dowel loaded in tension parallel to the wood fiber direction.

The connection can be designed for a large range of loads by using dowels of different diameters or by mounting multiple dowels. In addition, dowel-type connections are suitable for transferring normal forces in tension and compression as well as bending moments and transversal forces. Dowel-type connections are used as joints for beams of equal dimensions or when secondary structures are connected to primary structures, but they can also occur as frame corners or supports of timber structures (see Figure 2.4 for typical situations).

The load-carrying principle is equal for all connection variations, regardless if the overall connection is loaded by tension or compression forces and/or by bending moments. In all cases, the loads are transferred locally by contact forces acting between the steel dowel and the timber parts. These contact pressures act at very small areas compared to the total cross-section of the timber members. The load-bearing behavior of connections is therefore highly dependent on the load-bearing capacity (embedment strength) and the stiffness of the wood compressed by the dowel (embedment modulus). Both are influenced to a great extent by the anisotropy of wood. The determination of the embedment strength and the respective embedment modulus is regulated in EC5 for connections for the general case (see Chapter 2.3), a more detailed procedure is found in DIN EN 383 [25]. The area for load transfer, and therefore the connection strength of connections, is derived by comparing the compliances of the wood parts(s) and the dowel, whereby the geometric stiffness (member width, dowel diameter and length) as well as the strength of the materials (wood crushing strength and dowel yield strength) are taken into account.

The fundamental concept for the estimation of the load-bearing capacity of dowel-type timber connections was developed by Johansen [55]. He studied the load-bearing mechanisms of timber-to-timber connections for dowels in single shear as well as in double shear for various combinations of widths of the timber parts and dowel stiffnesses. Assuming plastic deformations of wood under compressive loads and of the dowel in bending, Johansen derived design rules by formulating equilibrium of forces and moments. Kine-

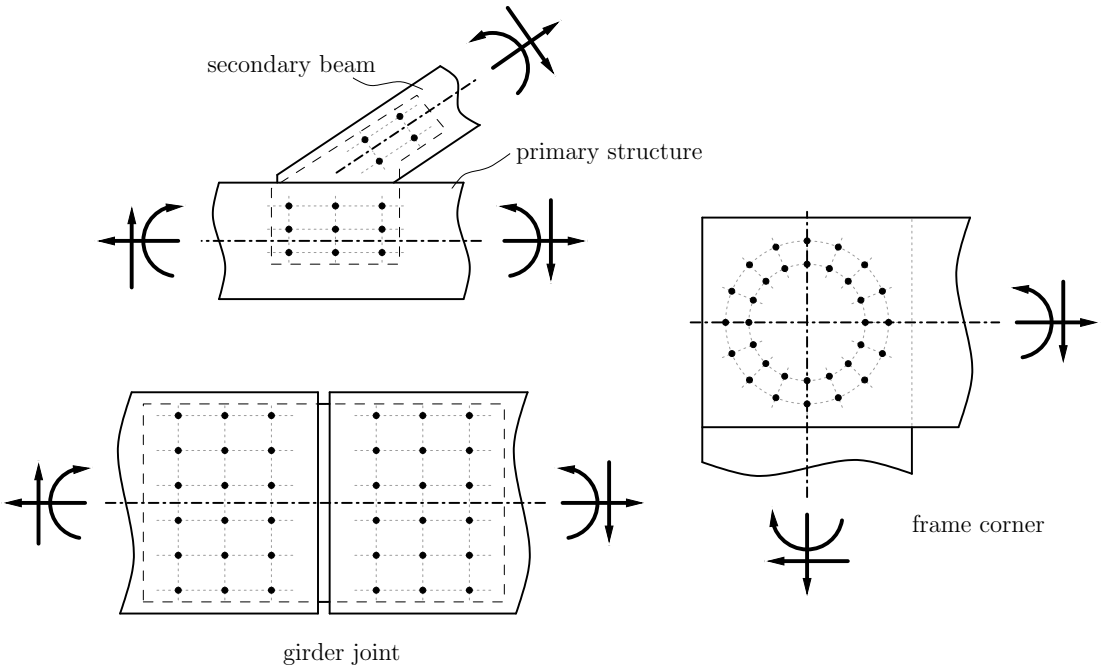


Figure 2.4: Multi-dowel connections loaded by general loads.

matic constraints were not considered. Johansen's findings are the basis for the design of timber-to-timber and steel-to-timber connections in the current design generation in timber engineering such as the EC 5 (see Section 2.3 for a detailed discussion of the design procedure). Johansen's equations are applied to all kinds of metal fasteners loaded in shear, such as dowels, bolts, screws, nails, and staples.

Since the thesis at hand primarily deals with double-shear steel-to-timber connections, the design guidelines in EC5 are presented for these types of connections only. Derived from Johansen's rules, three failure modes for symmetric steel-to-timber connections are distinguished based on the number of plastic hinges that form in the dowel. Connections with a low ratio of side width in wood to dowel diameter do not form a plastic hinge; connections of intermediate ratio form a single plastic hinge in the symmetry plane; and connections with a high ratio exhibit three plastic hinges at failure (Figure 2.5). All three failure modes are considered to behave ductile, since plasticity is considered in the dowel and also in wood under compressive load for arbitrary loading directions.

The influence of the main design parameters is outlined in the following:

- Side member thickness: The dowel is stiff compared to the wood in failure mode (f), so that with increased side member thickness, the contact area between dowel and wood increases linearly, which results in a linear increase of the load-bearing capacity of the connection. With further increased thickness, bending of the dowel leads to the formation of a plastic hinge in the dowel in the symmetry plane (failure mode (g)). In wide connections, the dowel gets in contact with the bore-hole on the outer end due to the bending, which leads to back-bending of the dowel and the formation of an additional plastic hinge (failure mode (h)).
- Wood density: The load-bearing capacity is increased for wood of high density,

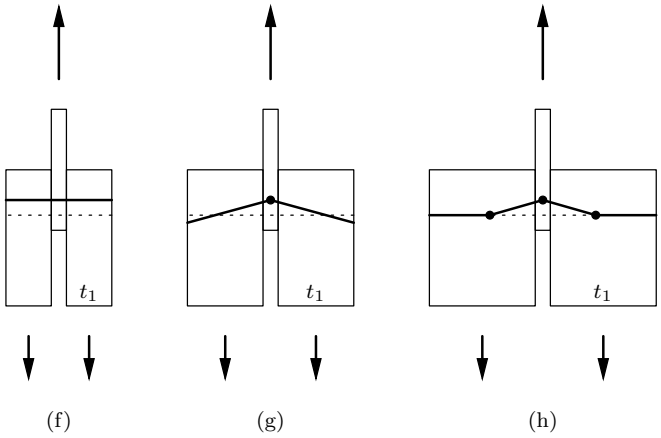


Figure 2.5: Plastic failure modes according to EC5 (numbering according to EC5), depending on ratio of connection width to dowel diameter

which shows higher embedment strength. Also the stiffness of the wood part is raised, which results in the formation of plastic hinges in the dowel at a lower thickness of the side members.

- Dowel diameter: At an increased diameter of the dowel, the plastic section modulus and, thus, the resisting moment in the dowel increase. This leads to an increased dowel stiffness compared to that of the side members. In consequence, the contact area increases in length and width, and a significantly higher load can be transferred for all failure modes.
- Steel quality: A dowel of better steel quality with higher yield and ultimate strength increases the load-bearing capacity of the connection, since the dowel can bear higher loads before forming plastic hinges.

Tension and shear stresses form when connections are loaded, which may lead to brittle failure. The prevention of brittle failure modes of connections is of great interest. Brittle failure occurs typically by transversal splitting in front of the dowels, by row shear of one or more dowel rows, or by block-shear failure (Figure 2.6). Brittle failure can be prevented by using slender dowels, which however reduce the load-carrying capacity of the connection. Alternatively, reinforcements by e.g. screws [9] or glued-on reinforcements [14] can reduce the risk of brittle splitting.

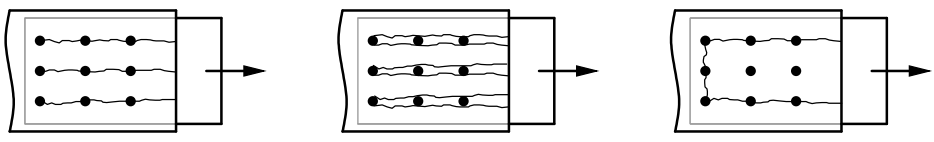


Figure 2.6: Typical brittle failure modes in multi-dowel connections.

In order to guarantee secure load transfer, a sufficient ductility of the connections has to be guaranteed. Considerable dowel deformations can only develop when non-fatal shear cracks occur. Ductility is of special interest in connections loaded by bending moments

and in multi-dowel connections, since each dowel reaches its maximum load often only at substantial displacements.

**Literature review**

- Dowel embedment: The embedment strength and respective stiffness are the basis for the design of connections and intensively explored. Bleron and Duchanois [10] investigated the effect of dowel friction for loads parallel and at an angle to the grain. Moraes et al. [65] studied the effects of temperature on the embedment strength, and Rammer and Winistorfer [73] determined the effects of varied wood moisture content. In Hwang and Komatsu [53], the wood specimens were loaded in the longitudinal, radial, and tangential section, whereby the dowel direction was varied. Awaludin et al. [4] tested specimens at different angles to the grain, which were subjected to compression and tension loads, respectively. The different embedment properties due to changed dowel diameter were studied by Sawata and Yasumura [80]. In Santos et al. [78], the influence of the test procedure on the resulting embedment strength, either according to the respective European [25] or the US standard [3], was investigated.

- Connection tests: The experimental data serves as a basis for deriving design rules and is of great importance for the verification of simulations. Schreyer et al. [85] tested connections under monotonic and cyclic loading, frame corners were subjected to dynamic rotational loads in Gnuschke et al. [45]. Moses [66] studied the effects of various parameters on the ultimate load, the ultimate displacement, and the failure mode of connections. Patton-Mallory et al. [69] performed a large number of connection tests under tension and compression loads, as did Santos et al. [77]. Special variations are also investigated, such as the behavior of connections under fire loads [60, 36] or the effects of decay on the performance of connections [79]. Sjödin and Johansson [88] and Sjödin and Serrano [90] subjected connections to variations of the moisture content. By means of real time radioscopy the deformations of the dowel during testing of connections was evaluated by Wehsener and Kasal [96]. Xu et al. [98] tested multi-dowel connections under tension, Fan et al. [37] tested connections with multiple plates.

- Loading at an angle: Since the behavior of connections loaded at an angle to the grain differs considerably from those loaded parallel to the grain direction, this field is of great interest. The performance of single dowels as well as the performance of dowel groups loaded perpendicular to the grain direction are studied in Ballerini and Rizzi [8], Borth et al. [11], Franke and Quenneville [39], Gattesco and Toffolo [44], and Schoenmakers et al. [84].

- Modeling and simulations: The prediction of the load-bearing behavior and capacity of connections by means of numerical simulations is gaining increased interest, and a large number of models have been developed. Common restrictions are the use of a purely elastic material behavior for wood and steel [77], where connection stiffness can be assessed only. In simulations where the two-dimensional models are used [89], only connections with a rigid dowel can be studied. More advanced models additionally simulate fracture behavior [39].

Using an elasto-plastic material description allows to simulate connections with slender dowels, so that dowel bending can be incorporated as well as a non-uniform stress distribution in thickness direction [12, 70, 71, 97]. Fracture mechanics has also been implemented in 3D models [47, 57, 76]. The simulations often show too high stiffnesses (e.g. in Resch and Kaliske [76]), so that some simulations consider a reduced wood stiffness in the vicinity of the dowel [52, 72].

A large variety of different approaches to model the behavior of dowel-type connections have been developed, which are often highly sophisticated and deliver interesting results and insight. On the other hand, the approaches are often contradicting, e.g. different failure models are applied to estimate the limit states of wood. Many simulations aim at a precise prediction of ultimate loads of connections but neglect a proper estimation of its stiffness. However with false predictions of stiffness, the calculated stress and strain states are obviously wrong, and it is therefore likely that the failure loads are predicted not correctly. The contact modeling in the simulations varies often dramatically, the uncertainties of proper contact modeling become apparent when considering that friction coefficients between 0.0 [77] and 0.7 [56] are employed in different simulations. Sjödin et al. [91] studied explicitly the importance of friction by a comparison of experiments and simulations with different coefficients of friction, and showed that very different stress states occur.

In the experiments on dowel-type timber connections and embedment tests, focus should be drawn to present the experimental set-up of the materials in great detail, e.g. of the wood material and the annual ring position should be recorded, the loading conditions explained in detail, more attention should be drawn on description of the bore-holes and the dowel properties. Furthermore, the behavior of the tested connections should be documented at all loading steps. This would allow to compare different experimental programs and their results more easily.

Regarding numerical simulations, focus should be drawn on the realistic description of the load-bearing behavior at all load stages, not only on e.g. the ultimate load. The documentation of the simulation models should also be increased in order to avoid irregularities between different approaches. The admissible boundaries of the simulations tools should be presented and observed. For realistic simulations, it is not always necessary to use the most advanced techniques which are used at later loading stages (e.g. crack formation tools), when there are discrepancies at more basic load stages.

## 2.3 Design situation

### 2.3.1 Stiffness determination

Stiffness in the Serviceability Limit State (SLS) is estimated by

$$K_{ser} = \varrho_m^{1.5}\, d \,/\, 23 \;, \tag{2.1}$$

with the slip modulus $K_{ser}$ in N/mm, where $\varrho_m$ is the density of the wood in kg/m$^3$ and $d$ the dowel diameter in mm. $K_{ser}$ is valid for a connection with a single shear plane and a single dowel, and was actually derived for timber-to-timber connections. When applied

to steel-to-timber connections, $K_{ser}$ should therefore be multiplied by 2.0 as suggested in EC5.

In the Ultimate Limit State (ULS), stiffness is reduced to two thirds of $K_{ser}$, so that $K_u = 2/3\, K_{ser}$ , with $K_u$ in N/mm. Both formulae for stiffnesses are empirically derived formulae.

Figure 2.7 gives the stiffness $K_{ser}$ for double-shear steel-to-timber connections for various dowel diameters in dependence of wood density $\varrho$. The influence of the dowel diameter on $K_{ser}$ is linear, while wood density is affecting $K_{ser}$ slightly over-linearly (a best-fit straight line in the considered density range results in a maximum deviation of 5%).

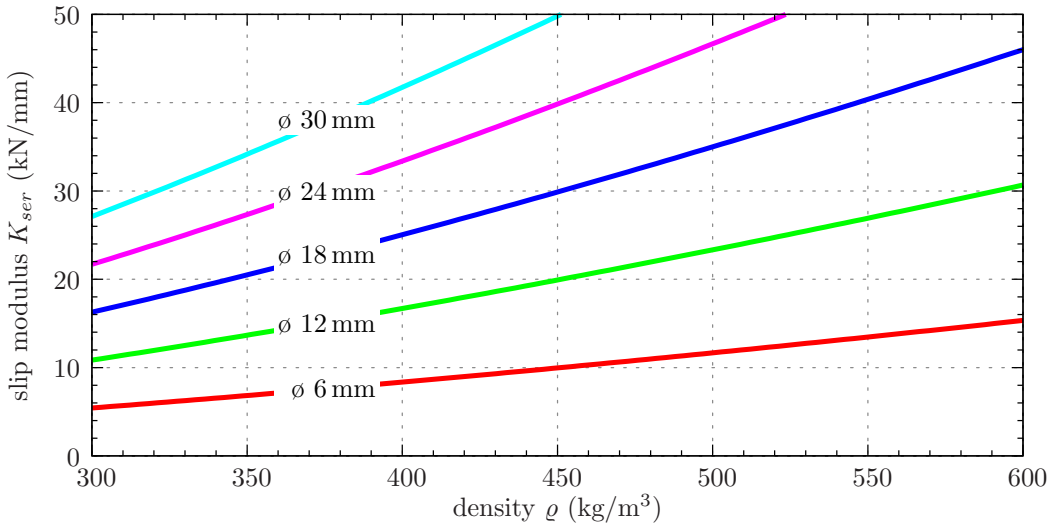


Figure 2.7: Slip modulus $K_{ser}$ for double-shear dowel-type steel-to-timber connections for a variation of dowel diameter, depending on wood density

### 2.3.2 Strength determination

The characteristic load-carrying capacity $F_{v,Rk}$ (in N) of a single shear plane in a dowel-type steel-to-timber connection according to EC5 follows from

$$F_{v,Rk} = \min \begin{cases} f_{h,1,k} t_1 d & \text{(f)} \\ f_{h,1,k} t_1 d \left[ \sqrt{2 + \dfrac{4 M_{y,Rk}}{f_{h,1,k} d t_1^2}} - 1 \right] & \text{(g)} \\ 2.3 \sqrt{M_{y,Rk} f_{h,1,k} d} & \text{(h)} \end{cases} \tag{2.2}$$

where (f), (g), and (h) denote the three characteristic failure modes (see Figure 2.5). The minimum of $F_{v,Rk}$ is always decisive. Mode $f$ describes connections without the formation of a plastic hinge, $g$ and $h$ describe connections with one or two plastic hinges, respectively.

In the formulae, $\varrho_k$ is the characteristic density of the wood in kg/m$^3$, $t_1$ the width of the wooden part in mm, $f_{h,1,k} = 0.082\,(1 - 0.01\,d)\,\varrho_k$ the characteristic embedment

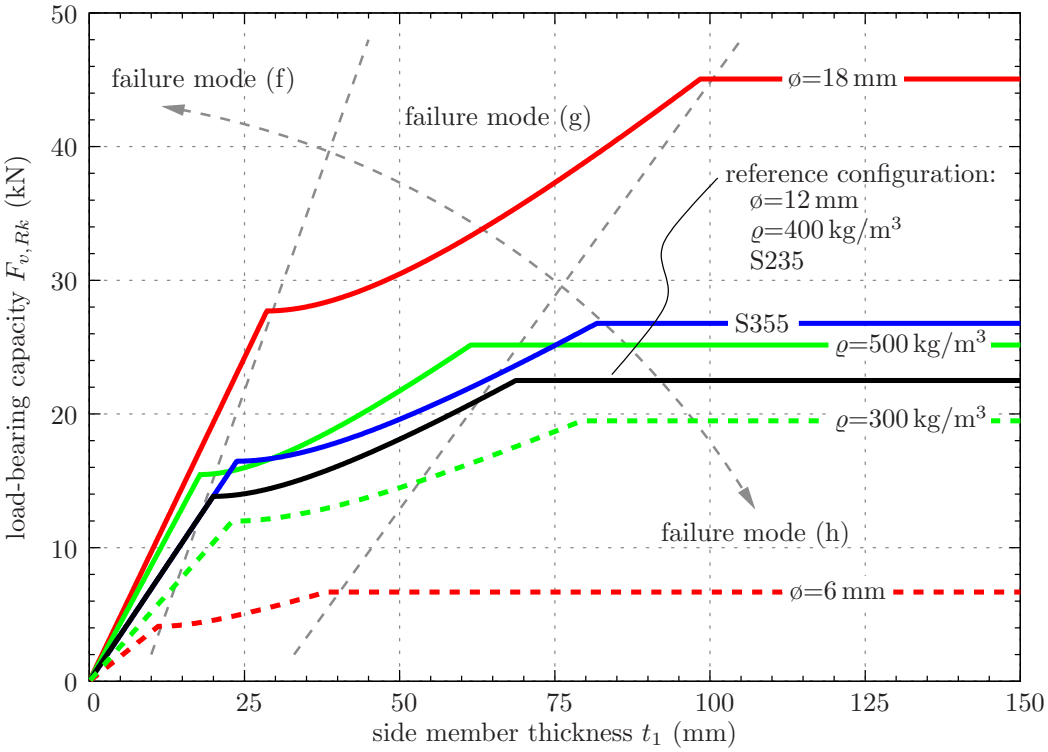


Figure 2.8: Load-carrying capacity $F_{v,Rk}$ for double-shear dowel-type steel-to-timber connections according to EC5 for a variation of wood density, dowel diameter, and steel quality, depending on the connection width

strength in N/mm$^2$, $d$ the dowel diameter in mm, $f_{u,k}$ the characteristic tensile strength of the dowel in N/mm$^2$, and $M_{y,Rk} = 0.3\, f_{u,k}\, d^{2.6}$ the characteristic plastic moment of the dowel in Nmm. The inconsistency of the units in the formulae underlines their (to a large extent) empirical origin. There are no restrictions on the maximum allowable displacements, and plastic deformations are allowed without limits. Effects of lateral reinforcement or increased friction between wood and dowel are not taken into account.

Figure 2.8 shows the load-carrying capacity $F_{v,Rk}$ for double-shear dowel-type steel-to-timber connections for a variation of dowel diameter and dowel yield strength as well as wood density in dependence of side member width.

In order to guarantee a secure load transfer, the geometry of the connection is subject to certain requirements on the minimum end and edge distances. In EC5, the minimum end distances are $a_{3,t} = \max(7\,d\,; 80\,\text{mm})$ and $a_{3,c} = 3\,d$ when loaded in tension and compression, respectively, and the minimum edge distance is $a_4 = 3\,d$ (Figure 2.9).

**Multi-dowel connections**

When the connection consists of multiple fasteners, the load-carrying capacity of the connection is defined through specifying an effective number of dowels $n_{ef}$. The effective number of a row of fasteners parallel to the grain depends on the dowel spacing in grain direction $a_1$, while it is independent of the number of rows parallel to the grain. These are not reproduced here since they go beyond the scope of the thesis.

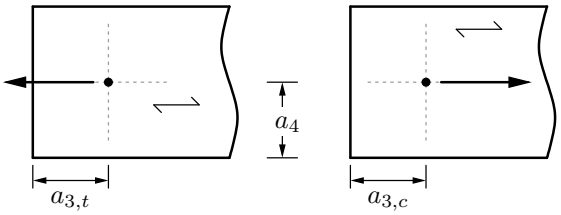


Figure 2.9: Minimum edge and end distances according to EC5 for single dowel connections loaded parallel to the grain direction.

**Loading at an angle**
Special rules apply when loads act at an angle to the grain. These are not reproduced here since they go beyond the scope of the thesis.

**Ductility**
The EC5 does not restrict the deformations of a single dowel connection, the assumption of plasticity is therefore not limited by any ultimate failure load.

## 2.4 Discussion

Dowel-type connections are commonly used in structural timber engineering for the transfer of a large variety of loads. Nevertheless, the design concepts currently used are far from sufficient for all of these many variations. The design rules are based to a great extent on empirical information. A stringent mechanical concept is not always followed, which becomes e.g. noticeable in the different approaches for strength and stiffness estimation: The first is formulated depending on side member width, while the latter is defined independently from side member width. In the design process, ductility of the connection is not taken into account, only minimum edge and end distances as well as dowel spacings have to be respected. The use of modern add-ons such as reinforcements are not considered in the EC5.

# Experiments

# Chapter 3

# Tests on single dowel-type timber connections

The following chapter presents a series of experiments on dowel-type steel-to-timber connections. Single dowel connections are tested, whereby the fiber orientation is aligned with the applied force.

The preparation of the test specimens as well as the testing procedure will be explained first. Next, the test results and particularly the effect of variations of material and geometrical parameters of the connections are presented. Finally, the experiments will be discussed, and an outlook on further investigations is given.

## 3.1 Introduction

In order to gain knowledge about the load-carrying behavior of dowel-type timber connections, a comprehensive test program was performed. In total, tests on 66 connections with 12 mm dowel diameter were carried out, whereby the influences of different material-related and geometrical parameters were systematically analyzed.

The width of the connections is varied, so that the three plastic failure modes according to EC5 [24] are covered. Additional variations of geometry concern the end distance and the edge distance based on the specimens with the standard dimensions. Wood density is significantly influencing the load-carrying behavior. The range of density of the used specimens is from 360 to 513 $kg/m^3$, the average being 430 $kg/m^3$. Little knowledge exists on the influence of friction between dowel and wood on the load-displacement characteristics of the connections, so that frictional properties of the dowel were varied by using smooth dowels, roughened dowels, and knurled dowels. Some of the specimens were tested with lateral reinforcements, so that splitting is prevented.

The experiments aim at a thorough understanding of the load-bearing behavior at all load stages, from initial formation of contact between the dowel and the bore-hole, to

the transition from elastic to plastic behavior in the dowel as well as in the wood, and up to the yield plateau and final failure of the connection (see Section 3.10). Parameters, which have significant influence on the respective loading stage will be identified.

## 3.2 Materials and methods

### 3.2.1 Preparation of wood specimens

The samples were prepared of Norway spruce [*Picea abies* (L.) H. Karst] taken from a wood trader. The poles were selected for appropriate length and the absence of knots in the area of interest. Four specimens were cut out exceedingly in longitudinal direction, which gives a series with good agreement of morphological and mechanical properties. Depending on the width of the poles, up to four series lying parallel were cut out.

The specimens were cut and planed to standard dimensions for length (868 mm) and thickness (72 mm). The specimens were produced in standard widths of 40, 100, and 200 mm, respectively (Figure 3.1). Variations of the basic geometry were applied later during testing. The slots for the steel sheets were cut out and the holes for the dowels drilled with a pistol grip drill, using an auger drill bit and a guiding device.

The steel plates for the load application were 8 mm thick and of steel quality S 355. The plates were rough and not coated. Conventional dowels of steel quality S 235 were used which were provided by HMR Jacob GmbH, Germany, a manufacturing company specialized on connection tools for timber engineering. The surface of the dowels was smooth in consequence of electrolytical galvanization.

### 3.2.2 Test set-up

The experimental program comprised tests on 66 specimens, which were grouped into 17 series (Table 3.1). A series contained four specimens by default, except for two series with only three specimens (Series 05 and 15) because of the limited length of the boards the specimens were cut from. Usually, specimens within a series were tested subsequently without changing the loading conditions in order to guarantee similar test conditions, except when the variation was done on purpose.

The experiments were carried out by means of a Walter & Bai LFM 150 uniaxial electromechanic universal testing machine. Measuring units used were a HBM Spider8 as well as a HBM QuantumX measurement unit, both being combined amplifiers and data acquisition systems, in addition to the measuring unit of the testing machine.

Strain transducers HBM DD1 with a nominal range of $\pm 2.5$ mm and inductive displacement transducers HBM WI with a measuring length of 10 mm were used to measure displacements, see Figure 3.2 for their positions. Displacements measured by transducers 1 to 4 and the strains measured by strain transducers A and B were used for internal reference only. The results obtained from the transducers 5 and 6 are the basis for the further evaluations. All measurement devices were applied symmetrically to the front and back side or the left and right side, respectively, in order to detect and avoid errors due to rotation or bending of the test set-up.

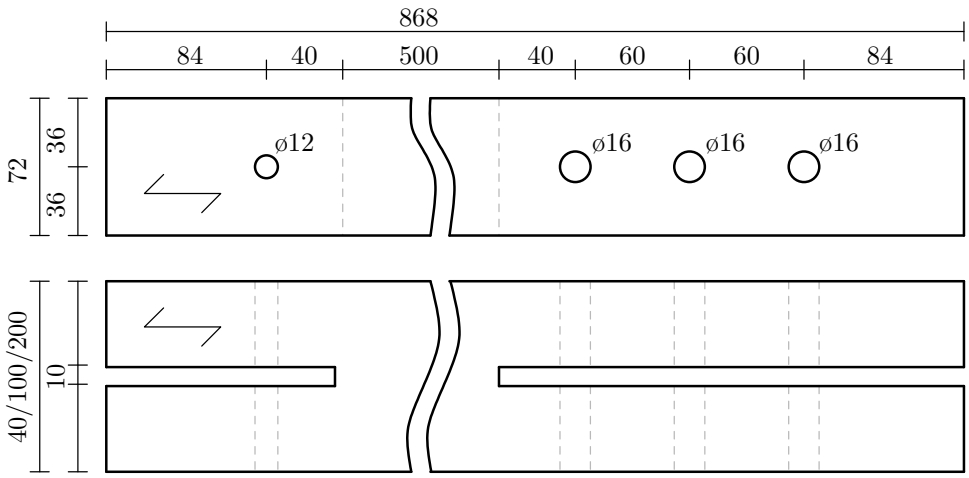


Figure 3.1: Dimensions (in mm) of test specimens

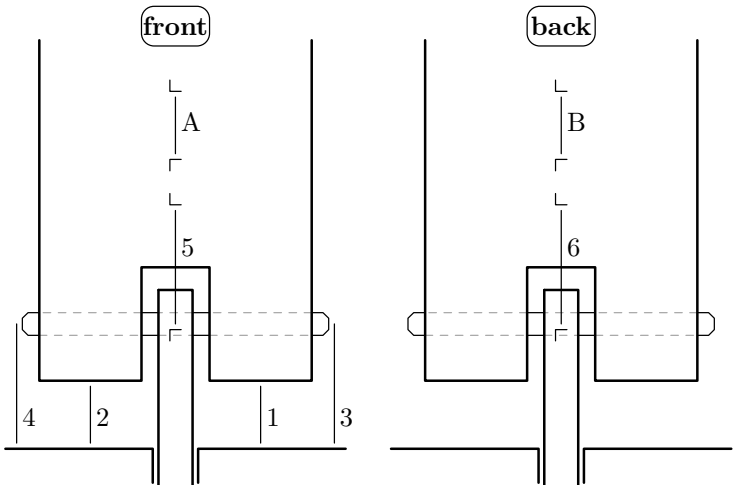


Figure 3.2: Typical application of measuring equipment; 1 to 6: inductive displacement transducers HBM WI; A and B: strain transducers HBM DD1

Right before testing, dimensions and weights of the specimens were measured. The holes were reamed so that the dowels fitted into the holes without applying excessive force. Specimen, plates and dowels were then assembled and placed into the testing machine.

The tests were performed displacement-driven. For most of the tests, unloading cycles at various load levels were carried out. Points of rest were chosen at steps of 5 kN for specimens of 100 and 200 mm wide, and at steps of 2 kN specimens for specimens 40 mm wide. An initial step of a load of 500 N with a resting time of 5 s was included in order to check whether the loading program of the testing machine was active and working properly. Figure 3.3 shows a typical loading scheme (Specimen 04_1), which is representative for all tests.

| Series | Width (mm) | Density (kg/m$^3$) | Variation |
|---|---|---|---|
| 01 | 100 | 485 | |
| 02 | 100 | 404 | |
| 04 | 100 | 502 | reduced end distance |
| 05 | 40 | 419 | |
| 05B | 100 | 374 | lateral reinforcement |
| 07 | 200 | 402 | |
| 08A | 100 | 513 | without unloading cycles |
| 08B | 100 | 489 | with lateral reinforcement |
| 09A | 40 | 458 | increased dowel roughness |
| 10 | 100 | 438 | |
| 13 | 100 | 495 | increased dowel roughness |
| 14 | 100 | 441 | reduced edge distance |
| 15 | 200 | 424 | increased dowel roughness |
| 16A | 100 | 384 | |
| 16B | 100 | 344 | reduced end distance |
| 16C | 100 | 360 | without unloading cycles |
| 16D | 100 | 374 | increased dowel roughness |

Table 3.1: Overview of test series

### 3.2.3 Test series

The influence of the loading speed during testing was examined in Series 01 and 02. No effect on the test results was detected within the range of applied loading rates of 0.1 and 2.0 mm/min. For the remaining tests the rate was fixed to 0.2 mm/min for specimens of 40 mm width, and to 1.0 mm/min for specimens of 100 and 200 mm width, respectively.

The influence of the following parameters was investigated:

- **Density:** Density varied between 360 and 513 kg/m$^3$. Its effects were tested in Series 01, 02, 08A, 10, 16A, and 16C on specimens of 100 mm width.

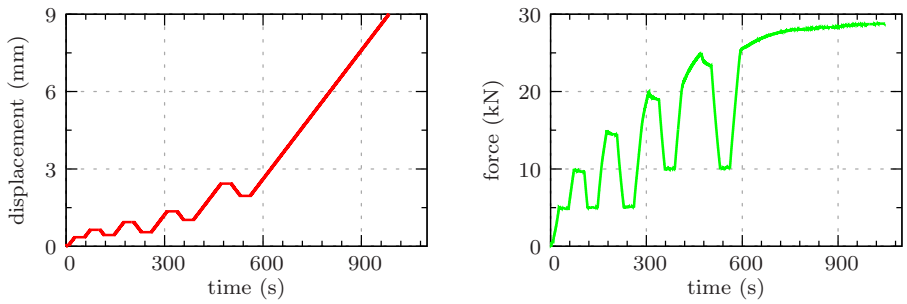


(a) time vs. displacement

(b) time vs. (responding) force

Figure 3.3: Typical loading scheme (Specimen 04_1): loading applied displacement-driven at a rate of 1 mm/min, rests of 30 s duration

- **Width:** The connection behavior at a standard width of 100 mm was compared to that of specimens of 40 and 200 mm width (Series 05 and 07, respectively), for specimens of intermediate density between 402 and 419 kg/m$^3$.
- **Dowel roughness:** Series 09A, 13, 15, and 16D were carried out using dowels of increased roughness. The dowels were sanded or engrailed, respectively. The effect of the roughness was investigated for all widths (40, 100, 200 mm), whereat for intermediate width, additionally density was varied.
- **End/edge distance:** In Series 16B and 04, the end distance of the dowels was reduced stepwise. Specimens of Series 14 were tested with a stepwise reduced edge distance.
- **Reinforcement:** Specimens of Series 05, 05B, and 08B were laterally reinforced with the help of clamps. The clamps help to prevent brittle failure in tension perpendicular to the fiber direction during loading and, hence, increase the maximum displacement at failure. The reinforcement was attached to specimens of small and intermediate widths, density variation was additionally studied on specimens of intermediate width.

## 3.3 Results

In the following, test results are presented and, in particular, the influences of the varied parameters on the load-bearing behavior are discussed. Thereby, a sample with standard dimensions and dowel characteristics serves as reference.

The load-displacement-curves shown are plotted for relative displacements between the wooden parts and the steel plate (mean value of results of transducers 5 and 6 in Figure 3.2). The maximum displacement of 10 mm that could be measured with the used devices was sometimes not sufficient to monitor the entire load-displacement path up to failure. As a remedy, the displacement transducers were repositioned during some tests, and the results assembled appropriately later.

### 3.3.1 Density

The density of all the samples varied considerably, between a maximum density of 513 kg/m$^3$ and a minimum density of 360 kg/m$^3$, the average being 430 kg/m$^3$. For the following comparison, all series with a width of 100 mm and an otherwise standard connection design were considered, i.e. Series 01, 02, 10, 08A, 16A, and 16C. These series cover the full range of densities with average values according to Table 3.2. In Figure 3.4(a), the load-displacement curves for the samples with the minimum and maximum density, respectively, of each series are shown.

The pronounced influence of density on the maximum load and on the connection stiffness is clearly visible. Normalizing the curves linearly to the average density ($\overline{F} = F\,\varrho/\varrho_{avg}$) results in very similar maximum loads for all curves (Figure 3.4(b)), which underlines the almost linear influence of density on this load-carrying characteristic.

Furthermore, density affects the load-carrying behavior in a qualitative way: Series with lighter wood tend to show higher displacements at failure and a longer yield plateau.

| | Series | | | | | |
|---|---|---|---|---|---|---|
| | 01 | 02 | 08A | 10 | 16A | 16C |
| $\varrho_{avg}$ (kg/m$^3$) | 485 | 404 | 513 | 438 | 384 | 360 |

Table 3.2: Mean densities of all specimens of the test series for analyzing the influence of density

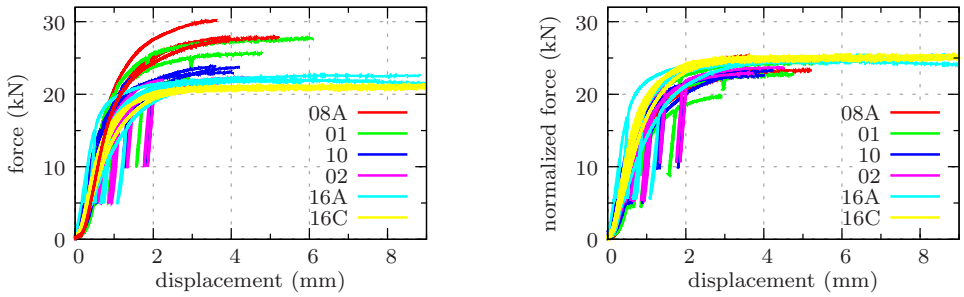


(a) regular (b) normalized by density

Figure 3.4: Load-displacement curves for all specimens of Series 01, 02, 10, 08A, 16A, and 16C ($\overline{F} = F\,\varrho/\varrho_{avg}$)

Light wood samples exhibit rather ductile failure modes, initiated by shearing off and followed by considerable displacements in the shear plane, until finally splitting failure occurs. Specimens of dense wood do not show a distinctive yield plateau, but a brittle failure mode with abrupt failure in the symmetry plane.

The different failure characteristics of light and dense wood result from the considerable influence of density on the behavior of wood under high compression, as they occur in front of the dowel. There, compaction is possible more easily for light wood with a higher percentage of lumens. Dense wood, cannot be compacted to a similar extent, and tensile forces in lateral direction lead to splitting failure at high displacements. Regarding stiffness, specimens with higher density are stiffer during first loading, while unloading stiffness is about the same for all densities.

### 3.3.2 Width

The width of the test specimens was varied in Series 02, 05, and 07, in which all specimens are of comparable densities in the middle range (Table 3.3). As mentioned in the introduction, the widths were chosen in order to produce the three main ductile failure modes of steel-to-timber dowel connections also considered in EC5, provided that premature splitting failure is excluded. The three different levels of failure loads, associated with different displacements at failure, are clearly distinguishable in Figure 3.5, which shows load-displacement curves for all series of the three test series.

Depending on the amount of bending of the dowel, controlled by its width-to-diameter ratio ($a/d$-ratio), considerably different contact situations are observed: In connections with a low $a/d$-ratio (Series 05), the dowel is in contact with the wood along the full length. This results in maximum utilization in terms of of the thickness-to-load ratio and a brittle failure mode. In connections with an intermediate $a/d$-ratio (Series 02), a

| Width | 02 | | | | 05 | | | 07 | | | |
|---|---|---|---|---|---|---|---|---|---|---|---|
| | 1 | 2 | 3 | 4 | 1 | 2 | 3 | 2 | 3 | 4 | 5 |
| 40 mm | | | | | x | x | x | | | | |
| 100 mm | x | x | x | x | | | | | | | |
| 200 mm | | | | | | | | x | x | x | x |
| $\varrho_{avg}$ (kg/m$^3$) | 404 | | | | 419 | | | 402 | | | |

Table 3.3: Series 02, 05 and 07 with variation of connection width

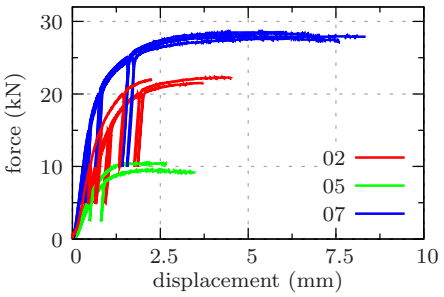


Figure 3.5: Load-displacement-curves for all specimens of Series 02, 05, and 07 with different failure modes

single plastic hinge forming in the symmetry plane results in concentration of the contact stresses in the center and detachment of the unloaded dowel ends from the surrounding wood. In connections with a high $a/d$-ratio (Series 07), the unloaded dowel ends get in contact with the wood opposed to the loaded side, causing back-bending of the dowel and the formation of secondary plastic hinges on both sides of the symmetry plane. A larger contact area is activated that way, and larger forces can be transferred by the connection. The displacements until failure increase significantly with increased width due to the more ductile failure mode and the reduced transverse splitting risk.

The stiffness during first loading is higher in wide connections, whereas the unloading and the reloading stiffnesses are about the same for all widths. Again, this is because of an enlarged contact area in wide connections.

### 3.3.3 Friction

The effect of friction between dowel and wood was investigated by using dowels with sanded or engrailed surfaces (Table 3.4). For the connection type with the standard width of 100 mm, two series were tested with low and with high wood density, respectively. Additionally, a single series was tested also for widths of 40 and 200 mm for specimens of medium density.

Due to the plastic deformations at the surface induced in the course of the engrailment, the engrailed dowels show a significantly greater outer diameter than the untreated smooth or sanded ones. Accordingly, the holes in the wooden samples were widened manually with the help of rasps. The net cross-section of these dowels, however, was reduced by the engrailment.

The higher friction of the roughened dowels significantly rises the maximum load and

| Roughness | 40 mm 09A | | | | 100 mm 13 | | | | 100 mm 16D | | | | 200 mm 15 | | | |
|---|---|---|---|---|---|---|---|---|---|---|---|---|---|---|---|---|
| | 1 | 2 | 3 | 4 | 1 | 2 | 3 | 4 | 1 | 2 | 3 | 4 | 1 | 2 | 3 | |
| Sanded | x | | | x | | x | | x | | x | | x | x | x | | |
| Engrailed | | x | x | | x | | x | | x | | x | | | | x | |
| $\varrho_{avg}$ (kg/m$^3$) | 458 | | | | 495 | | | | 374 | | | | 424 | | | |

| Reference series | 05 | | | 01 | | | | 16C | | | | 07 | | | |
|---|---|---|---|---|---|---|---|---|---|---|---|---|---|---|---|
| | 1 | 2 | 3 | 1 | 2 | 3 | 4 | 1 | 2 | 3 | 4 | 1 | 2 | 3 | 4 |
| $\varrho_{avg}$ (kg/m$^3$) | 419 | | | 485 | | | | 360 | | | | 402 | | | |

Table 3.4: Series with increased dowel roughness

the displacements at failure (Figures 3.6(a), (b)). These figures show load-displacement curves for Series 13 and 16D (both using specimens 100 mm wide) as well as of reference series with smooth dowels. The results confirm the expected effects of increased dowel roughness on the connection behavior, namely a significant rise of both maximum load and maximum displacement at failure. The impact is more pronounced in dense wood (Series 13) than in light wood (Series 16D), where the high compactibility of the wood already results in a very ductile behavior of the connection.

Unlike the behavior observed for the small and medium width samples, no differences were found between the use of engrailed or roughened dowels in Series 15 for the samples with a width of 200 mm (Figure 3.6(d)). All specimens could withstand displacements higher than 10 mm, where the displacement measurement was stopped prematurely before failure occurred.

When using smooth dowels, the width of the contact zone is only approximately half of the diameter of the dowels, resulting in a wedge-like action of the dowel. High tensile stresses in lateral direction will lead to splitting failure at low force and particularly at low displacements, and a characteristic brittle fracture occurs. Rough dowels reinforce the curved wood surface. They contribute to reducing lateral tensile stresses and to widening the contact area. Shear stresses are increased, and the maximal shear stresses occur at a greater distance from the symmetry plane of the connection. The combination of these effects leads to a higher load-carrying capacity and – because of the more ductile failure mode – higher displacements until failure.

The change of the failure mode from brittle to ductile in case of roughened dowels is confirmed by the observed fracture pattern. The high shear stresses evoked by the rough dowels lead to failure in the shear plane which is located nearly tangentially to the hole. Wood ruptures in the shear plane and is then crushed due to compression under the dowel. Lateral tension stresses, which could cause brittle, premature failure, do not develop in the symmetry plane.

The engrailed dowels are bent to a high degree so that, due to indentation, a significant tension force can be transferred in the direction of their axis in addition to the shear forces. This explains the considerable increase of the failure load of engrailed dowels

beyond that achieved with sanded dowels.

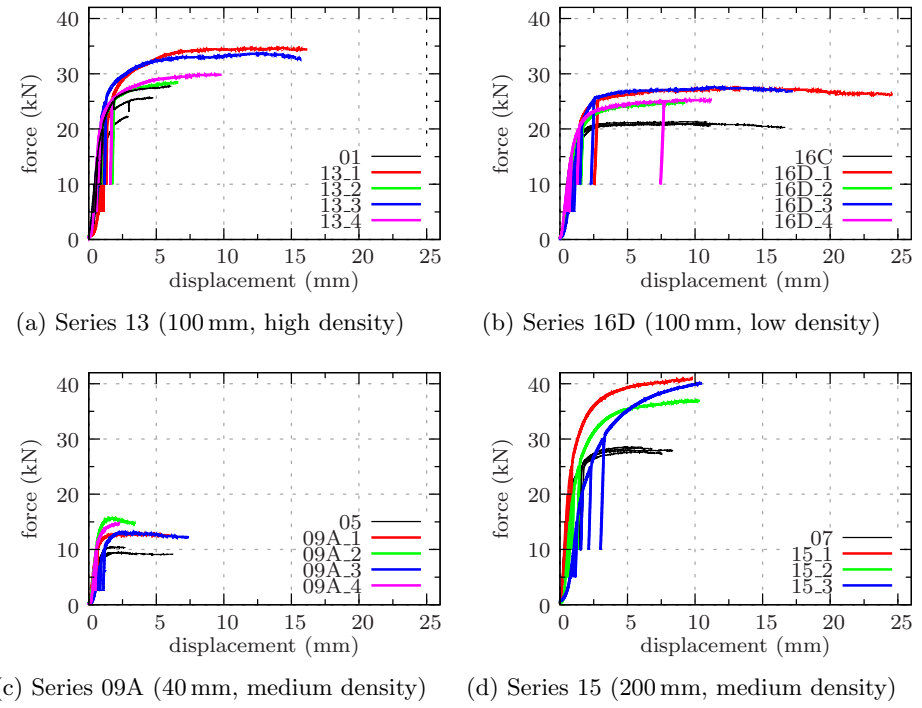


(a) Series 13 (100 mm, high density)

(b) Series 16D (100 mm, low density)

(c) Series 09A (40 mm, medium density)

(d) Series 15 (200 mm, medium density)

Figure 3.6: Load-displacement curves for all specimens of Series 13, 16D, 09A[1] and 15 with increased dowel roughness

### 3.3.4 End distance

The standard end distance of the dowels in the specimens was 84 mm, seven times the dowel diameter $d$, which is in line with the minimum end distance required in EC5. In Series 04 and 16B, the end distance of the samples with a width of 100 mm was reduced successively from this value to a minimum of 30 mm (2.5 $d$) in steps of 18 mm (1.5 $d$) (Table 3.5).

| | 100 mm | | | | | | | |
|---|---|---|---|---|---|---|---|---|
| End distance | 04 | | | | 16B | | | |
| | 1 | 2 | 3 | 4 | 1 | 2 | 3 | 4 |
| 84 mm (7.0 $d$) | x | | | | x | | | |
| 66 mm (5.5 $d$) | | x | | | | | | x |
| 48 mm (4.0 $d$) | | | x | | | | x | |
| 30 mm (2.5 $d$) | | | | x | | x | | |
| $\varrho_{avg}$ (kg/m$^3$) | 502 | | | | 344 | | | |

Table 3.5: Series 04 and 16B with specimens showing reduced end distance of dowel

[1] During testing of Specimen 09A_2, a machine error occurred, so that further testing until failure was not possible. Specimen 09A_4 failed prematurely before reaching the yield plateau.

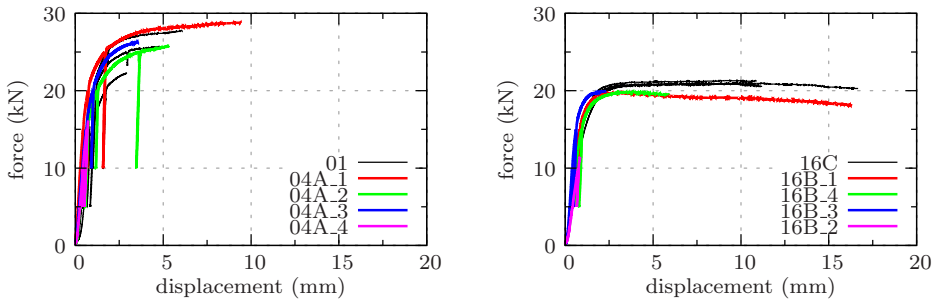


(a) Series 04 (100 mm, high density)

(b) Series 16B (100 mm, low density)

Figure 3.7: Load-displacement curves for all specimens of Series 04 and 16B with reduced end distance

A reduced end distance significantly reduces the maximum displacement (Figures 3.7(a), (b)), while the course of the load-displacement curves and the stiffnesses are not affected. Overly severe shortening results in reduced maximum load, since then the increased tension stresses in the specimens in front of the dowel can lead to premature splitting failure.

### 3.3.5 Edge distance

The edge distance of the regular specimens was set to 36 mm (3 d), again in line with the minimum edge distance according to EC5. This results in a total net thickness for transferring loads of 60 mm (5 $d$). In Series 14, the edge distance was reduced successively in steps of 6 mm (0.5 $d$) to 18 mm (1.5 $d$) (Table 3.6).

| | 100 mm | | | |
|---|---|---|---|---|
| Edge distance | 14 | | | |
| | 1 | 2 | 3 | 4 |
| 30 mm (2.5 $d$) | x | | | |
| 24 mm (2.0 $d$) | | | x | |
| 18 mm (1.5 $d$) | | | | x |
| $\varrho_{avg}$ (kg/m$^3$) | 441 | | | |

Table 3.6: Series 14 with samples with reduced edge distance of dowel

The observed load-displacement curves do not vary significantly for the different edge distances (Figure 3.8). Apparently, even the considerably reduced edge distance of 1.5 $d$ was sufficient to guarantee secure load transfer.

A bigger influence of the edge distance on the failure load had been assumed, since the pronounced anisotropy of wood with a very high stiffness in the fiber direction restricts transverse load distribution and, thus, load transfer to the outer parts of the connection. The stress concentrations around the hole seem to be lower than expected.

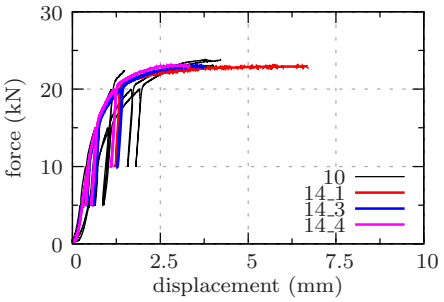


Figure 3.8: Load-displacement-curves for all specimens of Series 14 with reduced edge distance

### 3.3.6 Lateral reinforcement

In Series 05, 05B, and 08B, some of the specimens were tested with a lateral reinforcement (Table 3.9). Screw clamps were applied as external reinforcement, mimicking screws usually used as reinforcement in structural timber engineering.

| | 40 mm | | | 100 mm | | | | 100 mm | | | |
|---|---|---|---|---|---|---|---|---|---|---|---|
| | 05 | | | 08B | | | | 05B | | | |
| | 1 | 2 | 3 | 1 | 2 | 3 | 4 | 1 | 2 | 3 | 4 |
| Lateral reinforcement | | | x | x | x | x | x | x | | x | |
| W/o reinforcement | x | x | | | | | | | x | | |
| $\varrho_{avg}$ (kg/m$^3$) | 419 | | | 489 | | | | 374 | | | |

| | | | | | | | | | | | |
|---|---|---|---|---|---|---|---|---|---|---|---|
| Reference series | | | | 08A | | | | | | | |
| | | | | 1 | 2 | 3 | 4 | | | | |
| $\varrho_{avg}$ (kg/m$^3$) | | | | 513 | | | | | | | |

Table 3.7: Series 05 and 08B with lateral reinforcement

The load-displacement curves of Series 05 (40 mm) do not show significant differences regarding stiffness and maximum load (Figure 3.9(a)) but the displacements at failure are clearly higher for the reinforced Specimen 05_3. The lateral reinforcement retains lateral splitting, which enables to reach larger displacements and, thus, results in a more ductile behavior of the connection. It does not, however, increase the overall loading capacity of the connection. Respective gains in displacement amount to up to 50% in Series 08B with specimens of high density and to 50%-250% in Series 08B with specimens of medium density. The efficiency of a lateral reinforcement in wood of high density is limited, since at high loads the resulting splitting forces can exceed the load-carrying capacity of the reinforcement.

In Series 05B, only Specimen 05B_2 failed by lateral splitting in the symmetry plane, which was the expected failure mode. Specimens 05B_1 and 05B_3 split longitudinally in the clear wood section, which is a failure mode not commonly described.

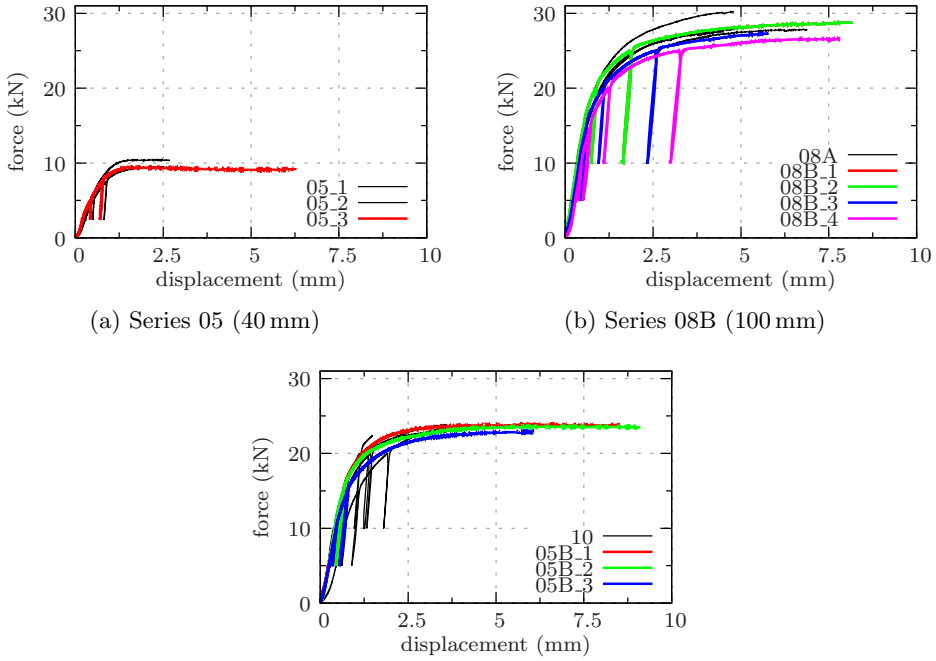


(a) Series 05 (40 mm)

(b) Series 08B (100 mm)

(c) Series 05B (100 mm)

Figure 3.9: Load-displacement-curves for all specimens of Series 05[2], 05B, and 08B with lateral reinforcement

## 3.4 Typical loading behavior

A wide variation of different set-ups and specimen properties was examined and resulted in very different failure loads and displacements. Nevertheless, except for outliers, all load-displacement curves show the same characteristic shape, and typical loading phases observed in all tests can be identified as marked in Figure 3.10.

### 3.4.1 Initial consolidation

The connections tested showed very low stiffness at the beginning of the loading process. Maximum stiffness was not reached until a significant load and displacement were applied.

This low stiffness is probably caused by imperfect contact between dowel and wood, which results from geometric roughness of the specimen in the contact zone as well as from imperfections of the contact surfaces. As regards the former, the axis of the borehole may not be drilled perfectly straight but with some curvature, and/or it may not be in exact right angles to the loading plane. The surface conditions of the dowel and the wood specimen affect the establishment of the load transmission. Depending on the drilling tool, the drilling speed, the wear of the tool, etc., the wood surface is not plane. It rather exhibits for example some waviness, as early wood and late wood are cut differently, or some roughness, as the fibers are not cut perfectly but in a frazzled

[2]Due to a machine-error, the test of Specimen 05_3 had to be stopped before failure occurred. Most likely an even higher displacement could have been reached.

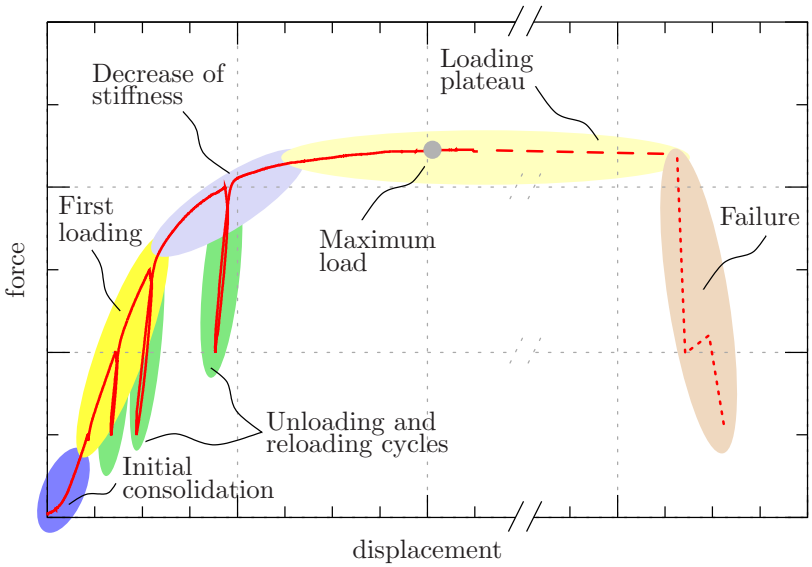


Figure 3.10: Individual loading phases of a typical dowel-type connection

manner. The effects of the quality of the surface of the bolt-hole on the load-deformation characteristics are described by Soltis [93] in detail.

Both, geometric and surface imperfections, lead to a softer connection stiffness at the beginning of the loading, as the contact between wood and dowel is not yet fully established. It is assumed, that the consolidation process occurs over the total length of the dowel simultaneously in connections with a low $a/d$-ratio. In connections with intermediate and high $a/d$-ratios, the contact area evolves continuously during increasing load due to the progressive bending of the dowel.

### 3.4.2 First loading

This term refers to the phase which directly follows the consolidation process, and in which the maximum stiffness during first loading (as distinguished from un- and reloading stiffness) of the connection is reached. Also in this region, a non-linear course of the load-displacement curve is observed in most tests, and an approximation by a straight line is only possible over short sections. Perfect linearity cannot be expected, since consolidation is still ongoing (especially in wider specimens), and the material behavior of the wood starts to be nonlinear (plasticity in compression). The smaller the region of initial consolidation, the more reliably a linear region of maximum first loading stiffness can be expected (cf. Series 16A).

### 3.4.3 Unloading and reloading cycles

The stiffness in unloading and reloading cycles significantly exceeds the maximum stiffness during first loading. Unlike the first loading, the un- and reloading cycles show an approximately linear elastic behavior. The deformations upon the consolidation in the contact area and the plastic deformations of the wood matrix do not recede, and the

wood does not deform back to its initial form and behaves linearly.

During reloading, the dowel perfectly fits the surrounding wood, and no further adaption resulting in permanent deformations occur. The reloading path follows the unloading path, showing a considerably higher stiffness than during first loading, up to the previously achieved maximum load level. When the specimen is loaded further beyond this level, and the displacements exceed the level reached before unloading, the loading curve bends, and the curve continuous along the course of the first loading.

An identical behavior and equal stiffnesses during unloading and reloading were observed for all variations and all load stages, also regardless of the basic density or of the width of the specimens.

### 3.4.4 Decrease of stiffness, yield plateau

During further loading, the stiffness decreases dramatically, and the maximum load is reached. This decrease is caused by reaching the compression strength in parts of the wood matrix and the growth of the plastic deformations. Additionally, plastic hinge(s) form in the dowel in connections with intermediate and high $a/d$-ratios. The maximum load level and the ductility (i.e. the displacement until failure) depend significantly on e.g. density, frictional behavior, and lateral reinforcement.

Displacements until final failure differ considerably; in some specimens (e.g. specimens of very dense wood) the yield plateau was hardly reached at all. On the other hand, displacements were up to over 20 mm in soft specimens (e.g. Series 16D). Lateral reinforcement allowed to reach such levels of displacement also for specimens of medium densities. In case of an extensive yield plateau, brittle failure in the local wood matrix occurs (shear failure), which, however, does not affect the ductile behavior on a global level. Thus, shear failure is actually a necessity for a high ductility of dowel-type connections.

### 3.4.5 Failure

The last stage in the load-displacement-diagrams is final failure, which occurs spontaneously and results in a sudden load drop. The failure mode differs in respect of the same parameters as mentioned before in relation to the maximum load level, namely density, friction, and lateral reinforcement. The following failure modes were observed (failure planes are highlighted in Figure 3.11):

*Lateral splitting* occurs at low friction between wood and dowel and high wood density. It is a highly brittle failure mode caused by high tensile forces normal to the symmetry plane of the connection through the dowels axis. The final fracture surface need not follow the annual ring pattern, which marks the transitions between lighter, weaker early wood and denser, stronger late wood.

*Shear failure* generally occurs in combination with tensile stresses in lateral direction. The failure planes are parallel to the symmetry plane of the connection through the dowels axis, at a distance of about two-thirds of the dowel radius. In principle,

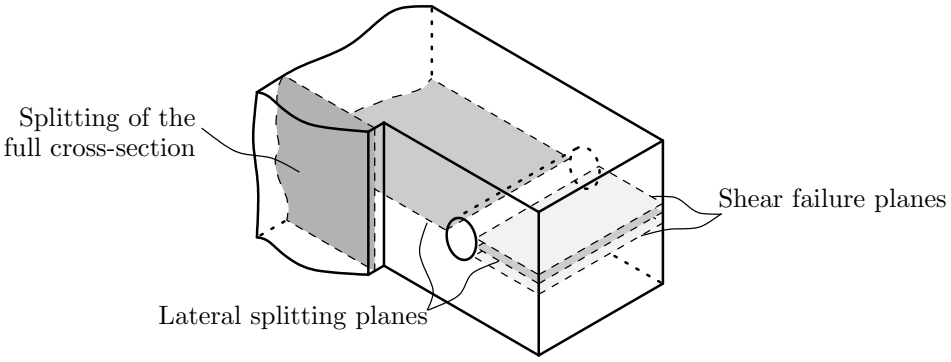


Figure 3.11: Observed failure modes

shear failure is a brittle failure mode, which nevertheless leads to ductile failure at the global level as described before.

Shear failure was observed in specimens with high friction between dowel and wood and in connections with lateral reinforcement. It occurs in cases where lateral splitting is prevented. Cracks do not propagate throughout the wood section, as shear stresses are highly dissipative, and high displacements can be reached before final failure occurs.

When an extensive yield plateau has developed upon local shear failure, lateral splitting is the final failure mode. Failure planes are then identical with the shear planes.

*Splitting of the full cross section* is the final failure mode when lateral splitting is prevented. Again, local shear failure occurs first, allowing large deformations and resulting in a globally ductile behavior. Finally, the highly bent dowel drives the wooden sections apart, so that tensile forces develop in the full cross section in the lateral part of the connection, acting on a plane normal to the dowel after the end of the slot.

## 3.5 Discussion

The extensive study performed has shown the distinct stages of the loading process, which certainly depend on each other. Bore-hole quality does not only influence the initial consolidation phase, when load transfer between dowel and wood is established, but does influence the maximum stiffness of the connections. Connection stiffness is additionally affected strongly by the connection width. The transition from elastic to plastic behavior is again influenced by the connection width: Connections with a low $a/d$-ratio show a rapid transition to the yield plateau, while stiffness is reduced more gradually in connections with medium and large $a/d$-ratios, exhibiting a single or three plastic hinges at failure. The maximum load depends again on the connection width, as a larger contact area is activated in wider connections and a higher load can be transferred. Additionally, wood density is strongly affecting the ultimate load, since it controls the compression strength and through that defines the load-bearing capacity at the bore-holes.

Friction has a significant influence on the ultimate load as well. The frictional shear stresses act as a reinforcement by preventing slipping of the dowels in circumferential direction and so prevent lateral splitting, consequently also increasing ductility. Additionally, a wider contact area can be activated when dowels with high frictional properties are used, which increases the loading capacity of the connection. The length of the yield plateau, i.e. the ductility of the connection, is affected by the connection width and the wood density. Lateral reinforcement has no significant influence on the ultimate load level, but it considerably increases ductility by preventing premature brittle splitting of the wood section. This effect is observed for specimens of all wood densities and widths tested, though the absolute increase is highest in wood of low and medium density and in connections with a small $a/d$-ratio.

In general, using wood of high density increases the load bearing capacity as well as the connection stiffness, but the risk of premature failure is raised due to crack formation. Light wood is therefore more favorable, when high ductility of the connections is required.

Compared to the maximum stiffnesses during first loading, a significant increase of the stiffnesses during unloading and reloading is observed in all specimens tested. This difference is caused by the adaption of the contact zone between dowel and wood under the compressive contact forces during the first loading, which result in non-reversible plastic deformations. Thus, the connection shows a decreased compliance during unloading and reloading than during first loading.

The end distance of the dowel from the unloaded end does influence the fracture behavior, since the cross section available for transfer of lateral tension stresses is reduced. A reduction of edge distance, on the contrary, does not affect the load-bearing capacity and the ductility.

### Outlook

The specimens tested are single-dowel connections with dowels of 12 mm diameter only, and the load is applied in wood fiber direction. Since this clearly does not represent the huge variety of possible connection designs, future tests should extend the scope of the current investigations.

The range of dowel diameters should be increased to its limits specified in EC5, which covers dowel diameters from 6 to 30 mm. This variation is essential, since it affects the varied ratio of the dowel diameter to the annual ring thickness. This ratio might affects the brittle failure modes observed and their occurrence in relation to connection design parameters.

To vary the load angle is of great importance as well. Experiments with loads applied in radial (or tangential) direction of the wood, or even at an arbitrary angle to the wood fiber directions should be carried out in order to cover the range of loading situations encountered in timber engineering. The behavior of wood in radial and tangential direction is fundamentally different from its behavior in longitudinal direction, particularly in compression, when hardening occurs once the yield limits are exceeded. Connections loaded at an angle to the fiber direction are commonly used when loads from (inclined) secondary structural members are transferred to main beams, which are usually loaded by tension forces and bending moments. Therefore, the stress field originating from the

connection is superimposed onto the stress field acting in the main beam, which results in very complex stress and strain distributions. The experiments should therefore consider the superposition of connection forces by the forces acting in the main beams.

Multi-dowel connections are of great practical interest as well, as the bearing capacity can be increased manifold compared to single-dowel connections. Additionally, bending moments and shear forces can be transferred by such connections. The disadvantage of testing multi-dowel connections is the statically indeterminate load distribution between the individual dowels, which complicates the evaluation of the results of these tests in term of forces acting on the individual dowels. The precision during manufacture is essential, especially for determining stiffness, since hole-clearance and contact properties are strongly affecting the load distribution. In the context of defining suitable design rules, which are generally formulated on the basis of the load-carrying capacity of a single dowel, the superposition of the stress and strain fields caused by the individual dowels is of great interest.

In all variations, the different loading behavior of connections loaded in tension or compression, respectively, should be investigated. The stress distribution around the boreholes is significantly different, since in compression the stresses are applied in the direction of the further load transfer, so that the influence of the shear stresses decreases significantly.

# Chapter 4

# Contact tests

In the following chapter, the procedure of determining the contact stiffness as a (non-linear) relation between contact pressure and contact deformation for wood on steel, based on experiments, will be explained.

An introduction to the topic will be given first which shall provide the underlying theoretical basis. Then the preparation of the test specimens will be described. The procedures for measuring their surface roughness properties and their deformation behavior under compression loads will be explained. Next, the procedure of determining contact stiffness from the compression tests will be explained.

## 4.1 Introduction

The term *weak boundary layers* (*WBL* was coined by Good [46], describing layers thicker than typical atomic dimensions with reduced mechanical properties compared to the bulk material. Stehr and Johansson [94] applied the concept of WBLs to wood. They distinguished between *mechanically* and *chemically weak boundary layers* (*MWBL* and *CWBL*), respectively. MWBLs are in general caused by mechanical treatment of wood, either by cutting or surface treatment. Surface features are typically sized in the range of $\mu$m to mm. CWBLs show in general molecular dimension, so they refer to a lower dimensional range, from Å to nm. The weak layers influence the mechanical behavior as well as the bonding behavior of glue and paint onto wooden surfaces.

In dowel-type connections, the load transfer takes place at surfaces in contact, e.g. between a steel dowel and wood. Stiffness and strength of the surface layers of the bore-hole are significantly lower than those of the surrounding bulk wood. The load carrying behavior at structural scale can therefore be influenced to a high degree by the surface layers, mostly in an undesirable way. Soltis [93] discusses the influence of the bore-hole quality briefly, stating that smooth bore-holes lead to higher bearing values and higher stiffness than rough bore-holes.

The surface texture is affected by the tools in use and varies depending on the technique applied, the feeding and cutting speed, and the wear of the tool. Additionally, wood morphology plays an important role: Wood species and density as well as certain wood features (e.g. the presence of knots) influence the surface texture and behavior.

### 4.1.1 Aim

The experiments aim on defining the contact behavior of wood surfaces. The goal is to identify relationships between the mechanical contact behavior and surface texture properties.

Norway spruce samples of three different densities, cut in the $R$-$T$-plane, were studied. Five different cutting techniques were applied to produce representative surfaces. Moreover, reference surfaces were created, which were cut by a microtome and a micro mill, respectively. In addition, drilled bore-holes in the same wood were examined.

The texture of the relevant surfaces of the specimens was investigated by means of a non-destructive sampling technique (Section 4.3). With this, sample-specific surface texture parameters were determined. The stiffness of the wood was determined by means of ultrasound measurements (Section 4.4). This bulk wood stiffness was later used for determining the contact stiffness.

In order to specify mechanical contact properties, compression tests were performed (Section 4.5). The measured deformations comprise deformations of the bulk wood as well as the surface layer. The contact displacements are extracted from the total displacement and separated into an elastic and plastic part. Mathematical relationshipsare defined for both.

Finally, the contact stiffness is related to the surface texture parameters determined beforehand. This allows to draw conclusions about the mechanical behavior from surface quality parameters measured by non-destructive techniques.

### 4.1.2 Basics of roughness determination

Surfaces of bodies can never be manufactured with absolute precision, so that real surfaces are always characterized by deviations from an ideal surface. Characteristic values of these deviations, which are used to describe the surface quality, are defined in national and international standards. These standards are jointly referred to as *geometric product specifications* (GPS) as specified in DIN V 32950 [31].

Surface texture describes repeated or random irregularities of the geometric surface area of the three-dimensional topography of surfaces. Six forms or orders of deviations are defined in DIN 4760 [23] at different scales, which provide information on the deviation from the ideal surface (Table 4.1). Deviations of first order are observed on the total area of the working piece. Deviations of second to fifth order are obvserved on sections of the working piece, showing decreasing feature size. Finally, deviations of sixth order are observed at the microstructural scale of the material. Terms, definitions and parameters of various shape deviations are specified in DIN EN ISO 8785 [30].

The surface texture is therefore a superposition of different shapes which gives the actual profile of a working piece (also termed primary profile). DIN EN ISO 11562 [26] defines

| Typical form of deviation | Order | |
|---|---|---|
| | $1^{st}$ | Primary profile (form deviation) |
| 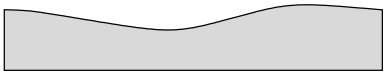 | $2^{nd}$ | Waviness profile |
| 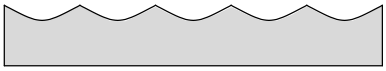 | $3^{rd}$ | Roughness profile |

Table 4.1: Form deviations of first to third order [23].

the transitions between the individual orders of deviation. The primary profile, the waviness profile, as well as the roughness profile are separated by filters.

DIN EN ISO 4287 [29] defines in the next stage individual parameters to characterize the surface deviations of different orders. These parameters are defined for two-dimensional analysis (i.e. analysis of profiles) only. The parameters typically determined are summarized in Table 4.2. The parameters are defined separately for the primary profile, $P$, the waviness profile, $W$, and the roughness profile, $R$, indicated by the capital letters in the parameters' names. Different kinds of parameters are specified: Some refer directly to the height profile and measure, for example, maximum heights or mean deviations. Others are derived from cumulative curves of the height distribution, such as the material ratio curve. Further explanations on the surface parameters are included in Appendix A.

| | | | | |
|---|---|---|---|---|
| Amplitude parameters (peak and valley) | | | | |
| $Pp$, | $Wp$, | $Rp$ | ... | maximum profile peak height |
| $Pv$, | $Wv$, | $Rv$ | ... | maximum profile valley depth |
| $Pz$, | $Wz$, | $Rz$ | ... | maximum height of profile |
| $Pt$, | $Wt$, | $Rt$ | ... | total height of profile |
| Amplitude parameters (average of ordinates) | | | | |
| $Pa$, | $Wa$, | $Ra$ | ... | arithmetical mean deviation |
| $Pq$, | $Wq$, | $Rq$ | ... | root mean square deviation |
| Curves and related parameters | | | | |
| Abbot Firestone curve | | | ... | material ratio curve |
| $Pk$, | $Wk$, | $Rk$ | ... | core roughness depth |
| $Ppk$, | $Wpk$, | $Rpk$ | ... | reduced peak height |
| $Pvk$, | $Wvk$, | $Rvk$ | ... | reduced valley depths |
| $PMr1$, | $WMr1$, | $RMr1$ | ... | material proportion 1 (peaks) |
| $PMr2$, | $WMr2$, | $RMr2$ | ... | material proportion 2 (valleys) |

Table 4.2: Surface profile parameters [29, 27] (a detailed description of the parameters is given in Appendix A).

An extension of the standards to a corresponding three-dimensional characterization is currently in progress [28]. The three-dimensional parameters are direct extensions of the two-dimensional parameters, and the respective formulae are modified appropriately. A

prefix *s* is used to denote such three-dimensional parameters. For example, *sRp* denotes the maximum peak within a sampling field. During the analysis of the experiments, only three-dimensional parameters were determined and evaluated,

## 4.2 Preparation of test specimens

The set of test specimens consisted of 45 cubes with dimensions $30 \times 30 \times 30\,\mathrm{mm}^3$, 12 cubes with dimensions $20 \times 20 \times 20\,\mathrm{mm}^3$, and specimens with half bore-holes of 12 mm diameter and a length of 30 mm. All specimens were prepared of Norway spruce (*Picea abies* [L. Karst]) with different densities and cutting techniques of the surfaces. Average densities were approx. 510, 440, and $390\,\mathrm{kg/m}^3$, respectively, so that a wide range of densities was covered. All preparation processes were performed in the Laboratory for Macroscopic Material Testing at Vienna University of Technology.

The wood samples were cut out from larger test specimens, which had been used prior for the tests on single dowel-type steel-to-timber connections described in Chapter 3. The samples were taken from the undamaged sections of the test specimens between dowel and back anchorage and cut into pieces of about 40 mm length (parallel to the stem axis) and a cross-section of approx. $72 \times 100\,\mathrm{mm}^2$ (Figure 4.1). The resulting specimens were free of knots.

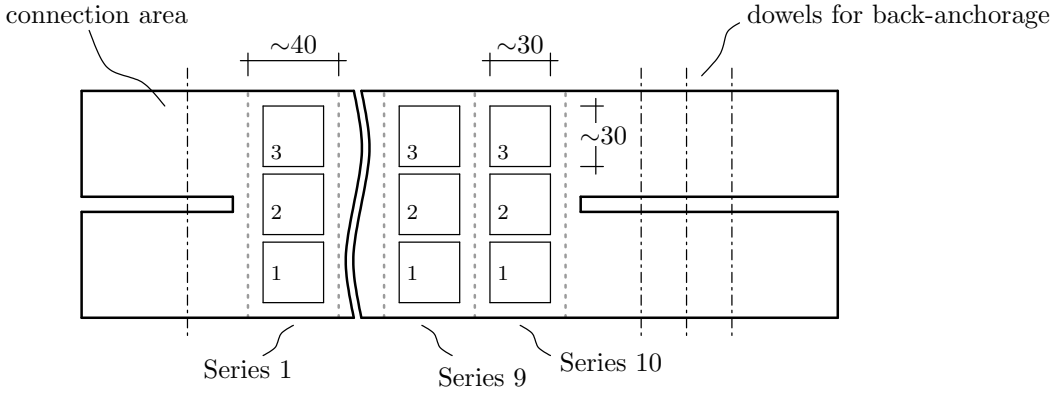


Figure 4.1: Preparation of specimens: Position of test series and specimens (dimensions in mm).

The pieces were then trimmed at both ends to a total length of approx. 30 mm. Different cutting tools were used in order to obtain surfaces of different qualities (the numbers in the enumeration are later used to refer to the different cutting styles):

1. Circular saw with a new blade: Optically, this gives a smooth and plane, continuous surface. Early wood and late wood rings are cut smoothly, with the early wood surface being rougher than the late wood one.

2. Circular saw with an old, worn-out blade: The surface is much rougher than with a new blade. The blade in use had blunt teeth, and some teeth were even missing. The roughness of early wood was distinctively higher than that of the late wood, but the surface was continuous.

3. Circular saw with an old, worn-out blade, running in the counter-direction: With this technique, the wood was not really cut but merely torn out. There was a distinctive difference between early wood and late wood surfaces. In low density specimens, the early wood was completely torn out and formed groove-like cavities. In wood of medium density, the early wood was again torn out in grooves, while the late wood surface was smooth. In high density wood, the cutting did not work properly anymore, as the wood was too dense to be cut and formed curved, non-parallel surfaces. Early wood was only partially torn out.

4. CNC milling machine using a face mill: Face milling produced plane surfaces with visible and sensible roughness. In total, a continuous surface was formed.

5. CNC milling machine using a peripheral milling cutter: This technique resulted in the smoothest surfaces. Due to the high compliance of wood compared to the stiff milling tool, vibrations during cutting occurred. A visible waviness was formed on the surface. Cutting was performed climb milling.

The wood pieces were next cut to cubes of approx. 30 mm side length. Series of three specimens each were produced with the same cutting technique, which were located next to each other (Figure 4.1), and therefore showed similar densities. The variation of the cutting tool in combination with wood of different density leads to very different surfaces, which are common in wood processing. Figure 4.2 gives an overview of the surfaces obtained with the different cutting styles.

**Microtome/Micromill surfaces**

In addition to these more or less common cutting techniques, surfaces were also cut by a microtome (cutting style 6) and a micromilling tool (cutting style 7) (Figure 4.3). Cubic samples of approx. $20 \times 20 \times 20\,\mathrm{mm}^3$, again with three different densities, were used for this purpose. The surfaces provide reference surfaces, at which the wood is cut at very high quality and the roughness is comparably low. The individual fibers are cut properly, so that there are no regions with torn-out or kinked fibers.

**Surfaces created by drilling**

All surfaces mentioned so far are created by techniques producing plane surfaces. However, a very common technique in wood manufacturing is drilling, e.g. for producing holes in dowel-type connections. During drilling, wood is cut at various angles to the fiber direction and both, conventional and climb milling zones are produced. Drilling speed and wear of the tool influence the quality of the surface (Figure 4.4). In order to investigate also such surfaces, test specimens from the dowel-type connections, showing three different densities, were cut into pieces of approx. 45 mm length, parallel to the axis of the bore-hole, with a cross-section of approx. $30 \times 30\,\mathrm{mm}^2$. These samples allow to qualitatively describe the surface of bore-holes (cutting style 8).

| Cutting style | Wood density: low | intermediate | high |
|---|---|---|---|
| 1 - Circular saw (new blade) | 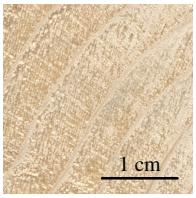 (a) 16B4-10-1 top | (b) 14_2-9-1 top | (c) 8A4-8-1 top |
| 2 - Circular saw (worn-out blade) | (d) 16B4-2-1 top | (e) 14_2-1-1 top | (f) 8A4-1-1 top |
| 3 - Circular saw (worn-out blade, counter-direction) | (g) 16B4-4-1 top | 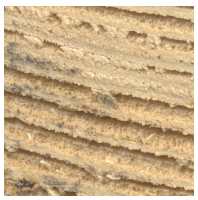 (h) 14_2-5-1 top | 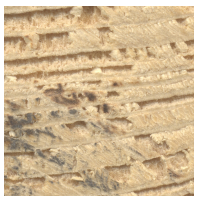 (i) 8A4-3-1 top |
| 4 - CNC (face mill) | 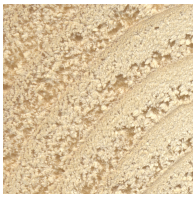 (j) 16B4-5-1 top | (k) 14_2-4-1 top | (l) 8A4-4-1 top |
| 5 - CNC (peripheral mill) | (m) 16B4-6-1 top | (n) 14_2-6-1 top | (o) 8A4-6-1 top |



Figure 4.2: Comparison of the surface quality produced with different cutting styles (samples of different series were lying aligned in stem direction).

| Cutting style | Wood density: low | intermediate | high |
|---|---|---|---|
| 6 - Microtome | (a) 16B4-1-1 top | (b) 14_2-2-1 top | (c) 8A4-2-1 top |
| 7 - Micromill | (d) 16B4-1-3 top | (e) 14_2-2-3 top | (f) 8A4-2-3 top |

Figure 4.3: Comparison of the surface quality of samples cut by a microtome and by a micromilling device, respectively (samples of the same density were lying parallel).

| Cutting style | Wood density: low | intermediate | high |
|---|---|---|---|
| 8 - Drilling | 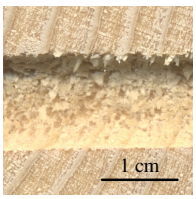  (a) 16B4 | (b) 14_2 | (c) 8A4 |

Figure 4.4: Comparison of the surface quality of samples with drilled bore-holes.

**Naming of the specimens**

The naming of the specimens follows a three-step procedure:

1. The first part refers to the specimen used in the tests on dowel-type connections, whereby 16B4 refers to the lowest, 14_2 to an intermediate, and 8A4 to the highest bulk wood density.

2. The next part, numbers between 1 and 10, gives the sequential arrangement of the cubical specimens within the piece of wood. Together with the first part, this defines a unique series of a certain combination of wood density and cutting type. The assignment to the cutting type is given in Figures 4.2 and 4.3.

3. The last part, gives the number of the specimen within a series. There are three specimens for cutting types one to five, and two specimens for cutting types six and seven.

Specimens of the bore-holes (cutting type 8) are solely denoted by the first part.

## 4.3 Determination of surface texture

### 4.3.1 Measuring system

The surface texture was measured by means of the optical surface measuring system FRT Microprof by Fries Research & Technology GmbH (FRT), Germany [41]. The system allows for contact-free measurement using different measurement systems for individual applications.

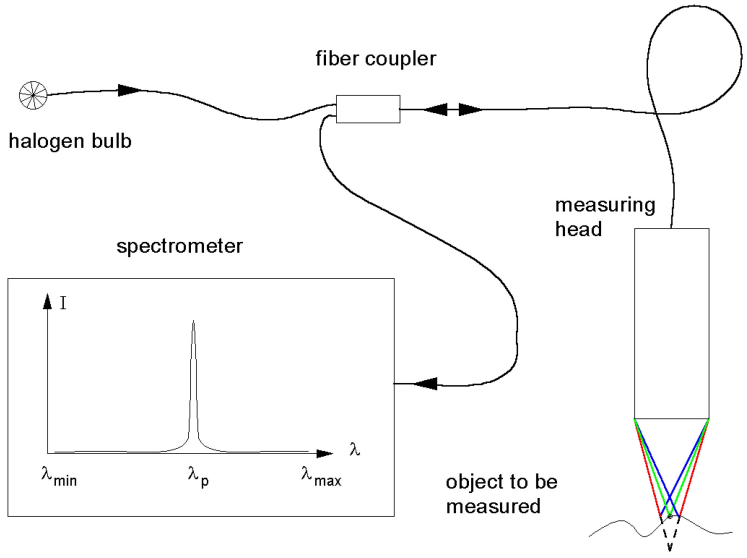


Figure 4.5: Confocal measuring principle [42].

Surface roughness measurements use white light, emitted from a halogen bulb as the light source. The light is focused onto the surface of the object, undergoing a certain chromatic aberration. Due to the chromatic aberration of the optical system, not a single point is in focus, but each wavelength is in focus at a specific distance to the source. The reflected light reaches a maximum for the wavelength actually in focus, which is seen as a pronounced peak in the spectrum of the reflected light. The wavelength of the peak gives information on the actual distance to the surface (Figure 4.5). The maximum range of measurement is 6 mm. The resolution is 200 nm in vertical and 8 $\mu$m in horizontal direction, respectively.

In horizontal direction, the samples are mounted onto a table, which moves in lateral direction. The maximum range of this movement is $350 \times 350\,\mathrm{mm}^2$, and the minimum distance between measured points is 0.6 $\mu$m.

If the height of the measured object is greater than the measurement range, multiple measurements can be performed with a varied basic distance of the sensor. The surface is scanned layer-wise. The total profile is then assembled from individual layer measurements (Figure 4.6). This measurement technique was applied when scanning bore-holes.

The software Acquire by FRT is used for controlling the measurements. It operates and controls the sensor as well as the movement of the mounting table and the vertical axis. Additionally, it allows for a real-time visual inspection of the results.

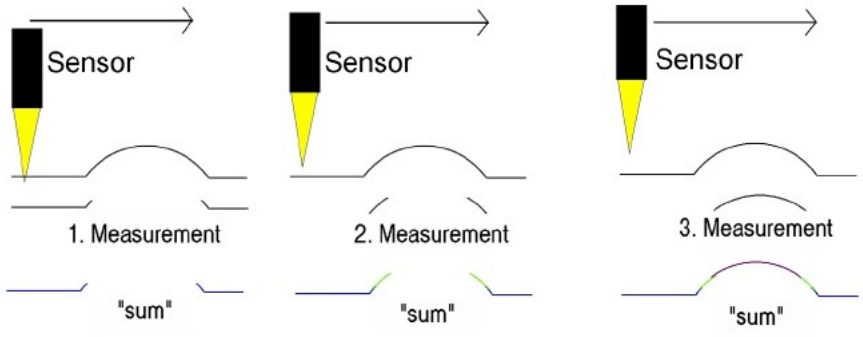


Figure 4.6: Multi-layer measuring principle [41].

### 4.3.2 Execution of measurements

The specimens were stored in warm and dry climate in the measurement room at a temperature of 27-28 °C and at a moisture content of 14 %MC. The climate was fixed due to other applications of the measurement system and could not be changed.

For the cubes sized 30 x 30 x 30 $mm^3$, a measuring field of 25 x 25 $mm^2$ was selected, which is smaller than the actual surface area, in order to not include surface irregularities close to the edges. The horizontal in-plane resolution was set to 25 $\mu$m in both directions, so that a grid of 1000 x 1000 px was recorded. The field was sufficiently wide to include several annual rings and to guarantee significant and reliable measurements. Nevertheless, the resolution was small enough to limit the duration of measurement to an acceptable period of approx. 50 min per surface scan. Additional measurements were performed with an in-plane resolution of 10 $\mu$m, which resulted in a field of 2500 x 2500 px. Only a single surface of each series was measured at this high resolution, since the measurement time was then as high as 300 min per surface scan. The high resolution scans were used as a reference for the standard tests with lower resolution.

The measurement field of the microtome-cut specimens was 15 x 15 $mm^2$ at a resolution of 25 $\mu$m, which yields in total 600 x 600 px. Additional reference scans of one surface per series were again done with 25 $\mu$m resolution (1500 x 1500 px).

The measurements yield the in-plane coordinates and the vertical distance in relation to the zero-point of the device. Additionally, the intensity of the reflected light is recorded. With the help of false color renderings of the vertical distance and of the intensity, respectively, the structure of the surface can be diagnosed in a first step. The pictures provide visual information on the average distances and height distributions, on the position and thickness of annual rings, and on the position of faults and rifts in the surface.

Figures 4.7 and 4.8 show false-color pictures of selected specimens. Dark colors refer to the lower boundary, light colors to the upper boundary of the height range. It is obvious, that samples of higher density show smoother surfaces, so that the color-range is more equally distributed for these samples.

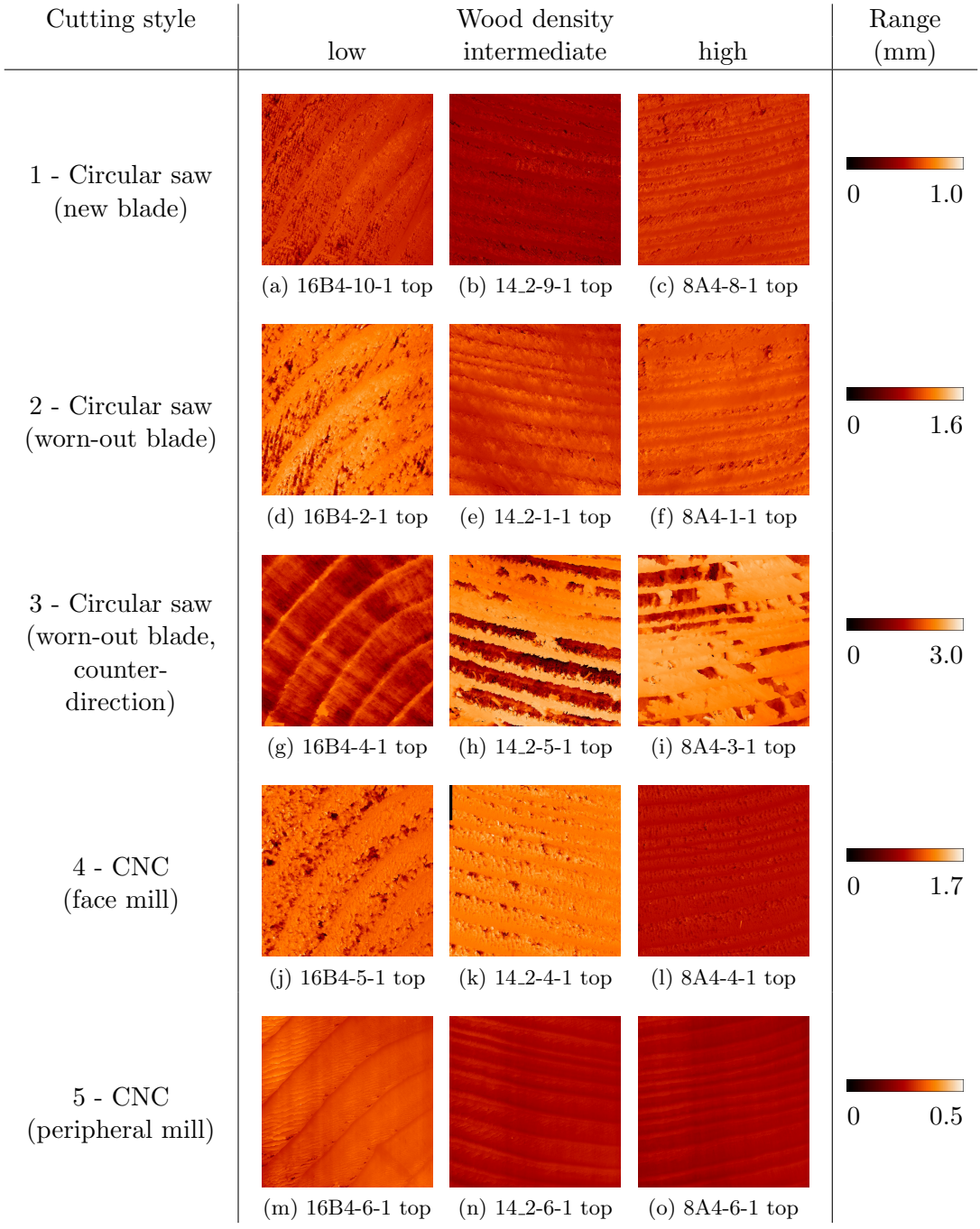


Figure 4.7: Typical results of surface texture measurements. The specified measurement range is valid for each cutting type (Dark colors denote the lower end and light colors the upper end of the height range, respectively.)

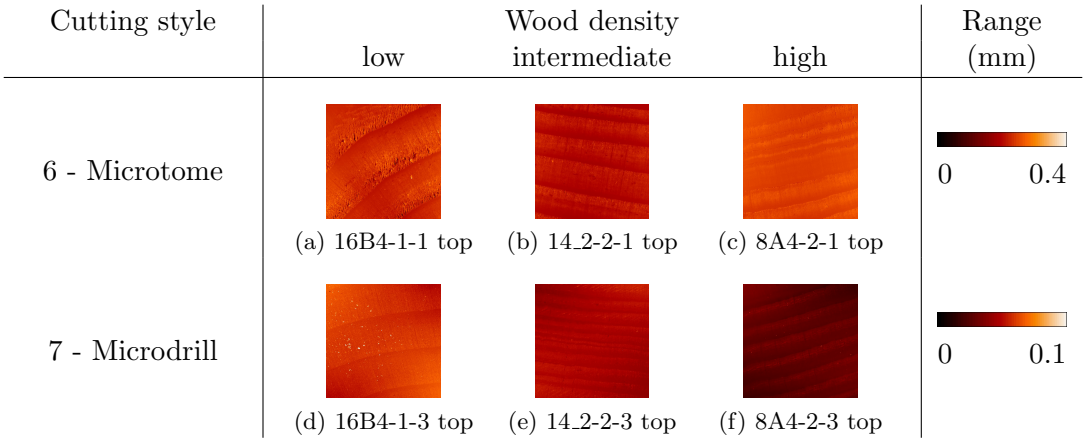


Figure 4.8: Comparison of the surface quality of microtome and microdrill-cut samples. (Samples of the same density were lying parallel)

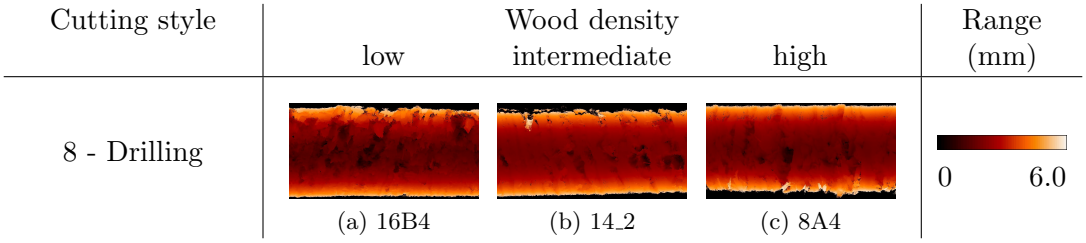


Figure 4.9: Comparison of the surface quality of samples with drilled bore-holes.

### 4.3.3 Evaluation of measurements

For evaluating the surface texture measurements, the program MARK III by FRT was used [40]. It allows for the analysis of measurement data for profiles (2D) and surfaces (3D). It reads *.frt-files produced by the Aquire-software as well as alternative data formats. For convenience, the program provides an interface for a batch execution of the evaluation process. MARK III determines the parameters defined in Section 4.1.2.

The sections for testing were $25 \times 25\,\mathrm{mm}^2$ with a resolution of $1000 \times 1000$ px. For determining the parameters a plane of first order was subtracted. The chosen cut-off length $\lambda_c = 5\,\mathrm{mm}$ is one seventh of the side length of the examined area. The full area was considered as relevant.

With the help of the software MATLAB R2010b, the results were further processed. The mean values and the standard deviations of the parameters of the primary profile, the waviness profile, and the roughness profile were calculated for each series of equal density and of the same cutting technique. Tables B.1–B.3, B.5–B.7, and B.9–B.11 in Appendix B provide an overview of the texture parameters.

**Surfaces created by drilling**

The surfaces of the drilled specimens could not be processed directly due to the curved surface. Five lines lying parallel to the bore-hole axis were defined for each specimen and

the profile along the lines determined. The length of the profiles was 25 mm so that the evaluation of the profile parameters was similar to the surface parameters determined. Again, the results of the profiles were averaged (Tables B.4, B.8, and B.12).

### 4.3.4 Comparison of bore-hole surfaces to plane surfaces

A comparison of the profile parameters for the bore-hole surfaces with the respective texture parameters for the flat surfaces allows to assess the quality of the bore-hole surfaces. An optical inspection of the bore-hole surfaces (Figures 4.4 and 4.9) already reveals that these surfaces are very coarse. They show valleys and peaks approximately following the annual ring pattern, which are more pronounced than for the flat surfaces created by cutting styles 1, 2, 4, and 5, but less distinctive than for cutting style 3.

A comparison of the texture parameters underlines the conclusions of the visual assessment. As Figures B.1–B.3 show for the Primary, the Waviness, and the Roughness profile, the parameters for the drilled surfaces are in the range between those for cutting types 2 and 4 and those of the very coarse cutting type 3.

## 4.4 Determination of clear wood stiffness

In order to mechanically characterize and categorize the wood samples, the stiffnesses of the samples were determined by means of ultrasonic (US) testing. US-testing is a simple and quick testing method, which enables determination of the (direction-dependent) stiffness of a material in a non-destructive manner, so that the surfaces of the cubes were not damaged.

### 4.4.1 Measuring system and data evaluation

The tests were performed using a pulser-receiver PR 5077 (Panametrics Inc.), a digital oscilloscope (WaveRunner62Xi), and a pair of ultrasonic transducers for longitudinal pulses with a frequency of 100 kHz. The setup was assembled by means of a mounting device with the specimen situated between delay lines shifting the signal by 3.77 $\mu$s time delay (Figure 4.10).

The tests were carried out in the transmission-through mode in longitudinal direction $L$ only. The oscilloscope gives the travel-time $t$ of the US-wave through the specimen with height $h$. The phase velocity follows therefrom as $v = h/t$. The component $C_{LLLL}$ of the elastic stiffness tensor is given under consideration of the wood density $\rho$ by

$$C_{LLLL} = \rho \, v^2 \, . \tag{4.1}$$

For the determination of contact deformations in the following, the elastic modulus in longitudinal direction, $E_L$, will be used. This is determined from results of the compression tests. US-testing provides an easy and reliable way to verify these results. For that purpose, the measured stiffness tensor component has to be converted into the corresponding elastic modulus. [59] used US-testing to determine the stiffness of Norway spruce samples in all three principal material directions. In addition, he measured the

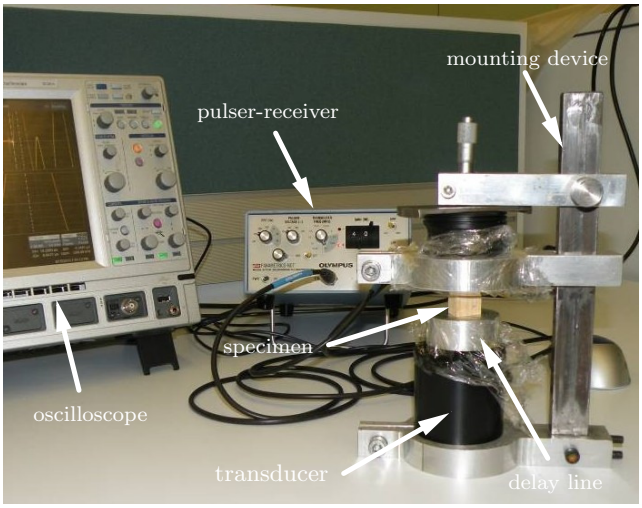


Figure 4.10: Setup for the ultrasonic tests (adapted from [7]).

modulus of elasticity by quasi-static tensile tests on samples originating from the same boards. The ratio of the stiffness tensor component and the respective modulus of elasticity in longitudinal direction amounted to about $C_{LLLL}/E_L = 1.10$ for a density range of approx. $0.45 - 0.49\,\mathrm{kg/m^3}$.

### 4.4.2 Results of US-measurements

The specimens used for the US-tests were weighed and measured in order to determine specific density and length of the individual cubes. The results of the US-measurements are compiled in Table (4.3) and Figure (4.11), respectively. The averages of all measured stiffnesses for the specimens of each series are 7.98, 13.36, and 16.00 GPa for small, medium and high density, respectively. Some of the surfaces were severely damaged so that the US-signal could not be interpreted properly. Hence no results are given for these specimens.

The results show a large variation depending on density and cutting type. This is partly due to the way of measuring density, in which the heights of the specimens are measured at their outer limits in longitudinal direction. This may cause uncertainties. Secondly, the surfaces' roughness might affect the accuracy of the results. The contact between the aluminum block used as delay line to the wood surface is not perfect, and the propagation of the US-wave may be disrupted by kinked fibers at the surface. In some of the specimens, only the late wood sections are is in contact with the aluminum block.

| Cutting style | Specimen | $h$ (mm) | $A$ (mm$^2$) | $\rho$ (kg/m$^3$) | $t$ ($\mu$s) | $C_{LLLL}$ (GPa) |
|---|---|---|---|---|---|---|
| 1 | 16B4-10-1 | 30.3 | 853 | 324 | 5.58 | 9.52 |
| 1 | 16B4-10-2 | 30.3 | 906 | 314 | 6.34 | 7.17 |
| 1 | 16B4-10-3 | 30.4 | 917 | 342 | 5.99 | 8.78 |
| 1 | 14_2-9-1 | 30.9 | 882 | 477 | N/A | N/A |
| 1 | 14_2-9-2 | 30.6 | 899 | 454 | N/A | N/A |
| 1 | 14_2-9-3 | 30.6 | 837 | 423 | N/A | N/A |
| 1 | 8A4-8-1 | 30.6 | 887 | 529 | 5.27 | 17.78 |
| 1 | 8A4-8-2 | 30.6 | 890 | 540 | 5.75 | 15.28 |
| 1 | 8A4-8-3 | 30.5 | 835 | 537 | 5.84 | 14.68 |
| 2 | 16B4-2-1 | 30.9 | 866 | 315 | 6.24 | 7.69 |
| 2 | 16B4-2-2 | 30.9 | 985 | 290 | 6.60 | 6.34 |
| 2 | 16B4-2-3 | 30.8 | 920 | 351 | 6.64 | 7.52 |
| 2 | 14_2-1-1 | 31.9 | 902 | 469 | 5.32 | 16.87 |
| 2 | 14_2-1-2 | 32.1 | 895 | 446 | 5.48 | 15.27 |
| 2 | 14_2-1-3 | 32.0 | 826 | 415 | 5.80 | 12.59 |
| 2 | 8A4-1-1 | 31.2 | 896 | 529 | 5.57 | 16.61 |
| 2 | 8A4-1-2 | 31.2 | 897 | 553 | 5.77 | 16.21 |
| 2 | 8A4-1-3 | 30.5 | 890 | 557 | 5.57 | 16.69 |
| 3 | 16B4-4-1 | 29.9 | 812 | 311 | 5.40 | 9.53 |
| 3 | 16B4-4-2 | 30.1 | 910 | 309 | 5.36 | 9.70 |
| 3 | 16B4-4-3 | 30.7 | 848 | 329 | 5.88 | 8.98 |
| 3 | 14_2-5-1 | 31.2 | 907 | 457 | 6.65 | 10.02 |
| 3 | 14_2-5-2 | 30.7 | 890 | 436 | 5.54 | 13.36 |
| 3 | 14_2-5-3 | 30.3 | 815 | 394 | N/A | N/A |
| 3 | 8A4-3-1 | 31.2 | 933 | 523 | N/A | N/A |
| 3 | 8A4-3-2 | 31.0 | 915 | 546 | N/A | N/A |
| 3 | 8A4-3-3 | 30.5 | 851 | 540 | N/A | N/A |
| 4 | 16B4-5-1 | 30.1 | 913 | 316 | 6.05 | 7.83 |
| 4 | 16B4-5-2 | 30.0 | 866 | 321 | 6.21 | 7.51 |
| 4 | 16B4-5-3 | 30.0 | 916 | 341 | 6.25 | 7.85 |
| 4 | 14_2-4-1 | 30.1 | 901 | 469 | 5.39 | 14.58 |
| 4 | 14_2-4-2 | 30.0 | 854 | 449 | 5.19 | 14.99 |
| 4 | 14_2-4-3 | 29.9 | 887 | 422 | 5.31 | 13.39 |
| 4 | 8A4-4-1 | 30.1 | 904 | 519 | 5.63 | 14.78 |
| 4 | 8A4-4-2 | 30.1 | 893 | 550 | 5.43 | 16.93 |
| 4 | 8A4-4-3 | 30.2 | 905 | 541 | 5.39 | 16.99 |
| 5 | 16B4-6-1 | 30.1 | 904 | 328 | 6.68 | 6.65 |
| 5 | 16B4-6-2 | 30.2 | 897 | 319 | 6.24 | 7.44 |
| 5 | 16B4-6-3 | 30.2 | 893 | 343 | 6.56 | 7.26 |
| 5 | 14_2-6-1 | 30.2 | 905 | 479 | 5.83 | 12.86 |
| 5 | 14_2-6-2 | 30.2 | 886 | 456 | 6.74 | 9.16 |
| 5 | 14_2-6-3 | 30.3 | 697 | 431 | 5.32 | 13.92 |
| 5 | 8A4-6-1 | 30.2 | 893 | 538 | 5.46 | 16.43 |
| 5 | 8A4-6-2 | 30.2 | 882 | 557 | 6.31 | 12.71 |
| 5 | 8A4-6-3 | 30.2 | 852 | 556 | 5.47 | 16.94 |

Table 4.3: Results of stiffness measurement by means of US-testing.

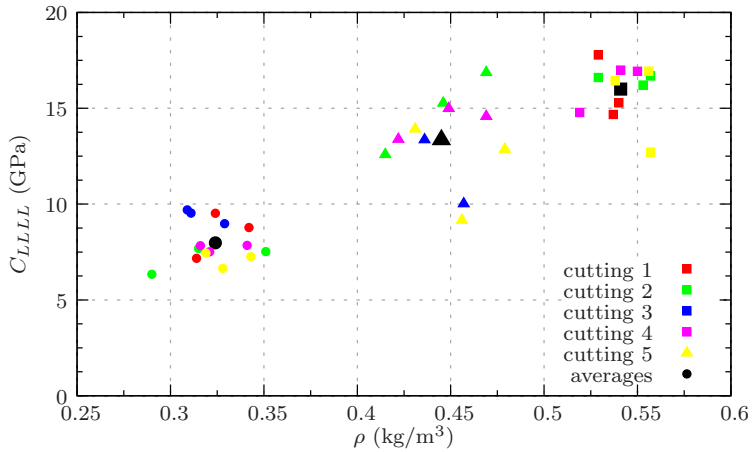


Figure 4.11: Correlation of stiffness tensor component $C_{LLLL}$ and wood density depending on cutting type.

## 4.5 Compression tests

### 4.5.1 Measuring system

The compression tests were performed at the Laboratory for Macroscopic Material Testing at Vienna University of Technology. The test cubes were inserted into a uni-axial testing machine (Walter & Bai LFM 150), and placed in between a purpose-built loading device. The loading was applied with a plunger, which allowed a rotation of the upper loading plate. This guarantees a uniform load transfer over the upper loaded surface also in cases of non-parallel loading planes (Figure 4.12).

Four inductive displacement transducers (HBM WI 10 [50]) were attached in the symmetry axes of the setup. The specimens were positioned in the center of the loading plate. The mean value of the measured results of the transducers thus gives the relative displacement of the loading plates.

A HBM Quantum X data acquisition system processed and recorded directly the data from the displacement transducers as well as the applied force. Machine displacement and applied force were additionally recorded directly by the compression test machine. The measuring equipment allowed for continuous logging of the applied forces and resulting displacements.

### 4.5.2 Performance of compression tests

The loading was performed displacement-driven in all tests at a rate of 0.5 mm/min, measured in terms of the machine displacement. The typical loading scheme consisted of several loading and unloading stages (Figure 4.13).

The specimen was put onto the lower loading plate, and the upper plate was lowered to the top of the specimen. The plunger was moved downwards until only a small gap was left opened.

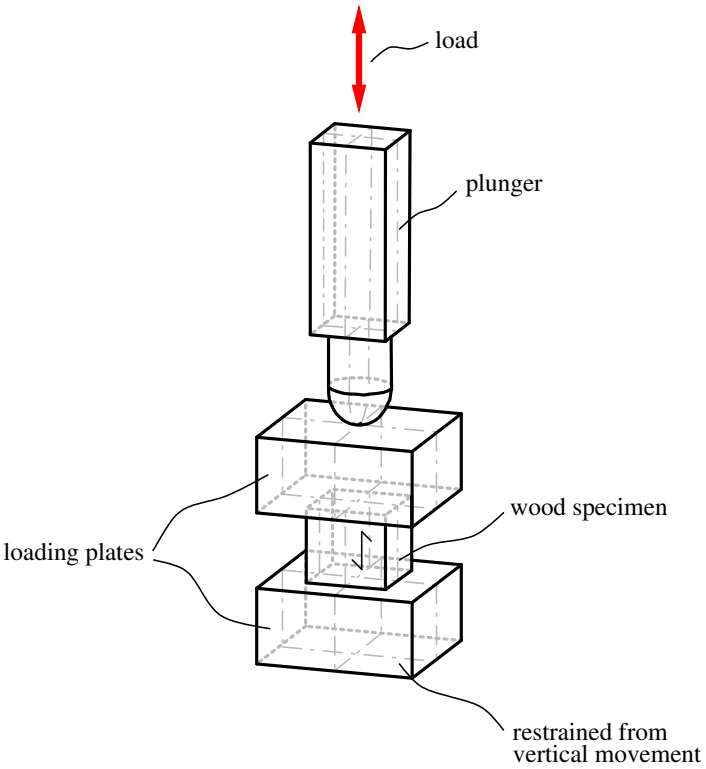


Figure 4.12: Setup of the loading device for the compression tests.

The actual test program started with applying a load of 1 kN. The load was fully released next, so that the plunger lost contact to the upper loading plate, and a small gap formed again. Then a load of 2 kN was applied and released again. Load steps, followed by full load releases, were done to load levels of 3, 4, and 5 kN; the following load steps were to 10 and 20 kN, respectively. In some of the tests two repetitive unloading and reloading cycles were performed at all load steps.

Depending on the yield load of the particular investigated wood sample, steps at higher loads were also added. Once the yielding plateau was reached, another unloading cycle was performed, followed by reloading to the yield plateau, and final unloading of the specimen.

The repetitive unloading and reloading enabled to obtain good results for the loading behavior also with increased contact stiffness. Furthermore, the development of non-recoverable displacements could be traced as well as the maximum load level and yield plateau.

### 4.5.3 Loading behavior during compression tests

The compression tests provide data on the relative movement between the upper and the lower surfaces of the specimen as well as the total force acting on the specimen. In the following, the typical load-displacement curve is discussed, and the main features are pointed out (Figure 4.14).

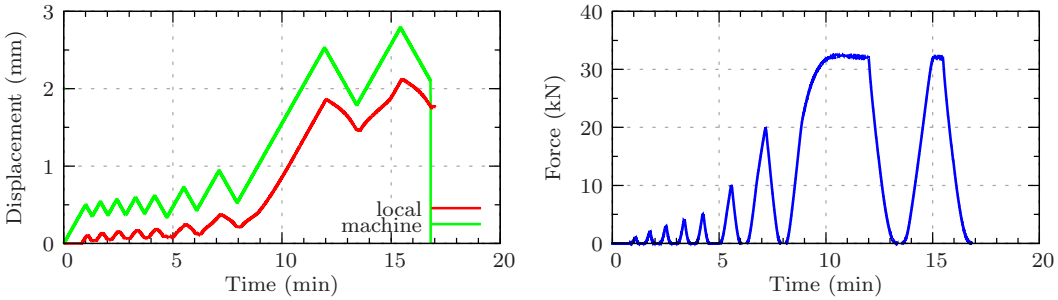


(a) Displacements (b) Reaction force

Figure 4.13: Typical loading scheme in compression test (Specimen 16B4-2-3).

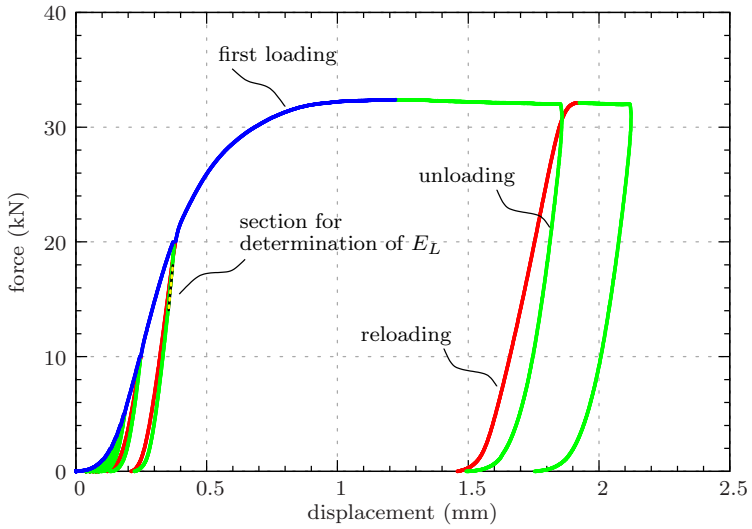


Figure 4.14: Typical load-displacement curve for compression test (Specimen 16B4-2-3). First loading (blue), unloading (green), reloading (red).

The main features are

- First loading: The term 'first loading' is used to refer to loading phases in which a particular load level is reached for the first time. Evidently, this is the case at the start of the test. Furthermore, it defines points after unloading and reloading when the load exceeds the previous maximum load.

  Initially, the first loading course is characterized by a low stiffness with a horizontal tangent, which is followed by an increase of stiffness. At increased displacement, a point of maximum stiffness is reached, before stiffness decreases again at further load increase. Once the yielding plateau is reached, the stiffness is almost zero, and the reaction force may even decrease.

  The low stiffness in the beginning is caused by the highly compliant interface zone, in which the contact between the loading plates and the wood sample is established. The interface zone undergoes plastic deformations. The decrease of stiffness is then caused by reaching the yield strength in the interface zone and later on in the bulk wood material itself.

- Unloading: Unloading occurs when the load is released. In the experiments, all unloading cycles were performed until full release of the load. The unloading stiffness is significantly higher at the beginning of unloading, but decreases when a lower load level is reached. The load-displacement curve shows almost a horizontal tangent again, corresponding to zero stiffness, right before the load is totally released.

  The unloading stiffness is mainly governed by the elastic stiffness of the wood material of the specimen. Only at very low loads, close to the point of total load release, the low elastic stiffness of the interface zone can increase the deformations.

  Distinctive permanent deformations remain, which are caused by a) plastic deformations in the interface zone at low loads, and b) plastic deformations of the bulk wood material at high loads.

- Reloading: The term 'reloading' is used to define regions in the load-displacement curve, where the load level had been reached at least once before. The reloading path follows qualitatively the unloading path in the load-displacement curve, with a higher curvature at low loads, but lower stiffness at higher loads.

### 4.5.4 Strength and stiffness determination

In order to characterize the wood samples and to finally be able to extract contact properties from the compression test results, strength and stiffness of the samples were evaluated first from the results of the compression tests.

**Stiffness**
It is assumed that the elastic stiffness of the wood is related to the stiffness of the unloading curve at high load levels. The relation between the measured quantities for the load $F$ and the compressive deformation $u$, and the modulus of elasticity $E_L$ in longitudinal direction is given by

$$E_L = \frac{\sigma_L}{\varepsilon} = \frac{F/A}{u/h} \ , \tag{4.2}$$

with $h$ denoting the height and $A$ the cross-section of the specimen. Interpolation of the almost linear part of the beginning part of the unloading curve yields the modulus of elasticity $E_L$ for the respective specimen (see Figure 4.14).

Figure 4.15 relates the modulus of elasticity $E_L$ to the respective density $\rho$ of the specimen. Comparing the stiffnesses determined from compression tests and from US-tests, respectively, yields a good correlation (Figure 4.16) and agrees well with ratios $E_L/C_{LLLL}$ of 1.0 - 1.2 given in literature [59].

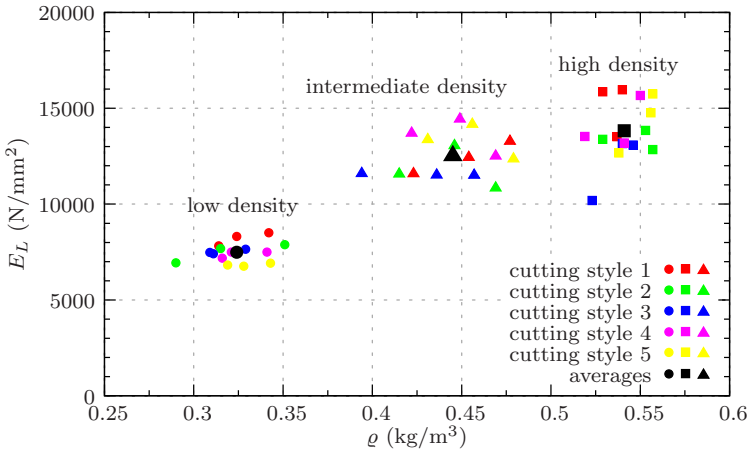


Figure 4.15: Relation of wood stiffness $E_L$, determined in compression tests, and wood density $\varrho$ depending on cutting type.

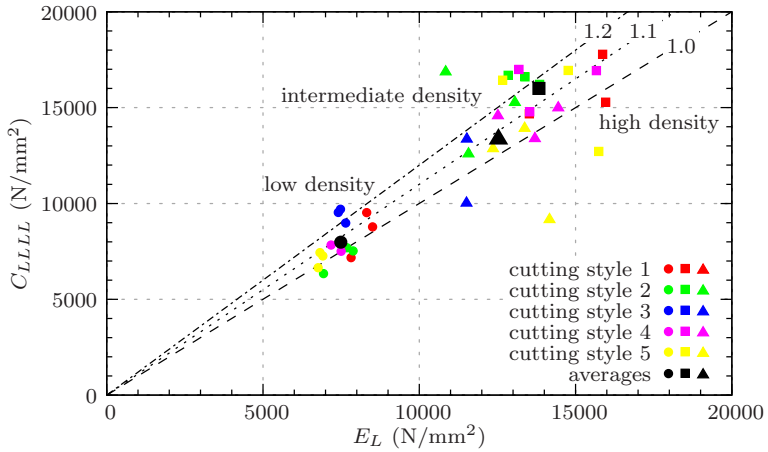


Figure 4.16: Wood stiffness $E_L$ from compression tests correlated to the tensor component $C_{LLLL}$ determined by US-tests, in dependence of wood density and cutting type.

**Strength**

The strength of the samples is determined by relating the measured maximum load $F_{ult}$ to the cross-sectional area $A$ of the specimen, so that

$$f_{y_{c_L}} = \frac{F_{ult}}{A} \ , \tag{4.3}$$

with $f_{y_{c_L}}$ the compressive strength in longitudinal direction. Figure 4.17 relates the yield strengths $f_{y_{c_L}}$ to the respective densities $\varrho$ of the specimens.

Table 4.4 provides average values of the stiffness and strength values for the bulk wood determined by means of compression tests for the three density categories, Table 4.5 for the individual specimens.

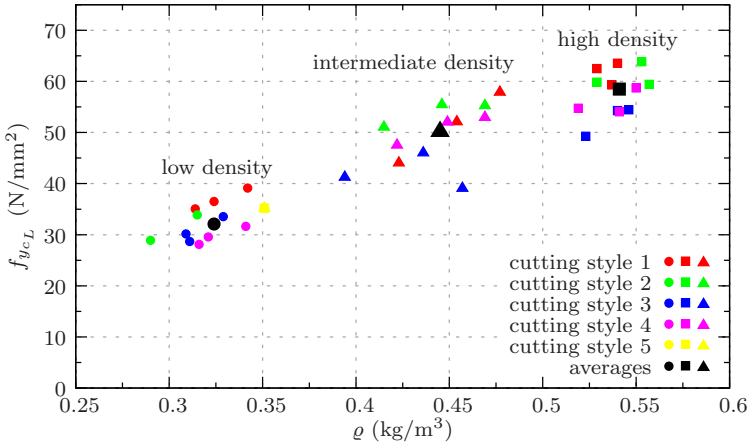


Figure 4.17: Relation of wood strength $f_{y_{c_L}}$, determined in compression tests, and wood density $\varrho$ depending on cutting type.

| | | Wood density | | |
|---|---|---|---|---|
| | | low | intermediate | high |
| $\varrho$ | (kg/m$^3$) | 324 | 445 | 541 |
| $f_{y_{c_L}}$ | (N/mm$^2$) | 32.1 | 50.2 | 58.5 |
| $E_L$ | (N/mm$^2$) | 7 491 | 12 533 | 13 828 |
| $C_{LLLL}$ | (N/mm$^2$) | 7 980 | 13 360 | 16 000 |

Table 4.4: Average stiffnesses and strengths for density categories determined from the results of the compression tests.

| Cutting style | Specimen | $\varrho$ (kg/m$^3$) | $f_{y_{c_L}}$ (N/mm$^2$) | $E_L$ (N/mm$^2$) |
|---|---|---|---|---|
| 1 | 16B4-10-1 | 324 | 36.5 | 8 316 |
| 1 | 16B4-10-2 | 314 | 35.0 | 7 820 |
| 1 | 16B4-10-3 | 342 | 39.1 | 8 508 |
| 1 | 14_2-9-1 | 477 | 57.9 | 13 286 |
| 1 | 14_2-9-2 | 454 | 52.1 | 12 444 |
| 1 | 14_2-9-3 | 423 | 44.1 | 11 594 |
| 1 | 8A4-8-1 | 529 | 62.5 | 15 866 |
| 1 | 8A4-8-2 | 540 | 63.6 | 15 963 |
| 1 | 8A4-8-3 | 537 | 59.3 | 13 523 |
| 2 | 16B4-2-1 | 315 | 33.9 | 7 683 |
| 2 | 16B4-2-2 | 290 | 28.9 | 6 937 |
| 2 | 16B4-2-3 | 351 | 35.2 | 7 883 |
| 2 | 14_2-1-1 | 469 | 55.3 | 10 847 |
| 2 | 14_2-1-2 | 446 | 55.5 | 13 060 |
| 2 | 14_2-1-3 | 415 | 51.1 | 11 576 |
| 2 | 8A4-1-1 | 529 | 59.8 | 13 384 |
| 2 | 8A4-1-2 | 553 | 63.8 | 13 847 |
| 2 | 8A4-1-3 | 557 | 59.4 | 12 843 |
| 3 | 16B4-4-1 | 311 | 28.7 | 7 408 |
| 3 | 16B4-4-2 | 309 | 30.1 | 7 480 |
| 3 | 16B4-4-3 | 329 | 33.5 | 7 647 |
| 3 | 14_2-5-1 | 457 | 39.1 | 11 512 |
| 3 | 14_2-5-2 | 436 | 46.0 | 11 521 |
| 3 | 14_2-5-3 | 394 | 41.3 | 11 597 |
| 3 | 8A4-3-1 | 523 | 49.2 | 10 190 |
| 3 | 8A4-3-2 | 546 | 54.4 | 13 083 |
| 3 | 8A4-3-3 | 540 | 54.3 | 13 164 |
| 4 | 16B4-5-1 | 316 | 28.1 | 7 178 |
| 4 | 16B4-5-2 | 321 | 29.6 | 7 499 |
| 4 | 16B4-5-3 | 341 | 31.6 | 7 497 |
| 4 | 14_2-4-1 | 469 | 53.0 | 12 515 |
| 4 | 14_2-4-2 | 449 | 52.1 | 14 444 |
| 4 | 14_2-4-3 | 422 | 47.5 | 13 701 |
| 4 | 8A4-4-1 | 519 | 54.8 | 13 532 |
| 4 | 8A4-4-2 | 550 | 58.7 | 15 668 |
| 4 | 8A4-4-3 | 541 | 54.0 | 13 188 |
| 5 | 16B4-6-1 | 328 | 29.3 | 6 764 |
| 5 | 16B4-6-2 | 319 | 29.6 | 6 822 |
| 5 | 16B4-6-3 | 343 | 32.7 | 6 916 |
| 5 | 14_2-6-1 | 479 | 56.5 | 12 362 |
| 5 | 14_2-6-2 | 456 | 52.8 | 14 165 |
| 5 | 14_2-6-3 | 431 | 49.5 | 13 368 |
| 5 | 8A4-6-1 | 538 | 59.3 | 12 668 |
| 5 | 8A4-6-2 | 557 | 63.8 | 15 744 |
| 5 | 8A4-6-3 | 556 | 61.1 | 14 762 |

Table 4.5: Stiffnesses and strengths determined from the results of the compression tests.

## 4.6 Contact stiffness

### 4.6.1 Mechanical model for contact stiffness

The results of the experiments indicate that the contact behavior shows distinctively different characteristics during first loading and during unloading and reloading, respectively. The behavior is more compliant during first loading due to non-recoverable, plastic deformations, mainly on the contact surface of the wood. Figure 4.18 shows the resulting course of the pressure-contact displacement course, which corresponds to the test results.

The contact stiffness, which refers to the ratio of pressure to deformation, is assumed to increasing monotonically with increased load, until the pressure-contact displacement curve shows a vertical tangent at high deformations, corresponding to infinite contact stiffness. The contact pressure is therefore not capped by absolute maximum. Nevertheless, contact pressures cannot exceed the yield strength of the clear wood.

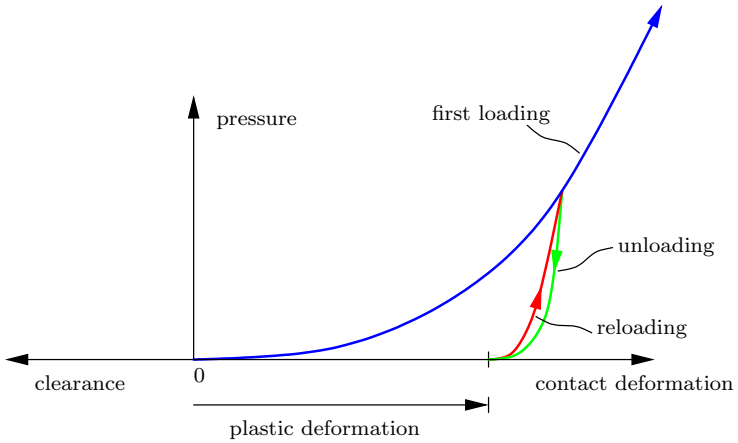


Figure 4.18: Pressure-contact displacement-relationship for contact behavior in normal direction.

Aiming at a mathematical description of the contact behavior, the courses of the first loading path and of the unloading and reloading path shall be described separately.

The deformations measured consist of four different contributions:

- plastic (non-recoverable) deformations of the contact layer, $u_{inter}^{pl}$,
- elastic deformations of the contact layer, $u_{inter}^{el}$,
- elastic deformations of the bulk wood of the specimen, $u_{wood}^{el}$, and
- plastic (non-recoverable) deformations of the bulk wood of the specimen, $u_{wood}^{pl}$.

In the following, the contact deformations of a single contact layer are determined. The deformations measured in the compression tests are divided by two which gives the average deformation of the two interface zones at the top and the bottom of the specimen, assuming equal behavior of these two interface zones.

The previously listed contributions sum up to the total deformation as

$$u_{tot} = u_{inter} + u_{wood} = u_{inter}^{pl} + u_{inter}^{el} + u_{wood}^{el} + u_{wood}^{pl} \ , \tag{4.4}$$

which is a function of the applied pressure $\sigma_L$. Additionally, the contributions depend on the wood material, especially on its density and on the cutting type of the respective specimen. The first two contributions in Equation (4.4), summarized as $u_{inter}$, describe the contact behavior in normal direction, while the latter two describe the elasto-plastic material behavior of the wood in longitudinal direction, referred to as $u_{wood}$.

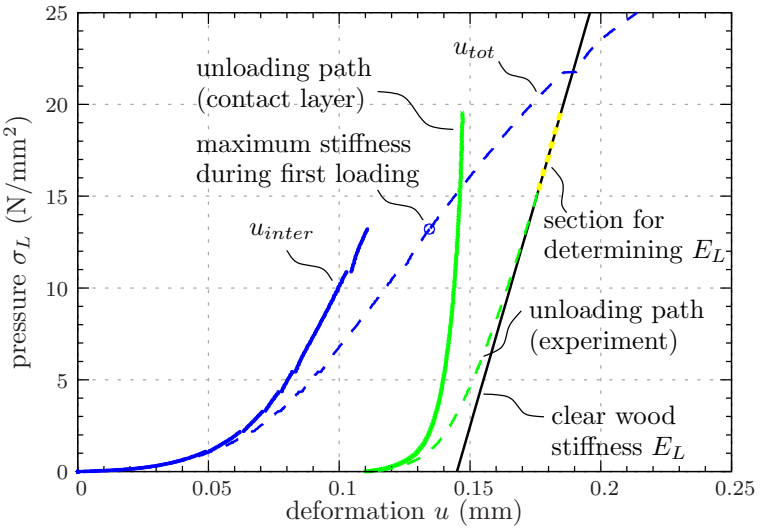


Figure 4.19: Separation of contact behavior from total deformation (exemplary for Specimen 16B4-2-3).

In order to separate the different contributions to the overall deformations and to distinguish between contact behavior and clear wood compression, the following assumptions are made:

Assumption I: Yielding in the bulk wood starts around the point where the initial loading curve shows its maximum stiffness and thus maximum slope. The reduction of the overall stiffness thereafter originates mainly from the limited load-bearing capacity of wood and the resulting plastic deformations. Up to the load level at maximum stiffness, plastic deformations have not yet developed ($u_{wood}^{pl} = 0$), so that the elastic deformation can be determined by means of Equation (4.5).

Assumption II: The elastic part of the compression of the bulk wood can be identified based its elastic stiffness $E_L$. Thus the elastic deformations can be determined from

$$u_{wood}^{el} = \frac{h}{2} \frac{\sigma_L}{E_L} \ , \tag{4.5}$$

with $h$ denoting the undeformed height of the specimen. A linear geometric relationship is assumed here, which is admissible as the deformations up to this point are small compared to the total height of the specimen.

Assumption III: Based on the observations of the experiments, it is assumed that unloading and reloading are fully elastic processes. Furthermore, the unloading and the reloading paths are considered to be of identical course, regardless of the load level when unloading starts.

**First loading curve**
With these assumptions, Equation (4.4) simplifies to

$$u_{tot} = u_{inter} + u_{wood} = u_{inter}^{pl} + u_{inter}^{el} + u_{wood}^{el} + 0 \ , \tag{4.6}$$

when applied to the region before plastic deformation in the bulk wood start to develop. Using Equation (4.5), the pressure-contact displacement-relationship for a single interface zone in this region is given by

$$u_{inter} = u_{tot} - u_{wood} = u_{tot} - \frac{h}{2} \frac{\sigma_L}{E_L} \ . \tag{4.7}$$

**Plastic deformations**
Separating elastic and plastic parts of the total contact displacement follows a similar approach as separating interface behavior and bulk material behavior. Now, the unloading curve serves as the basis.

Eliminating the elastic deformations of the bulk wood from the unloading curve results in the pressure-contact displacement-relationship for unloading, reading as

$$u_{inter}^{el} = u_{unloading} - \frac{h}{2} \frac{\sigma_L}{E_L} \ . \tag{4.8}$$

The elastic compliance of the interface zone is highly dependent on the applied pressure. At low applied forces, the elastic stiffness is very low. However, at higher loads it shows a dramatic increase leading finally to an almost vertical trend.

The amount of plastic deformations is a function of the maximum applied pressure before the last unloading and increases monotonically with rising pressure during loading. The relationship for the plastic deformations in the interaction zone is finally

$$u_{inter}^{pl} = u_{inter} - u_{inter}^{el} \ . \tag{4.9}$$

### 4.6.2 Mathematical description of the pressure-contact displacement relation

When choosing a mathematical formulation to describe the observed pressure-contact displacement-curves, the following characteristics have to be taken into account:

- zero contact pressure at zero contact displacement,
- non-negative tangent at zero pressure,
- monotonic increase of the pressure-compliance relation,
- almost vertical tangent (infinite) stiffness of unloading and reloading curve at high levels of applied pressure.

A generalized LAMÉ curve (see Appendix C for a more detailed discussion) fulfills these requirements. It reads for the total contact displacement $u_{inter}$ as

$$\left(\frac{u_{inter}}{u_0}\right)^{n_u} + \left(\frac{\sigma_0 - \sigma_L}{\sigma_0}\right)^{n_\sigma} = 1 \ , \tag{4.10}$$

in the pressure-contact displacement-space $u_{inter}$ - $\sigma$. The parameters $u_0$ and $\sigma_0$ and the exponents $n_u$ and $n_\sigma$ are positive numbers to be defined by suitable curve fitting methods. The semi-diameters of the curve, $u_0$ and $\sigma_0$, define the points with horizontal and vertical tangents, respectively. The curvature in the corner regions is adjusted by changing the exponents $n_u$ and $n_\sigma$.

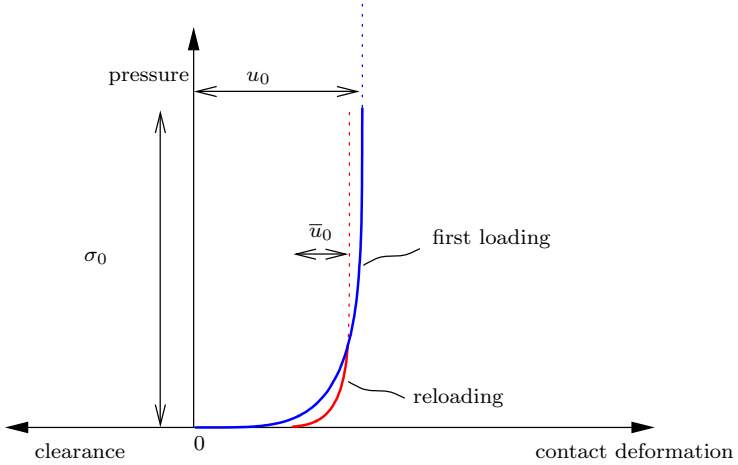


Figure 4.20: LAMÉ curves for the first loading curve and the unloading curve with specification of parameters for curve-fitting.

Reformatting Equation (4.10) yields explicit equations for the compliance $u_{inter}$ and the pressure $\sigma_L$

$$u_{inter}(\sigma_L) = u_0 \cdot \sqrt[n_u]{1 - \left(\frac{\sigma_0 - \sigma_L}{\sigma_0}\right)^{n_\sigma}} \ , \qquad \sigma_L(u) = \sigma_0 \cdot \left(1 - \sqrt[n_\sigma]{1 - \left(\frac{u}{u_0}\right)^{n_u}}\right) \ . \tag{4.11}$$

Different choices of the parameters $u_0$, $\sigma_0$, $n_u$, and $n_\sigma$ allow to fit individual curves for the first loading curve and the unloading curve. Denoting the parameters $u_0$, $\sigma_0$, $n_u$, and $n_\sigma$ for the first loading and $\overline{u}_0$, $\overline{\sigma}_0$, $\overline{n}_u$, and $\overline{n}_\sigma$ for the unloading, the explicit formulae for contact displacement as a function of applied stress $\sigma_L$ are given as

$$u_{inter} = u_0 \cdot \sqrt[n_u]{1 - \left(\frac{\sigma_0 - \sigma_L}{\sigma_0}\right)^{n_\sigma}} \ , \text{and} \tag{4.12}$$

$$u^{el}_{inter} = \overline{u}_0 \cdot \sqrt[\overline{n}_u]{1 - \left(\frac{\overline{\sigma}_0 - \sigma_L}{\overline{\sigma}_0}\right)^{\overline{n}_\sigma}} \ . \tag{4.13}$$

The non-reversible plastic compliance of the interface zone can then be identified by inserting the results of Equations (4.12) and (4.13) into Equation (4.9).

### 4.6.3 Curve fitting

Identifying the parameters for the LAMÉ curves from the results of the compression tests requires the following steps, which are carried out automatically by means of a Matlab script:

- separating the experimental results into first loading and unloading and reloading sections,
- determining clear wood stiffness $E_L$ and yield strength $f_{y_{c_L}}$,
- defining initial yield point (see Figure 4.19), and
- defining fitting parameters of the LAMÉ curves describing the first loading and the unloading, respectively.

The strength parameters $\sigma_0$ and $\overline{\sigma}_0$ were set equal to the maximum compressive strength of the material, so that the identity

$$\sigma_0 = \overline{\sigma}_0 = f_{y_{c_L}} \tag{4.14}$$

holds. According to the definition of the LAMÉ curve, this implies that contact stresses $\sigma_L \geq \overline{\sigma}_0$ can not occur. This is also mechanically reasonable since the yield strength of the basic wood material cannot be exceeded.

All exponents $n_\sigma$, $n_u$, $\overline{n}_\sigma$, and $\overline{n}_u$ were set to values larger than one. Exponents lower or equal to one would lead to singularities in the corner regions. A smooth change from loading to unloading would not be possible then.

The curve fitting was done separately for each test specimen. Figure 4.21 shows typical fitting curves. The curves approach the data from the experiments very well.

In order to obtain one set of representative contact parameters for each series of equal density and equal cutting style, the LAMÉ parameters of all specimens of this series were averaged. The fitting parameters obtained are compiled in Table 4.6, and Figure 4.22 shows the resulting LAMÉ curves for each series. See Appendix D for a complete list of parameters for each test.

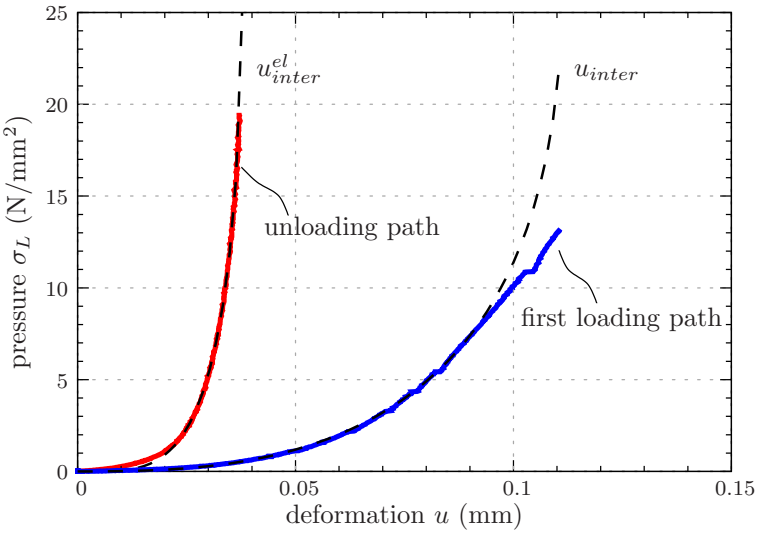


Figure 4.21: Curve fitting of the first loading curve and the unloading curve by adequate LAMÉ curves (exemplary for Specimen 16B4-2-3), with the parameters $u_0 = 0.114\,\text{mm}$, $\sigma_0 = 35.2\,\text{N/mm}^2$, $n_u = 2.77$, $n_\sigma = 3.12$ for first loading, and $\overline{u}_0 = 0.038\,\text{mm}$, $\overline{\sigma}_0 = 35.2\,\text{N/mm}^2$, $\overline{n}_u = 4.05$, and $\overline{n}_\sigma = 2.98$ for unloading and reloading.

| Cutting style | Series | $\varrho$ | $\sigma_0$ | $n_\sigma$ | $u_0$ | $n_u$ | $\overline{\sigma}_0$ | $\overline{n}_\sigma$ | $\overline{u}_0$ | $\overline{n}_u$ |
|---|---|---|---|---|---|---|---|---|---|---|
| 1 | 16B4-10 | 327 | 36.9 | 1.11 | 0.084 | 3.04 | 36.9 | 1.61 | 0.030 | 3.55 |
| 1 | 14_2-9 | 451 | 51.4 | 1.50 | 0.104 | 3.99 | 51.4 | 3.62 | 0.036 | 4.58 |
| 1 | 8A4-8 | 535 | 61.8 | 1.15 | 0.081 | 4.72 | 61.8 | 1.81 | 0.030 | 3.54 |
| 2 | 16B4-2 | 319 | 32.7 | 1.87 | 0.188 | 2.64 | 32.7 | 2.94 | 0.040 | 4.19 |
| 2 | 14_2-1 | 443 | 54.0 | 1.10 | 0.256 | 3.91 | 54.0 | 4.24 | 0.045 | 4.48 |
| 2 | 8A4-1 | 546 | 61.0 | 1.40 | 0.180 | 4.26 | 61.0 | 2.36 | 0.048 | 4.04 |
| 3 | 16B4-4 | 316 | 30.8 | 1.68 | 1.011 | 1.74 | 30.8 | 2.78 | 0.091 | 4.76 |
| 3 | 14_2-5 | 429 | 42.1 | 1.54 | 0.725 | 1.81 | 42.1 | 3.01 | 0.097 | 4.41 |
| 3 | 8A4-3 | 536 | 52.6 | 1.14 | 0.376 | 2.54 | 52.6 | 5.10 | 0.106 | 3.60 |
| 4 | 16B4-5 | 326 | 29.8 | 2.55 | 0.219 | 2.75 | 29.8 | 2.05 | 0.051 | 4.12 |
| 4 | 14_2-4 | 447 | 50.9 | 2.06 | 0.194 | 4.45 | 50.9 | 2.14 | 0.055 | 6.78 |
| 4 | 8A4-4 | 536 | 55.8 | 1.81 | 0.135 | 5.70 | 55.8 | 3.28 | 0.035 | 4.80 |
| 5 | 16B4-6 | 330 | 30.5 | 1.79 | 0.099 | 3.92 | 30.5 | 2.11 | 0.050 | 4.06 |
| 5 | 14_2-6 | 455 | 52.9 | 1.47 | 0.100 | 4.54 | 52.9 | 3.05 | 0.047 | 3.67 |
| 5 | 8A4-6 | 550 | 61.4 | 1.25 | 0.077 | 3.82 | 61.4 | 3.42 | 0.047 | 3.86 |

Table 4.6: Averaged LAMÉ parameters for each series, representative of the investigated density level and cutting type ($\varrho$ in kg/m$^3$, $\sigma_0$ and $\overline{\sigma}_0$ in N/mm$^2$, $u_0$ and $\overline{u}_0$ in mm).

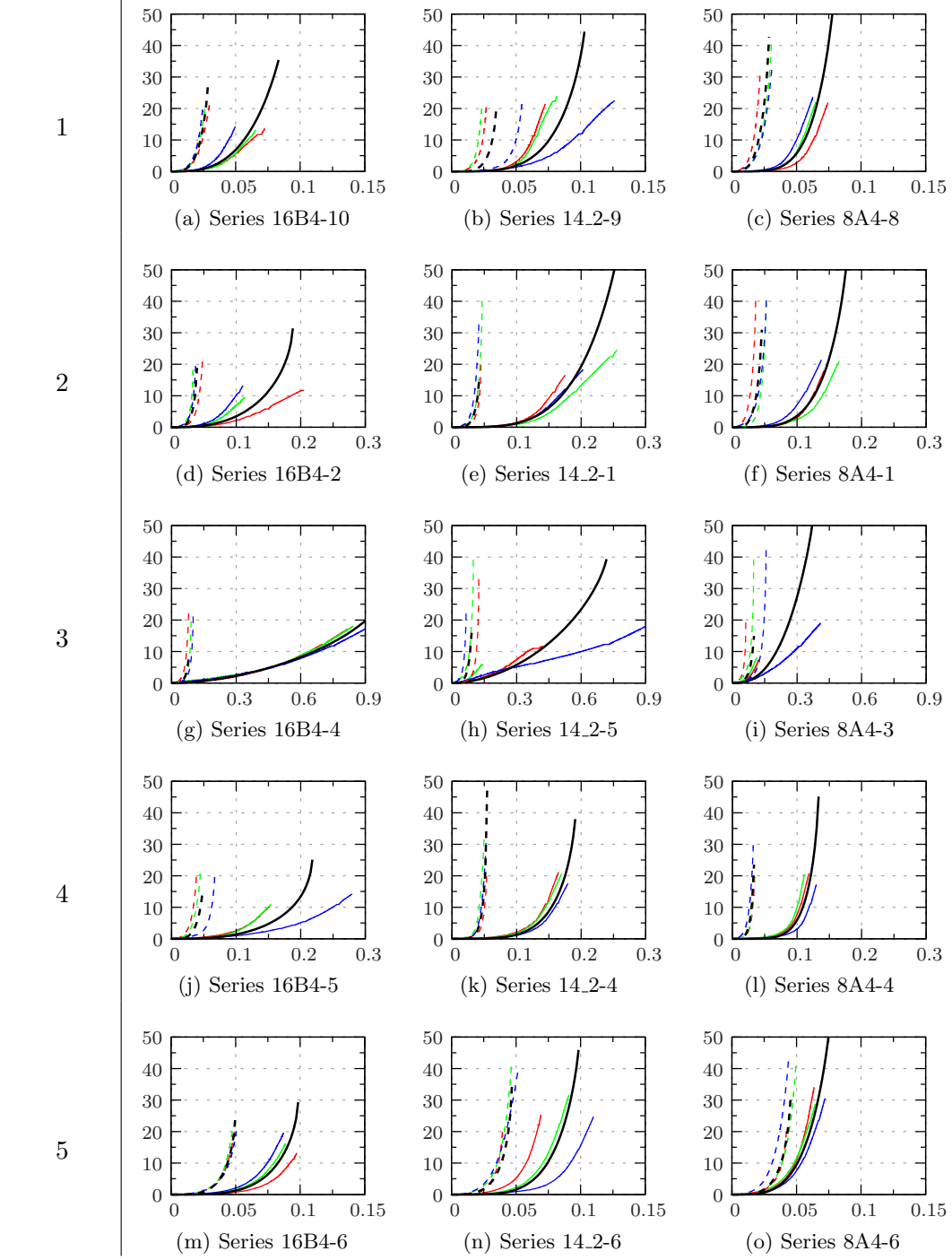


Figure 4.22: Contact curves for each sample (1-3) of each series with the respective averaged fitted curves (see Table 4.6) for first loading and for unloading and reloading, respectively. (Contact displacement $u$ (mm) on abscissa, contact pressure $\sigma_L$ (N/mm$^2$) on ordinate; for specimens 1 (red), 2 (green), and 3 (blue), and average fitted curve for first loading (solid black) and unloading and reloading (dashed black).)

## 4.7 Discussion

The interface layer at the surface of a wood piece plays an important role during the transfer of pressure loads from connectors. The particular influence of the surface compliance depends on the field of application. The larger the observed structure, the lower the influence of the contact zones and the higher the influence of elasto-plastic properties of the installed members. When studying the load transfer very locally, the weak interface can have a great effect on the load-bearing properties. In the field of dowel-type connections, the compliant interface plays a substantial role. It increases deformations to a high degree and especially reduces the stiffness of the connection.

This chapter has clearly shown how the surface quality affects the contact behavior. Contact stiffnesses vary considerably depending on wood density and drilling technique (cutting style, drilling, etc.). A method for identifying the elastic and plastic parts of the contact deformation has been proposed. Furthermore, a suitable mathematical description of the relationship between pressure and the contact deformation has been developed. Is is revealed, that the rougher surfaces (created by cutting types 2, 3, and 4) are more compliant than the comparably flat surfaces (created by cutting types 1 and 5).

In the study, only transverse sections in the $R$-$T$-plane of Norway spruce samples were covered. The extension to other wood species provides an interesting field for future work. Furthermore, it would be interesting to extend the scope of the studies to the contact behavior at loading under an arbitrary angle to the grain. This is relevant for plane, inclined loading conditions, but also for the loading of the curved surface of bore-holes.

In the current study, only normal behavior of the surfaces in contact was considered. In many engineering problems, friction plays a crucial role, and is a factor of high importance especially on the load-carrying behavior of dowel-type connections. As little information is available on friction of steel on wood, the determination of reliable friction properties possesses potential for another field of investigation, whereby an enormous combination can be assessed by a variation and combination of e.g. wood density, the cutting plane and cutting style of the wood surface, the direction of sliding, and the roughness of the steel surface.

# Simulations

# Chapter 5

# Contact behavior

The following chapter deals with the implementation of a simulation model for the contact of wood on steel into a Finite-Element code. The necessity of a proper simulation tool for interaction properties has been demonstrated in Chapter 3, while the contact behavior of wood on steel has been studied experimentally in Chapter 4.

The model considers compressive contact deformations in normal direction with a non-linear pressure-clearance relation, representing therefore the experimental results of Section 4.6. This behavior is a consequence of the waviness and roughness of wooden surfaces which depends strongly on the properties of the wood (density, wood species) and on the used cutting device (cutting speed, feed rate, wear of the tools). The model allows for consideration of non-recoverable (plastic) deformations, which develop particularly at higher contact pressures.

First, the requirements on such a model will be recalled and the parameters involved discussed. The outline of the algorithm will be presented and its implementation into the Finite Element code shown. In the last section, the model and its implementation will be verified by a simple example.

## 5.1 Normal behavior

The normal behavior describes the relation between contact pressure and the clearance/overclosure of the respective surfaces. The description is based on the assumption, that the contact deformation in normal direction to the surface is primarily affected by the wooden surface properties. In contact of wood and steel, the great difference in stiffness between the two parts suggests to choose the steel surface as the stiff *master surface* and the wood surface as the compliant *slave surface*.

The model allows for a penetration of the slave surface by the master surface (Figure 5.1). This penetration is called *overclosure*, since in the initial, unloaded state, it describes the overlap of the surfaces. Depending on the magnitude of the overclosure,

a contact pressure is formulated which controls the force transfer between the two surfaces (Figure 5.2). In Section 4.6, the contact deformation was determined by means of experiments, and is assumed to be small compared to the dimensions of the main structure. The contact deformations are therefore assigned to the overclosure in the pressure-overclosure relationship.

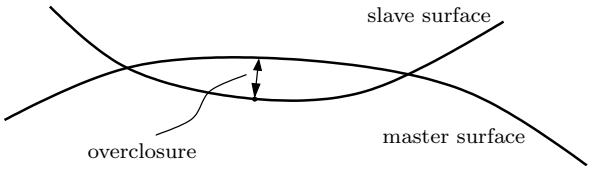


Figure 5.1: Penetration (overclosure) of the master surface into the slave surface.

### 5.1.1 Contact states

The pressure-overclosure relation assigns different contact states to different loading situations and histories. The definition of the states is derived from the findings of the contact experiments (Chapter 4.6).

For the first loading of a previously unloaded surface, a non-linear pressure-clearance relation with increasing contact stiffness is the main feature. Plastic deformations occur during the loading process because of inelastic deformations of the material in the contact zone.

Due to the plastic deformations, unloading does not follow the curve of initial loading. Therefore, a distinction of typical load-cases is necessary. The differentiation of two separate curves for first loading and unloading/reloading, respectively, is elucidated in Figure 5.2.

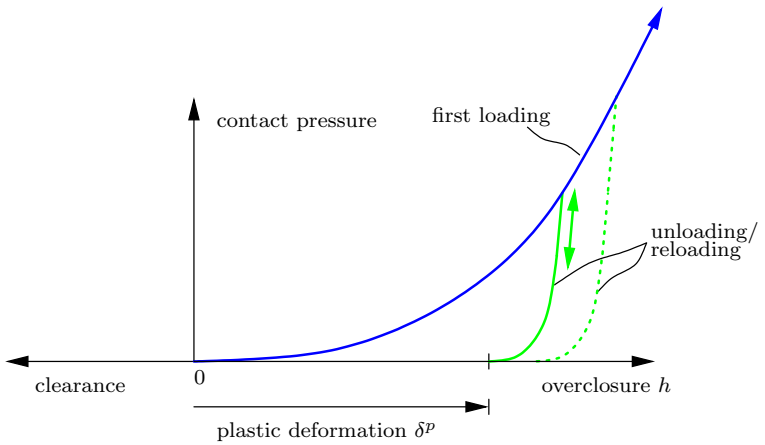


Figure 5.2: Pressure-overclosure relation for first loading and unloading/reloading, considering plastic deformations.

The algorithm takes into account three different contact states: *Open*, *Closed I*, and *Closed II*, between which the algorithm switches appropriately.

- *Open*: The contact status is regarded as opened when no load transfer takes places. This status is active when the surfaces are situated at a distance from each other, before loading starts. Once the surfaces are unloaded and plastic deformations have occurred, the contact status is again *Open*, when the overclosure is smaller than the accumulated plastic deformations. In this case, an algorithmic penetration of the two surfaces is possible, but only to a maximum of the (total accumulated) plastic deformation $\delta^p$, which is defined by Equation 4.9.

- *Closed I* - first loading: When the surfaces are loaded for the first time, the pressure-overclosure relationship follows the soft, first loading curve. Points on this curve can be passed through only once. The pressure-overclosure function for first loading is derived in Section 4.6.3. Equation 4.11, describing contact pressure $\sigma_n$ depending on overclosure $h$, leads to

$$\sigma_n(h) = f_{y_{c_L}} \cdot \left(1 - \sqrt[n_\sigma]{1 - \left(\frac{h}{h_0}\right)^{n_h}}\right) \ , \tag{5.1}$$

  whereby $f_{y_{c_L}} = \sigma_0$, $h_0 = u_0$, $n_h = n_u$, and $n_\sigma$ are defined in Section 4.6.2.

- *Closed II* - unloading/reloading: During unloading and reloading, the pressure-overclosure relationship follows the stiffer unloading/reloading curve. If the overclosure during reloading is lower than the maximum overclosure during the first loading, this curve can be followed several times. The pressure-overclosure function for unloading/reloading is defined in Section 4.6.3. Equation 4.11, specified for the unloading/reloading parameters and considering the plastic deformations, leads to

$$\sigma_n(h) = f_{y_{c_L}} \cdot \left(1 - \sqrt[\overline{n}_\sigma]{1 - \left(\frac{h - \delta^p}{\overline{h}_0}\right)^{\overline{n}_h}}\right) \ . \tag{5.2}$$

  Again, the parameters $\overline{h}_0 = \overline{u}_0$, $\overline{n}_h = \overline{n}_u$, and $\overline{n}_\sigma$ are defined in Section 4.6.2.

### 5.1.2 Algorithmic implementation

The algorithm is displacement-driven, and the total nodal displacements and possible increments thereof are the main input parameters. The displacements are the basis for the determination of contact status and contact pressure, which are the main outputs of the algorithm.

For algorithmic implementation, the contact status has to be known at every loading stage. Due to the occurrence of plastic deformations, the model is path-dependent and requires internal state variables. Therefore, the maximum overclosure during previous loadings, $h_{max}$, as well as the total accumulated plastic deformation, $\delta^p$, are recorded at every time $t_n$. By means of the state variables, the precise state can then be retrieved in the next load step at time $t_{n+1}$.

In the following, the possible combinations of starting point and increment are presented, and their algorithmic treatment is discussed. It is assumed, that the state at time $t_n$ is converged and that the state variables $h_{max}$ and $\delta^p$ at this time are known.

- $(h_{n+1} > h_{max})$: The increase of overclosure is positive, $\Delta h = h_{n+1} - h_n > 0$. This can only happen when mode *Closed I* is active, or when mode *Closed II* changes to mode *Closed I*. In both cases, an increase of contact pressure occurs, following the first loading curve. The state variables maximum overclosure and plastic deformations are updated to $h_{max} = h_{n+1}$ and $\delta^p = \delta^p_{n+1}$. The update of $\delta^p$ is done according to Equation 4.9.

- $(h_{n+1} < h_{max}) \cap (h_{n+1} > \delta^p)$: Either unloading or reloading takes place. Thus, the status is *Closed II*. The contact pressures are determined by evaluating the unloading pressure-overclosure relationship. No update of state variables is necessary.

- $(h_{n+1} \leq \delta^p)$: In this case, the contact status is *Open*. If $\delta^p = 0$, the contact surface is undisturbed, loading of the contact surface has not yet occurred. If $\delta^p > 0$, the contact was closed before, but has opened due to changes of the loading situation. It is therefore possible, that there is an overclosure of the surfaces, which is nevertheless too small for load transfer to take place. No update of the state variables is necessary.

The plastic part of the overclosure, $\delta^p$, is a function of the maximum overclosure, $h_{max}$. Inserting Equations (4.12) and (4.13) into (4.9) yields

$$\delta^p\left(h_{max}\right) = h_{max} - u^{el}_{inter}\left(\sigma_n(h_{max})\right) \ . \tag{5.3}$$

## 5.2 Finite Element implementation

The contact model is implemented into the Finite Element code ABAQUS by means of a user-subroutine UINTER. UINTER allows to define a *U*ser-define *INTER*face model, and is used, when the built-in constitutive models are not sufficient. UINTER processes all operations at the nodal points of the slave surface.

ABAQUS passes over all necessary information for updating the contact status to UINTER. These are, amongst others not relevant for the simulation, RDISP and DRDISP. RDISP is the relative position of the two surfaces at the end of the load increment in normal and tangential direction, and DRDISP is the increment in relative position since the last increment.

State variables STATEV contain the maximum overclosure $h_{max}$ and the maximum plastic deformation occurred since the beginning of the simulation $\delta^p$. The state variables are passed over to UINTER, updated when necessary, and returned to ABAQUS.

Further variables returned to ABAQUS include the contact stresses in normal and tangential direction (STRESS) and the interface stiffness (DDSDDR). Additionally the control variable LOPENCLOSE is returned which is set to 0 when the interface is opened, Status *Open*, and set to 1 when closed, Status *Closed I* and *Closed II*, respectively. Changes from one value to the other will cause severe discontinuity iterations in ABAQUS.

## 5.3 Verification examples

The implemented code is verified by means of a small example. This example shall demonstrate the correct functioning of the UINTER subroutine. The geometry, material, boundary conditions, and loading are chosen to result in homogenous stress and strain distribution.

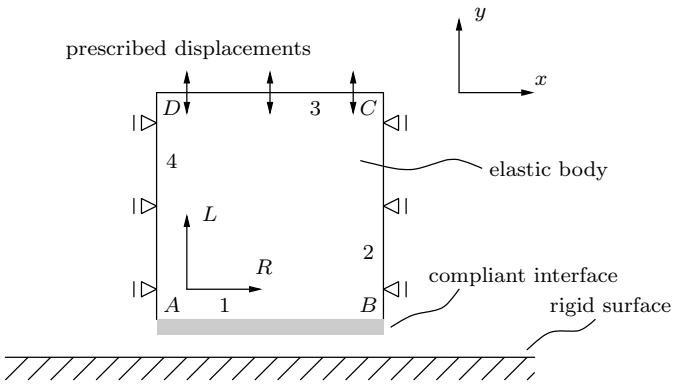


Figure 5.3: Configuration of the verification example.

**Geometry** A quadratic body with a side length of 1 mm is situated with an initial clearance of 0.1 mm in $y$-direction from a rigid surface. Contact will later be established between the square body and the rigid surface.

**Discretization** The body is represented by a single element of type CPS4, a linear, fully integrated plain stress element with 4 nodes.

**Material behavior** The material is considered as purely elastic. Elastic stiffness is given by the orthotropic stiffness matrix (in $\mathrm{N/mm^2}$)

$$\mathbb{C} = \begin{bmatrix} 10800 & 535 & 427 & 0 & 0 & 0 \\ 535 & 1110 & 520 & 0 & 0 & 0 \\ 427 & 520 & 752 & 0 & 0 & 0 \\ 0 & 0 & 0 & 205.5 & 0 & 0 \\ 0 & 0 & 0 & 0 & 712 & 0 \\ 0 & 0 & 0 & 0 & 0 & 726 \end{bmatrix}, \tag{5.4}$$

which is chosen typical for softwood. The order of entries is $LL$, $RR$, $TT$, $RT$, $TL$, and $LR$. Material orientation is marked in Figure 5.3.

**Contact behavior** The LAMÉ parameters for the pressure-overclosure relation are specified in Table 5.1.

**Boundary conditions & loading** The body is restrained at both sides in $x$-direction, so that movement is only possible in $y$-direction, $u_x^{(2)} = u_x^{(4)} = 0$ for edges marked with

| | $\sigma_0$ (N/mm$^2$) | $n_\sigma$ | $u_0$ (mm) | $n_u$ |
|---|---|---|---|---|
| First loading | 55.0 | 1.10 | 0.26 | 3.9 |
| Unloading/Reloading | 55.0 | 4.20 | 0.045 | 4.5 |

Table 5.1: LAMÉ parameters.

2 and 4 in Figure 5.3. At the upper boundary the loads are applied by prescribed cyclic displacements in $y$-direction: $u_y^{(3)} = u_y^{(3)}(t)$. The load history (Figure 5.4) consists of six steps which are subdivided into 100 increments each.

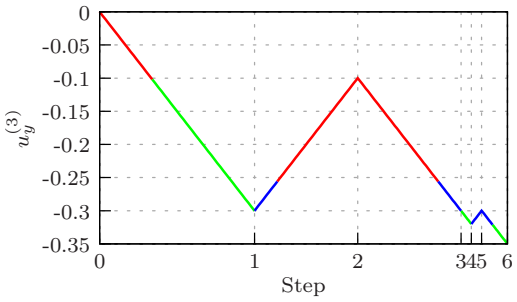


| Step | $u_y^{(3)}$ (mm) | $\Delta u_y^{(3)}$ (mm) |
|---|---|---|
| 0 | 0 | 0 |
| 1 | −0.30 | −0.30 |
| 2 | −0.10 | +0.20 |
| 3 | −0.30 | −0.20 |
| 4 | −0.32 | −0.02 |
| 5 | −0.30 | +0.02 |
| 6 | −0.35 | −0.05 |

Figure 5.4: Load history (Red: *Open*, Green: *Closed I*, Blue: *Closed II*).

**Results** The resulting contact pressure $\sigma_n$ due to loading is given in Figure 5.5a. The individual load stages and the corresponding contact status are clearly visible. Contact pressure can only exceed previously reached maximum contact pressure when in mode *Closed I*.

Figure 5.5b presents the overclosure as a function of the load steps. The plastic deformations of the interface zone $\delta^p$ and maximum overclosure $h_{max}$ are increasing only when mode *Closed I* is active. The transition between modes *Closed II* and *Open* during unloading occurs when the overclosure becomes smaller than the plastic deformations.

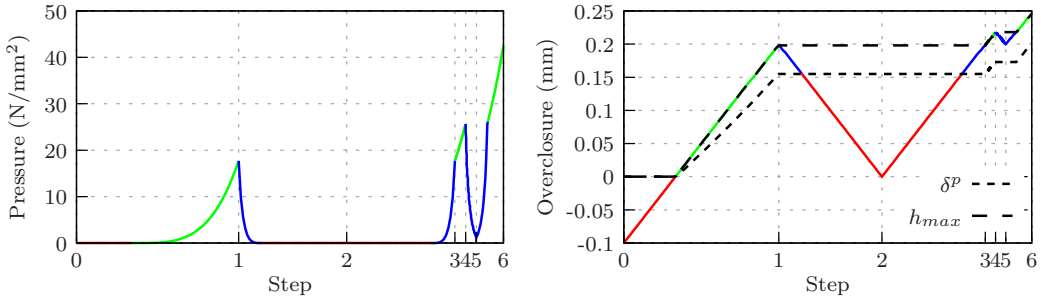


Figure 5.5: (a) Contact pressure $\sigma_n$ and (b) overclosure $h$ depending on the contact status (Red: *Open*, Green: *Closed I*, Blue: *Closed II*)

In Figure 5.6, the pressure-overclosure relationship is shown, whereby the contact modi

are again highlighted. The first loading curve starts with a horizontal tangent and shows increasing stiffness at higher overclosure levels. The unloading curves are of significantly higher stiffness. The shift of the two unloading curves is clearly visible, which relates to the increased plastic deformations in the interface at the second unloading. A full release of load when unloaded (end of step 2, start of step 3) leads to an open interface without load transfer although there is remaining overclosure.

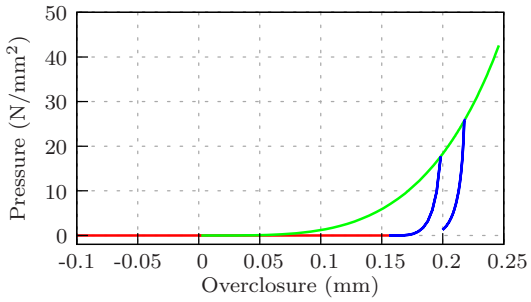


Figure 5.6: Overclosure-contact pressure-relationship depending on the contact status (Red: *Open*, Green: *Closed I*, Blue: *Closed II*)

# Chapter 6

# Elasto-plastic model for wood

In the following, the derivation of a three-dimensional elasto-plastic model for wood will be presented. The constitutive model is suitable for wood and covers orthotropy in stiffness as well as strength. Perfect plasticity is considered, hardening (or softening) mechanisms are not included.

First, some basic preliminaries about the intended fields of application will be given. These define the requirements on the material formulation in terms of load scenarios and levels. The theoretical basis of material modelling will be provided subsequently. This includes elastic orthotropy as well as the foundation of the used orthotropic plasticity model. In the following, the implementation of the material model into a Finite Element environment will be shown. and the code will be verified on a single-element example.

## 6.1 Fields of application

In Chapter 2.1, the mechanical properties of wood are discussed. The simulation model presented in the following does not cover all the characteristics, such as cracking under tension or shear loads. Rather, a simplified model will be formulated that is sufficient to describe the material behavior for the intended applications. In the contex of this thesis, the main requirements on the material model are as follows:

- Simple material model: The introduced material model should be easy to implement and provide results within reasonable computational time.
- Focus on the elastic limit state: The model shall give information on the utilization level for different stress states. The assumption of perfect plasticity allows therefore to assess the material behavior to be expected once the elastic limit state has just been exceeded.
- (Quasi-)Static loading: The material model is rate-independent, i.e. time-dependent effects are not considered. The application of the material model does not cover

dynamic loading or viscoelastic effects.

These assumptions enable realistic simulations of wooden structures when the area of application is chosen appropriately. The thesis aims at a proper desription of the loading process of dowel-type timber connections up to the Sericeability Limit State. This state is usually characterized by reversible deformations once the load is released. With the material model the stress distribution can be determined as well as the actual impact of small plastifying zones in the wood. Limits within which plastification is allowed can therefore be stated.

## 6.2 Theory of elasto-plastic material modeling

In the following, wood is described as a continuum, its heterogenous microstructure is not considered in the context of the Finite Element simulations. The differences in strength and stiffness within and between the annual rings are not taken into account.

All operations are performed in relation to the main material directions $L$, $R$, and $T$ at each individual material point, regardless of the actual position or orientation of these directions within the overall model. Transformations of quantities from the local to the global coordinate system on the integration point level are done by the Finite Element program, which allows for an easier handling of material orientations.

The description is based on the general reference books for plasticity theory by Simo and Hughes [87], Zienkiewicz and Taylor [99], and de Souza Neto et al. [22].

### 6.2.1 Additive decomposition of strains

The theory presented is formulated within the theory of small strains and displacements. In this context, the total strain $\boldsymbol{\varepsilon}$ is splitted additively into the elastic part $\boldsymbol{\varepsilon}^e$ and the plastic part $\boldsymbol{\varepsilon}^p$, so that

$$\boldsymbol{\varepsilon} = \boldsymbol{\varepsilon}^e + \boldsymbol{\varepsilon}^p \ . \tag{6.1}$$

The additive decomposition for strain rates reads as

$$\frac{\partial \boldsymbol{\varepsilon}}{\partial t} = \dot{\boldsymbol{\varepsilon}} = \dot{\boldsymbol{\varepsilon}}^e + \dot{\boldsymbol{\varepsilon}}^p \ . \tag{6.2}$$

The rate form is commonly used in the theory of plasticity. The deformation state is dependent on the load history, and the formulation therefore called path-dependent.

### 6.2.2 Free energy potential and the elastic law

From the free energy function $\psi$, the relation between stresses and strains can be directly derived. In an elasto-plastic framework, the free energy function $\psi$ is defined by

$$\psi = \psi(\boldsymbol{\varepsilon}, \boldsymbol{\varepsilon}^p, \boldsymbol{\alpha}) \ , \tag{6.3}$$

which is dependent on the total strain $\boldsymbol{\varepsilon}$ and on the plastic strain $\boldsymbol{\varepsilon}^p$, the later acting as an internal variable, and the internal hardening parameter $\boldsymbol{\alpha}$. The free energy function $\psi$ can be split into an elastic contribution $\psi^e$ and a hardening contribution $\psi^p$ as

$$\psi(\boldsymbol{\varepsilon}, \boldsymbol{\varepsilon}^p, \boldsymbol{\alpha}) = \psi^e(\boldsymbol{\varepsilon} - \boldsymbol{\varepsilon}^p) + \psi^p(\boldsymbol{\alpha}) \ . \tag{6.4}$$

In the context of perfect plasticity hardening is not considered, which is expressed by $\boldsymbol{\alpha} = 0$, $\psi^p(\boldsymbol{\alpha}) = 0$, and $\psi = \psi(\boldsymbol{\varepsilon}, \boldsymbol{\varepsilon}^p) = \psi^e$.

For linear elastic materials, the elastic part can be written as

$$\psi^e(\boldsymbol{\varepsilon} - \boldsymbol{\varepsilon}^p) = \frac{1}{2}(\boldsymbol{\varepsilon} - \boldsymbol{\varepsilon}^p) : \mathbb{C} : (\boldsymbol{\varepsilon} - \boldsymbol{\varepsilon}^p) \ , \tag{6.5}$$

with the stiffness tensor $\mathbb{C}$. Differentiation by $\boldsymbol{\varepsilon}$ and insertion of Equation (6.1) yields the generalized HOOKE's law

$$\boldsymbol{\sigma} = \frac{\partial \psi(\boldsymbol{\varepsilon}, \boldsymbol{\varepsilon}^p)}{\partial \boldsymbol{\varepsilon}} = \mathbb{C} : (\boldsymbol{\varepsilon} - \boldsymbol{\varepsilon}^p) = \mathbb{C} : \boldsymbol{\varepsilon}^e \ . \tag{6.6}$$

The inverse of the stiffness tensor is the compliance tensor $\mathbb{D} = \mathbb{C}^{-1}$, both tensors are symmetric. In incremental form, HOOKE's law takes in VOIGT notation the form

$$\underbrace{\begin{Bmatrix} d\varepsilon_L \\ d\varepsilon_R \\ d\varepsilon_T \\ 2\ d\varepsilon_{RT} \\ 2\ d\varepsilon_{TL} \\ 2\ d\varepsilon_{LR} \end{Bmatrix}}_{= d\boldsymbol{\varepsilon}} = \underbrace{\begin{bmatrix} \frac{1}{E_L} & -\frac{\nu_{LR}}{E_R} & -\frac{\nu_{LT}}{E_T} & 0 & 0 & 0 \\ -\frac{\nu_{RL}}{E_L} & \frac{1}{E_R} & -\frac{\nu_{RT}}{E_T} & 0 & 0 & 0 \\ -\frac{\nu_{TL}}{E_L} & -\frac{\nu_{TR}}{E_R} & \frac{1}{E_T} & 0 & 0 & 0 \\ 0 & 0 & 0 & \frac{1}{G_{RT}} & 0 & 0 \\ 0 & 0 & 0 & 0 & \frac{1}{G_{TL}} & 0 \\ 0 & 0 & 0 & 0 & 0 & \frac{1}{G_{LR}} \end{bmatrix}}_{= \mathbb{D}} \cdot \underbrace{\begin{Bmatrix} d\sigma_L \\ d\sigma_R \\ d\sigma_T \\ d\tau_{RT} \\ d\tau_{TL} \\ d\tau_{LR} \end{Bmatrix}}_{= d\boldsymbol{\sigma}} \tag{6.7}$$

The orthotropic compliance tensor $\mathbb{D}$ contains 12 unique parameters $E_i$, $G_{ij} = G_{ji}$ and $\nu_{ij} \neq \nu_{ij}$ for $i, j = L, R, T$. The Poisson's ratios $\nu_{ij}$ are defined to describe a variation of stress in the $j$-direction under changing strain in the $i$-direction. Due to the fact that $\mathbb{D}$ is symmetric, the following identities apply

$$\frac{\nu_{LR}}{E_R} = \frac{\nu_{RL}}{E_L}, \quad \frac{\nu_{LT}}{E_T} = \frac{\nu_{TL}}{E_L}, \quad \frac{\nu_{RT}}{E_T} = \frac{\nu_{TR}}{E_R} \ , \tag{6.8}$$

so that only nine independent elastic material parameters remain.

In case of transversal orthotropy, the number of independent parameters is further reduced to five due to the identities

$$E_R = E_T, \quad G_{TL} = G_{LR}, \quad \nu_{RL} = \nu_{TL}, \quad G_{RT} = \frac{E_R}{2(1 + \nu_{TR})} \ . \tag{6.9}$$

By assuming transversal isotropy, the $R$ and $T$ direction are considered to behave identically. This is motivated by quite similar mechanical behavior in these material directions compared to the fiber direction $L$.

Equation (6.7) allows the derivation of increments of the stress vector $d\boldsymbol{\sigma}$ from (incremental) changes of the strain vector $d\boldsymbol{\varepsilon}$ – and vice versa. In linear elastic materials it is not necessary to use the incremental form of HOOKE's law, the direct form $\boldsymbol{\varepsilon} = \mathbb{D} : \boldsymbol{\sigma}$ allows determination of strains at all stress states. The incremental form is used for describing the relation between stresses and strains in the plastic domain, when path-dependent effects exist.

### 6.2.3 Yield criterion and yield surface

A yield criterion allows to identify the elastic limit state. The corresponding yield function $\Phi$ is defined as

$$\Phi(\boldsymbol{\sigma}) \leq 0 \ , \tag{6.10}$$

whereby $\Phi(\boldsymbol{\sigma}) < 0$ defines the elastic domain, and $\Phi(\boldsymbol{\sigma}) = 0$ the plastic domain. States of $\Phi(\boldsymbol{\sigma}) > 0$ are not admissible. The state $\Phi = 0$ can be interpreted by a $n-1$ dimensional surface in the $n$-dimensional stress space, which motivates the terminuns yield surface.

The typical failure modes of wood were already listed in Section 2.1. The abrupt-brittle tension and shear failure modes and the plastic-ductile compression failure mode are of substantially different origin and characteristic. These differences in the behavior are often covered by applying alternative failure criteria, e.g. in the framework of multi-surface plasticity models [58, 81]. Each failure criterion is assigned a failure surface in the stress space in these models, which together mark the boundary of the elastic regime. This differentiation allows for a more sophisticated post-failure description with hardening laws when ductile behavior occurs or with discrete crack opening (e.g. using cohesive elements) or softening laws in brittle failure modes. A multi-surface description is far more complicated to implement than single-surface descriptions. For example, the algorithmic treatment of edges of adjacent surfaces requires attention.

In this work, a single-surface, perfect plasticity approach is used, regardless of the failure mode. This simplification is in accordance with the scope of the work, which aims mainly at detection of the elastic limit state at a structural level (see Chapter 7) rather than the investigation of the post-failure characteristics and the maximum load.

A single-surface model describes material failure by evaluation of a single inequation. In case of a TSAI-WU failure criterion [95], this inequality reads as

$$\Phi(\boldsymbol{\sigma}) = a_{ij}\ \sigma_{ij} + b_{ijkl}\ \sigma_{ij}\ \sigma_{kl} + c_{ijklmn}\ \sigma_{ij}\ \sigma_{kl}\ \sigma_{mn} + ... - 1 \leq 0 \qquad \text{for } i,j,k,l,m,n,... = L,R,T, \tag{6.11}$$

The TSAI-WU failure criterion was originally developed for composite materials and is suitable for orthotropic failure behavior. It is commonly applied to wood, either as a single surface criterion [34] or to describe individual surfaces in a multi-surface criterion [58, 75].

For the purpose of easy application, a quadratic formulation is applied, for which Equation (6.11) degenerates to

$$\Phi(\boldsymbol{\sigma}) = a_{ij}\ \sigma_{ij} + b_{ijkl}\ \sigma_{ij}\ \sigma_{kl} - 1 \leq 0\ , \quad i,j,k,l = L,R,T\ . \tag{6.12}$$

Since symmetry of shear strength is assumed, $a_{ij} = 0$ for $i \neq j$. Stress interactions between normal stresses $\sigma_{ii}$ and shear stresses $\tau_{ij}$ as well as among shear stresses $\tau_{ij}$ themselves are neglected in the following. Furthermore, symmetries $b_{iijj} = b_{jjii}$ and $b_{ijij} = b_{jiji}$ apply. This reduces the number of independent material parameters $a_{ij}$ and $b_{ijkl}$ to twelve and yields the following inequation:

$$\begin{aligned}
\Phi(\boldsymbol{\sigma}) &= a_{LL}\ \sigma_{LL} + a_{RR}\ \sigma_{RR} + a_{TT}\ \sigma_{TT}\ ... \\
&+ b_{LLLL}\ \sigma_{LL}^2 + b_{RRRR}\ \sigma_{RR}^2 + b_{TTTT}\ \sigma_{TT}^2\ ... \\
&+ 2\ b_{LLRR}\ \sigma_{LL}\ \sigma_{RR} + 2\ b_{RRTT}\ \sigma_{RR}\ \sigma_{TT} + 2\ b_{TTLL}\ \sigma_{TT}\ \sigma_{LL}\ ... \\
&+ 4\ b_{LRLR}\ \tau_{LR}^2 + 4\ b_{RTRT}\ \tau_{RT}^2 + 4\ b_{TLTL}\ \tau_{TL}^2 - 1 \\
&\leq 0
\end{aligned} \tag{6.13}$$

Expressing the parameters $a_{ij}$ and $b_{ijkl}$ in terms of uniaxial strengths and shear strengths in the respective principal material directions leads to

$$\begin{aligned}
a_{LL} &= \frac{1}{f_{y_{t_L}}} + \frac{1}{f_{y_{c_L}}}\ , \quad a_{RR} = \frac{1}{f_{y_{t_R}}} + \frac{1}{f_{y_{c_R}}}\ , \quad a_{TT} = \frac{1}{f_{y_{t_T}}} + \frac{1}{f_{y_{c_T}}}\ , \\
b_{LLLL} &= -\frac{1}{f_{y_{t_L}} f_{y_{c_L}}}\ , \quad b_{RRRR} = -\frac{1}{f_{y_{t_R}} f_{y_{c_R}}}\ , \quad b_{TTTT} = -\frac{1}{f_{y_{t_T}} f_{y_{c_T}}}, \\
b_{LRLR} &= \frac{1}{4 f_{y_{LR}}^2}\ , \quad b_{RTRT} = \frac{1}{4 f_{y_{RT}}^2}\ , \quad b_{TLTL} = \frac{1}{4 f_{y_{TL}}^2}\ .
\end{aligned} \tag{6.14}$$

The index '$y$' indicates ultimate or yield strength, indices '$t$' and '$c$' tension and compression, respectively. Strengths are defined with signs herein: Tension strength is of positive sign ($f_{y_{t_i}} > 0$) whereas compressive strength is of negative sign ($f_{y_{c_i}} < 0$).

Unlike the parameters defind in Equation (6.14), parameters $b_{iijj}$, which link stresses in different material directions, cannot be related to uniaxial strength values. These parameters can be assessed by means of biaxial strength tests [34] or estimated by micromechanical modeling [6]. Biaxial strengths used in the following are defined by $\sigma_i = \sigma_j = \sigma_{ij}^{biax}$, while the third normal stress $\sigma_k$ as well as the shear stresses $\tau_{ij}$ are zero. This yields the biaxial parameters

$$\begin{aligned}
b_{LLRR} &= \frac{1 - \sigma_{LR}^{biax}\ (a_{LL} + a_{RR}) - (\sigma_{LR}^{biax})^2\ (b_{LLLL} + b_{RRRR})}{2\ (\sigma_{LR}^{biax})^2}\ , \\
b_{RRTT} &= \frac{1 - \sigma_{RT}^{biax}\ (a_{RR} + a_{TT}) - (\sigma_{RT}^{biax})^2\ (b_{RRRR} + b_{TTTT})}{2\ (\sigma_{RT}^{biax})^2}\ , \text{ and} \\
b_{TTLL} &= \frac{1 - \sigma_{TL}^{biax}\ (a_{TT} + a_{LL}) - (\sigma_{TL}^{biax})^2\ (b_{TTTT} + b_{LLLL})}{2\ (\sigma_{RL}^{biax})^2}\ .
\end{aligned} \tag{6.15}$$

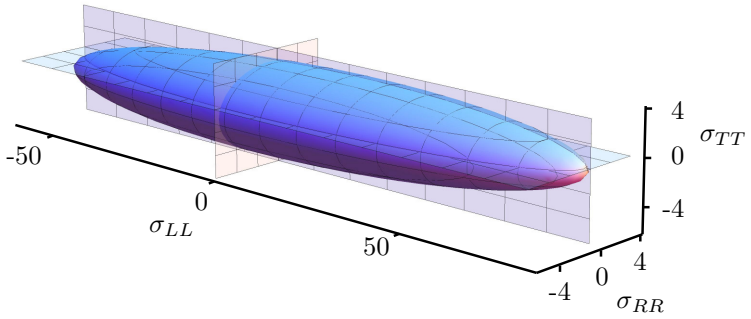


Figure 6.1: Geometric interpretation of the TSAI-WU failure surface in the $\sigma_{LL}$-$\sigma_{RR}$-$\sigma_{TT}$ stress space with typical parameters for spruce, where $\tau_{RT} = \tau_{TL} = \tau_{LR} = 0$.

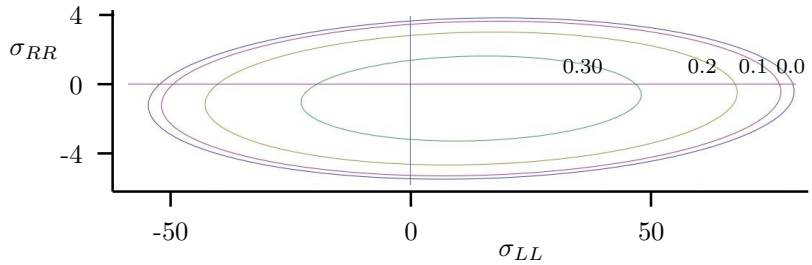


Figure 6.2: Cross-sections of the failure surface with typical parameters for spruce at $\sigma_{TT} = \tau_{RT} = \tau_{TL} = 0$, $\tau_{LR}$ at various levels: $\tau_{LR} = 0.0/0.10/0.20/0.30\, f_{y_{LR}}$.

The biaxial parameters are mainly responsible for a rotation of the yield surface in the stress space. As the biaxial strengths of wood are quite hard to determine, the respective parameters are set equal to zero in some publications so that $b_{iijj} = 0$, [82].

In mathematical terms, Equation (6.13) is the formula for describing generalized conic sections. In case of

$$b_{iiii} b_{jjjj} - b_{iijj}^2 \geq 0 \ , \tag{6.16}$$

the failure surface is closed; otherwise the failure surface is open. In a single-surface failure criterion for wood, Equation (6.16) must be fulfilled in order to guarantee a closed surface. In case of multi-surface models, open surfaces can describe one or more of the respective surfaces. Only in total the failure surface must be closed.

For three-dimensional stress states, a geometric representation of the failure surface is not directly possible because of the six dimensions of the stress space. A geometric interpretation of the failure surface can be given, when three (four) stresses are set to fixed values so that three-(two-)dimensional plots can be drawn (Figures 6.1 and 6.2).

It is noteworthy, that uniaxial strengths are not necessarily equal to maximum (minimum) stresses in the respective material direction, and that shear strengths do not

necessarily coincide with the maximum allowable shear stresses in the respective shear plane. That means

$$\max \sigma_{ii} \neq f_{y_{t_i}} \ , \quad \min \sigma_{ii} \neq f_{y_{c_i}} \ , \quad \max \tau_{ij} \neq f_{y_{ij}} \tag{6.17}$$

in the general case. Because of the interaction of stress terms in the TSAI-WU failure criterion, maximum stresses occur under certain load (stress) combinations. Maximum (minimum) axial and shear stresses can be derived by differentiating Equation (6.13) with respect to the respective stress.

**Transversal orthotropy**

For transversal orthotropy, the number of material parameters in Equation (6.13) is further reduced due to the identities $a_{RR} = a_{TT}$, $b_{RRRR} = b_{TTTT}$, $b_{LLRR} = b_{TTLL}$, $b_{LRLR} = b_{TLTL}$, and $b_{RTRT} = (b_{RRRR} - b_{RRTT})/2$. The result is a simpler description of the failure surface with seven independent strength-related parameters

$$\begin{aligned} \Phi(\boldsymbol{\sigma}) &= a_{LL}\ \sigma_{LL} + a_{RR}\ (\sigma_{RR} + \sigma_{TT}) \ ... \\ &+ b_{LLLL}\ \sigma_{LL}^2 + b_{RRRR}\ (\sigma_{RR}^2 + \sigma_{TT}^2) \ ... \\ &+ 2\ b_{LLRR}\ \sigma_{LL}\ (\sigma_{RR} + \sigma_{TT}) + 2\ b_{RRTT}\ \sigma_{RR}\ \sigma_{TT} \ ... \\ &+ 4\ b_{LRLR}\ (\tau_{LR}^2 + \tau_{TL}^2) + 2\ (b_{RRRR} - b_{RRTT})\ \tau_{RT}^2 - 1 \leq 0 \end{aligned} \tag{6.18}$$

### 6.2.4 (Associated) Plastic flow rule

The plastic flow rule describes the direction of evolution of the plastic strain, once plasticity occurs ($\Phi(\boldsymbol{\sigma}) = 0$). The rate of change of the plastic strain is defined by

$$\dot{\boldsymbol{\varepsilon}}^p = \dot{\gamma}\ \mathbf{N}(\boldsymbol{\sigma}) \ , \tag{6.19}$$

where $\mathbf{N}$ is the flow vector and $\dot{\gamma}$ the plastic multiplier, which is defined in Section 6.2.6. In general, $\mathbf{N}$ is derived from a flow potential $\Psi = \Psi(\boldsymbol{\sigma})$, so that

$$\mathbf{N}(\boldsymbol{\sigma}) = \frac{\partial \Psi(\boldsymbol{\sigma})}{\partial \boldsymbol{\sigma}} \ . \tag{6.20}$$

If $\Psi \neq \Phi$, the flow rule is called a non-associated flow rule. If $\Psi = \Phi$, i.e. if the same function is used as for the failure surface, the flow vector becomes

$$\mathbf{N}(\boldsymbol{\sigma}) = \frac{\partial \Psi(\boldsymbol{\sigma})}{\partial \boldsymbol{\sigma}} = \frac{\partial \Phi(\boldsymbol{\sigma})}{\partial \boldsymbol{\sigma}} \ . \tag{6.21}$$

In this case, the flow direction is normal to the yield surface in the respective point. Consequently, the flow rule is called an associated flow rule.

The model presented herein uses an associated flow rule.

### 6.2.5 Loading/Unloading conditions

The loading and unloading conditions define the state when plastic loading occurs. These conditions are commonly called KUHN-TUCKER-conditions and read

$$\dot{\gamma} \geq 0 \ , \quad \Phi(\boldsymbol{\sigma}) \leq 0 \ , \quad \dot{\gamma}\ \Phi(\boldsymbol{\sigma}) = 0 \ . \tag{6.22}$$

The conditions allow a distinction between elastic loading and unloading, neutral loading, and plastic loading:

$$\Phi(\boldsymbol{\sigma}) < 0 \quad \text{and} \quad \dot{\gamma} = 0 \quad \text{elastic loading or unloading,} \tag{6.23}$$

$$\Phi(\boldsymbol{\sigma}) = 0 \quad \text{and} \quad \dot{\gamma} = 0 \quad \text{neutral loading,} \tag{6.24}$$

$$\Phi(\boldsymbol{\sigma}) = 0 \quad \text{and} \quad \dot{\gamma} > 0 \quad \text{plastic loading.} \tag{6.25}$$

### 6.2.6 The plastic multiplier

In addition to the KUHN-TUCKER-conditions (6.22), the consistency condition hasto be fulfilled, reading as

$$\dot{\gamma}\ \dot{\Phi}(\boldsymbol{\sigma}) = 0\ . \tag{6.26}$$

This implies that, once the material point is in the plastic domain,

$$\dot{\Phi}(\boldsymbol{\sigma}) = 0 \tag{6.27}$$

because of $\dot{\gamma} > 0$. Together with the additive strain split (6.1), the generalized HOOKE's law (6.6), and the plastic flow rule (6.19), this yields

$$\begin{aligned}\dot{\Phi}(\boldsymbol{\sigma}) &= \frac{\partial \Phi}{\partial \boldsymbol{\sigma}} : \dot{\boldsymbol{\sigma}} \\ &= \frac{\partial \Phi}{\partial \boldsymbol{\sigma}} : \mathbb{C} : \dot{\boldsymbol{\varepsilon}} - \frac{\partial \Phi}{\partial \boldsymbol{\sigma}} : \mathbb{C} : \dot{\boldsymbol{\varepsilon}}^p \\ &= \frac{\partial \Phi}{\partial \boldsymbol{\sigma}} : \mathbb{C} : \dot{\boldsymbol{\varepsilon}} - \frac{\partial \Phi}{\partial \boldsymbol{\sigma}} : \mathbb{C} : \dot{\gamma} \frac{\partial \Psi}{\partial \boldsymbol{\sigma}} = 0\ .\end{aligned} \tag{6.28}$$

Consecutively, this leads to an equation for determining $\dot{\gamma}$:

$$\dot{\gamma} = \frac{\dfrac{\partial \Phi}{\partial \boldsymbol{\sigma}} : \mathbb{C} : \dot{\boldsymbol{\varepsilon}}}{\dfrac{\partial \Phi}{\partial \boldsymbol{\sigma}} : \mathbb{C} : \dfrac{\partial \Psi}{\partial \boldsymbol{\sigma}}} = \frac{\mathbf{N} : \mathbb{C} : \dot{\boldsymbol{\varepsilon}}}{\mathbf{N} : \mathbb{C} : \mathbf{N}}\ . \tag{6.29}$$

### 6.2.7 Elasto-plastic tangent operator

In the plastic domain, the rate form of the elastic constitutive equation

$$\dot{\boldsymbol{\sigma}} = \mathbb{C} : \dot{\boldsymbol{\varepsilon}} = \mathbb{C} : \dot{\boldsymbol{\varepsilon}}^e \tag{6.30}$$

is replaced by

$$\dot{\boldsymbol{\sigma}} = \mathbb{C}^{ep} : \dot{\boldsymbol{\varepsilon}} = \mathbb{C}^{ep} : (\dot{\boldsymbol{\varepsilon}}^e + \dot{\boldsymbol{\varepsilon}}^p) \tag{6.31}$$

where $\mathbb{C}^{ep}$ is the elasto-plastic tangent operator. By substituting $\dot{\gamma}$ according to Equation (6.29) in (6.19) and inserting the result in (6.31), the elasto-plastic tangent operator is obtained as

$$\mathbb{C}^{ep} = \mathbb{C} - \frac{(\mathbb{C} : \mathbf{N}) \ \otimes \ (\mathbb{C} : \mathbf{N})}{\dfrac{\partial \Phi}{\partial \boldsymbol{\sigma}} \ : \ \mathbb{C} \ : \ \mathbf{N}}\ . \tag{6.32}$$

The elasto-plastic tangent operator is non-symmetric in the general case of non-associative plasticity, but symmetric for associated plasticity.

## 6.3 Algorithmic implementation

The algorithm described here uses the return-map algorithm for determining stresses and (in-)elastic strains once the material is in the plastic domain. In general, the algorithm is nonlinear so that an iterative solution concept is necessary. A NEWTON-RAPHSON-scheme is used which guarantees a quadratic rate of convergence and is computationally efficient.

In the following, the rate formulation is replaced by a formulation using finite increments in the interval $\Delta t = t_{n+1} - t_n$. It is assumed, that the algorithm has already converged at time $t_n$, and that the elastic strains $\boldsymbol{\varepsilon}_n$, the plastic strains $\boldsymbol{\varepsilon}^p_n$, and the stresses $\boldsymbol{\sigma}_n$ are therefore known.

Basically, this algorithm consists of two steps:

1. Elastic predictor step:

In the elastic predictor step, the stresses are calculated based on the assumption of elastic behavior (*trial stress*) with constant plastic strains. This results in

$$\boldsymbol{\varepsilon}^{p\ trial}_{n+1} = \boldsymbol{\varepsilon}^p_n \ , \tag{6.33}$$

$$\boldsymbol{\sigma}^{trial}_{n+1} = \mathbb{C} : (\boldsymbol{\varepsilon}_{n+1} - \boldsymbol{\varepsilon}^{p\ trial}_{n+1}) = \mathbb{C} : (\boldsymbol{\varepsilon}_{n+1} - \boldsymbol{\varepsilon}^p_n) \ . \tag{6.34}$$

The yield function is evaluated as $\Phi^{trial}_{n+1} = \Phi(\boldsymbol{\sigma}^{trial}_{n+1})$. If $\Phi^{trial}_{n+1} < 0$, the increment is elastic and, considering Equation (6.23), the plastic multiplier becomes $\gamma_{n+1} = 0$. The trial state is then accepted as the solution for the increment.

If $\Phi^{trial}_{n+1} \geq 0$, the trial state lies outside or on the yield surface. The increment is plastic and therefore $\gamma_{n+1} \geq 0$. In this case, the stresses and strains are calculated by performing the plastic corrector step.

2. Plastic corrector step:

$\boldsymbol{\varepsilon}^p_{n+1}$ is updated by the plastic corrector using Equation (6.19) and the constraint of a positive plastic multiplier

$$\boldsymbol{\varepsilon}^p_{n+1} = \boldsymbol{\varepsilon}^p_n + \gamma_{n+1}\mathbf{N}_{n+1} \ , \tag{6.35}$$

$$\Phi(\boldsymbol{\sigma}_{n+1}) = 0 \ . \tag{6.36}$$

The return-map algorithm projects the trial stresses back onto the yield surface, so that the yield condition is not violated. Equation (6.35) can be transformed into

$$\boldsymbol{\varepsilon}^e_{n+1} = \boldsymbol{\varepsilon}^{e\ trial}_{n+1} - \gamma_{n+1}\ \mathbf{N}_{n+1} \quad \text{and, subsequently,} \tag{6.37}$$

$$\boldsymbol{\sigma}_{n+1} = \boldsymbol{\sigma}^{trial}_{n+1} - \gamma_{n+1}\ \mathbb{C} : \mathbf{N}_{n+1} \ . \tag{6.38}$$

Figure 6.3 gives a geometric interpretation of the latter equation and explains the motivation of the term 'return-mapping'. In the current case of perfect plasticity with an associated flow rule, this is also known as the closest point projection of the trial stresses

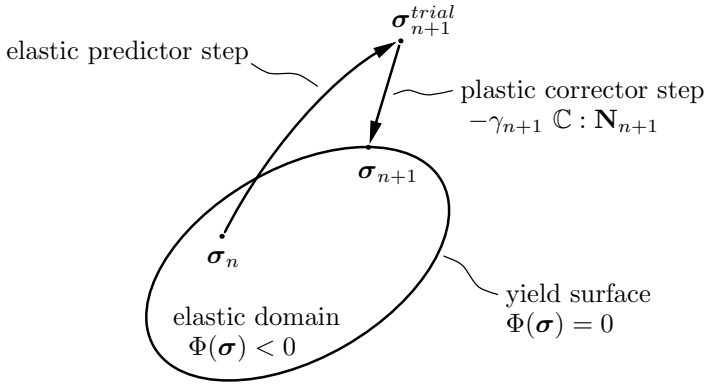


Figure 6.3: Geometric interpretation of the return map algorithm for elastic materials with perfect plastic behavior.

as $\boldsymbol{\sigma}_{n+1}$ is the closest point to $\boldsymbol{\sigma}_{n+1}^{trial}$ lying on the yield surface in the $\mathbb{C}$-metric. The procedure is a fully implicit scheme.

In most parts, the algorithmic implementation follows the procedure presented by Fleischmann [38]. There an elasto-plastic material model for wood under plain stress conditons was developed. The model includes hardening and softening and uses an associated flow rule. Therein, the detailed algorithmic procedure for solving the Newton-Raphson-scheme can be found.

## 6.4 Finite Element implementation

The implementation into the Finite-Element package ABAQUS is done by using the user-subroutine UMAT. In an UMAT-subroutine, a *U*ser-defined *MAT*erial can be specified for constitutive behavior not covered by the built-in functionality of ABAQUS. UMAT processes all necessary operations on the material level at each integration point of each element. In addition, it allows to store and use state variables if necessary.

The ABAQUS-framework passes over all necessary information to UMAT. For the present material model, these are stresses $\boldsymbol{\sigma}_n$, strains $\boldsymbol{\varepsilon}_n$, and state variables $\boldsymbol{\varepsilon}_n^{pl}$ at time $t_n$. In addition, the increment in strains $\Delta\boldsymbol{\varepsilon} = \boldsymbol{\varepsilon}_{n+1} - \boldsymbol{\varepsilon}_n$ is passed over.

With this at hand, the UMAT does the above shown iterative scheme and returns the converged results to ABAQUS. These are the stresses $\boldsymbol{\sigma}_{n+1}$ and the plastic strains $\boldsymbol{\varepsilon}_{n+1}^{p}$ at time $t_{n+1}$, as well as the elasto-plastic tangent operator $\mathbb{C}_{n+1}^{ep}$.

The global assembly of the (tangent) stiffness matrix and the solution of the resulting system of equations (global equilibrium iterations) are again performed automatically by ABAQUS. A fully implicit solution scheme is used in all simulations.

### 6.4.1 Input of parameters

The subroutine offers an interface to define elastic and plastic properties of the material. In addition to that, a set of variables is used to switch between various options. A basic switch allows to chose between alternative ways to provide input parameters. Either

hard-coded data is used, or data from the ABAQUS-interface are passed over. A second switch allows to turn off plastic material behavior so that elasticity is assumed, even when the yield criterion is violated. This may help to pre-estimate the most vulnerable parts of a structure with very little computational cost.

In the general case of orthotropy, a set of input parameters for UMAT comprises nine independent parameters defining the stiffness matrix as well as twelve independent strength parameters. The latter can be defined either directly as TSAI-WU-parameters $a_{ij}$ and $b_{ijkl}$, in order to directly define the yield surface. Alternatively, strength parameters $f_y$ can be passed over, which are then converted internally into the respective TSAI-WU-parameters.

### 6.4.2 Results from Finite Element simulations

In addition to the variables described above, the code has been designed to provide the value of $\Phi(\boldsymbol{\sigma})$. This allows to gain insight into the grade of utilization in each material point. The occurring failure mode can then be identified by comparing the stress state with the utilization grade. Areas within the structure, which are at the limit of their bearing-capacity, can be identified.

When performing purely elastic simulations, the parameter provides quick information about weak points in the structure without the need of computationally expensive simulations.

## 6.5 Verification example

In this section, the verification of the implemented code is shown by means of a small example. The example demonstrates the algorithmically correct behavior of the UMAT subroutine. The geometry, material orientation, boundary conditions, and loading of the example are chosen to result in homogenous stress and strain distributions.

**Geometry**
A cube of length 50 mm length is simulated (Figure 6.4). The material axes are given by vectors $\mathbf{n}_L = \{1.0/0.3/0.0\}^T$, $\mathbf{n}_R = \{-0.3/1.0/0.0\}^T$, and $\mathbf{n}_L = \{0.0/0.0/1.0\}^T$, the $L$-axis is therefore inclined by approx. 16.7° to the $x$-axis.

**Discretization**
The cube is represented by a single element of type C3D8, which is a linear, fully integrated hexaeder with 8 nodes.

**Material behavior**
The material is considered to be orthotropic with linear-elastic, perfect plastic behavior. Stiffnesses and strengths are set to typical values for wood of medium density. According to Equation (6.7), the elastic stiffness, using VOIGT notation, is given by the orthotropic

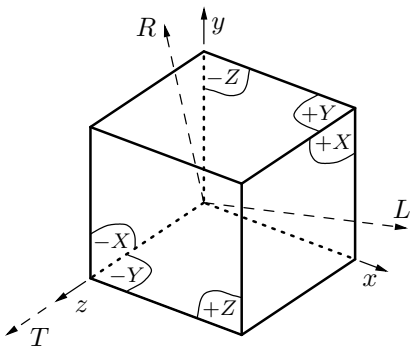


Figure 6.4: Configuration of the verification example.

stiffness matrix (in $\mathrm{N/mm^2}$)

$$\mathbb{C} = \begin{bmatrix} 12\,625 & 314 & 248 & 0 & 0 & 0 \\ 314 & 988 & 463 & 0 & 0 & 0 \\ 248 & 463 & 659 & 0 & 0 & 0 \\ 0 & 0 & 0 & 46 & 0 & 0 \\ 0 & 0 & 0 & 0 & 337 & 0 \\ 0 & 0 & 0 & 0 & 0 & 344 \end{bmatrix}, \tag{6.39}$$

with the order $L$, $R$, and $T$ for the normal, and $RT$, $TL$, and $LR$ for the shear components.

The uniaxial strength values in the principal material directions are

$$\begin{aligned} f_{y_{t_L}} &= \phantom{-}79.44\,\mathrm{N/mm^2}, \quad f_{y_{t_R}} = \phantom{-}3.64\,\mathrm{N/mm^2}, \quad f_{y_{t_T}} = \phantom{-}2.94\,\mathrm{N/mm^2}, \\ f_{y_{c_L}} &= -52.09\,\mathrm{N/mm^2}, \quad f_{y_{c_R}} = -5.45\,\mathrm{N/mm^2}\text{ , and } \quad f_{y_{c_T}} = -4.40\,\mathrm{N/mm^2} \end{aligned} \tag{6.40}$$

for tension and compression, respectively. The shear yield strengths are

$$f_{y_{LR}} = 4.62\,\mathrm{N/mm^2}, \quad f_{y_{RT}} = 1.57\,\mathrm{N/mm^2}\text{ , and } \quad f_{y_{TL}} = 4.57\,\mathrm{N/mm^2}\text{ ,} \tag{6.41}$$

and the biaxial strengths are given by

$$f^{biax}_{y_{LR}} = 3.705\,\mathrm{N/mm^2}, \quad f^{biax}_{y_{RT}} = 2.153\,\mathrm{N/mm^2}\text{ , and } \quad f^{biax}_{y_{TL}} = 2.986\,\mathrm{N/mm^2}\text{ .} \tag{6.42}$$

The resulting Tsai-Wu parameters $a_{ij}$ and $b_{ijkl}$ are determined from the strength values by means of Equation (6.14).

**Boundary conditions & loading**
The cube is retained on its side faces, so that displacements $u_x(x = 0) = 0$, $u_y(y = 0) = 0$, and $u_z(z = 0) = 0$. In the first loading step, loads are linearly applied displacement-driven, up to $u_x(x = 50) = -0.2\,\mathrm{mm}$ and $u_y(y = 50) = -0.6\,\mathrm{mm}$ at the end of the step. In the second step, the prescribed displacements of step one are taken back so that $u_x(x = 50) = 0\,\mathrm{mm}$ and $u_y(y = 50) = 0\,\mathrm{mm}$, respectively. Teh side face $+Z$ is free to deform.

**Results**

Stresses as well as total and plastic strains are determined during the analysis. Therefrom, the elastic strains follow from by $\varepsilon^{el} = \varepsilon - \varepsilon^{pl}$. The relation $\boldsymbol{\sigma} = \mathbb{C} : \boldsymbol{\varepsilon}^{el}$ is used as a control and holds for all increments.

The resulting axial and shear strains are depicted in Figure 6.5. Although the cube expands as expected in the $T$-direction during elastic loading, it contracts once plastic deformations start to develop. This behavior is caused by the chosen associated plastic flow rule, which governs the development of (negative) plastic strains in $R$-direction.

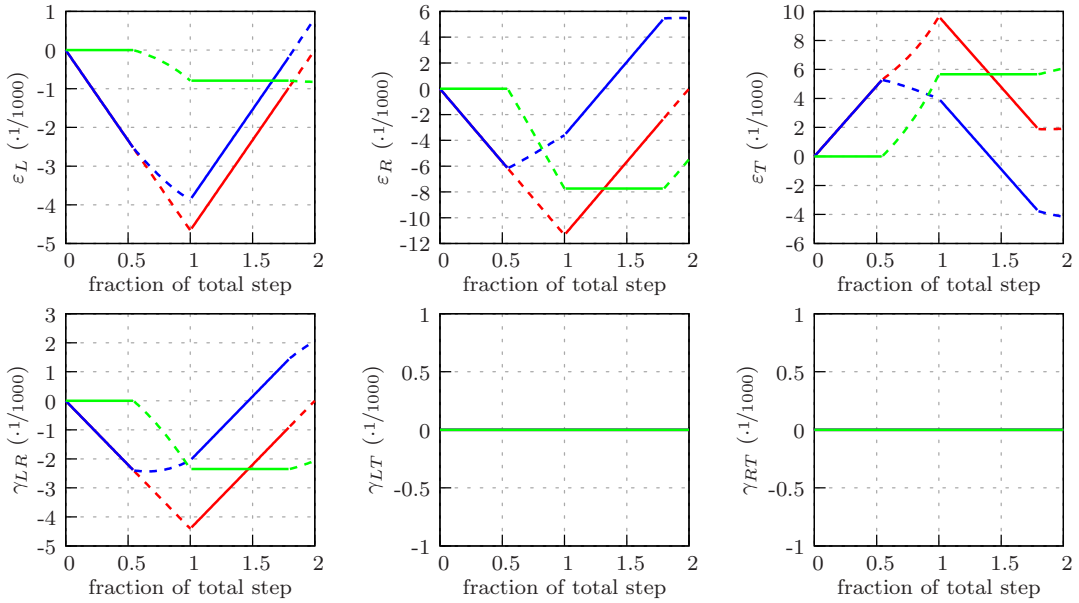


Figure 6.5: Evolution of total $\varepsilon$ (red), elastic $\varepsilon^{el}$ (blue), and accumulated plastic $\varepsilon^{pl}$ (green) axial and shear strains in the material directions. (Continuous lines denote elastic, dashed lines plastic material behavior.)

the resulting axial and shear stresses are plotted in Figure 6.6. Stresses increase or decrease proportionally until yielding starts. From that moment onwards, the stress points stay on the yield surface in the stress space but stress redistribution occurs. At the beginning of step 2, elastic unloading starts, so that the stress point falls within the yield surface. The effects of plastic deformations are clearly visible, as tension stresses remain in $L$-direction at the end of step 2, although the cube's dimensions in $x$ and $y$-direction are back to their initial values. Figure 6.7 shows the evoulution of stresses in the $\sigma_L$-$\sigma_R$-$\tau_{LR}$-stress space.

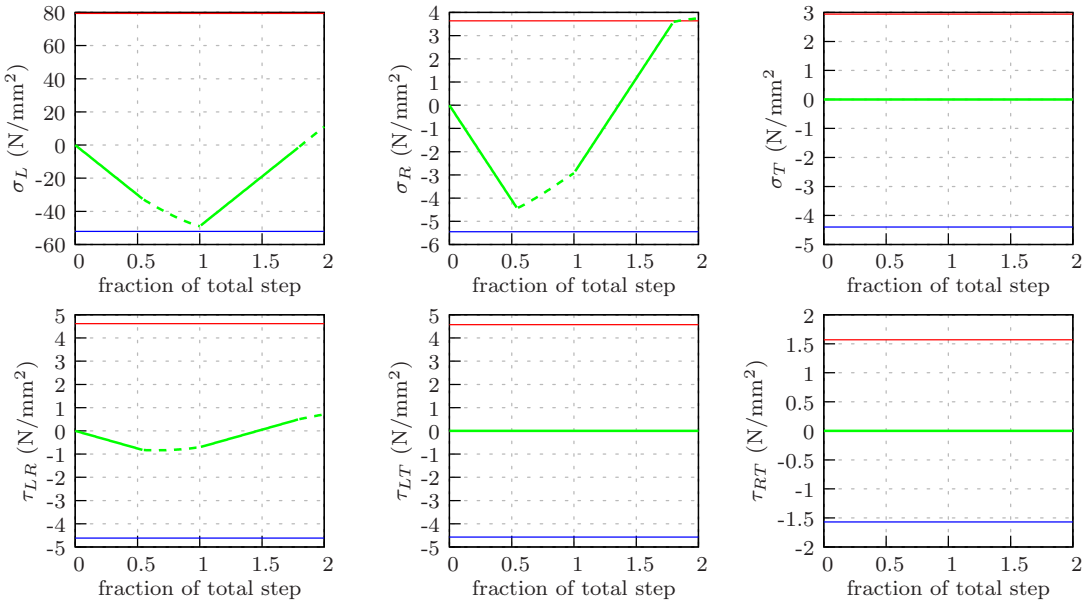


Figure 6.6: Evolution of axial and shear stresses in the material directions. (Continuous lines denote elastic, dashed lines plastic material behavior, red and blue lines denote maximum/minimum uniaxial yield stresses in the respective material direction.)

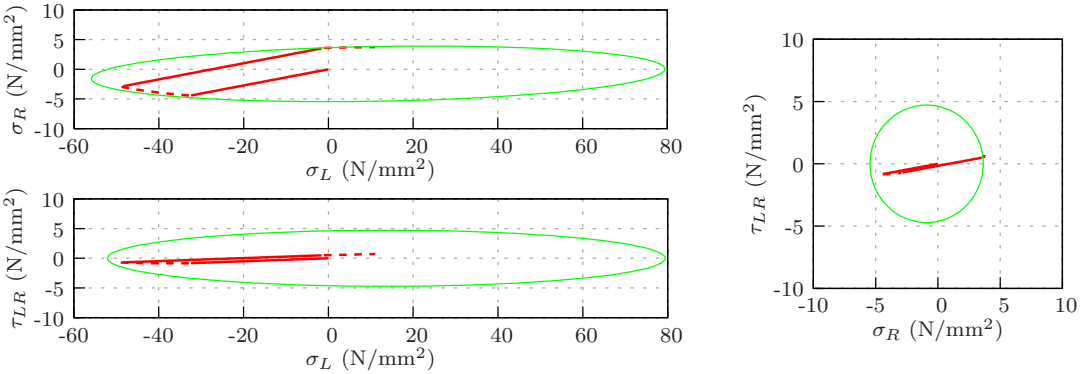


Figure 6.7: Stress interaction and cuts through the yield surface in the $\sigma_L$-$\sigma_R$-$\tau_{LR}$-stress space. (Continuous lines denote elastic, dashed lines plastic material behavior.)

## 6.6 Discussion

This chapter has described the elasto-plastic material model used for the numerical simulations of dowel-type connections. The requirements on the comprehensiveness and complexity of the material description in the intended field of applications were stated (Section 6.1) and admissible simplifications derived therefrom.

In the elastic domain, the material model defines the reversible stress-strain relationship for orthotropic materials (Section 6.2.2). Failure of the material is described by

a Tsai-Wu failure surface (Section 6.2.3). Once the material has exceeded the elastic limit, pefect plastic material behavior is assumed, regardless the nature of the failure (in wood, tension and shear failure are usually a brittle failure modes, while compression failure is usually ductile). The theory of elasto-plasticity has been summarized, and the basics of the algorithmic implementation were (Section 6.3). The implementation into the commercial Finite-Element code ABAQUS was briefly presented (Section 6.4) and verified by means of a simple example (Section 6.5).

The assumption of plastic post-failure behavior without distinguishing between the real failure modes is naturally a bold simplification. Perfect plasticity is assumed, so that the yield surface does not change once the material is in the plastic domain. Hardening of the material, observed for example when wood is compression load, is therefore not taken into account. Additionally, the assumption of an associated plastic flow rule may not be fully appropriate, but since knowledge thereof is limited, it is nevertheless used.

The field of application is mainly to in define the elastic limit state applied at structural simulations. When simulating dowel-type timber connections (Section 7), the Serviceability Limit State is of interest. Therein, using the simplified material behavior and perfect plasticity gives a feeling of the upper limits of elastic structural behavior. Additionally, the regions of high tension and shear stresses, which may lead to brittle failure, can be determined.

# Chapter 7

# Structural simulations

The following chapter deals with numerical simulations of dowel-type timber connections by means of the Finite Element Method. The previously presented modeling approaches for the contact behavior (Chapter 5) and the elasto-plastic behavior of wood (Chapter 6) are combined with standard simulation algorithms in order to simulate the structural behavior of these connections.

The modeling strategy is presented with the help of a specific example first. The Finite Element environment is briefly sketched, together with short descriptions of the features used. The simulation results of this typical example are shown and discussed in detail. Next, a parametric study shall give an impression of the changes of the connections behavior in consequence of variations of selected input parameters. Finally, the capabilities and limitations of the modeling approach are discussed, together with an outlook on various possibilities to overcome these limitations.

## 7.1 Reference simulation

### 7.1.1 Definition of the reference simulation

The Finite Element program ABAQUS, version 6.11, is used for the simulations [1]. The models are created with the pre and post-processing interface ABAQUS CAE. The built-in features are combined with a user-defined material behavior for wood, which enables realistic simulations of dowel-type timber connections.

**Geometry**
The connection is of 100 mm ($2\,a$) width with a dowel of $d = 12$ mm diameter. Regarding side member width (36 mm) and edge distance (84 mm), the geometry is following the minimum requirements of EC5. The dimensions are chosen to give a connection with intermediate $a/d$-ratio, for which a single plastic hinge forms in the dowel during loading. The cut-in slot for the steel plate is of 10 mm thickness. The total length of the wood

part is 400 mm, which is long enough so that the back anchorage does not influence the load distribution in the area of the connection. Figure 7.1 shows the main dimensions and the layout of the reference connection.

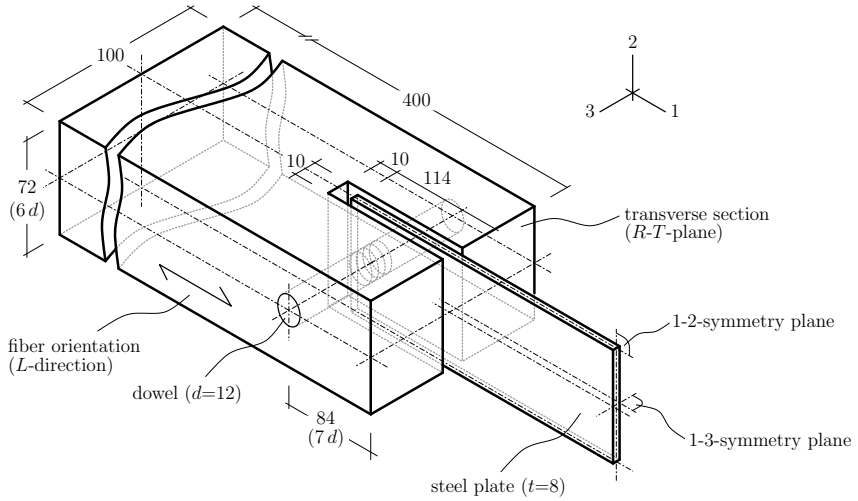


Figure 7.1: Layout of the reference simulation with the main dimensions (in mm).

The back-anchorage of the connection, which is necessary for the load application in the experiments, is simplified in the simulation model. The wood piece is completely restrained at a cross-sectional plane sufficiently far from the connection to guarantee a uniform stress distribution.

The dowel is modeled as a cylinder of 12 mm diameter with a straight axis, positioned initially at a right angle to the steel plate. The clearance between the dowel and the bore-hole is set to zero, so that both surfaces are perfectly fitting before load application.

The steel plate is of 8 mm thickness and 72 mm width. The plate is sufficiently long (250 mm) to guarantee uniform load distribution at the clamped end. The edge distance to the unloaded end of the plate is 30 mm ($= 2.5\,d$).

**Wood properties**

The wooden part is modeled with transversal isotropic material behavior regarding stiffness and strength. Therefore, the orientations of the radial and the tangential direction and the pith location do not play a role. The wood fiber direction is aligned with the main elongation of the connection and the direction of the force. Due to the transversal isotropy, it is sufficient to model only a quarter and to use symmetry boundary conditions, which significantly reduces the simulation effort.

Wood of intermediate density is considered in the example, and the stiffness and strength values are chosen in agreement with typical experimental results obtained for wood of this category. In the compression tests of specimens of Series 14_2 (mean density $\varrho = 445\,\mathrm{kg/m^3}$), a mean modulus of elasticity of $E_L = 12\,533\,\mathrm{N/mm^2}$ and a mean compressive strength of $f_{y_{c_L}} = 50.2\,\mathrm{N/mm^2}$ were measured (see Table 4.4). The remaining values for the entire stiffness tensor and the yield strengths are estimated by means of micromechanical modeling. Therein, the microstructural characteristics are chosen such that

the control values for stiffness and strength from the compression tests are reproduced. The results of the micromechanical model yields orthotropic material properties, which are transformed to transversal isotropic properties by applying the following rules:

$$\begin{aligned}
E_R = E_T &= (E_R^* + E_T^*)/2\ , & G_{TL} = G_{LR} &= (G_{TL}^* + G_{LR}^*)/2\ , \\
\nu_{RL} = \nu_{TL} &= (\nu_{RL}^* + \nu_{TL}^*)/2\ , & \nu_{RT} = \nu_{TR} &= (\nu_{RT}^* + \nu_{TR}^*)/2\ , \\
G_{RT} &= \frac{E_R^*}{2\,(1+\nu_{RT}^*)}\ , & & \\
\nu_{LR} &= \nu_{RL}\,E_R/E_L\ , \text{and} & \nu_{LT} &= \nu_{TL}\,E_T/E_L\ ,
\end{aligned} \tag{7.1}$$

whereby quantities marked with $^*$ are orthotropic quantities. The resulting stiffness matrix (in N/mm$^2$) reads, using VOIGT notation, as

$$\mathbb{C} = \begin{bmatrix}
12\,631 & 292 & 292 & 0 & 0 & 0 \\
292 & 840 & 492 & 0 & 0 & 0 \\
292 & 492 & 840 & 0 & 0 & 0 \\
0 & 0 & 0 & 174 & 0 & 0 \\
0 & 0 & 0 & 0 & 341 & 0 \\
0 & 0 & 0 & 0 & 0 & 341
\end{bmatrix}, \tag{7.2}$$

with the order $L$, $R$, and $T$ for the normal, and $RT$, $TL$, and $LR$ for the shear components. The respective elastic constants are compiled in Table 7.1.

| $E_L$ | $E_R$ | $E_T$ | $G_{RT}$ | $G_{TL}$ | $G_{LR}$ |
|---|---|---|---|---|---|
| 12 503 | 551 | 551 | 174 | 341 | 341 |

| $\nu_{LR}$ | $\nu_{LT}$ | $\nu_{RL}$ | $\nu_{RT}$ | $\nu_{TL}$ | $\nu_{TR}$ |
|---|---|---|---|---|---|
| 0.009 66 | 0.009 66 | 0.219 | 0.582 | 0.219 | 0.582 |

Table 7.1: Elastic moduli (in N/mm$^2$) and POISSON's ratios for transversal isotropic behavior and wood of medium density.

Yield strengths (in N/mm$^2$) are given by

$$\begin{aligned}
f_{y_{t_L}} &= 79.0, & f_{y_{t_R}} &= 3.3, & f_{y_{t_T}} &= 3.3, \\
f_{y_{c_L}} &= -52.0, & f_{y_{c_R}} &= -4.6, & f_{y_{c_T}} &= -4.6, \\
f_{y_{LR}} &= 4.6, & f_{y_{RT}} &= 2.9, & f_{y_{TL}} &= 4.6, \\
f_{y_{LR}}^{biax} &= 3.337, & f_{y_{RT}}^{biax} &= 2.181, \text{ and} & f_{y_{TL}}^{biax} &= 3.337.
\end{aligned} \tag{7.3}$$

Biaxial yield strengths are defined so that the respective biaxial TSAI-WU-parameters $b_{LLRR} = b_{RRTT} = b_{TTLL} = 0$. The respective TSAI-WU-parameters (units for $a_{ij}$ and $b_{ijkl}$ are $(\text{N/mm}^2)^{-1}$ and $(\text{N/mm}^2)^{-2}$, respectively) are therefore

$$\begin{aligned}
a_L &= -0.006\,573, & a_R &= 0.085\,64, & a_T &= 0.085\,64, \\
b_{LLLL} &= 0.000\,243\,4, & b_{RRRR} &= 0.065\,88, & b_{TTTT} &= 0.065\,88, \\
b_{LLRR} &= 0, & b_{RRTT} &= 0, & b_{TTLL} &= 0, \\
b_{LRLR} &= 0.011\,81, & b_{RTRT} &= 0.029\,73, \text{ and} & b_{TLTL} &= 0.011\,81.
\end{aligned} \tag{7.4}$$

The user-subroutine UMAT (specified in Section 6) is used for modeling the behavior of the wood section.

**Steel dowel & plate**
Dowel and plate are made of steel, modeled with an isotropic material behavior and VON MISES perfect plasticity. The material is chosen to be of quality S 235 for the dowel and of quality S 355 for the plate, showing a modulus of elasticity of $E = 210\,000\,\mathrm{N/mm^2}$, and yield strengths of $f_y = 235\,\mathrm{N/mm^2}$ and $f_y = 355\,\mathrm{N/mm^2}$, respectively.

**Contact modeling**
Three different contact planes are relevant for the load-carrying behavior of the connection:

- Dowel to wood: The simulation uses the built-in contact model with a nonlinear pressure-overclosure relationship, which is defined by means of a table containing appropriate pairs of these values. The pressure-overclosure relationship follows the course derived in Section 4, the according LAMÉ parameters are given in Table 7.2.

| $\sigma_0$ | $n_\sigma$ | $u_0$ | $n_u$ |
|---|---|---|---|
| $(\mathrm{N/mm^2})$ | | (mm) | |
| 55.0 | 1.10 | 0.350 | 3.90 |

Table 7.2: LAMÉ parameters, used to define the dowel-to-wood contact in the reference simulation.

  The surface of the dowel is regarded as the master surface, while the wood surface serves as the slave surface. A so-called "surface to surface discretization" is used, which enforces the contact constraints in an average sense over a finite region [1]. The positions of the slave nodes are adjusted when necessary, so that they are lying on the master surface in the initial state. This removes overclosure as well as possible gaps at the interface.

  Friction between the two parts is considered to be isotropic with a constant frictional coefficient of $\mu = 0.40$. The penalty method is used.

- Dowel to steel plate: Contact between the steel plate and the dowel is modeled with "hard-contact", whereby no penetration of the surfaces in contact is allowed, the load transfer is instantaneous, and the magnitude of the contact pressure is not limited [1]. The steel plate provides the master surface while the dowel surface serves as the slave surface. Again, surface to surface discretization is used, and the positions of the slave nodes are adjusted.

  Isotropic friction with a frictional coefficient $\mu = 0.70$ is assumed, and again the penalty method is used.

- Plate to wood: Contact between the steel plate and the wood is of minor importance. When the connection is loaded by tension forces, the side members move outwards. In contrast, the side members would move towards the plate under compression loads. In this case wood might get into contact with the steel plate and load transfer would take place.

  In the reference simulation, an initial gap of 1 mm is modeled between the steel plate and wood, so that contact between the two surfaces will not occur, even when compression loads are applied.

**Mesh generation**
The Finite-Element mesh is generated with the mesh generator of ABAQUS. In order to suitably model the concave section of the bore-hole in the wood part, tetraeder elements are used in the wood part. Elements of type C3D10M are employed, which are fully integrated elements with quadratic interpolation of the displacements. Globally, the mesh size is set to 14 mm, a local mesh refinement to intermediate element size (approximately 8 mm) is selected for the wooden side parts of the connection. A fine mesh is selected for the area in the vicinity of the dowel, with element sizes of typically 4 mm. The element length is therefore varying between 14 mm in the back of the wood part and 3.5 mm near the dowel (Figure 7.3).

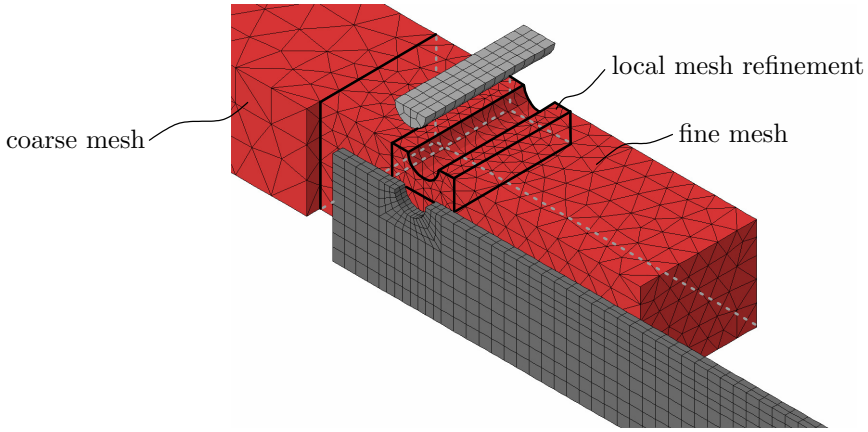


Figure 7.2: Exploded view of the model showing the mesh.

For the dowel and the steel plate, fully integrated, quadratic brick elements of type C3D20 are used. The element length varies between approximately 2.5 and 4.5 mm in the dowel. For the steel plate, a global mesh width of 5 mm and a local mesh refinement in the vicinity of the contact to the dowel to element sizes of typically 1.2 mm is chosen. Depending on the position in the steel plate, the element length is between 1.2 and 4.8 mm. In thickness direction, two elements are enforced.

**Boundary conditions & loading**
As only a quarter of the connection is modeled, appropriate symmetry boundary conditions are applied. Thus, the 1-2-symmetry plane is restrained in 3-direction, $u_3 = 0$, and in the 1-3-symmetry plane in 2-direction, $u_2 = 0$ (Figure 7.3). At the back anchorage, the cross-section is restrained in load direction, $u_1 = 0$.

The load is applied displacement-driven at the end of the steel plate, up to a total displacement of 2 mm.

**Incrementation**
The total load is applied in a single step, divided into 100 equally-sized increments. After each increment output values are stored. This pre-set incrementation can be automatically adjusted – using the option "automatic incrementation" of ABAQUS – in case of slow or no convergence.

In order to increase the performance of the simulation, the iteration strategy is changed

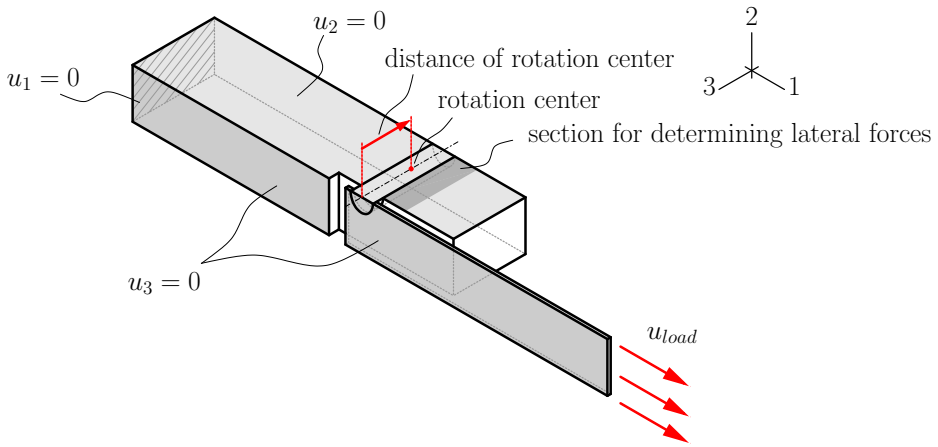


Figure 7.3: Boundary conditions and load application of the double-symmetric model.

compared to the default settings in ABAQUS. In detail, the allowable total number of iterations per increment is increased, which gives more attempts for obtaining a solution in a specific increment. Additionally, the maximum allowable residuum was increased from 0.005 to 0.05, which reduces the accuracy requirements in the increment. These changes do not affect the overall simulation behavior significantly, so that they apparently do not introduce additional error and uncertainties to the simulation, but allow for more efficient simulations.

### 7.1.2 Results of the reference simulation

**Load-displacement curve**

The computed load-displacement curve (Figure 7.4) clearly shows the nonlinear mechanical behavior of the connection. Low stiffness at the beginning of the loading marks the initial phase, characterized by a very compliant contact behavior at the interfaces between the dowel and the bore-hole. This is caused by the compliant contact behavior at the interface between the dowel and the bore-hole. Contact is established along the length of the dowel on its compressive side first. Due to bending of the dowel, the contact pressure is thereby increasing rapidly in the innermost sections.

After the initial phase, there is an approximately linear increase of stiffness until the maximum stiffness (approx. 40 kN/mm) is reached at a total load of 6.2 kN. The phase of almost constant stiffness, characterized by a linear part of the load-displacement curve, is not very pronounced. This phase is followed by an again approximately linear decrease of stiffness. At a total load of 10.9 kN, stiffness has dropped to 75% of its maximum value. The decrease in stiffness is reduced again at a load of approximately 16.6 kN, after which the decrease is almost linear.

Even before the connection reaches its maximum stiffness, first plastic zones in the tension zone of the dowel form at a load of approx. 4.8 kN. First yielding in wood starts at a load of 5.5 kN.

The maximum load is 19.6 kN. At this stage of the simulation, many of the elements already show strains that dramatically exceed the area of validity of small strain/small

displacement theory. First elements with strains greater than 5% occur at a load of 15.0 kN. It is noted, that results obtained after that point are beyond the validity of the simulation tool and the features detected are – at best! – only indicators of possible phenomena in the structure.

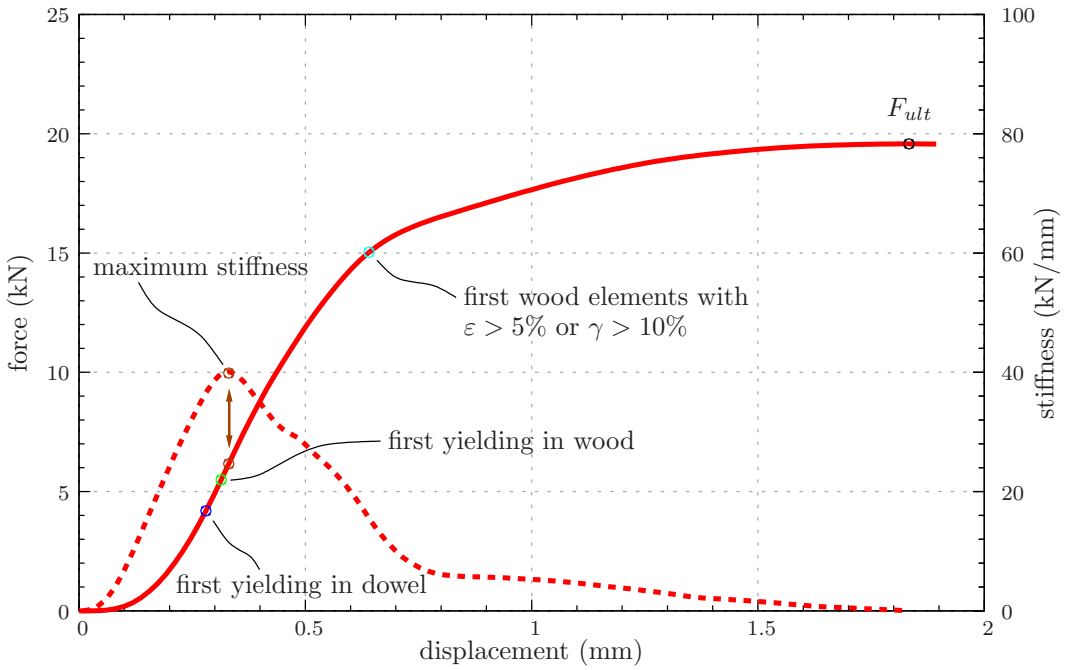


Figure 7.4: Load-displacement curve (solid line) for the reference simulation with the respective stiffness course (dashed line) and specification of the main features (colored dots).

**Wood forces**

The wood is under high compressive load in the innermost parts. This leads to plastification in these areas, which evolves from the 1-2-symmetry plane outwards with increased loading (Figures 7.5 and 7.6).

Transversal forces in the 1-3-symmetry plane develop, which may lead to splitting when reaching high levels in tension.

In the standard simulation, a compressive force develops in this plane in the vicinity of the dowel (cf. Figure 7.9 (a)), which is obtained by summing up the reaction forces at the nodes within the area marked in Figure 7.3. The reason for observing a compression force is that frictional shear stresses in the circumferential direction of the bore-hole prevent the formation of tensile forces. Consequently, splitting in the symmetry plane is likely to be prevented for the investigated configuration, so that this globally brittle failure mode will not occur.

Tensions stresses in lateral direction rather occur in the bulk wood at a distance of about 3.5 mm from the 1-3-symmetry plane, which is approx. 60% of the dowel radius (Figures 7.7). Maximum shear stresses occur at a distance of about 4.3 mm from the symmetry plane, which equals approx. 70% of the dowel radius (Figure 7.8). The combination of shear stresses and tension stresses in lateral direction may lead to a

combined tension/shear failure in the respective region. In the reference simulation, a highly ductile failure mode is to be expected with an elongated loading plateau without a significant or abrupt load drop after reaching the ultimate load until final failure.

Remarkably high tension stresses develop at the unloaded end of the wood part but do not influence the load-carrying behavior of the connection.

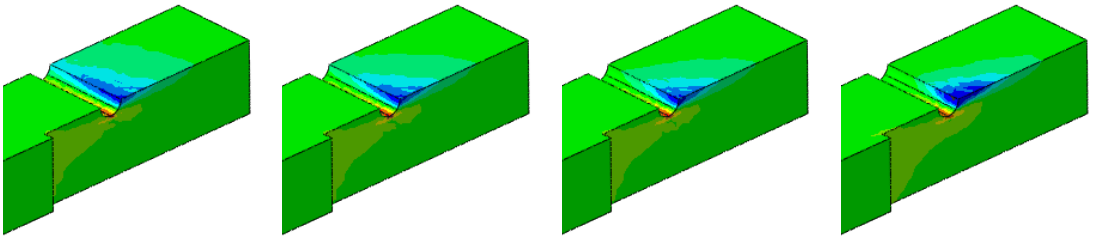

(a) range: $\pm 2\,\mathrm{N/mm^2}$ (b) range: $\pm 14\,\mathrm{N/mm^2}$ (c) range: $\pm 37\,\mathrm{N/mm^2}$ (d) range: $\pm 57\,\mathrm{N/mm^2}$

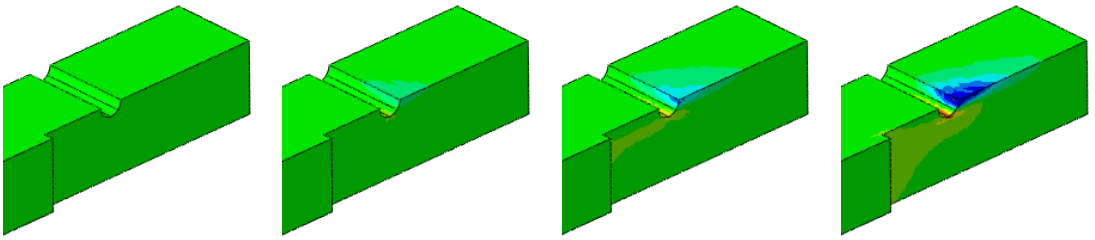

(e) range: $\pm 57\,\mathrm{N/mm^2}$ (f) range: $\pm 57\,\mathrm{N/mm^2}$ (g) range: $\pm 57\,\mathrm{N/mm^2}$ (h) range: $\pm 57\,\mathrm{N/mm^2}$

Figure 7.5: Evolution of normal stresses $\sigma_{11}$ at various load steps: (a,e) 0.8 kN, (b,f) 4.8 kN, (c,g) 10.4 kN, (d,h) 15.0 kN

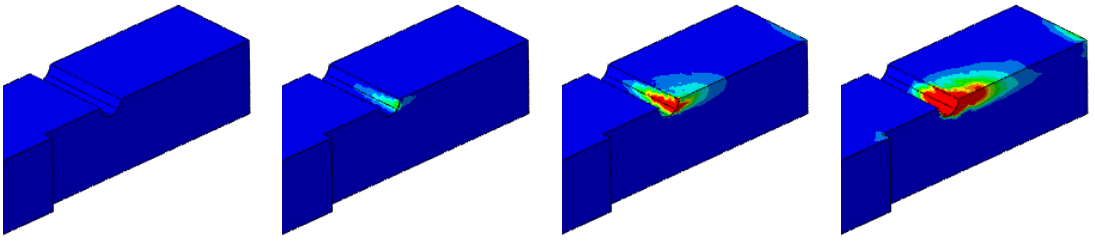

(a) range: $-1/0$ (b) range: $-1/0$ (c) range: $-1/0$ (d) range: $-1/0$

Figure 7.6: Evolution of Tsai-Wu-value $\Phi(\boldsymbol{\sigma})$, denoting active yielding areas, at various load steps: (a) 0.8 kN, (b) 4.8 kN, (c) 10.4 kN, (d) 15.0 kN

**Dowel forces**

All loads are transferred by bending and shearing of the dowel, which therefore naturally is a highly stressed part. Figure 7.9 (a) shows the bending moment in the dowel. Additionally, the elastic and plastic bending moments are added as a reference ($M_{el} = f_y\,\pi d^3/32 = 4.0\,\mathrm{kNcm}$, $M_{pl} = f_y\,d^3/6 = 6.8\,\mathrm{kNcm}$). The moment in the dowel is rapidly increasing and shows a maximum of 7.4 kNcm at a total load of 11.9 kN.

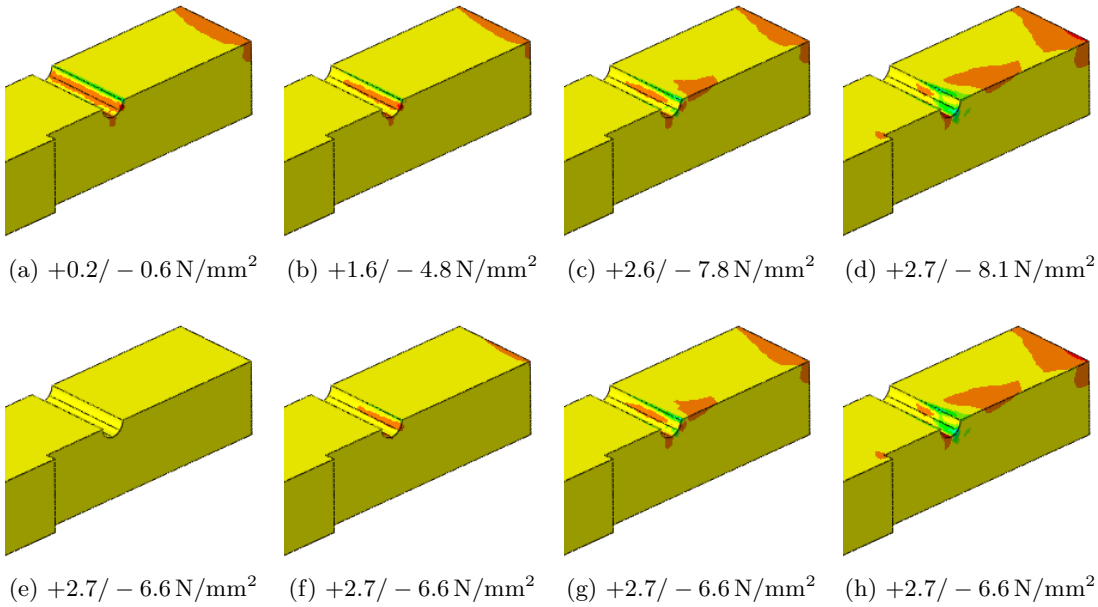

(a) $+0.2/-0.6\,\mathrm{N/mm^2}$ (b) $+1.6/-4.8\,\mathrm{N/mm^2}$ (c) $+2.6/-7.8\,\mathrm{N/mm^2}$ (d) $+2.7/-8.1\,\mathrm{N/mm^2}$

(e) $+2.7/-6.6\,\mathrm{N/mm^2}$ (f) $+2.7/-6.6\,\mathrm{N/mm^2}$ (g) $+2.7/-6.6\,\mathrm{N/mm^2}$ (h) $+2.7/-6.6\,\mathrm{N/mm^2}$

Figure 7.7: Evolution of normal stresses $\sigma_{33}$ at various load steps: (a, e) 0.8 kN, (b, f) 4.8 kN, (c, g) 10.4 kN, (d, h) 15.0 kN.

After reaching the maximum, the bending moment is decreasing slowly at higher displacements.

The dowel rotates only slightly first at the beginning of the load application. With initiation of yielding in the dowel, the rotation increases over-linearly (Figure 7.9 (b)). The increase is finally slowing down once the dowel gets in contact with the wood on the opposite end.

It is noted again, that the observed characteristics are likely to be not properly derived, since the models limits in relation to the used theoretical framework have been exceeded.

**Contact behavior**

The dowel is in contact with the wood at the full length of the hole on the loaded side from the beginning until a total load of 15 kN. This is obvious from evaluating the contact status in the output of the simulation, but also when studying the course of the distance of the rotation center of the dowel from the 1-2-symmetry plane (Figure 7.9 (b)). The rotation center defines the point in the dowel where the displacement in direction of the load is zero (see Figure 7.3). Points closer to the symmetry plane than the rotation center thus deform in load direction, while points further outwards move in the opposite direction. In the beginning, the rotation center is at a distance of about 100 mm from the 1-2-symmetry plane, and the dowel moves in direction of the load. With increased load, the rotation center moves towards the 1-2-symmetry plane. Once its distance is smaller than the side width of the wood, contact between the dowel and the bore-hole is lost, and the outer end of the dowel gets in contact with the wood on the opposite side. This also marks approximately the point when the dowel rotation is again slowed down at increased load (Figure 7.9 (b)).

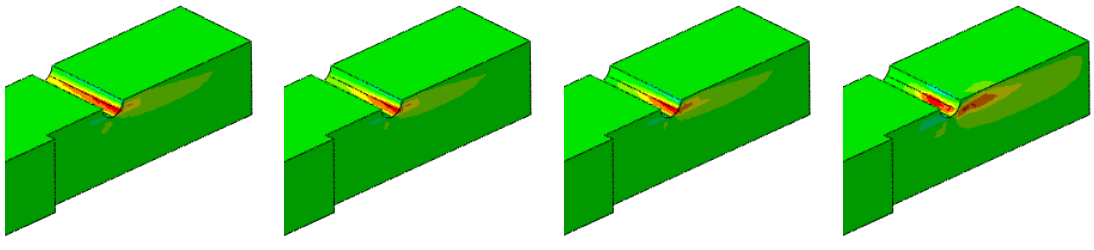

(a) $\pm 0.35\,\mathrm{N/mm^2}$ (b) $\pm 2.7\,\mathrm{N/mm^2}$ (c) $\pm 6.4\,\mathrm{N/mm^2}$ (d) $\pm 6.1\,\mathrm{N/mm^2}$

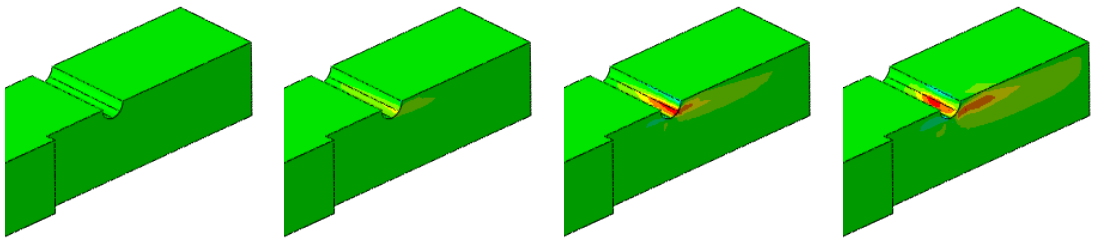

(e) $\pm 6.4\,\mathrm{N/mm^2}$ (f) $\pm 6.4\,\mathrm{N/mm^2}$ (g) $\pm 6.4\,\mathrm{N/mm^2}$ (h) $\pm 6.4\,\mathrm{N/mm^2}$

Figure 7.8: Evolution of shear stresses $\tau_{13}$ at various load steps: (a, e) 0.8 kN, (b, f) 4.8 kN, (c, g) 10.4 kN, (d, h) 15.0 kN.

The distribution of the contact pressure is highly non-uniform due to the soft contact at the interface, although large areas are in contact (Figure 7.10). The distribution of the shear stresses in circumferential direction is almost identical to that of the contact pressure (Figure 7.11). The transition to zero shear stress takes place at about the same distance from the symmetry plane at which the maximum shear stresses and lateral tension stresses in the wood occur.

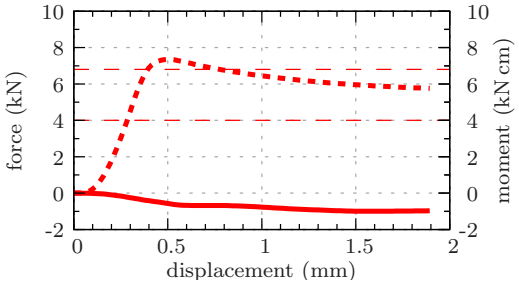


(a) Transversal force in wood (solid) and bending moment in the dowel (dashed)

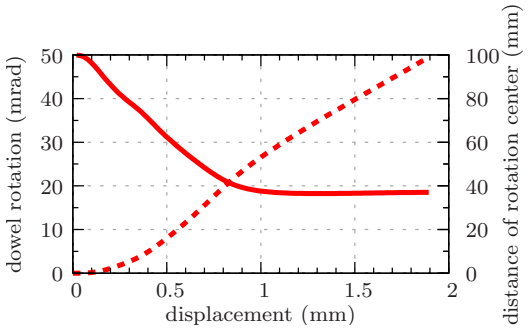


(b) Rotation of dowel axis (solid) and distance of rotation center (dashed)

Figure 7.9: Reaction forces, moments, and dowel rotation (see Figure 7.4 for legend).

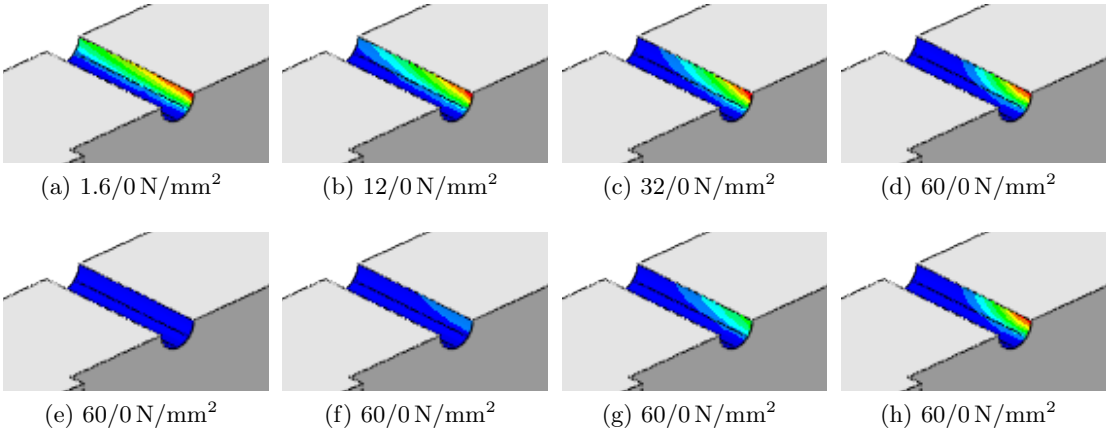

(a) 1.6/0 N/mm$^2$ (b) 12/0 N/mm$^2$ (c) 32/0 N/mm$^2$ (d) 60/0 N/mm$^2$

(e) 60/0 N/mm$^2$ (f) 60/0 N/mm$^2$ (g) 60/0 N/mm$^2$ (h) 60/0 N/mm$^2$

Figure 7.10: Evolution of contact pressure at various load steps: (a, e) 0.8 kN, (b, f) 4.8 kN, (c, g) 10.4 kN, (d, h) 15.0 kN.

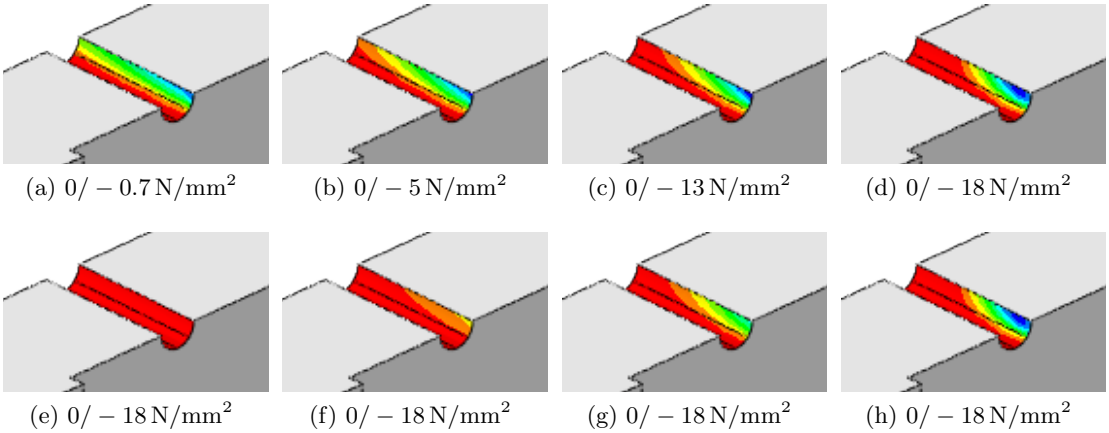

(a) $0/-0.7$ N/mm$^2$ (b) $0/-5$ N/mm$^2$ (c) $0/-13$ N/mm$^2$ (d) $0/-18$ N/mm$^2$

(e) $0/-18$ N/mm$^2$ (f) $0/-18$ N/mm$^2$ (g) $0/-18$ N/mm$^2$ (h) $0/-18$ N/mm$^2$

Figure 7.11: Evolution of frictional shear stress in circumferential direction at various load steps: (a, e) 0.8 kN, (b, f) 4.8 kN, (c, g) 10.4 kN, (d, h) 15.0 kN.

## 7.2 Verification of the simulation approach

In the reference model, the material was considered to be transversal isotropic in the $R$-$T$-plane for reasons of simplicity. This assumption will be verified in the following by comparing results of simulations using this material definition with those obtained for an equivalent orthotropic material behavior.

Furthermore, a small study will be performed to assess mesh dependency (Section 7.2.2).

### 7.2.1 Transversal isotropy

**Variations from the reference model**
In the following, the fully orthotropic stiffnesses and strengths are used, whereby the tangential material direction $T$ is chosen to be either parallel to the dowel axis (Model 4), or perpendicual to the dowel axis (Model 5).

The orthotropic stiffness matrix (in $\mathrm{N/mm^2}$) for wood reads as

$$\mathbb{C} = \begin{bmatrix} 12\,625 & 314 & 248 & 0 & 0 & 0 \\ 314 & 988 & 463 & 0 & 0 & 0 \\ 248 & 463 & 659 & 0 & 0 & 0 \\ 0 & 0 & 0 & 46 & 0 & 0 \\ 0 & 0 & 0 & 0 & 337 & 0 \\ 0 & 0 & 0 & 0 & 0 & 344 \end{bmatrix}, \tag{7.5}$$

with the order $L$, $R$, and $T$ for the normal, and $RT$, $TL$, and $LR$ for the shear components.

The orthotropic yield strengths (in $\mathrm{N/mm^2}$) are given by

$$\begin{aligned} f_{y_{t_L}} &= 79.0, & f_{y_{t_R}} &= 3.6, & f_{y_{t_T}} &= 2.9, \\ f_{y_{c_L}} &= -52.0, & f_{y_{c_R}} &= -5.5, & f_{y_{c_T}} &= -4.4, \\ f_{y_{LR}} &= 4.6, & f_{y_{RT}} &= 1.6, & f_{y_{TL}} &= 4.6, \\ f^{biax}_{y_{LR}} &= 3.645, & f^{biax}_{y_{RT}} &= 2.078, \text{ and} & f^{biax}_{y_{TL}} &= 2.930. \end{aligned} \tag{7.6}$$

All other parameters are not changed compared to the reference simulation.

**Changes observed**
Figure 7.12 shows the load-displacement curves derived in the reference simulations. The differences to the respective curves resulting with an orthotropic material behavior are very small in relation to the overall behavior of the simulations. The orthotropic material definition leads to slightly higher loads at given displacements. This confirms, that the assumption of a transversal isotropic material behavior is admissible.

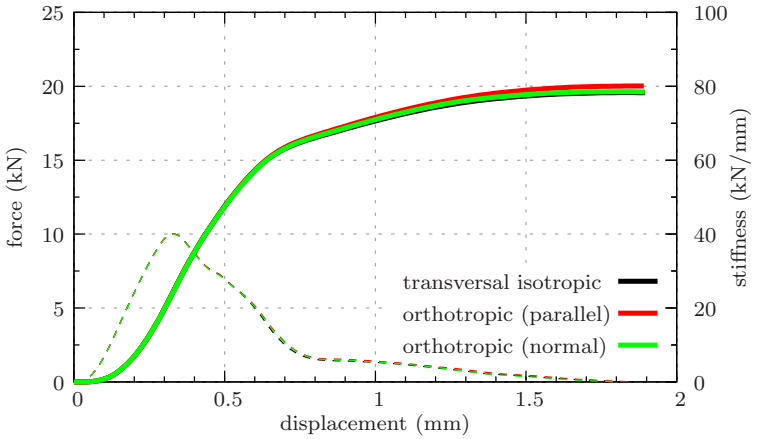


Figure 7.12: Load-displacement curves (solid) with the respective stiffness course (dashed) for the different material descriptions.

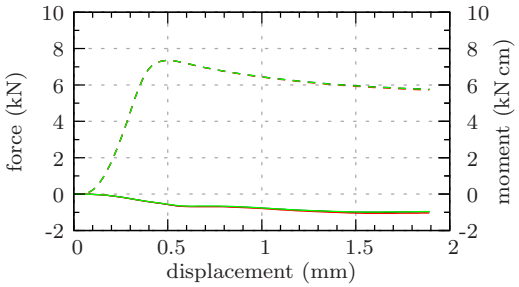


(a) Transversal force in wood (solid) and bending moment in the dowel (dashed)

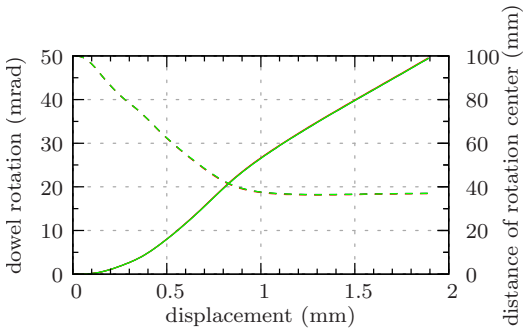


(b) Rotation of dowel axis (solid) and distance of rotation center (dashed)

Figure 7.13: Reaction forces, moments, and dowel rotation for the different material descriptions (see Figure 7.12 for legend).

### 7.2.2 Mesh dependency

**Variations from the reference model**
Mesh dependency is studied in order to define borders of validity of the numerical simulations. First, the elements type is changed from quadratic elements to linear elements in all parts of the connection. In particular, fully integrated brick elements with linear interpolation functions (C3D8) are used for the dowel and the plate, while tetrahedron elements (C3D4) are used for the wooden part (Model 22).

Additionally, the models are evaluated for a refined mesh. The typical element length is approximately halved for this purpose, which increases the number of elements about seven-fold. Refined simulations are studied with both quadratic elements (Model 23) and linear elements (Model 24).

While the reference simulation is performed with relaxed convergence criteria, the tighter default criteria are applied here (Model 41).

| Model number | 1 | 22 | 23 | 24 | 41 |
|---|---|---|---|---|---|
| Mesh size | coarse | | refined | | coarse |
| Element type | quadratic | linear | quadratic | linear | quadratic |
| Convergence criteria | relaxed | relaxed | relaxed | relaxed | tight |
| No. of elements | 10 749 | 10 469 | 72 474 | 70 834 | 10 749 |
| No. of variables | 90 627 | 12 414 | 530 319 | 51 315 | 90 627 |
| No. of increments | 100 | 100 | 108 | 100 | 100 |
| No. of iterations | 300 | 349 | 462 | 308 | 341 |
| Running time (s) | 3 858 | 536 | 144 069 | 3 308 | 4 043 |

Table 7.3: Comparison of typical model parameters and computational characteristics for Finite-Element simulations with different meshes and

All other parameters are not changed compared to the reference simulation.

**Changes observed**
The chosen mesh mostly affects the maximum load, which is significantly higher when using the coarse mesh with linear elements (+25% from reference simulation). Using a refined mesh with linear or quadratic elements leads to an only small decrease of ultimate load of minor magnitude compared to the reference mesh. The effect of the mesh on connection stiffness is in general less than on maximum load.

In the region of load transfer, the elements closest to the bore-hole start yielding first. The smaller these elements are, the earlier they start to yield. Once the elements are yielding, their stiffness is reduced, and, in addition, most of the (plastic) deformations are localized there. In combination, this reduces stiffness dramatically and, consequently, also strength. Since the model is only valid within the limits of small strain/small displacement theory, the strains exceed locally the admissible ranges already at rather low loads. On the other hand, a too coarse mesh leads to a too rough estimation of the stress and strain distributions, so that the accuracy of the simulation is limited.

The results of the simulation with tighter convergence criteria do not lead to any significant change of the results compared to the relaxed criteria, which therefore are assumed to be valid.

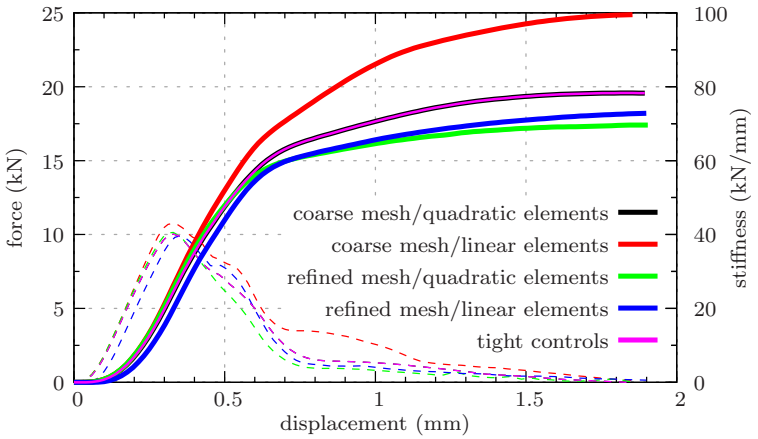


Figure 7.14: Load-displacement (solid) and stiffness curves (dashed) for a variation of mesh size and element formulation.

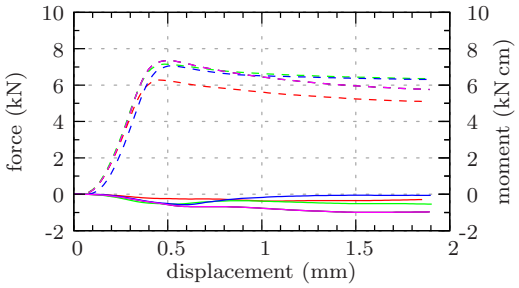


(a) Transversal force in wood (solid) and bending moment in the dowel (dashed)

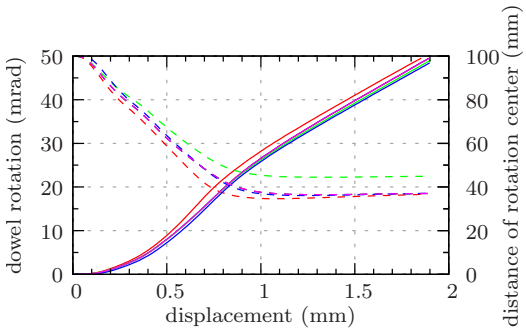


(b) Rotation of dowel axis (solid) and distance of rotation center (dashed)

Figure 7.15: Reaction forces, moments, and dowel rotation for a variation of mesh size and element formulation (see Figure 7.14 for legend).

## 7.3 Parametric study

In the following, the influences of individual parameters of the connection model on the simulation results will be investigated. For this purpose, the results of the modified models are compared to that of the reference simulation, and the differences in the load-carrying behavior are discussed.

The performed variations are typical for dowel-type timber connections in timber engineering, and are grouped as follows (see Table 7.4 for an overview):

- **Geometry:** Geometric influences studied include the width of the connection, in order to give results for the three ductile failure modes according to EC5, as well as the end distance and the edge distance of the connection.
- **Material:** Wood of low, intermediate, and high density is considered. Additionally, the influence of steel quality is studied.
- **Interface:** The interaction properties are changed to model varying frictional conditions. Moreover, the stiffness of the contact formulation is changed within the generally applied soft contact formulation, and in one run, the contact model for hard contact is chosen. Finally, the consequences of increased and decreased bore-hole diameters are studied, in order to assess the significant influence of the fitting of the dowel in the bore-hole on the interaction characteristics.
- **Loading:** The effect of the loading mode is investigated by performing repeated unloading and reloading cycles, as well as by reversing the load direction so that a compression load is applied.

| Variation | Model No. | Section |
|---|---|---|
| Standard simulation | 1 | Section 7.1 |
| Connection width | 7, 8 | Section 7.3.1 |
| End distance | 25–27 | Section 7.3.2 |
| Edge distance | 28–30 | Section 7.3.3 |
| Density variation | 2, 3 | Section 7.3.4 |
| Dowel material | 17 | Section 7.3.5 |
| Contact behavior | 6, 36–40 | Section 7.3.6 |
| Frictional properties | 9–16 | Section 7.3.7 |
| Bore-hole size | 31–35 | Section 7.3.8 |
| Compression loading | 19 | Section 7.3.9 |
| Unloading cycles | 20, 21 | Section 7.3.10 |

Table 7.4: Overview of the simulations within the parametric study.

### 7.3.1 Connection width

**Variations from the reference model**

The reference simulation considers a specimen of intermediate width, where a single plastic hinge forms in the 1-2-symmetry plane. In order to obtain the other failure modes according to EC5, the overall connection width is changed to 40 mm (Model 7) and to 200 mm (Model 8), respectively. No plastic hinge will form in the 40 mm wide connection, while a second plastic hinge will form in the 200 mm wide connection.

All other parameters are not changed compared to the reference simulation.

**Changes observed**

The course of the load-displacement curves and the stiffness curves (Figure 7.16) for the 100 and 200 mm wide connections are virtually identical until maximum stiffness is reached, which itself is identical for both widths. In the 40 mm wide connection, stiffness increases more slowly, and maximum stiffness is lower than for the other widths. After reaching its maximum, the stiffness decreases more quickly in the 40 mm wide connection than in the 100 mm wide connection, while it decreases more slowly in the 200 mm wide connection.

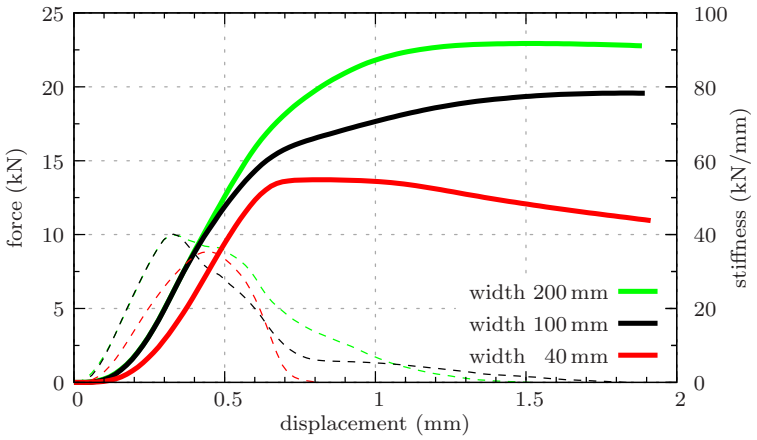


Figure 7.16: Load-displacement curve (solid) and the respective stiffness course (dashed) for a variation of connection width.

The transition to the yield plateau is rapid in the 40 mm wide connection, which shows a maximum load of 13.7 kN. The yield plateau remains constant for a considerable increase of displacement. Due to the back-bending of the dowel in the 200 mm wide connection, the maximum load is significantly higher there than for the other widths.

The course of the bending moments in the dowel over the overall displacements (Figure 7.17(a)) is again nearly identical for the 100 and 200 mm wide connections, while it does not reach the yield moment in the narrow connection (even not a single integration point reaches the yield point). In front of the dowel, a compression force forms for all widths, indicating that splitting is prevented and a ductile behavior of all three connections can be expected.

The dowel rotation is low in the 40 mm wide connection compared to the other widths (Figure 7.17(b)), resulting in full contact along the length of the dowel. In contrast to

that, contact length is lowest in the 100 mm wide connection, which also shows highest dowel rotation. Due to restrained bending of the dowel in the 200 mm wide connection (intermediate dowel rotation), a large contact area can be activated in this connection, which results in the largest transferable load.

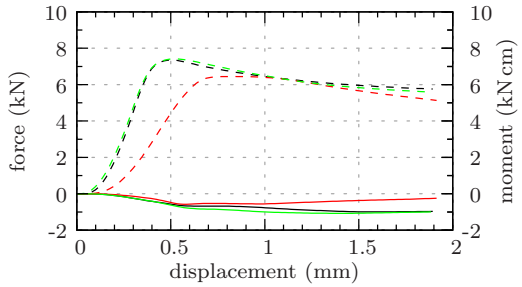


(a) Transversal force in wood (solid) and bending moment in the dowel (dashed)

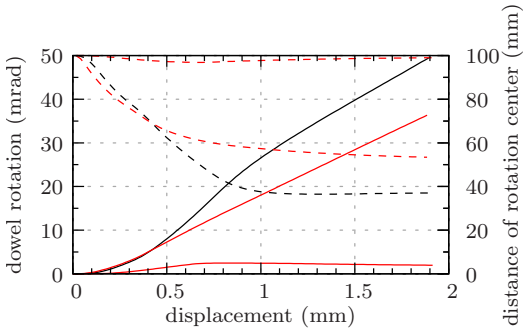


(b) Rotation of dowel axis (solid) and distance of rotation center (dashed)

Figure 7.17: Reaction forces, moments, and dowel rotation for a variation of connection width (see Figure 7.16 for legend).

### 7.3.2 End distance

**Variations from the reference model**

The end distance (i.e. the distance between the dowel and the unloaded end of the wood) is reduced step-wise by 18 mm (1.5 $d$). The resulting end distances are therefore 84 mm in the reference simulation (Model 1), and 66, 48, and 30 mm, in Models 25, 26, and 27).

All other parameters are not changed compared to the reference simulation.

**Changes observed**

The load-displacement curves (Figure 7.18) show nearly identical results for connections with end distances of 84, 66, and 48 mm regarding the strength and stiffness courses. Dowel bending moments and lateral forces as well as dowel rotation are also approximately identical for these connections (Figure 7.19).

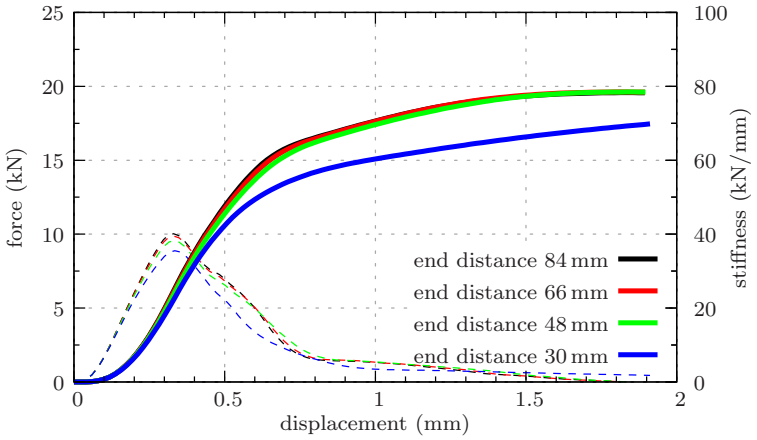


Figure 7.18: Load-displacement curve (solid) and the respective stiffness course (dashed) for a variation of end distance.

In contrast, the shortest connection shows still about the same initial and maximum stiffness, but significantly lower maximum strength. Examining the lateral stresses in the 1-2-symmetry plane shows that tension strength is reached at the end of the connection, and yielding starts according to the elasto-plastic approach adopted in the simulations. Finally, the full end of the wood in front of the dowel yields in addition to the already yielding section close to the dowel (Figure 7.20). However, the high lateral tension stresses rather indicate the occurrence of brittle cracking. Thus, the assumption of perfect plastic behavior is not suitable in this case and prevents to derive realistic estimates of the ultimate load in the simulations for extremely short end distances.

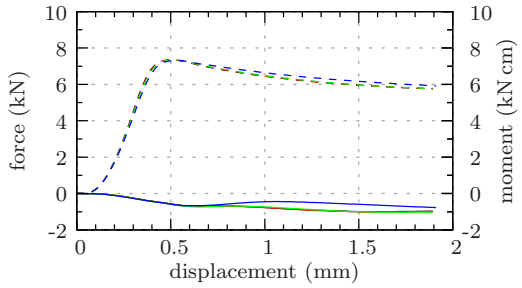


(a) Transversal force in wood (solid) and bending moment in the dowel (dashed)

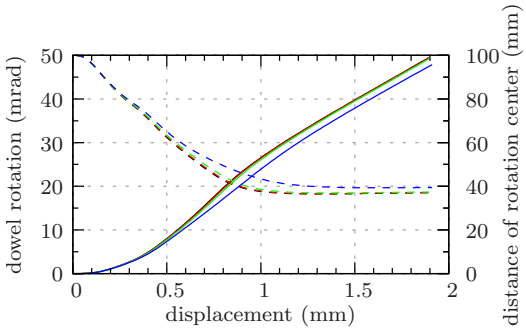


(b) Rotation of dowel axis (solid) and distance of rotation center (dashed)

Figure 7.19: Reaction forces, moments, and dowel rotation for a variation of end distance (see Figure 7.18 for legend).

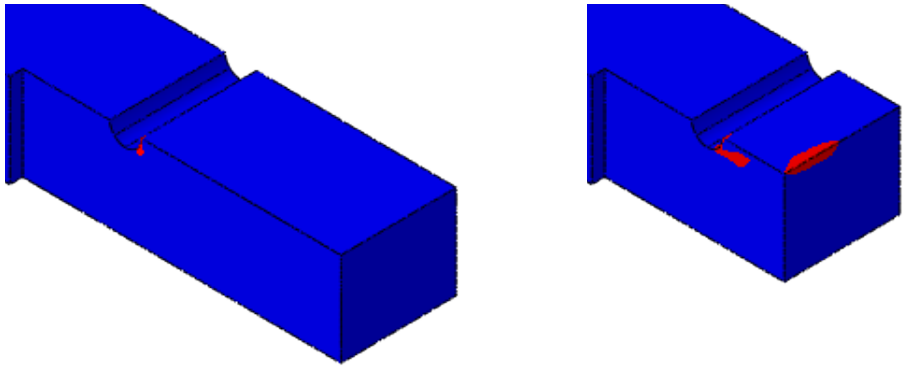

(a) end distance 84 mm

(b) end distance 30 mm

Figure 7.20: Active yielding areas (red) in the simulations with reduced end distance at a load of 10.4 kN.

### 7.3.3 Edge distance

**Variations from the reference model**

The edge distance in the wood part is 36 mm in the reference simulation. It is reduced step-wise by 6 mm, resulting in edge distances of 30, 24, and 18 mm, respectively, in Models 28, 29, and 30.

All other parameters are not changed compared to the reference simulation.

**Changes observed**

The reduction of the edge distance does influence the overall loading behavior only marginally. Particularly maximum stiffness is reduced slightly with reduced edge distance (Figure 7.21). The courses of the bending moment of the dowel and of the transversal compression force in front of the dowel are almost identical, and also the rotation of the dowel is only slightly influenced (Figure 7.22).

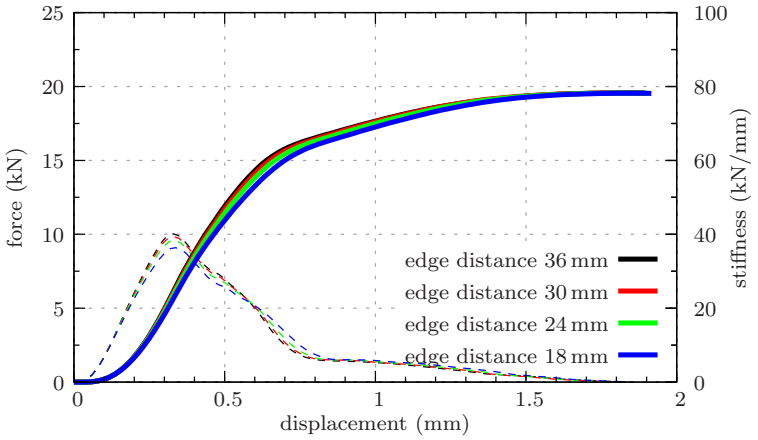


Figure 7.21: Load-displacement curve (solid) and the respective stiffness course (dashed) for a variation of edge distance.

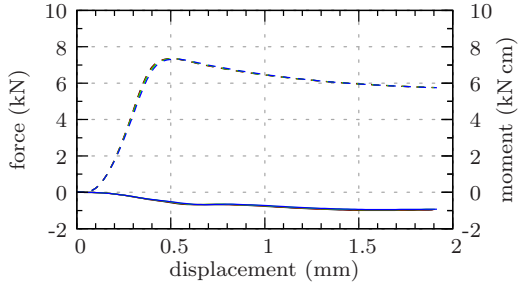


(a) Transversal force in wood (solid) and bending moment in the dowel (dashed)

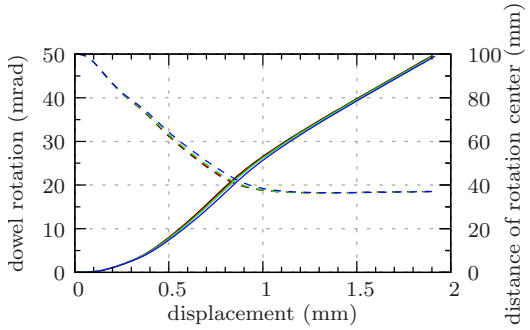


(b) Rotation of dowel axis (solid) and distance of rotation center (dashed)

Figure 7.22: Reaction forces, moments, and dowel rotation for a variation of edge distance (see Figure 7.21 for legend).

### 7.3.4 Density variation

**Variations from the reference model**

The density of the wood specimen is once reduced to $\varrho = 324\,\mathrm{kg/m^3}$ (Model 2) and once increased to $\varrho = 541\,\mathrm{kg/m^3}$ (Model 3). The corresponding material properties are derived by means of a micro-mechanical model as done in the reference simulation for wood of medium density. The modulus of elasticity $E_L$ and the uniaxial compressive strength $f_{y_{c_L}}$ in longitudinal direction, obtained by compression tests (see Section 4.5), are used for calibrating the micro-mechanical model. Transversal isotropy in the $R$-$T$-plane is assumed. The finally resulting stiffness properties for wood of low and high density, respectively, are compiled in Table 7.5.

| | $E_L$ | $E_R$ | $E_T$ | $G_{RT}$ | $G_{TL}$ | $G_{LR}$ |
|---|---|---|---|---|---|---|
| low density: | 7 556 | 243 | 243 | 70 | 441 | 441 |
| | $\nu_{LR}$ | $\nu_{LT}$ | $\nu_{RL}$ | $\nu_{RT}$ | $\nu_{TL}$ | $\nu_{TR}$ |
| | 0.010 8 | 0.010 8 | 0.337 | 0.736 | 0.337 | 0.736 |

| | $E_L$ | $E_R$ | $E_T$ | $G_{RT}$ | $G_{TL}$ | $G_{LR}$ |
|---|---|---|---|---|---|---|
| high density: | 13 888 | 885 | 885 | 299 | 606 | 606 |
| | $\nu_{LR}$ | $\nu_{LT}$ | $\nu_{RL}$ | $\nu_{RT}$ | $\nu_{TL}$ | $\nu_{TR}$ |
| | 0.016 3 | 0.016 3 | 0.256 | 0.482 | 0.256 | 0.482 |

Table 7.5: Elastic moduli (in $\mathrm{N/mm^2}$) and Poisson's ratios for transversal isotropy and wood of low and high density, respectively.

Yield strengths (in $\mathrm{N/mm^2}$) are given by

$$
\begin{aligned}
\text{low density:}\quad & f_{y_{t_L}} = 46.0, && f_{y_{t_R}} = 1.9, && f_{y_{t_T}} = 1.9,\\
& f_{y_{c_L}} = -30.0, && f_{y_{c_R}} = -2.8, && f_{y_{c_T}} = -2.8,\\
& f_{y_{LR}} = 6.8, && f_{y_{RT}} = 1.6, && f_{y_{TL}} = 6.8,\\
& f^{biax}_{y_{LR}} = 1.922, && f^{biax}_{y_{RT}} = 1.242, && f^{biax}_{y_{TL}} = 1.922,\\
\text{high density:}\quad & f_{y_{t_L}} = 88.0, && f_{y_{t_R}} = 4.7, && f_{y_{t_T}} = 4.7,\\
& f_{y_{c_L}} = -58.0, && f_{y_{c_R}} = -7.0, && f_{y_{c_T}} = -7.0,\\
& f_{y_{LR}} = 8.6, && f_{y_{RT}} = 4.1, && f_{y_{TL}} = 8.6,\\
& f^{biax}_{y_{LR}} = 4.766, && f^{biax}_{y_{RT}} = 3.066, && f^{biax}_{y_{TL}} = 4.766.
\end{aligned}
\tag{7.7}
$$

All other parameters are not changed compared to the reference simulation.

**Changes observed**

The variation of the wood density and, thus, of the stiffness and strength properties has significant influence on the load-carrying behavior (Figure 7.23). While the maximum connection stiffnesses are approximately the same for all densities – 38.2 kN/mm for low density wood and 44.1 kN/mm for high density wood – the connection strength is clearly affected to a much higher extent. Connection strength is mainly governed by

the compressive strength of the wood, which in high density wood is about two-fold the value of low density wood.

Courses of dowel bending moments and dowel rotation over the displacements are about the same for all densities (Figure 7.24).

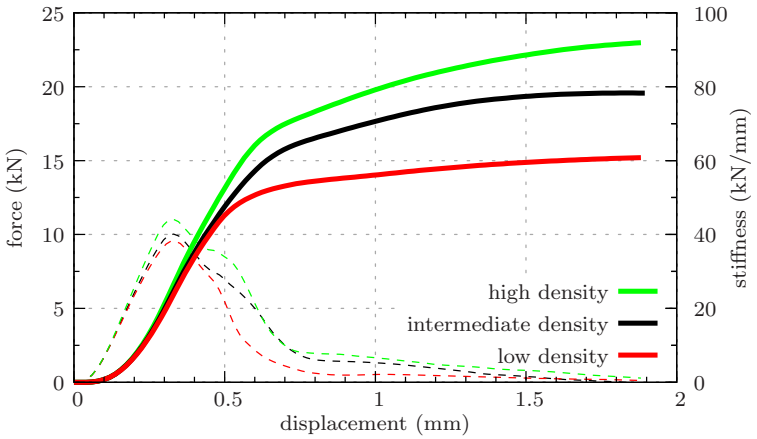


Figure 7.23: Load-displacement curve (solid) and the respective stiffness course (dashed) for a variation of wood density.

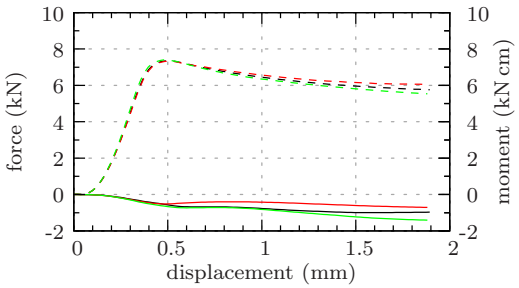


(a) Transversal force in wood (solid) and bending moment in the dowel (dashed)

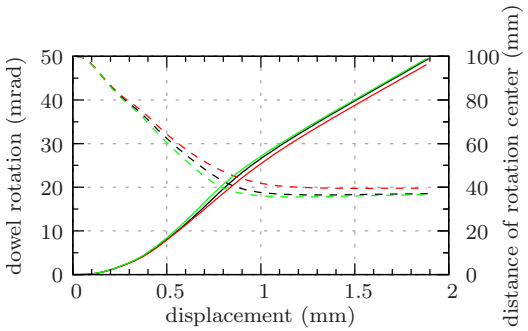


(b) Rotation of dowel axis (solid) and distance of rotation center (dashed)

Figure 7.24: Reaction forces, moments, and dowel rotation for a variation of wood density (see Figure 7.23 for legend).

### 7.3.5 Dowel material

**Variations from the reference model**

The material of the dowel is changed from steel quality S235 to steel quality S355. The latter shows a yield strength of $f_y = 355\,\mathrm{N/mm^2}$ (Model 17), which is about 50% higher than that for steel of quality S235.

All other parameters are not changed compared to the reference simulation.

**Changes observed**

Using a dowel of steel quality S355 does not affect the initial phase before yielding of the dowel starts in the reference simulation (Figure 7.25). The maximum stiffness is increased by about 18% to 47.3 kN/mm, as the resisting moment in the dowel before full yielding is significantly higher for the better steel quality. Due to the increased dowel stiffness, the rotation in the dowel is lower, and an extended contact area can be activated. This results in a higher load level and a higher maximum stiffness (Figure 7.26).

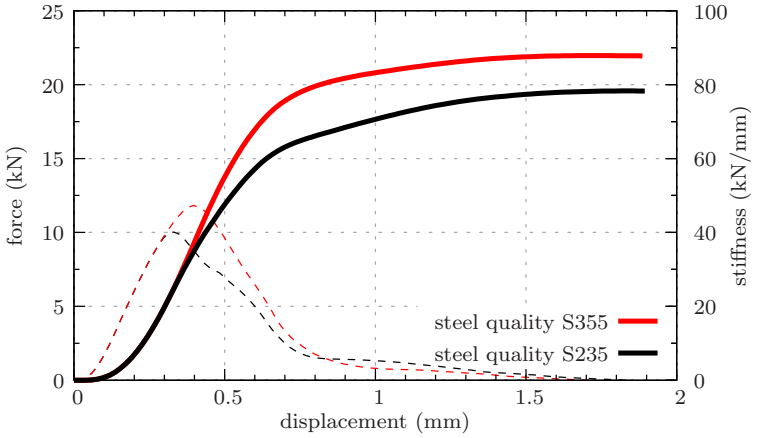


Figure 7.25: Load-displacement curve (solid) and the respective stiffness course (dashed) for a variation variation of dowel material.

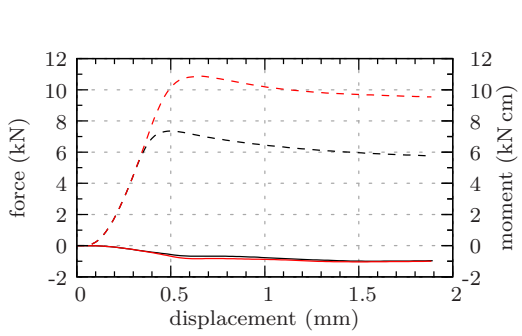


(a) Transversal force in wood (solid) and bending moment in the dowel (dashed)

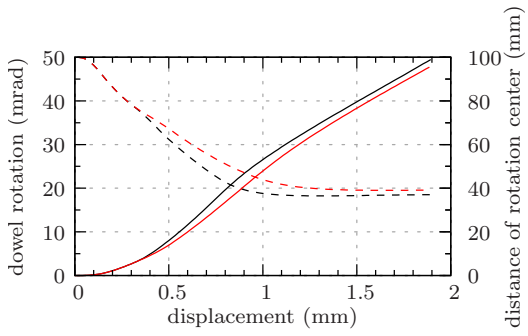


(b) Rotation of dowel axis (solid) and distance of rotation center (dashed)

Figure 7.26: Reaction forces, moments, and dowel rotation for a variation of dowel material (see Figure 7.25 for legend).

### 7.3.6 Contact behavior

**Variations from the reference model**

In order to estimate the influence of using a soft contact formulation, allowing a certain overclosure between the wood and the dowel surfaces, the contact is modeled alternatively with a hard contact formulation (Model 6). Additionally, the variability of the soft contact formulation is presented by modifying the interaction properties as defined in Section 4.6. The respective LAMÉ parameters are chosen to represent different surface cutting types and are compiled in Table 7.6, Figure 7.27 shows the resulting contact pressure-overclosure relations. The frictional behavior is not changed compared to the reference simulation.

| Model | $\sigma_0$ ($\mathrm{N/mm^2}$) | $n_\sigma$ | $u_0$ (mm) | $n_u$ | Cutting type |
|---|---|---|---|---|---|
| 36 | 51.8 | 1.50 | 0.104 | 3.99 | 1 |
| 37 | 54.5 | 1.10 | 0.256 | 3.91 | 2 |
| 38 | 42.4 | 1.54 | 0.725 | 1.81 | 3 |
| 39 | 51.4 | 2.06 | 0.194 | 4.45 | 4 |
| 40 | 53.5 | 1.47 | 0.100 | 4.54 | 5 |
| 1 | 55.0 | 1.10 | 0.350 | 3.90 | — |
| 6 | hard contact | | | | — |

Table 7.6: Parameters for contact pressure-overclosure relationship for a variation of the contact behavior, considering an intermediate wood density and different cutting types (Table 4.6)

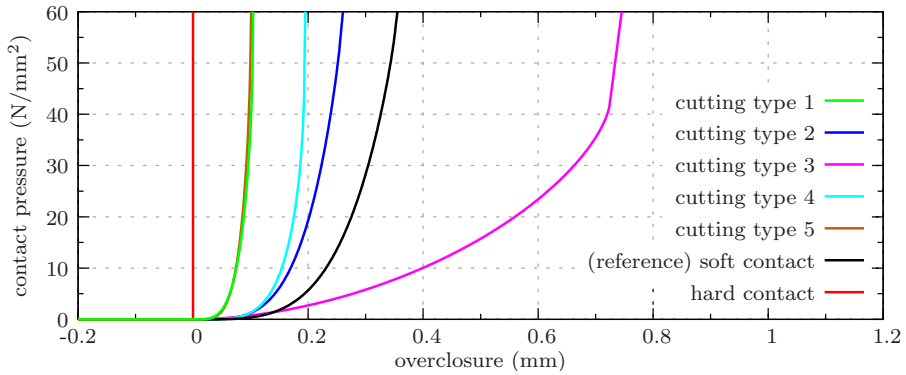


Figure 7.27: Contact pressure-overclosure relations for a variation of the contact behavior.

All other parameters are not changed compared to the reference simulation.

**Changes observed**

The connection stiffness of the simulation using a hard contact formulation is considerably higher in general and starts already with a high value when the first loading is applied. The maximum stiffness of 84.0 kN/m is more than two times higher than in the reference simulations with soft contact (Figure 7.28). The rotated dowel is already in contact with the wood at the outer side right from the beginning. A significant load

transfer takes place, resulting in back-bending of the dowel and the formation of a high bending moment in the dowel, so that even plastic zones develop at about 30 mm distance from the 1-2-symmetry plane at a displacement of approx. 0.65 mm. In consequence, the failure mode changes, which also explains the higher maximum load. A significant tension force in front of the dowel forms (Figure 7.29).

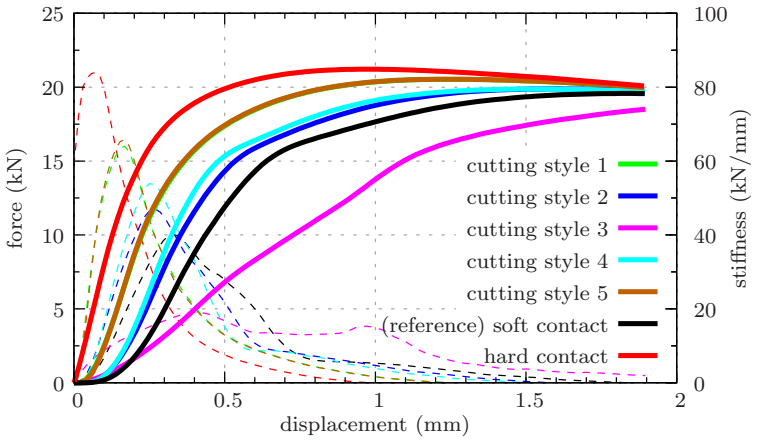


Figure 7.28: Load-displacement curve (solid) and the respective stiffness course (dashed) for a variation of contact behavior.

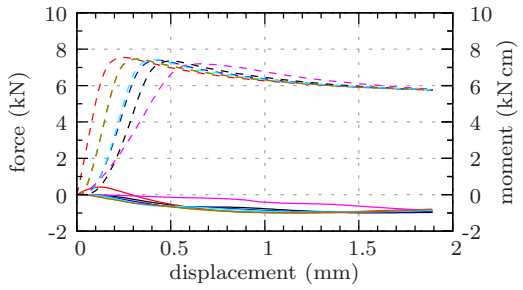


(a) Transversal force in wood (solid) and bending moment in the dowel (dashed)

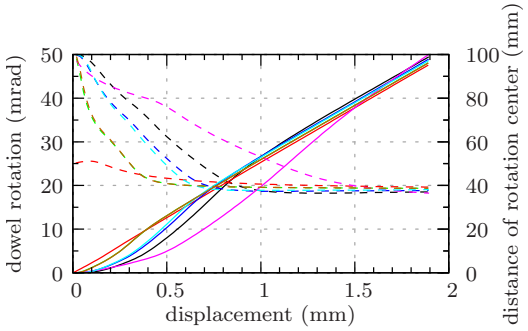


(b) Rotation of dowel axis (solid) and distance of rotation center (dashed)

Figure 7.29: Reaction forces, moments, and dowel rotation for a variation of contact behavior (see Figure 7.28 for legend).

Considering the variation of the soft contact properties, representing different cutting types, the connection stiffness decreases with increasing compliance of the interface: Simulations with cutting types 1 and 5 show highest stiffnesses (64 and 66 kN/mm), simulations with cutting types 2 and 4 are of intermediate stiffness (47 and 54 kN/mm), while the simulation with cutting type 3 is of lowest maximum stiffness (19 kN/mm). The maximum load level is reached at significantly higher displacements (Figure 7.28) in simulations with more compliant interfaces. In contrast to the simulation with hard contact, only compression forces form in front of the dowel (Figure 7.29(a)). For cutting type 3, the most compliant interface, these forces are very low. Connections with highly compliant interfaces show lower dowel rotation in the beginning (cutting types 3, 2, and 4), which increases to similar levels for all interface types at larger displacements

(Figure 7.29(b)). A similar trend is observed for the dowel bending moment and the distance of the rotation center.

### 7.3.7 Frictional properties

**Variations from the reference model**

The frictional behavior is changed by setting the frictional coefficients $\mu$ to lower (0.00, 0.10, 0.20, 0.30) and higher values (0.50, 0.60, 0.70, 0.80), respectively, than in the reference simulation (Models 9-12 and 13-16).

The contact behavior in normal direction and all other parameters are not changed compared to the reference simulation.

**Changes observed**

The significant influence of friction on the connection behavior is clearly visible. Increased friction positively affects the maximum load, while stiffnesses are influenced less significantly and range only between 37.0 and 42.7 kN/mm (Figure 7.30). The rotation of the dowel and the resulting bending moment in the dowel are only slightly affected (Figure 7.31).

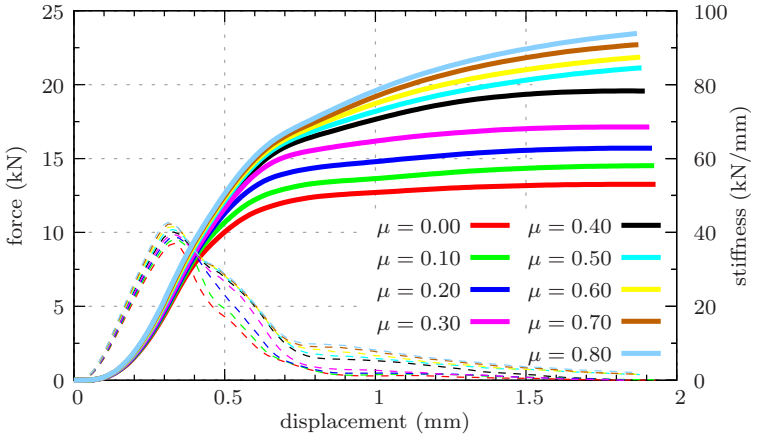


Figure 7.30: Load-displacement curve (solid) and the respective stiffness course (dashed) for a variation of frictional properties.

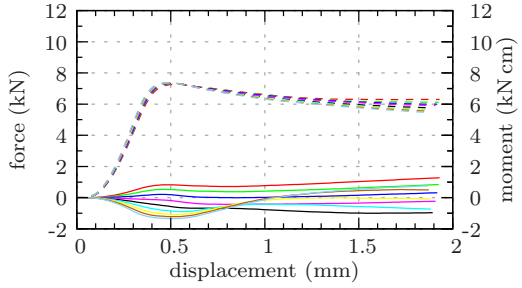


(a) Transversal force in wood (solid) and bending moment in the dowel (dashed)

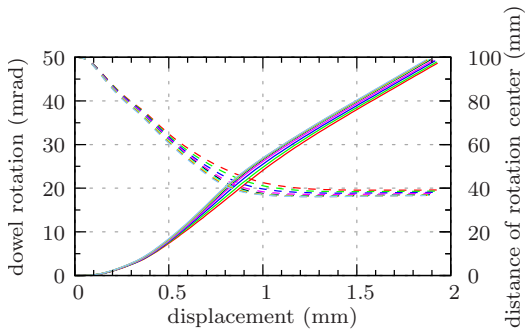


(b) Rotation of dowel axis (solid) and distance of rotation center (dashed)

Figure 7.31: Reaction forces, moments, and dowel rotation for a variation of frictional properties (see Figure 7.30 for legend).

At low friction ($\mu = 0.00 - 0.20$), the dowel acts similar to a wedge, which drives the wood apart. Hence, tension forces build up which may likely cause brittle tension failure (Figure 7.31(a)). In contrast, at increased friction ($\mu > 0.30$), the dowel acts a kind of reinforcement in circumferential direction of the bore-hole, so that the contact area is increased.

Figures 7.32 allow a more detailed insight into the stress distributions and the differences caused by variation of frictional coefficients. Although the total load for the three variations studied is approximately the same (approx. 10.4 kN), the stress distribution is significantly different. The active yielding area is largest in the simulation with lowest friction, caused by high longitudinal stresses $\sigma_{11}$ and tension stresses $\sigma_{33}$ in these areas, lateral splitting is likely to limit the load-bearing capacity.

In the simulation with a friction coefficient of $\mu = 0.80$, the yielding area is about the same, but compression stresses $\sigma_{11}$ are significantly lower and compression stresses $\sigma_{33}$ are formed. The maximum load can therefore be increased in simulations with higher coefficients of friction due to spare compression stress capacity, which can be activated by stress redistribution.

The distance of the location of highest shear stresses $\tau_{13}$ to the 1-2-symmetry-plane is increasing with increased frictional coefficients. The area where largest tension stresses $\sigma_{33}$ occur shows a similar trend. The combination of both gives a hint that in connections with increased friction the formation of shear-failure planes takes place, which is globally a ductile failure mode with an extended yield plateau. In contrast to that, low friction between dowel and wood results in the mentioned tension stresses $\sigma_{33}$, which lead to a brittle failure mode of the connection.

$\mu = 0.00$ $\mu = 0.40$ $\mu = 0.80$

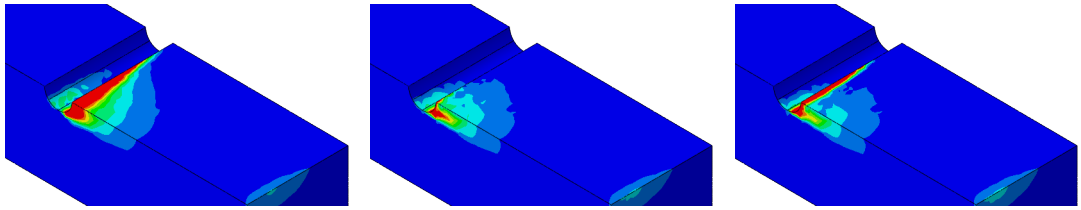

(a) TSAI-WU-value $\Phi(\boldsymbol{\sigma})$: limits -1–0 (blue –red)

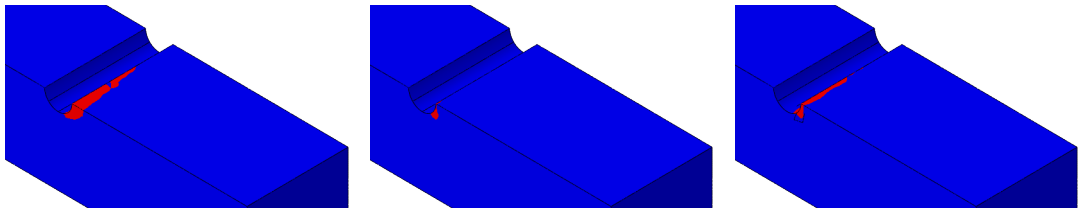

(b) active yielding areas: limits 0–1 ((blue, not yielding – red, yielding)

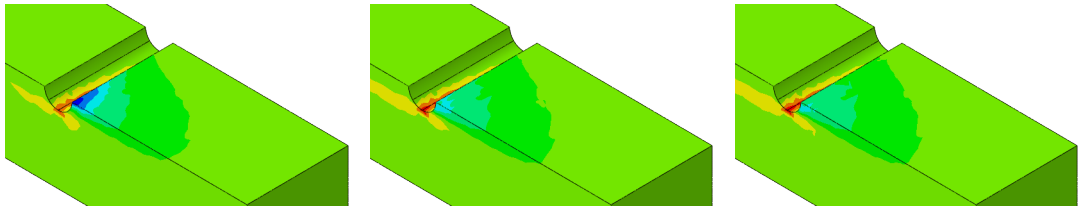

(c) normal stress $\sigma_{11}$: -60–40 N/mm$^2$ (blue–red)

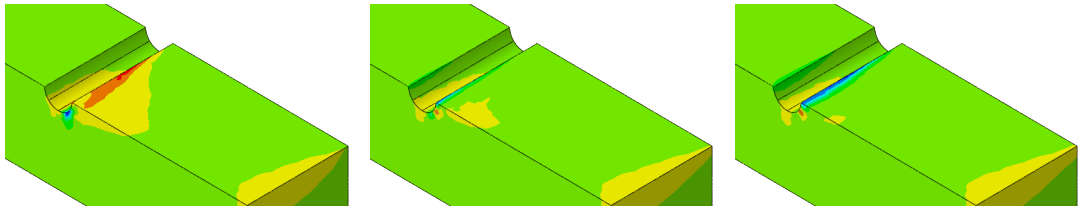

(d) normal stress $\sigma_{33}$: -7–4 N/mm$^2$ (blue–red)

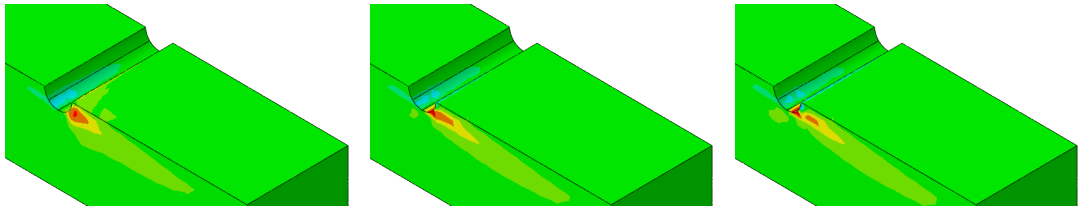

(e) shear stress $\tau_{13}$: -6–6 N/mm$^2$ (blue–red)

Figure 7.32: Stress distribution in selected simulations with a variation of frictional properties at a load of 10.4 kN.

### 7.3.8 Bore-hole size

**Variations from the reference model**

In the reference simulation, the bore-hole fits the dowel perfectly, both having a diameter of 6 mm. Additionally, overclosures and gaps between the two surfaces are removed by adjusting nodes of the slave surface (bore-hole surface) before the simulation starts.

In the first variation (Model 31), the adjustment for overclosure is not performed. Some of the master nodes (on the dowel's surface) are therefore penetrating the slave surface (of the bore hole) in the initial stage, so that load transfer between the two surfaces may already take place.

In the other simulations, the bore-hole diameter is changed additionally. It is widened to 12.2 mm and 12.4 mm (Models 32 and 33), as well as reduced to 11.8 mm and 11.6 mm (Models 34 and 35). Due to widening, a hole clearance occurs, and contact between the dowel and the bore-hole is established only at a considerable displacement. In contrast, tighter bore-holes lead to penetrations of the dowel surface into the bore-hole surface so that contact stresses occur before the actual loading starts.

All other parameters are not changed compared to the reference simulation.

**Changes observed**

Skipping the node adjustment significantly changes the stiffness of the connection, while maximum load is only slightly affected (Figure 7.33). As there are some areas at the interface in contact initially, loads can be transferred from the first loading onwards. The maximum stiffness is not affected.

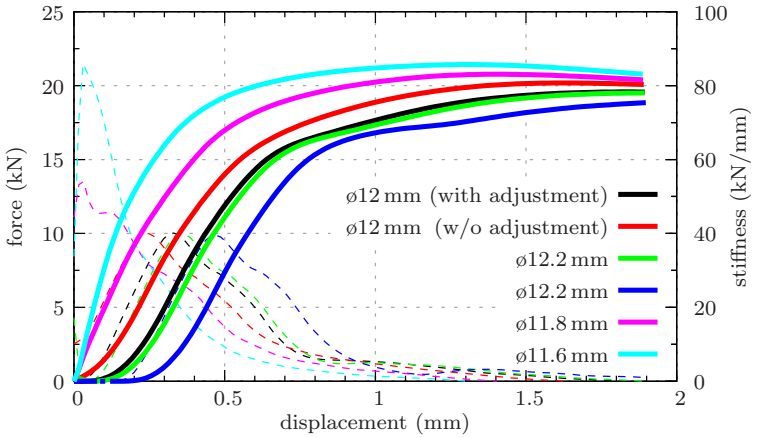


Figure 7.33: Load-displacement curve (solid) and the respective stiffness course (dashed) for a variation of bore-hole diameter.

A reduction of the bore-hole diameter increases stiffness notably, and no initial phase of low stiffness is observed anymore. The load-displacement curves are similar to those obtained with a hard contact formulation, or when a soft contact formulation with a very low compliance. Tight bore-holes lead to the build-up of significant lateral stresses (Figure 7.22) even at comparably low loads, which may increase the likeliness of brittle splitting. Widening the bore-hole does not change the overall course of the load-displacement curves and of the stiffness curves qualitatively, but a shift is observed which reflects hole

clearance.

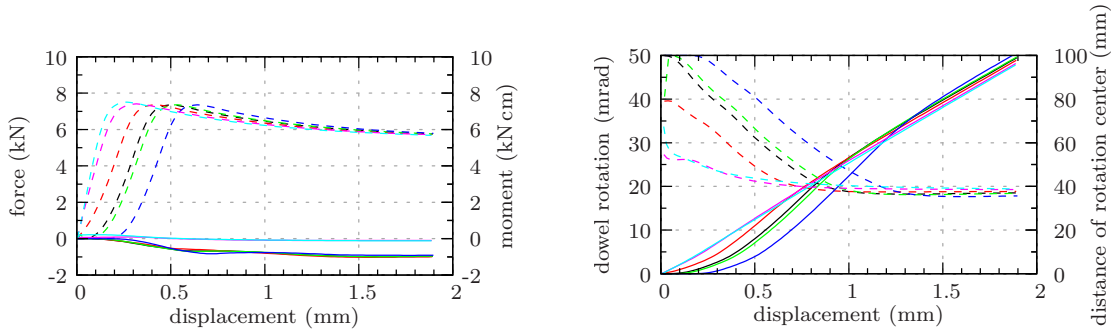


(a) Transversal force in wood (solid) and bending moment in the dowel (dashed)

(b) Rotation of dowel axis (solid) and distance of rotation center (dashed)

Figure 7.34: Reaction forces, moments, and dowel rotation for a variation of bore-hole diameter (see Figure 7.33 for legend).

### 7.3.9 Compression loading

**Variations from the reference model**

In contrast to the reference simulation considering tensile loading of the connection, a compression load of $u = -2\,\text{mm}$ is applied in this simulation (Model 19).

All other parameters are not changed compared to the reference simulation.

**Changes observed**

In the beginning of the loading, the load-displacement and stiffness courses do not vary significantly up to a load of approx. 5 kN (Figure 7.35). From this point on, the connection becomes stiffer than the respective connection loaded in tension, reaching a maximum stiffness of 44 kN/mm. The decrease in stiffness is then more pronounced in compression, so that the courses closely approach each other again. The courses for the bending moment and the tension force in the dowel do not change. Neither differs the dowel rotation (Figure 7.36).

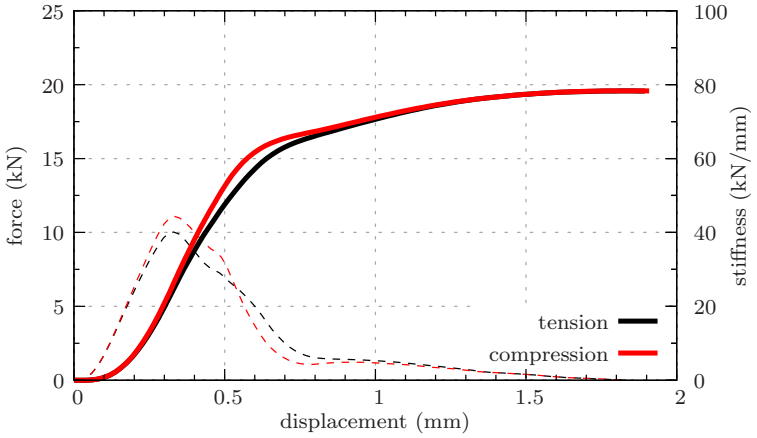


Figure 7.35: Load-displacement curve (solid) and the respective stiffness course (dashed) for a variation of loading direction.

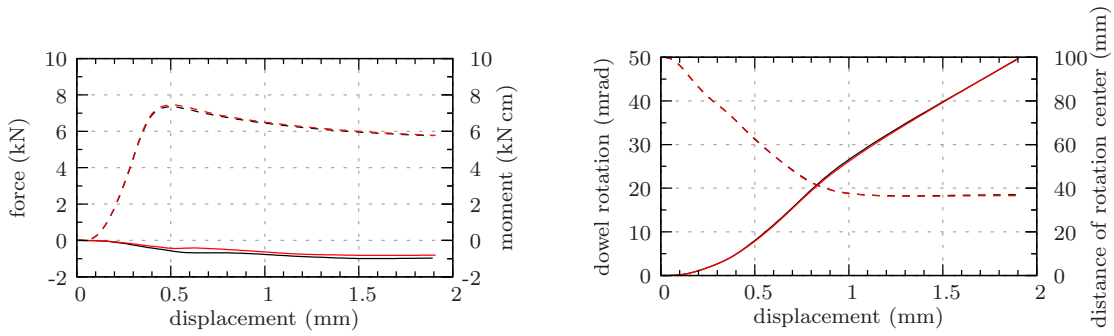


(a) Transversal force in wood (solid) and bending moment in the dowel (dashed)

(b) Rotation of dowel axis (solid) and distance of rotation center (dashed)

Figure 7.36: Reaction forces, moments, and dowel rotation for a variation of loading direction (see Figure 7.35 for legend).

In connections loaded in tension, shear stresses develop, which transfer the compression stresses in the contact surface into tension stresses in the bulk wood (Figure 7.37(a)). In connections loaded in compression, this transformation is not required because the compression stresses under the dowel are directly taken over by compression stresses in the bulk wood (Figure 7.37(b)). The connection therefore behaves stiffer until yielding in the wood is initiated.

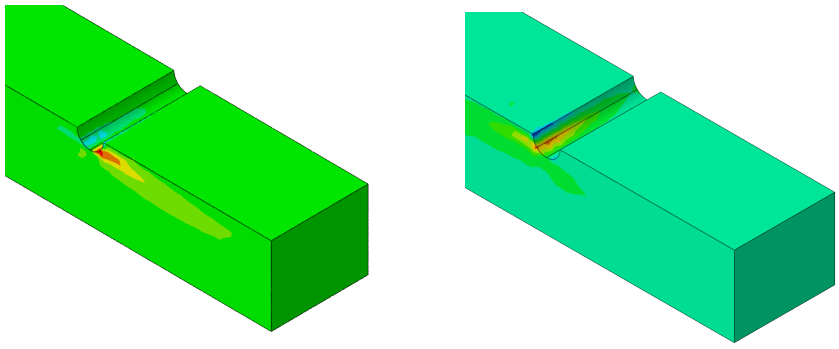

(a) tension load (b) compression load

Figure 7.37: Distribution of shear stress $\tau_{13}$ in simulations loaded in tension and in compression, respectively, at an absolute load of 10.4 kN.

### 7.3.10 Unloading cycles

**Variations from the reference model**

Simulations with unloading cycles are performed in order to study the change in connection stiffness during un- and reloading. Several loading steps are introduced in the simulation, which are applied through load control (Table 7.7). Only at the final loading step, the displacements are increased in order to track the maximum load and the yield plateau. Simulations were performed both with soft contact behavior (Model 20) and with hard contact behavior (Model 21) between the dowel and the wood.

| Step | Load (kN) | Displacement (mm) |
|---|---|---|
| 1 | 10 | — |
| 2 | 5 | — |
| 3 | 10 | — |
| 4 | 15 | — |
| 5 | 5 | — |
| 6 | 15 | — |
| 7 | — | 2.00 |

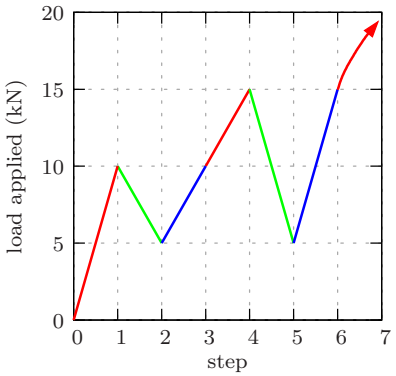


Table 7.7: Load history for simulations with repeated loading and unloading cycles: first loading (red), unloading (green), reloading (blue).

All other parameters are not changed compared to the reference simulation.

**Changes observed**

The overall load-carrying behavior, in terms of the sequence of the loading sections of the load-displacement curve, does not significantly change from the simulations loaded in one step (Figure 7.38). For the simulation with compliant contact behavior, the stiffnesses during unloading and reloading are considerably higher (maximum approx. 60 kN/mm) than during the first loading (maximum approx. 40 kN/mm), while the increase is less in the simulation with a hard contact formulation. In the hard contact simulation, unloading stiffness is only driven by elasticity of the bulk wood, whereas in the simulation with soft contact behavior, also the compliant interface contributes to the overall stiffness. Since the latter is of significantly lower stiffness than bulk wood stiffness, also the total stiffness decreases.

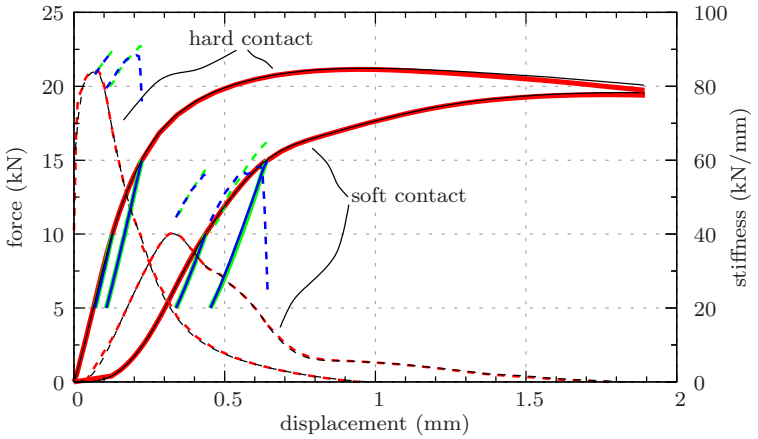


Figure 7.38: Load-displacement curves for simulations with unloading and reloading cycles for soft and hard contact: first loading (red), unloading (green), reloading (blue); black lines denote refer to simulations loaded in one step.

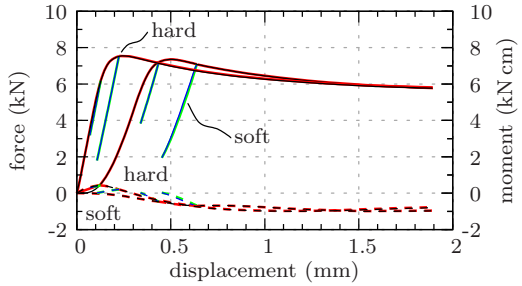


(a) Transversal force in wood (solid) and bending moment in the dowel (dashed)

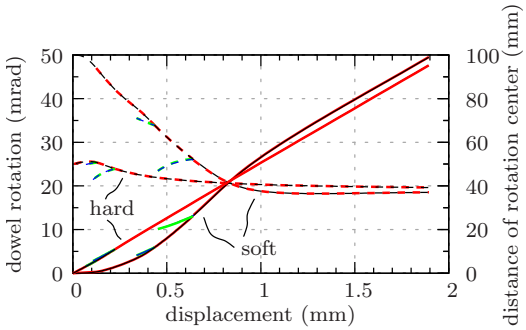


(b) Rotation of dowel axis (solid) and distance of rotation center (dashed)

Figure 7.39: Reaction forces, moments, and dowel rotation for simulation with unloading and reloading cycles for soft and hard contact (see Figure 7.38 for legend)

## 7.4 Discussion

By means of the presented numerical simulation approach, the overall load-carrying behavior of dowel-type connections is captured to a high degree, so that the main features observed in experiments are covered (see Figure 3.10). These include the consolidation phase due to a compliant contact, the first loading path with maximum stiffness, and the decrease of stiffness during transformation from elastic to plastic behavior in steel and wood, as well as the distinctively different stiffnesses during unloading and reloading cycles.

The simulation tool is able to provide information on the individual effects of the variation of properties of the connection. This can be done qualitatively as well quantitatively, which has been shown in an extensive parametric study. By means of the simulation tool, insight into the structure can be given, so that the distributions of e.g. stresses and strains, as well as of contact formation and contact pressure can be studied intensively. The points of yielding in wood and dowel can be identified, beyond which non-reversible deformations occur which limit the usability in real structures.

The influence of contact stiffness on the connection stiffness is shown to be significant, while it less effects the load level. In contrast, the variation of bulk wood density, resulting in different wood stiffnesses and strengths, is influencing the load level more than the connection stiffness. It can be concluded, that the friction behavior between wood and dowel is a critical parameter, since lateral tensile stresses form when applying low frictional coefficients, which may lead to globally brittle failure. High frictional coefficients induce the formation of shear-failure planes, which result in globally ductile behavior and an increased ultimate load. The three main ductile failure modes with no, a single, and three plastic hinges could be reproduced by varying the connection width. The likeliness of brittle failure modes increases with reduced end distance, whereas no significant changes were observed when varying edge distance.

The other features typically observed in a load-displacement diagram of a dowel connection (the point of maximum load, the length of the yield plateau, and the description of the final failure mode) are not well reproduced by the simulations for they occur at displacements and strains that exceed the theoretical scope of the simulation approach. Nevertheless, likeliness of crack formation in the wood can be assessed by studying the occurrence, level, and distribution of tensile stresses. Together with the formation of shear stresses, this gives information if an overall ductile or brittle behavior is to be expected. Although the reliable prediction of the ultimate load is not possible within the limits of the simulation approach, the influence of various parameters on the ultimate load level can nevertheless be estimated.

**Suggestions for improvement**

In order to overcome the above-mentioned restrictions, some suggestions for improvement of the simulation model will be given. These will be divided into changes on a global as well as on a local level.

On a global level, the simulations are limited by a small strain/small displacement formulation. An extension of the simulation model to geometric non-linearity will help to overcome some of the limitations. With this, strains can exceed the currently restraining limits, and e.g. hardening of wood under compression loads can be taken into

account. This may influence the load distribution significantly, especially at higher total displacements. In addition, the influence of mesh size should be reduced by application of a geometrically nonlinear formulation. Also very small elements can be used then, so that the accuracy of stress and strain fields can be increased. Another feature currently restricting the informative value of the simulations are missing capabilities to represent cracking behavior, and, thus, to model brittle failure modes. Especially, lateral cracking and the formation of shear cracks are significantly changing the overall loading behavior, the first defining ultimate failure, the latter being essential for a globally ductile connection behavior. This can be modeled by including softening of the material, or by implementation of discrete cracks, using e.g. the XFEM-technology or cohesive elements.

On a local level, the contact behavior should be further studied and the contact formulation suitably enhanced. Currently, plastic deformations in the interface are not taken into account. However, these play an important role, especially during unloading. Friction is also modeled rather roughly, anisotropic friction and pressure-dependent friction may lead to more accurate results. Concerning the bulk wood material, a proper description of hardening and eventually softening would increase the prediction capabilities of the simulations. This can be combined with alternative definitions of the failure surface by either using a multi-surface approach or the use of more advanced single failure criteria, which cover the interaction of multiple stresses more appropriately.

# Discussion

# Chapter 8

# Validation of the Finite Element simulations

In the following chapter, the Finite Element simulation procedure for dowel-type timber connections (Section 7) is verified by comparison of the results with the obtained experimental data (Section 3). First, similarities and differences between experimental and simulation results will be identified and discussed for connections of 100 mm width (referred to as standard connection in the following). Next, the variations of the basic connection type will be studied. It will be assessed, if the influences observed in the experiments are suitably reproduced by the simulations.

## 8.1 Standard connection

**Description**
The standard connection with 100 mm width (displayed in Sections 7.1.1 and 3.2.1) shows a plastic failure mode with a single plastic hinge in the symmetry plane. The specimens of Series 10 had an average density of $\varrho_{avg} = 438\,\mathrm{kg/m^3}$, which is representative for wood of intermediate density. The standard simulation was performed for wood of density $\varrho = 445\,\mathrm{kg/m^3}$, so that the wood is comparable.

**Discussion**
Figure 8.1 shows the load-displacement curves for the experiments on all specimens of Series 10 as well as that obtained in the standard simulation (Model 1). The experiments and the simulations both feature a distinct zone of low stiffness at the beginning of the load application, where contact between dowel and the bore-hole is established. Specimens 1 and 2 show a significant stiffness already at the start, indicating that load transfer already happens at low displacements. In contrast, Specimens 3 and 4 exhibit a is considerably higher compliance. The stiffness predicted by the simulation starts at a low level, with an increase approximately between that of Specimens 1 and 2 and

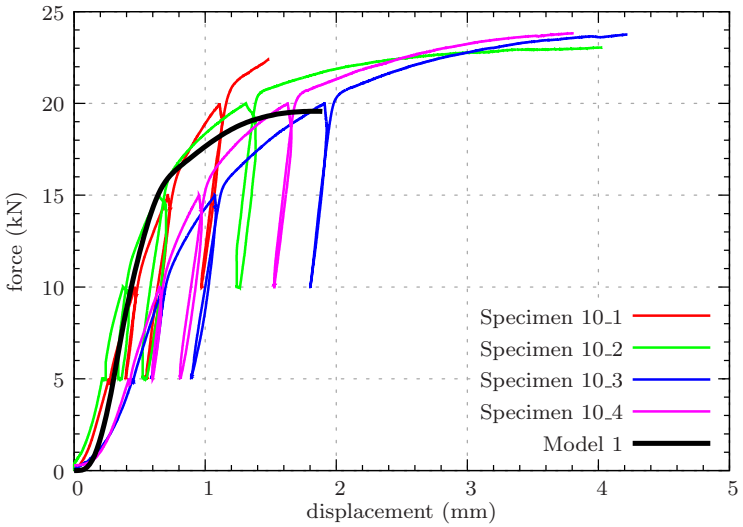


Figure 8.1: Comparison of the load-displacement curves of experiments on specimens of Series 10 with the respective standard simulation (Model 1).

Specimens 3 and 4, respectively.

The zone of approximately linear connection behavior is well defined for both, the experiments and the simulations, whereby stiffnesses in the experiments are varying to a great extent. The stiffness found in the simulation in the linear range is in the upper range of the stiffnesses observed in the experiments.

The transition to reduced stiffness, upon the onset of yielding in the wood and the dowel, is smooth in the experiments, while it appears as a sharp bend in the simulation at a load of about 15 kN. The total load can be considerably increased in the experiments in Specimens 2 to 4, which exhibit a yield plateau of comparable level. In contrast, Specimen 10_1 already fails at that load, showing that this load may already be critical in some specimens. The possible load increase in the simulation beyond the load level at the beginning of yielding is less pronounced. The yield plateau is reached at a displacement of approximately 1.8 mm. However, this value has to be judged with caution since the load and displacement levels at this stage go beyond the limits of a geometrically linear theory, which is underlying the presented model.

## 8.2 Influence of bore-hole properties

The bore-hole quality has great influence on the connection behavior. The effects of varied contact properties, bore-hole diameter, and frictional properties, predicted by the simulations, are compared to the corresponding experimental observations in the following.

### 8.2.1 Contact stiffness

**Description**
Variations of the contact stiffness were presented in Section 7.3.6 for the simulations. The investigated parameter settings were derived from the experimental results discussed in Section 4, in which contact properties for different cutting types of wood surfaces were studied (Cutting types 1 to 5). The relation between model number and the respective set of contact properties is specified in Table 7.6. Models 36 and 40 show a comparably stiff contact behavior (cutting types 1 and 5, respectively), and Models 37 and 39 a comparably soft contact behavior (cutting types 2 and 4, respectively). The contact properties in Model 38 are for a very compliant contact model (cutting type 3).

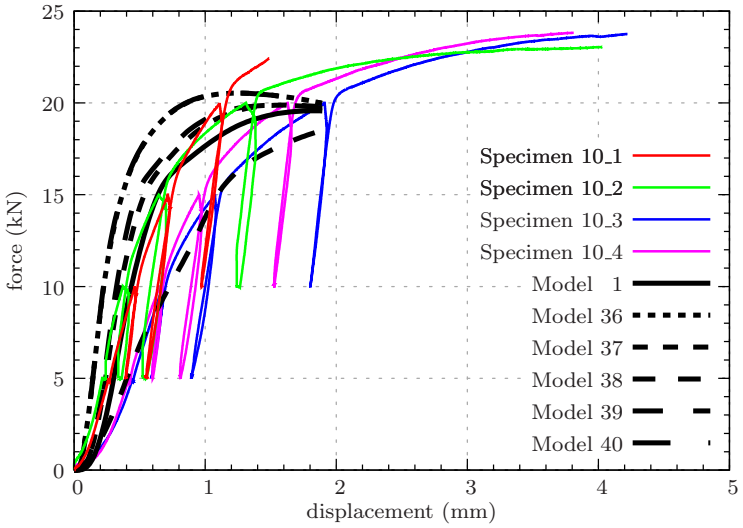


Figure 8.2: Comparison of the load-displacement curves of experiments on specimens of Series 10 with respective curves of the simulations featuring a variation of contact stiffness (Models 1, and 36 to 40).

**Discussion**
The high influence of contact stiffness, not only on the initial consolidation phase but also on the overall stiffness of dowel-type connections, is revealed in Figure 8.2, where results of simulations with changed contact properties are depicted in the load-displacement diagram. All simulations show zero stiffness in the beginning, as the interaction properties are chosen such that the pressure-contact deformation curves start with a horizontal tangents. The stiffnesses increase quickly in Models 36 and 40 (stiff contact), which show an overly stiff initial phase compared to the test results, and which overestimate also

the maximum stiffness. Models 37 and 39 (soft contact) are on the upper limit of the stiffness spectrum of the experiments, while Model 38 (very soft contact) is on the lower end. The transition zone from elastic behavior to plastic behavior in the simulations is sharper than in the experiments for the stiff interfaces (Models 36 and 40), but similar to the experimentally observed behavior with a more compliant interface (Model 38).

The surface quality of the bore-holes is apparently varying significantly, and its influence on the overall connection behavior is non-negligible. The comparison of the experiments with corresponding simulations shows that the variability of the experimentally observed behavior can be reproduced reasonably well with the proposed interaction model.

### 8.2.2 Bore-hole size

**Description**

The bore-hole of the standard simulation perfectly fits the dowel diameter. The additional adjustment of the nodes on the wood surface removes possible overclosures or gaps between the wood surface and the dowel surface. In Model 31, the node adjustment is not performed. In Models 34 and 35, the bore-hole diameters are additionally reduced, while they are increased in Models 32 and 33.

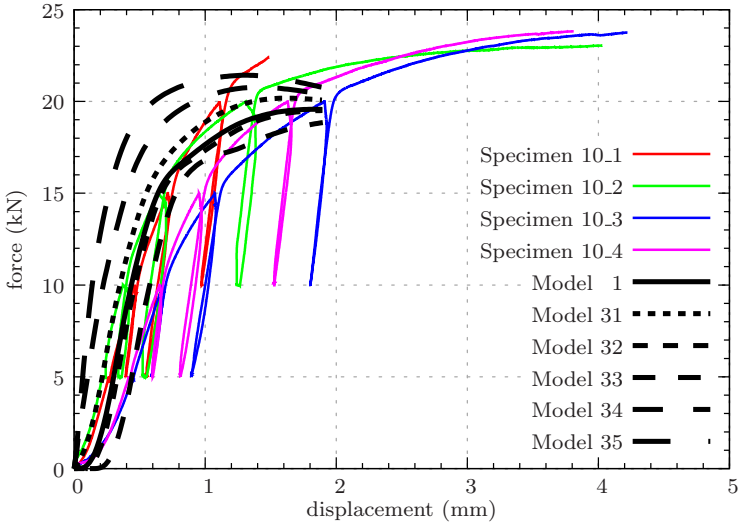


Figure 8.3: Comparison of the load-displacement curves of experiments on specimens of Series 10 with respective curves of the simulations featuring a variation of the bore-hole diameter (Models 1 and 31 to 35).

**Discussion**

Without node adjustment, the dowel is clamped into the surrounding wood also when no loads are transferred. Full contact is given in the simulations from the beginning of the loading process (Figure 8.3). At low loads, the connections already exhibit significant stiffnesses, and the initial consolidation phase is reduced (Model 31). Apparently, this comes close to the situations in practical timer engineering, where the bore-hole is usually of a slightly smaller diameter than the dowel, so that the dowel is pressed into the bore-hole.

An increase of bore-hole diameter does change the overall behavior significantly. It more or less results in a shift of the load-displacement curve along the displacement axis (Models 32 and 33).

Models 34 and 35 with significantly reduced bore-hole diameter show too high a stiffness compared to the experiments. No initial consolidation is recognizable anymore.

### 8.2.3 Friction

**Description**

The Specimens 01_4, and 13_2 and 13_3, which are of similar densities ranging from 485 to 495 kg/m$^3$, were tested with a smooth, a roughened and an engrailed dowel, respectively. Their test results are compared to that of selected simulations with varying frictional coefficients in the dowel-wood-interface of $\mu$ =0.10, 0.40, and 0.70 in the Models 10, 1, and 15, respectively.

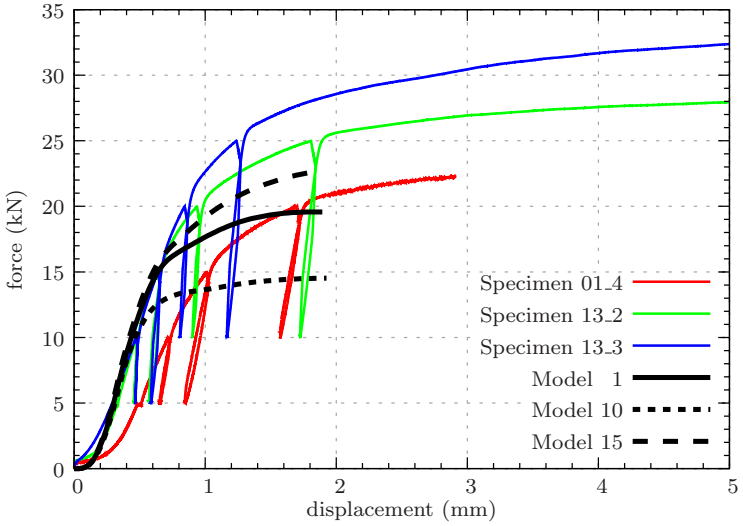


Figure 8.4: Comparison of the load-displacement curves of experiments on specimens of Series 10 with the respective curves of simulations featuring a variation of the friction properties between dowel and bore-hole surface (Models 1, 10, and 15).

**Discussion**

Although the densities of the specimens in the experiments and the simulations were different, the consequences of different frictional conditions can nevertheless be studied based on the relative differences of the individual load-displacement curves. In the experiments, the overall connection stiffness is not significantly affected by a variation of friction. However, maximum load as well as ductility are influenced considerably (Figure 8.4), as is obvious from the increased load level of the yield plateau in the experiments.

## 8.3 Influence of wood density

**Description**

The specimens of Series 16C, 10, and 08A were all of 100 mm width, but their average densities varied as 360, 438, and 513 kg/m$^3$, respectively. Selected test results of these series are compared to numerical results for Models 1, 2, and 3, which were carried out for wood densities of 324, 445, and 541 kg/m$^3$.

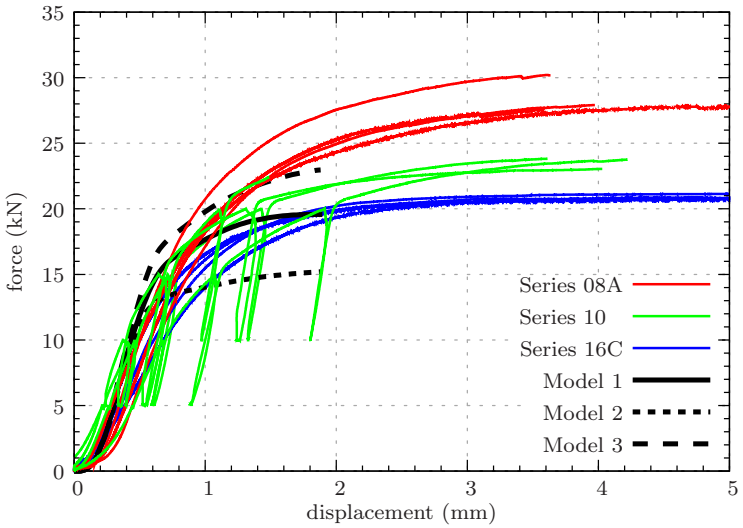


Figure 8.5: Comparison of the load-displacement curves of experiments on specimens of Series 08A, 10, and 16C with the respective curves of the simulations featuring variation of wood density (Models 1, 2, and 3).

**Discussion**

In the simulations, a variation of wood density does not change connection stiffness significantly. In the experiments, a pronounced scatter of the connection stiffness is observed, which, however, depends considerably on contact properties not varied in the presented simulations. The level of ultimate load is not predicted properly by the simulations, but the trend of increased ultimate load for wood of higher density is well reproduced (Figure 8.5).

## 8.4 Influence of geometry

### 8.4.1 Width of specimen

**Description**

The specimen width controls the ductile failure modes, which can involve no, one, or three plastic hinges in the dowel. In order to show how well these failure modes are reproduced by the simulations, experimental results of the specimens of Series 05, 02, and 07 with widths of 40, 100, and 200 mm, respectively, are compared to that of Models 1, 7, and 8 with corresponding specimen widths.

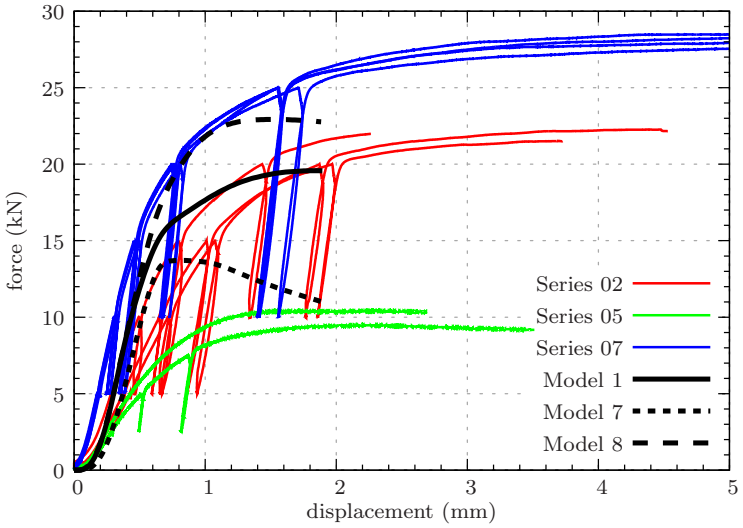


Figure 8.6: Comparison of the load-displacement curves of experiments on specimens of Series 02, 05, and 07 with the respective curves of the simulations featuring a variation of connection width (Models 1, 7, and 8).

**Discussion**

The different load-carrying characteristics of connections with varying widths observed in the experiments are well reflected by the simulations (Figure 8.6). In the simulations, the differences of stiffness due to a variation of the width are less pronounced than the differences of the ultimate loads. These are under-predicted in wide and intermediate specimens, while they are over-predicted in narrow connections. The transition from elastic to plastic material behavior, which occurs gradually in the experiments, happens more abruptly in the simulations. This is caused by disregarding hardening of the wood material in the simulations, which would evoke a gradual transition in the simulations as well and require larger deformations before reaching the same load level. Furthermore, material hardening may also reduce the ultimate load, since higher deformations provoke a smaller area of load transfer between dowel and wood. This behavior is more pronounced for connections with a small $a/d$-ratio, since connections with higher ratios allow for the activation of larger connection areas and, therefore, for the transfer of higher loads.

### 8.4.2 End distance

**Description**

In the experiments, the specimens of Series 04A were tested with subsequently reduced end distance and were of 502 kg/m$^3$ average density. The geometries of the specimens in the Models 26, 26, and 27 reflect these changes to the standard geometry.

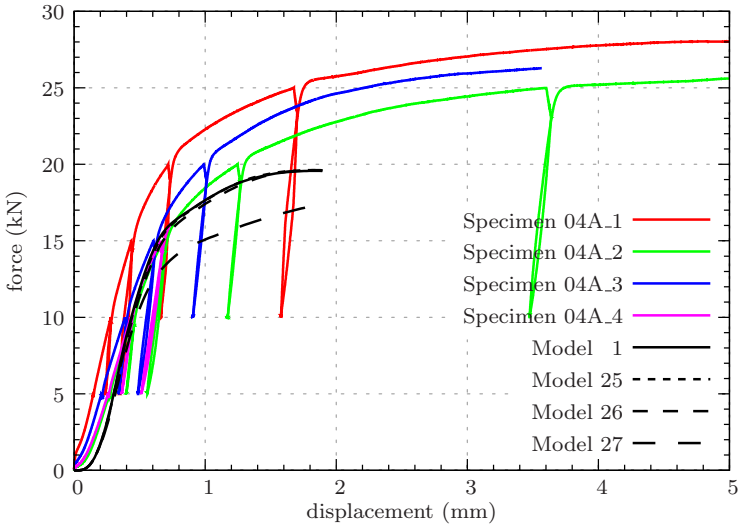


Figure 8.7: Comparison of the load-displacement curves of experiments on specimens of Series 04A with the respective curves of the simulations featuring a step-wise reduced end distance (Models 1, 25, 26, and 27).

**Discussion**

The main effect of a reduced end distance on the load-carrying behavior of connections is the increased likeliness of premature formation of lateral cracks, so that the length of the yield plateau is reduced, or such a plateau is not even reached. The simulation results show significant deviations from the standard course in the load-displacement diagram only for the shortest end distance (Figure 8.7). In the experiments, a reduced end distance led to premature splitting. In the simulations, a reduction of the ultimate load is observed, since an elasto-plastic approach is adopted. Excessive lateral tensile stresses cause plastic behavior therein.

### 8.4.3 Edge distance

**Description**

In the specimens of Series 14, the edge distance was reduced subsequently, so that the net cross-section for transferring tension loads was reduced significantly. Analogously, the edge distance was reduced in the Models 28, 29, and 30.

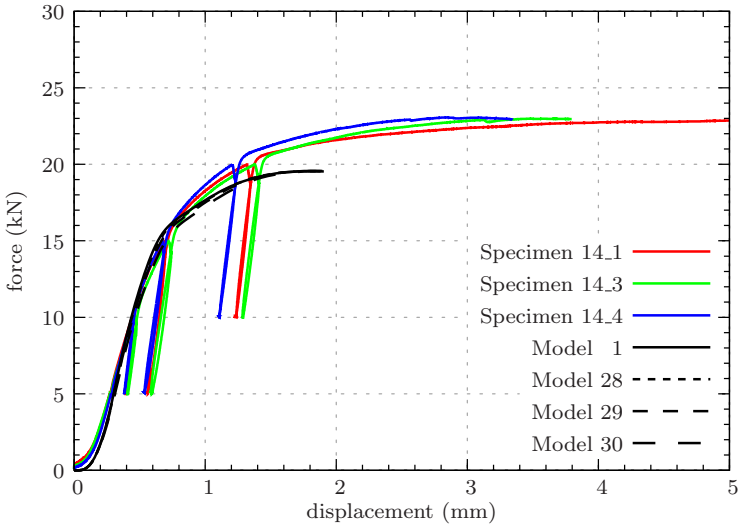


Figure 8.8: Comparison of the load-displacement curves of experiments on specimens of Series 10 with the respective curves of the simulations featuring a reduced edge distance (Models 1, 28, 29, and 30).

**Discussion**

The overall course of the load-displacement-curves did not change in the experiments upon a reduction of the edge distance. Accordingly, the simulations showed nearly identical results, underlining a good agreement of the simulations with the experiments (Figure 8.8).

## 8.5 Unloading and reloading cycles

**Description**

Most of the experiments were conducted with unloading and reloading cycles at various load stages. Model 20 was performed in a similar manner with unloading cycles at 10 and 15 kN, respectively. Its results are compared to the results of experimental Series 10 in the following.

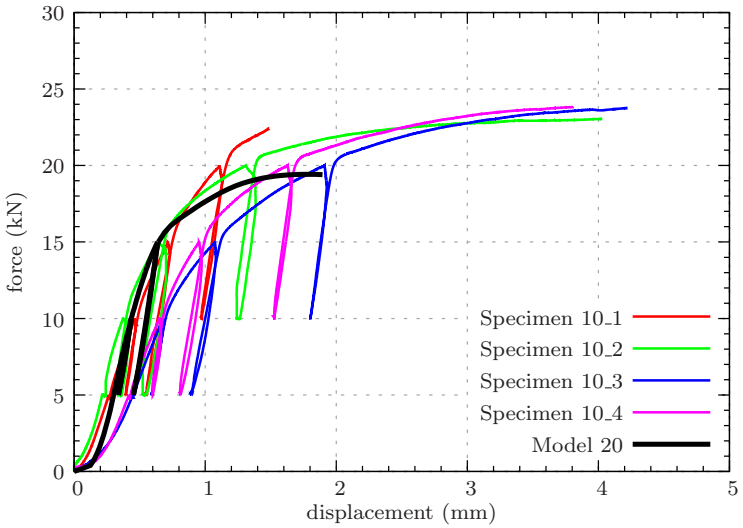


Figure 8.9: Comparison of the load-displacement curves of experiments on specimens of Series 10 with the respective curve of the simulation performed with repeated unloading cycles (Model 20).

**Discussion**

The load-displacement curve of Model 20 shows good agreement with the experimental results. The unloading and reloading curves in the simulation are of distinctively higher stiffness and approximately parallel to the experimental unloading curves (Figure 8.9).

## 8.6 Discussion

The simulation tool for assessing the load-carrying behavior of dowel-type timber connections (Chapter 7) was validated against corresponding results from experiments on such connections (Chapter 3). Starting from a standard connection, a large variety of connection designs was studied. The comparisons showed a good agreement of the experimental results and the simulation results across most of the investigated variations.

The initial load phase of connections, during which the often highly compliant contact zone controls the loading behavior, is mainly influenced by the bore-hole quality. The weak stiffness of the wood surface and the fitting of the dowel into the bore-hole play important roles there. The dependance of connection stiffness on the interaction properties between wood and dowel, on wood stiffness, and on connection width could be verified qualitatively and also to a large extent quantitatively.

The transition from elastic to plastic behavior is more abrupt in the simulations than in the experiments. An assessment of the ultimate loads is not possible with the current simulation approach since at this loading stage the limits of validity of the simulation approach, based on small strain/small displacement theory, are exceeded. Due to this limitation, the ultimate load, the length of the yield plateau as well as ultimate (brittle) failure modes cannot be estimated. Proposals how to overcome these restrictions were already given in Section 7.4.

Chapter 9

# Comparison of experimental results with the design concept of EC5

In the following, the results of the experiments on single-dowel steel-to-timber connection (Chapter 3) are compared to the current generation of European standards Eurocode 5 (EC5) [24] (Chapter 2) with respect to stiffness, ultimate load, and failure mode, as well as to influences of density and other parameters. The comparison shall give indications about the reliability and efficiency of the current design formulae and elucidate influences so far not captured (appropriately) by the formulae.

## 9.1 Introduction

Table 9.1 shows the projected design values for strength and stiffness of all test series according to EC5. The design values are also specified for samples of average density and the three standard configurations with different widths. These values will serve for normalizing the test results in the following.

Calculations are done according to Equation (2.1) for determination of stiffnesses, and Equation (2.2) for determination of strengths, respectively. For determining values in Table 9.1, the tensile strength for steel quality S 235 is $f_{u,k} = 360\,\mathrm{N/mm^2}$, and the width $t_1 = (2\,a - 10)/2$ is half of the width of the wood net-section.

| Series | Width (mm) | Density (kg/m$^3$) | $F_{v,Rk}$ (kN) | $K_{ser}$ (N/mm) |
|---|---|---|---|---|
| 05 | 40 | 419 | 10.9 | 17 900 |
| 09A | 40 | 458 | 11.9 | 20 500 |
| 01 | 100 | 485 | 19.8 | 22 300 |
| 02 | 100 | 404 | 17.2 | 16 900 |
| 04 | 100 | 502 | 19.8 | 23 500 |
| 05B | 100 | 374 | 16.2 | 15 100 |
| 08A | 100 | 513 | 20.7 | 24 200 |
| 08B | 100 | 489 | 20.0 | 22 600 |
| 10 | 100 | 513 | 20.7 | 24 200 |
| 13 | 100 | 495 | 20.2 | 23 000 |
| 14 | 100 | 441 | 18.4 | 19 300 |
| 16A | 100 | 384 | 16.5 | 15 700 |
| 16B | 100 | 344 | 15.2 | 13 300 |
| 16C | 100 | 360 | 15.7 | 14 300 |
| 16D | 100 | 374 | 16.2 | 15 100 |
| 15 | 200 | 424 | 23.2 | 18 200 |
| 07 | 200 | 402 | 22.6 | 16 800 |
| $\varrho_{avg}$ | 40 | 430 | 11.2 | 18 600 |
| $\varrho_{avg}$ | 100 | 430 | 18.0 | 18 600 |
| $\varrho_{avg}$ | 200 | 430 | 23.3 | 18 600 |

Table 9.1: Comparison of design strength, $F_{v,Rk}$, and stiffness, $K_{ser}$, according to EC 5, for each experimental series and for fictive connections using wood of mean density

## 9.2 Stiffness

Figure 9.1 compares stiffnesses observed in the experiments with corresponding design stiffnesses according to EC5 for specimens of 100 mm width and varying density. For this purpose, lines with a slope equal to the design stiffness are included into plots of the measured load-displacement curves of the series used for studying the density influence (Section 3.3.1). Specimens with higher density tend to exhibit higher stiffnesses during initial loading, which is accurately predicted by EC5. Unloading stiffness is about the same for all densities ($\approx 55$ kN/mm) and significantly higher than initial loading stiffness.

Only for specimens with a width of 100 mm (Figures 9.1 and 9.2(b)) the stiffnesses specified by EC5 are appropriate. In narrow and wide connections, the EC5 formulae underestimates or overestimates the observed stiffnesses, respectively (Figures 9.2(a) and (c)). The formulae for stiffness estimation do not cover the influence of connection width, for example by differentiation of possible failure modes, like it is done in strength design.

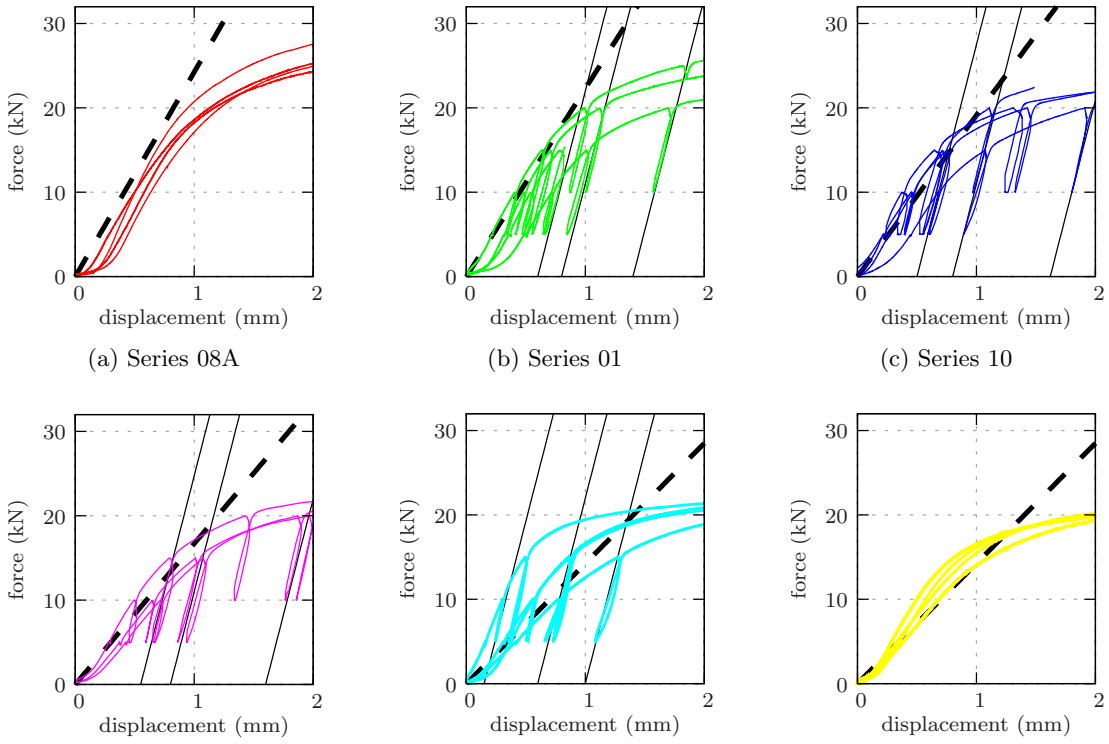


(a) Series 08A (b) Series 01 (c) Series 10

(d) Series 02 (e) Series 16A (f) Series 16C

Figure 9.1: Details of load-displacement curves of 100 mm wide specimens of Series 08A, 01, 10, 02, 16A and 16C (sorted by descending average density of all specimens): respective stiffness according to EC5 (dashed lines), approximated stiffness for un- and reloading (black lines, 55 kN/mm for all specimens)

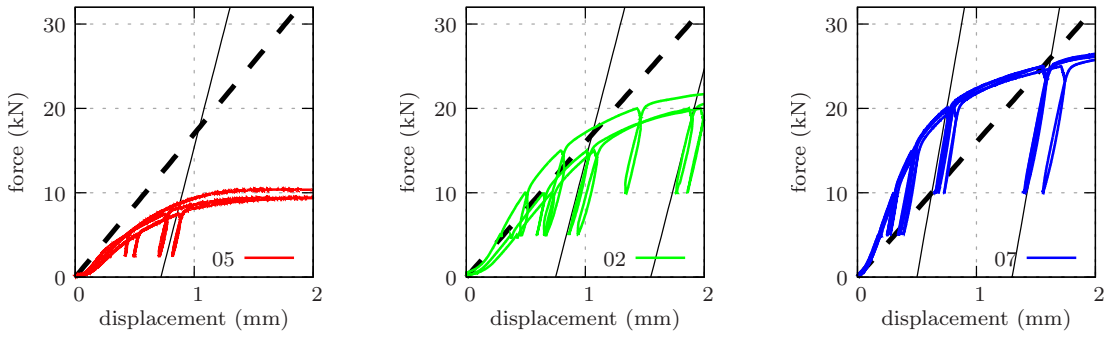


(a) Specimens with width of 40 mm (b) Specimens with width of 100 mm (c) Specimens with width of 200 mm

Figure 9.2: Comparison of experimentally determined stiffnesses of selected tests with corresponding design values from EC5 for different widths: respective stiffness according to EC5 (dashed lines), approximated stiffnesses for unloading and reloading (black lines, 55 kN/mm for all specimens with widths of 40 or 100 mm, 80 kN/mm for specimens with widths of 200 mm)

## 9.3 Strength

In the formulae of EC5, most of the influences studied in the experiments are covered by the embedment strength $f_{h,1,k}$, which linearly depends on density. Additionally, the friction between dowel and wood as well as a reduction of end distance affect the embedment strength. A variation of the connection width is captured by the direct influence of $t_1$.

Figures 9.3(a) to (c) re-illustrate the test results, now classified according to the plastic failure modes (no, one, or two plastic hinges of the dowel), which follows the different sample width. The shown forces are normalized to $\varrho_{avg} = 430\,\mathrm{kg/m^3}$ ($\overline{F} = F\,\varrho/\varrho_{avg}$) by means of the data included at the bottom of Table 9.1. The figures clearly show the influence of various parameters on the ultimate loads.

The comparison of the experimental results with the design values indicates that the design values are conservatively determined for connections with intermediate and high $a/d$-ratios. $F_{v,Rk}$ is well below actual experimental values for such connections. In connections with a small $a/d$-ratio, the design value overestimate the measured connection strength for Specimen 05_2. The figures show that a distinctively higher load than given by the design formulae by up to 50% can be achieved with engrailed dowels (Specimens 09A_2, 13_1, 15_3, 16D_1) or lateral reinforcement (Specimen 05B_1).

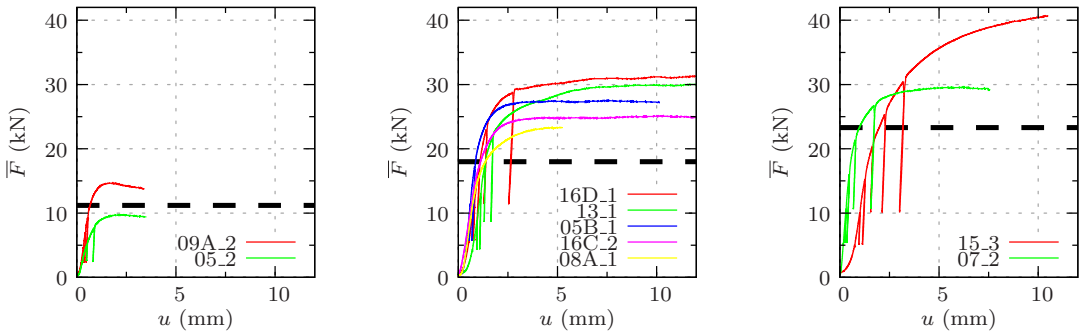


(a) Specimens with width of 40 mm

(b) Specimens with width of 100 mm

(c) Specimens with width of 200 mm

Figure 9.3: Comparison of strength of selected tests with design values from EC5 (normalized linearly to $\varrho_{avg} = 430\,\mathrm{kg/m^3}$; $\overline{F} = F\,\varrho/\varrho_{avg}$)

## 9.4 Discussion

In EC5, the connection width is not taken into account when determining stiffness. However, the tests showed a pronounced influence of the connection width on its stiffness, which also follows from basic static reasoning. Thus, design stiffness is clearly specified with insufficient accuracy and might lead to unreliable results in static design. A differentiation of connection stiffness according to the connection width, similar to the procedure for strength determination, would improve the design.

Furthermore, the design rules do not differentiate between the stiffness during first loading and that during (repeated) unloading and reloading. Also a possible widening of the

hole and increased hole-clearance should be considered then. A suitable concept for assessing stiffness should be introduced in order to represent the nonlinear behavior during loading up to the Ultimate Limit State and the yield plateau. This relationship may be considerably different for single and multi-dowel connections. In the latter, the statically non-determinant load transfer results in different contributions of the individual dowels to the overall stiffness.

The experiments have shown, that EC5 provides conservative design values for strength for connections of intermediate and high $a/d$-ratio. A better utilization might be possible with improved design rules in these connection types. Design strength for connections of 40 mm width is higher than the ultimate load determined by the experiments. Bearing strength of these connections is therefore overrated, and the design rules should be revised in order to avoid undersizing of structures with potentially severe consequences.

The EC5 provides no information on the ductility of connections and the deformations of the bore-holes are not bounded by any limit. The experiments have shown, that ductility is influenced by wood density, whereby wood of low density is more favorable in terms of high structural ductility. Lateral reinforcement restrains the formation of brittle failure modes, which can give rise to a significant gain in ductility. The use of dowels with high roughness increases ductility and ultimate load for all densities studied. It would be worthwhile to extend the design rules in order to include the positive consequences of such measurements improving utilization.

# Chapter 10

# Conclusions

In this thesis, the load-bearing behavior of dowel-type steel-to-timber connections was studied. In particular, single-dowel connections under tension loads were investigated, whereby the loads were applied in grain direction. The investigations on single-dowel connections allowed to study the distribution of forces more easily compared to multi-dowel configurations since these connections are statically determinant.

First, the connection behavior was investigated by conducting experiments on a large number of connections. The influence of a variety of parameters was studied, which included connection width in order to study the main failure modes according to Johansen's theory and wood density (between 360 and 513 $\mathrm{kg/m^3}$). The dowel roughness was artificially increased, which significantly raised the load-bearing capacity and also improved ductility of the connections. Lateral reinforcement was added to some specimens, which had positive effects on the ductility of the connection by restraining brittle failure. Additionally, changes to the standard geometry by varying end and edge distances were explored. The resulting differences of the stiffness properties and of ultimate strength were pointed out and discussed. Furthermore, the failure behavior and the effects of the variations on the ductility were analyzed. A main output of this thesis is the detailed description of the loading process, which is separated into several stages.

The results of the experiments were then compared to the results of connections design according to the Eurocode 5 (EC5) [24] for strength and stiffness. The influence of wood density as well as of connection width on ultimate load was well predicted by EC5. It was shown, that the ultimate load was usually estimated conservatively, only for slender connections ultimate load was overestimated. Connection stiffness was estimated properly for connections of intermediate width, but overestimated for slender connections and underestimated for wide connections. This was mainly due to the reason that connection width was not influencing connection stiffness in EC5, while it was clearly affecting the ultimate load.

The dominant influence of the contact conditions at the dowel-wood interface on the load carrying behavior of the connection motivated an intensive investigation of the interface

properties between dowel and wood. The results of the experiments on connections have shown a highly nonlinear behavior at lower loads, before plastification in the dowel or the bulk wood can be expected. In this loading range, the connection stiffness was very low but quickly increasing over with increasing load. It was concluded, that the soft contact behavior between the dowel and the wood was responsible for the low stiffness. Soft stiffness was caused by the rough surface of the bore-hole, which often exhibited pronounced ripples, valleys, and peaks. Due to increased pressure on the surface at higher loads, the ripples were deformed non-reversibly, so that the contact surface was enlarged and therefore, the connection stiffness increased. The contact properties in normal direction were studied experimentally by conducting compressive tests on cubes with very different surface profiles resulting from a variation of wood density and by using different cutting techniques. It could be confirmed, that the different cutting techniques had enormous influence on the contact stiffness, but not on the ultimate load of the test specimens. From the experimental results, a non-linear pressure-contact displacement relation was derived, which did also include the significantly higher stiffness during unloading and reloading of previously loaded surfaces compared to the stiffness during first loading. Finally, the contact model was implemented into the Finite-Element code ABAQUS by means of a user-subroutine UINTER.

In order to simulate the behavior of dowel-type connections by means of numerical analysis, a three-dimensional elasto-plastic material model for clear wood was developed, formulated within the theory of small strains and small displacements. A Tsai-Wu failure criterion was adopted for assessing failure due to the ultimate multi-axial stress level in wood. Once failure occurs, a perfect plastic behavior was assumed. The model was especially suitable for the behavior in the pressure domain in all material direction, since the material behavior of clear wood under compressive loads is generally assumed to be plastic. The material model was also implemented into the Finite-Element code ABAQUS, using a user-subroutine UMAT.

The combination of the models for the material behavior of clear wood as well as for the contact behavior was used to simulate the load-bearing behavior of dowel-type connections by means of Finite Element analysis. The preparation of the simulation model was shown in great detail for the geometry, including explanations of the material definition, the contact definitions, the loading and boundary conditions, as well as the mesh generation. Diverse parametric studies were performed, whereby, amongst other parameters, the wood density, the contact behavior in normal as well in tangential direction, and the connection geometry were varied. The simulations did also reproduce the differences between the unloading and the reloading path from first the loading path, the latter being significantly stiffer than the first loading path.

In a final step, the results of the simulations were compared to the results of the experiments on dowel-type connections. It could be concluded, that the simulations were able to predict connection behavior in a satisfyingly manner up to the limits of applicability of the simulation model. The course of the load-displacement curves of the simulations showed the same features as the experimentally determined curves. The connection stiffness of the simulations agreed well, also the unloading and reloading path was properly predicted. This was mostly thanks to the developed contact model, which was a unique feature in this thesis.

**Outlook**

Despite the good agreement of the simulations with the experimental results, the current state of the simulation tool is only able to provide insight into the connection behavior up to limited plastic deformations, and fracture mechanical models are not at all included. A reliable assessment of the ultimate load and of the final failure in consequence of crack formation is not possible. Hence, it is desirable to extend the material description for wood to large strains and displacements to overcome the current limitations. Additionally, the introduction of brittle failure criteria would allow to determine critical stress states.

Regarding the simulations by other authors, it would be essential to provide full information on the models applied. Currently, often only limited information is given about critical parameters and formulations used in the simulations. Moreover, existing simulation approaches frequently aim at the estimation of the ultimate load and on brittle failure modes only, thereby neglecting a suitable reproduction of the mechanical behavior over the entire load range. It is therefore not secured, that the stress states fully reflect reality. The work at hand has shown the significant influence on the simulations results by simply varying the size of the Finite Element mesh or by applying different frictional coefficients. Many of the addressed publications provide no or little information about that, it would be desirable to establish common standards.

The application of powerful simulation tools will help to gain insight into the behavior of connections. On the one hand, full-scale experiments can be avoided in many cases, which are usually cost and time consuming procedures. On the other hand, they may contribute to improve the quality of the design codes by clarifying open questions and unsolved problems. Also the functionality of novel connection techniques and add-ons such as reinforcement may be assessed and then implemented in the design codes.

# Appendix

# Appendix A

# Roughness Parameters

In the following, the roughness parameters used in Section 4.3 are defined. The parameters were determined following the rules given in the respective international standards for determining surface properties.

**Amplitude parameters (peak and valley) [29]**

- $Pp$, $Wp$, $Rp$ - Maximum profile peak height
  The maximum profile peak height is the largest profile peak height $Zp$ within a sampling length as defined by

$$Rp = \max\big(Z(x)\big) \tag{A.1}$$

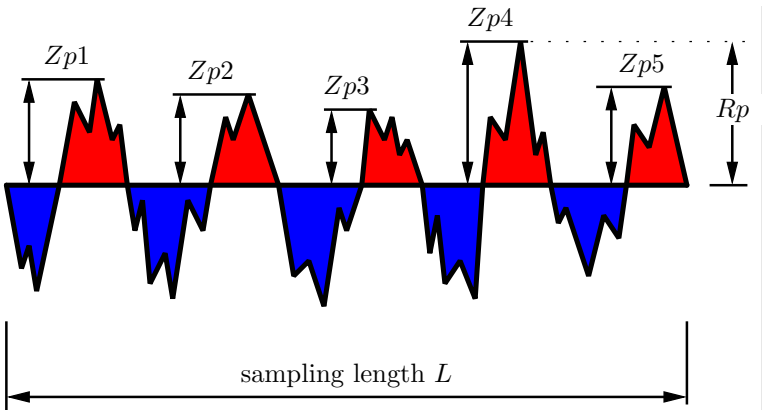


Figure A.1: $Pp$, $Wp$, $Rp$ - Maximum profile peak height

- $Pv$, $Wv$, $Rv$ - Maximum profile valley depth
  The maximum profile valley depth is the largest profile valley depth $Zv$ within a sampling length as defined by

$$Rp = \min\big(Z(x)\big) \tag{A.2}$$

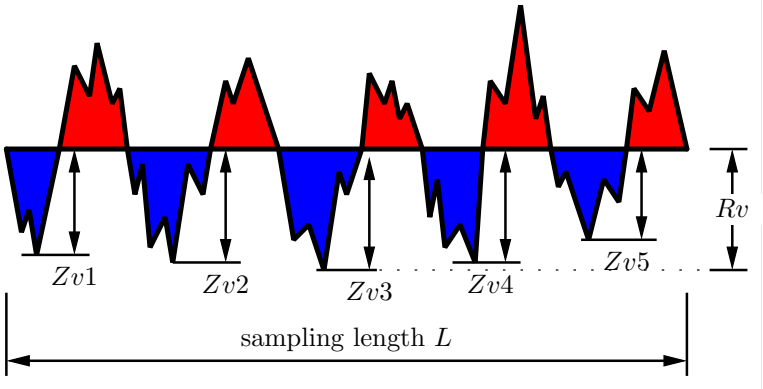


Figure A.2: $Pv$, $Wv$, $Rv$ - Maximum profile valley depth

- $Pz$, $Wz$, $Rz$ - Maximum height of profile
  The maximum height of profile is the sum of the largest profile peak height $Zp$ and the largest profile valley depth $Zv$ within a sampling length as defined by

$$Rz = Rp + Rv \tag{A.3}$$

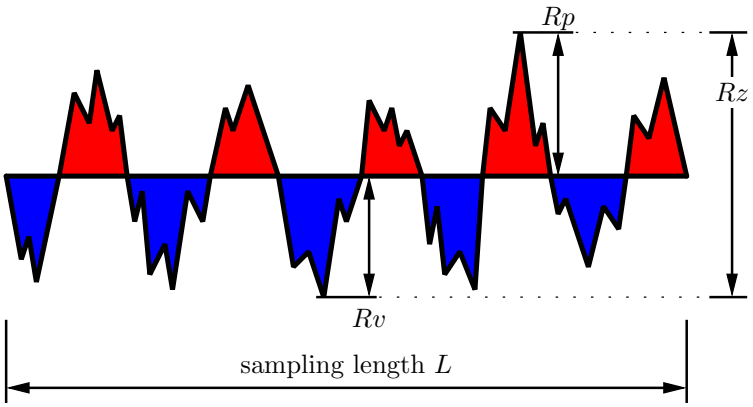


Figure A.3: $Pz$, $Wz$, $Rz$ - Maximum height of profile

- $Pt$, $Wt$, $Rt$ - Total height of profile
  The total height of profile is the sum of the height of the largest profile peak height $Zp$ and the largest profile valley $Rv$ within an evaluation length as defined by

$$Rt = \max(Rpi) + \max(Rvi) \tag{A.4}$$

  Due to the different definition lengths, $Pt$, $Wt$ and $Rt$ are always larger than or equal to $Pz$, $Wz$ and $Rz$, respectively.

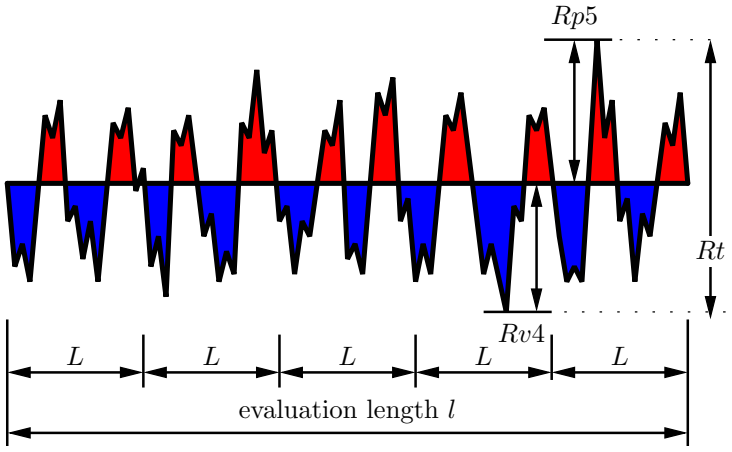


Figure A.4: $Pt$, $Wt$, $Rt$ - Total height of profile

**Amplitude parameters (average of ordinates) [29]**

- $Pa$, $Wa$, $Ra$ - Arithmetical mean deviation of the assessed profile
  The arithmetical mean deviation of the assessed profile is the arithmetic mean of the absolute ordinate values $Z(x)$ within a sampling length as defined by

$$Pa, Wa, Ra = \frac{1}{l} \int_0^l |Z(x)| dx \tag{A.5}$$

  with $l = lp$, $lr$ or $lw$ according to the case.

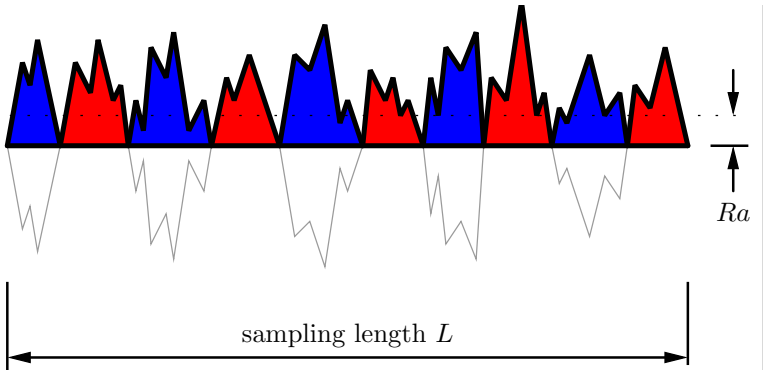


Figure A.5: $Pa$, $Wa$, $Ra$ - Arithmetical mean deviation of the assessed profile

- $Pq$, $Wq$, $Rq$ - Root mean square deviation of the assessed profile
  The root mean square deviation of the assessed profile is the root mean square value of the ordinate values $Z(x)$ within a sampling length as defined by

$$Pq, Wq, Rq = \sqrt{\frac{1}{l}\int_0^l Z(x)^2 dx} \tag{A.6}$$

  with $l = lp$, $lr$ or $lw$ according to the case.

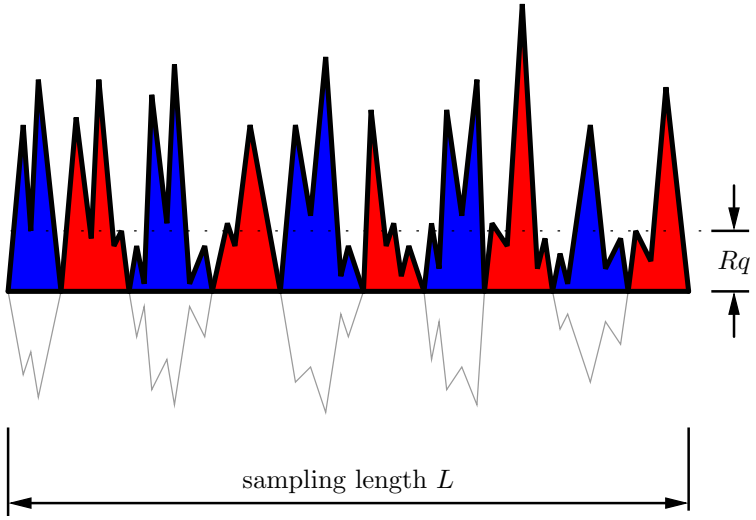


Figure A.6: $Pq$, $Wq$, $Rq$ - Root mean square deviation of the assessed profile

**Curves and related parameters [29, 27]**

- Abbot Firestone curve - Material ratio curve of the profile
  The curve representing the material ratio of the profile as a function of level $c$. The curve can be interpreted as the sample cumulative probability function of the ordinate values $Z(x)$ within the evaluation length.

- $Pk$, $Wk$, $Rk$ - Core roughness depth
  Depth of the core profile, defined by the secant line for $\Delta Mr = 40\%$ which has the smallest gradient.

- $Ppk$, $Wpk$, $Rpk$ - Reduced peak height
  The average height of the protruding peaks above roughness core profile.

- $Pvk$, $Wvk$, $Rvk$ - Reduced valley depths
  The average depth of the profile valleys projecting through the roughness core profile.

- $PMr1$, $WMr1$, $RMr1$ - Material proportion 1 (peaks)
  Level in %, determined for the intersection line which separates the protruding peaks from the roughness core profile.

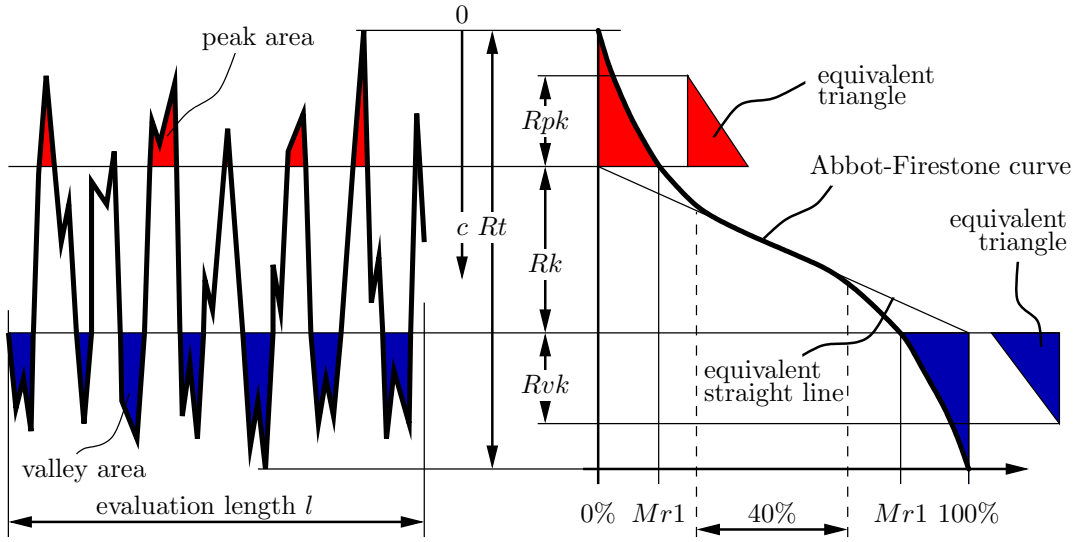


Figure A.7: Abbot-Firestone curve and derived parameters.

- $PMr2$, $WMr2$, $RMr2$ - Material proportion 2 (valleys)
  Level in %, determined for the intersection line which separates the deep valleys from the roughness core profile.

The curves and related parameters are defined over the evaluation length rather than the sampling length, as this provides more stable curves and related parameters.

# Appendix B

# Results of the roughness measurements

In the following, the surface texture parameters (Table 4.2) determined by means of an optical measurement system (Section 4.3) are compiled.

The results of all specimens of a specific series of different wood density and cutting style are averaged. In Tables B.1-B.4, the results for the surfaces of wood of low average density are given, followed by the results for wood of intermediate density (Tables B.2-B.8), and wood of high density (Tables B.3-B.12), respectively.

**Parameters for the primary profile**

| Parameter | | Cutting type | | | | |
|---|---|---|---|---|---|---|
| | | 1 | 2 | 3 | 4 | 5 |
| $sPp$ | $\mu$m | 350.7 | 507.5 | 1160 | 574.1 | 204.5 |
| $sPv$ | $\mu$m | 768 | 1203 | 1185 | 1390 | 205.4 |
| $sPz$ | $\mu$m | 741.8 | 1425 | 2004 | 1593 | 289.4 |
| $sPt$ | $\mu$m | 1119 | 1710 | 2345 | 1964 | 409.9 |
| $sPa$ | $\mu$m | 31.18 | 99 | 237.2 | 94.34 | 12.2 |
| $sPq$ | $\mu$m | 52.02 | 141.5 | 309.9 | 145.9 | 17.11 |
| $sPk$ | $\mu$m | 76.05 | 213.3 | 677.4 | 177.2 | 35.34 |
| $sPpk$ | $\mu$m | 38.73 | 77 | 515.2 | 101.9 | 22.98 |
| $sPvk$ | $\mu$m | 103.4 | 314.2 | 215.5 | 350.2 | 21.41 |
| $sPMr1$ | % | 9.278 | 7.425 | 14.52 | 9.67 | 11.13 |
| $sPMr2$ | % | 85.66 | 81.43 | 92.61 | 81.58 | 89.35 |

Table B.1: Surface texture parameters for the primary profile for specimens of low wood density (Series 16B4).

| Parameter | | Cutting type | | | | |
|---|---|---|---|---|---|---|
| | | 1 | 2 | 3 | 4 | 5 |
| $sPp$ | $\mu$m | 535.5 | 521.9 | 1777 | 501.1 | 116.7 |
| $sPv$ | $\mu$m | 1022 | 956.8 | 1784 | 1588 | 97.6 |
| $sPz$ | $\mu$m | 934.2 | 1118 | 2784 | 1484 | 141.2 |
| $sPt$ | $\mu$m | 1558 | 1479 | 3560 | 2089 | 214.3 |
| $sPa$ | $\mu$m | 112.5 | 55.84 | 470.8 | 56.92 | 11.4 |
| $sPq$ | $\mu$m | 165.6 | 78.27 | 543.4 | 89.25 | 14.42 |
| $sPk$ | $\mu$m | 305 | 155.5 | 1183 | 131.6 | 36.67 |
| $sPpk$ | $\mu$m | 80.16 | 67.96 | 316.4 | 106.1 | 13.86 |
| $sPvk$ | $\mu$m | 438 | 143.8 | 497.1 | 177.1 | 13.87 |
| $sPMr1$ | % | 14.54 | 10.13 | 12.01 | 14.69 | 9.547 |
| $sPMr2$ | % | 90.62 | 88.37 | 83.1 | 86.96 | 90.37 |

Table B.2: Texture parameters for the primary-profile for specimens of intermediate wood density (Series 14_2).

| Parameter | | Cutting type | | | | |
|---|---|---|---|---|---|---|
| | | 1 | 2 | 3 | 4 | 5 |
| $sPp$ | $\mu$m | 284.9 | 422.8 | 734.5 | 427.3 | 117.5 |
| $sPv$ | $\mu$m | 434.5 | 890.2 | 1739 | 860.5 | 60.91 |
| $sPz$ | $\mu$m | 557.6 | 1057 | 2089 | 934.4 | 121.9 |
| $sPt$ | $\mu$m | 719.4 | 1313 | 2474 | 1288 | 178.4 |
| $sPa$ | $\mu$m | 20.12 | 45.21 | 301.3 | 34.41 | 10.93 |
| $sPq$ | $\mu$m | 31.23 | 68.9 | 372.5 | 56.71 | 13.79 |
| $sPk$ | $\mu$m | 48.22 | 116.7 | 515.5 | 79.87 | 34.81 |
| $sPpk$ | $\mu$m | 34.55 | 70.01 | 121.9 | 63.46 | 12.96 |
| $sPvk$ | $\mu$m | 67.56 | 153.5 | 747.8 | 124.5 | 14.5 |
| $sPMr1$ | % | 13.9 | 12.98 | 6.574 | 13.83 | 9.405 |
| $sPMr2$ | % | 88.65 | 89.42 | 71.85 | 88.29 | 89.9 |

Table B.3: Texture parameters for the primary-profile for specimens of high wood density (Series 8A4).

| Parameter | | Density | | |
|---|---|---|---|---|
| | | low | intermediate | high |
| $Pp$ | $\mu$m | 507.3 | 121.4 | 360.5 |
| $Pv$ | $\mu$m | 1064 | 147.8 | 1963 |
| $Pz$ | $\mu$m | 973.9 | 230.7 | 1119 |
| $Pt$ | $\mu$m | 1572 | 257.4 | 2324 |
| $Pa$ | $\mu$m | 182.7 | 32.85 | 139.9 |
| $Pq$ | $\mu$m | 244.6 | 36.47 | 230.2 |
| $Pk$ | $\mu$m | 482.5 | 111.8 | 238.3 |
| $Ppk$ | $\mu$m | 152 | 43.95 | 138.9 |
| $Pvk$ | $\mu$m | 490.5 | 26.54 | 520.2 |
| $PMr1$ | % | 6.937 | 1.338 | 12.76 |
| $PMr2$ | % | 85.07 | 1.74 | 81.66 |

Table B.4: Surface texture parameters for the primary profile for specimens with a drilled bore hole.

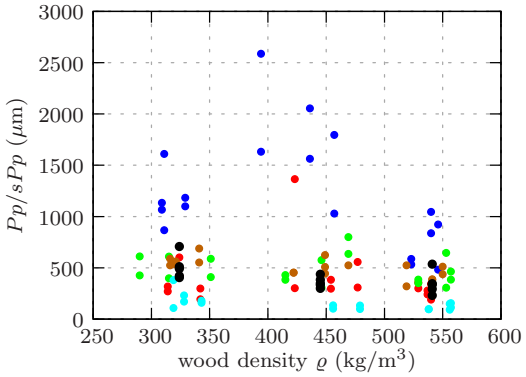


(a) maximum profile peak height $Pp/sPp$

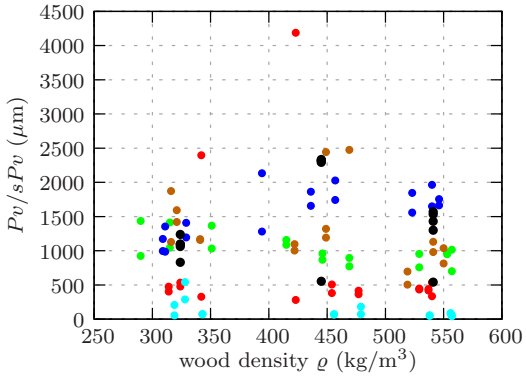


(b) maximum profile valley depth $Pv/sPv$

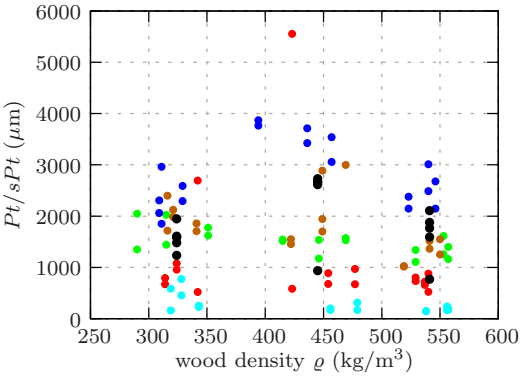


(c) total height of profile $Pt/sPt$

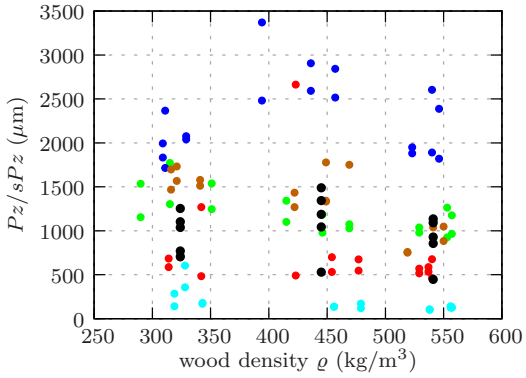


(d) maximum height of profile $Pz/sPz$

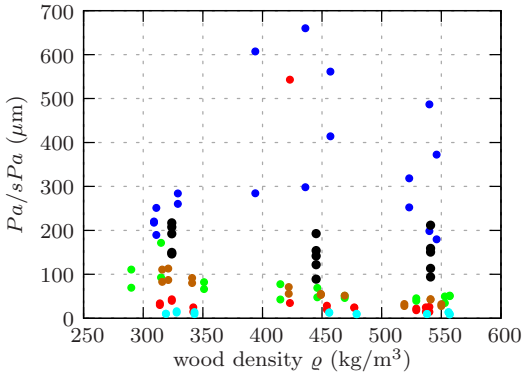


(e) total arithmetic mean deviation $Pa/sPa$

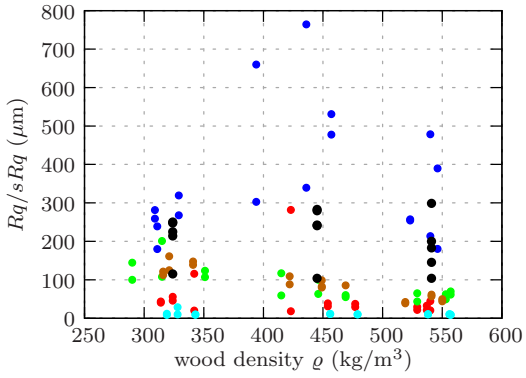


(f) root mean square deviation $Pq/sPq$

Figure B.1: Primary surface texture parameters for the plane surfaces cut by means of different cutting tools and primary profile parameters for the bore-hole surfaces: cutting style 1 (red), 2 (green), 3 (blue), 4 (brown), 5 (cyan), and 8 (black)

**Parameters for the waviness profile**

| Parameter | | Cutting type | | | | |
|---|---|---|---|---|---|---|
| | | 1 | 2 | 3 | 4 | 5 |
| $sWp$ | $\mu$m | 16.09 | 56.68 | 229.8 | 50.86 | 15.59 |
| $sWv$ | $\mu$m | 47.36 | 97.22 | 212.1 | 136.6 | 14.94 |
| $sWz$ | $\mu$m | 38.11 | 110.5 | 330.6 | 106.6 | 22.16 |
| $sWt$ | $\mu$m | 63.45 | 153.9 | 441.9 | 187.4 | 30.53 |
| $sWa$ | $\mu$m | 7.544 | 23.86 | 75.41 | 23.03 | 4.892 |
| $sWq$ | $\mu$m | 10.87 | 29.81 | 93.05 | 30.15 | 6.023 |
| $sWk$ | $\mu$m | 19.43 | 70.03 | 245.9 | 56.66 | 16.21 |
| $sWpk$ | $\mu$m | 4.025 | 15.01 | 96.56 | 13.06 | 4.229 |
| $sWvk$ | $\mu$m | 23.75 | 41.31 | 55.8 | 51.79 | 5.247 |
| $sWMr1$ | % | 6.867 | 7.355 | 11.78 | 7.168 | 6.784 |
| $sWMr2$ | % | 87.79 | 85.84 | 75.34 | 82.92 | 91.16 |

Table B.5: Texture parameters for the waviness-profile for specimens of low wood density (Series 16B4).

| Parameter | | Cutting type | | | | |
|---|---|---|---|---|---|---|
| | | 1 | 2 | 3 | 4 | 5 |
| $sWp$ | $\mu$m | 123.3 | 30.49 | 282.5 | 19.8 | 15.51 |
| $sWv$ | $\mu$m | 221.3 | 39.69 | 244.3 | 24.21 | 9.595 |
| $sWz$ | $\mu$m | 180.1 | 54.24 | 350.5 | 31.1 | 18.41 |
| $sWt$ | $\mu$m | 344.6 | 70.18 | 526.8 | 44.01 | 25.11 |
| $sWa$ | $\mu$m | 45.97 | 13.28 | 104.4 | 6.693 | 3.918 |
| $sWq$ | $\mu$m | 59.05 | 16.08 | 121.5 | 8.389 | 4.904 |
| $sWk$ | $\mu$m | 135.8 | 40.57 | 308.9 | 20.54 | 11.35 |
| $sWpk$ | $\mu$m | 40.33 | 8.808 | 124.5 | 6.302 | 7.145 |
| $sWvk$ | $\mu$m | 80.8 | 13.86 | 45.62 | 9.331 | 2.45 |
| $sWMr1$ | % | 15.99 | 11.69 | 17.14 | 7.331 | 16.56 |
| $sWMr2$ | % | 88.27 | 89.99 | 94.91 | 86.84 | 93.84 |

Table B.6: Texture parameters for the waviness-profile for specimens of intermediate wood density (Series 14_2).

| Parameter | | Cutting type | | | | |
|---|---|---|---|---|---|---|
| | | 1 | 2 | 3 | 4 | 5 |
| $sWp$ | $\mu$m | 10.86 | 36.85 | 246.4 | 15.48 | 14.99 |
| $sWv$ | $\mu$m | 18.91 | 46.86 | 265.4 | 19.87 | 12.32 |
| $sWz$ | $\mu$m | 19.23 | 59.71 | 342.4 | 22.96 | 18.71 |
| $sWt$ | $\mu$m | 29.77 | 83.71 | 511.7 | 35.35 | 27.31 |
| $sWa$ | $\mu$m | 4.76 | 15.13 | 82.93 | 6.181 | 4.751 |
| $sWq$ | $\mu$m | 5.807 | 18.34 | 102.7 | 7.703 | 5.787 |
| $sWk$ | $\mu$m | 13.78 | 44.77 | 244.1 | 16.23 | 14.46 |
| $sWpk$ | $\mu$m | 3.598 | 11.32 | 112.4 | 4.196 | 5.012 |
| $sWvk$ | $\mu$m | 6.334 | 16.14 | 79 | 11.07 | 3.542 |
| $sWMr1$ | % | 10.53 | 10.96 | 11.99 | 9.986 | 9.288 |
| $sWMr2$ | % | 88.33 | 87.19 | 91.99 | 86.3 | 90.91 |

Table B.7: Texture parameters for the waviness-profile for specimens of high wood density (Series 8A4).

| Parameter | | Density | | |
|---|---|---|---|---|
| | | low | intermediate | high |
| $Wp$ | $\mu$m | 146.6 | 37.87 | 104.5 |
| $Wv$ | $\mu$m | 192.2 | 62.04 | 163.7 |
| $Wz$ | $\mu$m | 120.3 | 17.93 | 105.7 |
| $Wt$ | $\mu$m | 338.8 | 97.47 | 268.2 |
| $Wa$ | $\mu$m | 81.14 | 22.54 | 65.71 |
| $Wq$ | $\mu$m | 96.38 | 26.77 | 79.08 |
| $Wk$ | $\mu$m | 247.2 | 76.82 | 164.1 |
| $Wpk$ | $\mu$m | 22.09 | 12.82 | 7.658 |
| $Wvk$ | $\mu$m | 92.69 | 60.6 | 131.9 |
| $WMr1$ | % | 7.326 | 4.597 | 24.5 |
| $WMr2$ | % | 85.17 | 6.403 | 79.27 |

Table B.8: Surface texture parameters for the waviness profile for specimens with a drilled bore hole.

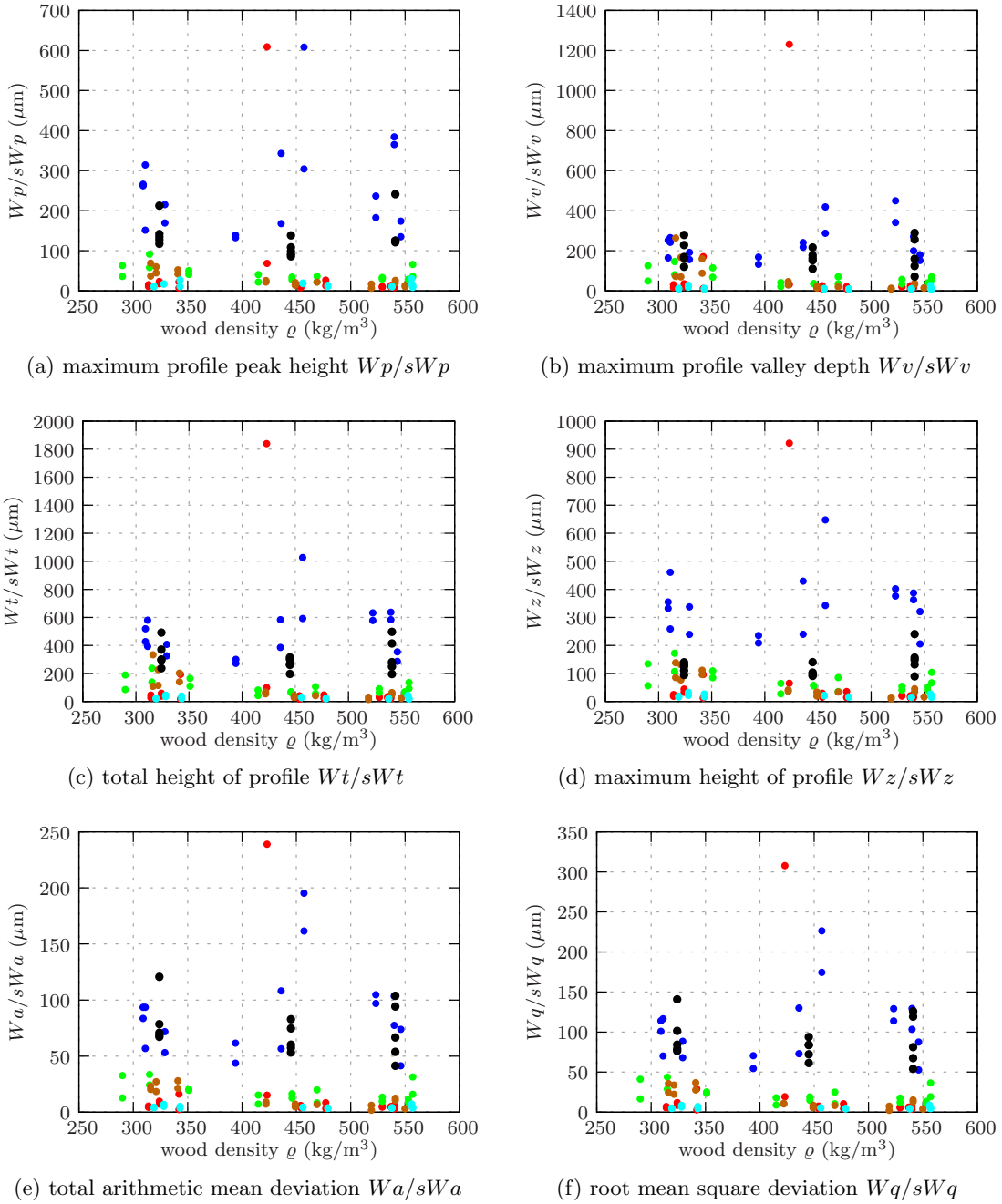


(a) maximum profile peak height $Wp/sWp$

(b) maximum profile valley depth $Wv/sWv$

(c) total height of profile $Wt/sWt$

(d) maximum height of profile $Wz/sWz$

(e) total arithmetic mean deviation $Wa/sWa$

(f) root mean square deviation $Wq/sWq$

Figure B.2: Waviness surface texture parameters for the plane surfaces cut by means of different cutting tools and waviness profile parameters for the bore-hole surfaces: cutting style 1 (red), 2 (green), 3 (blue), 4 (brown), 5 (cyan), and 8 (black)

**Parameters for the roughness profile**

| Parameter | | Cutting type | | | | |
|---|---|---|---|---|---|---|
| | | 1 | 2 | 3 | 4 | 5 |
| $sRp$ | $\mu$m | 262.2 | 462.9 | 1004 | 538.3 | 177 |
| $sRv$ | $\mu$m | 704.8 | 1081 | 975.5 | 998.4 | 147.6 |
| $sRz$ | $\mu$m | 601.9 | 1231 | 1683 | 1330 | 216.4 |
| $sRt$ | $\mu$m | 966.9 | 1544 | 1980 | 1537 | 324.6 |
| $sRa$ | $\mu$m | 28.5 | 88.62 | 191.7 | 90.73 | 8.615 |
| $sRq$ | $\mu$m | 53.71 | 130.7 | 257.7 | 134.5 | 13.11 |
| $sRk$ | $\mu$m | 60.13 | 175.2 | 491.4 | 184.5 | 24.36 |
| $sRpk$ | $\mu$m | 41.48 | 76.3 | 485.8 | 109.4 | 14.84 |
| $sRvk$ | $\mu$m | 110.8 | 302.5 | 196.5 | 304.2 | 21.34 |
| $sRMr1$ | % | 11.31 | 9.322 | 16.23 | 10.04 | 10.08 |
| $sRMr2$ | % | 84.54 | 80.98 | 91.61 | 81.85 | 87.88 |

Table B.9: Texture parameters for the roughness-profile for specimens of low wood density (Series 16B4).

| Parameter | | Cutting type | | | | |
|---|---|---|---|---|---|---|
| | | 1 | 2 | 3 | 4 | 5 |
| $sRp$ | $\mu$m | 453.7 | 381.2 | 1373 | 447.4 | 98.75 |
| $sRv$ | $\mu$m | 534.6 | 728.9 | 1668 | 940.6 | 50.58 |
| $sRz$ | $\mu$m | 627.4 | 910.7 | 2460 | 1166 | 92.55 |
| $sRt$ | $\mu$m | 988.3 | 1110 | 3041 | 1388 | 149.3 |
| $sRa$ | $\mu$m | 41.58 | 53 | 433.6 | 60.19 | 8.874 |
| $sRq$ | $\mu$m | 72.8 | 75.85 | 512.4 | 90.75 | 10.78 |
| $sRk$ | $\mu$m | 51.11 | 142.4 | 1061 | 148.9 | 27.16 |
| $sRpk$ | $\mu$m | 118.1 | 68.5 | 443.4 | 94.6 | 7.754 |
| $sRvk$ | $\mu$m | 194.5 | 146 | 461.5 | 176 | 10.97 |
| $sRMr1$ | % | 19.61 | 10.8 | 14.63 | 14.11 | 6.477 |
| $sRMr2$ | % | 88.61 | 88.03 | 83.45 | 87.21 | 86.65 |

Table B.10: Texture parameters for the roughness-profile for specimens of intermediate wood density (Series 14_2).

| Parameter | | Cutting type | | | | |
|---|---|---|---|---|---|---|
| | | 1 | 2 | 3 | 4 | 5 |
| $sRp$ | $\mu$m | 203.2 | 379.1 | 603.1 | 380.8 | 63.14 |
| $sRv$ | $\mu$m | 362.9 | 727.2 | 1478 | 598.2 | 35.67 |
| $sRz$ | $\mu$m | 456.9 | 865.6 | 1757 | 770.8 | 75.39 |
| $sRt$ | $\mu$m | 566.1 | 1106 | 2081 | 978.9 | 98.81 |
| $sRa$ | $\mu$m | 17.48 | 38.01 | 229.4 | 31.48 | 8.318 |
| $sRq$ | $\mu$m | 28.46 | 58.68 | 295.6 | 48.99 | 10.06 |
| $sRk$ | $\mu$m | 36.84 | 93.13 | 509.3 | 72.14 | 26.02 |
| $sRpk$ | $\mu$m | 33.51 | 63.66 | 108 | 57.6 | 6.957 |
| $sRvk$ | $\mu$m | 67.25 | 141.5 | 574.2 | 102.8 | 9.269 |
| $sRMr1$ | % | 16.92 | 14.46 | 11.19 | 15.1 | 6.765 |
| $sRMr2$ | % | 89.15 | 90.15 | 80.48 | 87.43 | 87.29 |

Table B.11: Texture parameters for the roughness-profile for specimens of high wood density (Series 8A4).

| Parameter | | Density | | |
|---|---|---|---|---|
| | | low | intermediate | high |
| $Rp$ | $\mu$m | 420 | 124 | 366.9 |
| $Rv$ | $\mu$m | 864.9 | 357.7 | 1837 |
| $Rz$ | $\mu$m | 783.7 | 258.1 | 1030 |
| $Rt$ | $\mu$m | 1285 | 456.2 | 2204 |
| $Ra$ | $\mu$m | 156.8 | 40.13 | 138.9 |
| $Rq$ | $\mu$m | 210.5 | 55.41 | 230 |
| $Rk$ | $\mu$m | 342.1 | 93.77 | 257.9 |
| $Rpk$ | $\mu$m | 140.7 | 71.24 | 153.5 |
| $Rvk$ | $\mu$m | 410.8 | 172.8 | 463.9 |
| $RMr1$ | % | 9.128 | 4.288 | 11.1 |
| $RMr2$ | % | 79.32 | 2.894 | 81.07 |

Table B.12: Surface texture parameters for the roughness profile for specimens with a drilled bore hole.

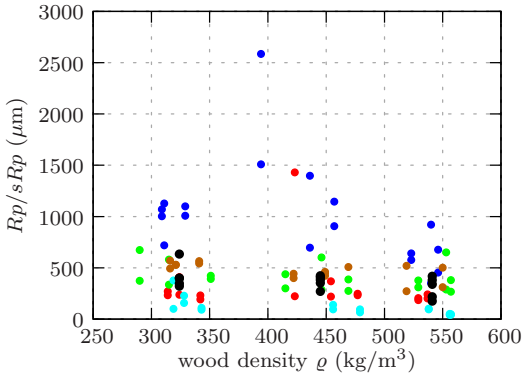


(a) maximum profile peak height $Rp/sRp$

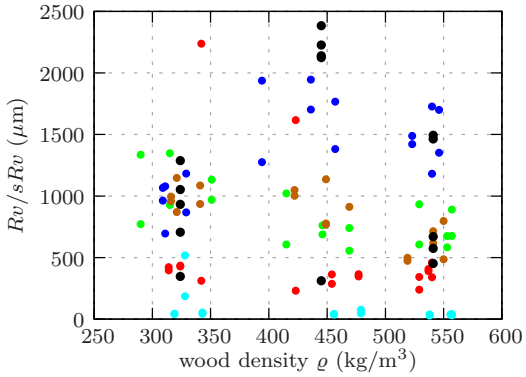


(b) maximum profile valley depth $Rv/sRv$

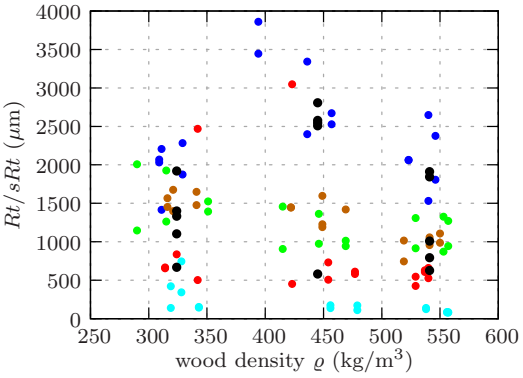


(c) total height of profile $Rt/sRt$

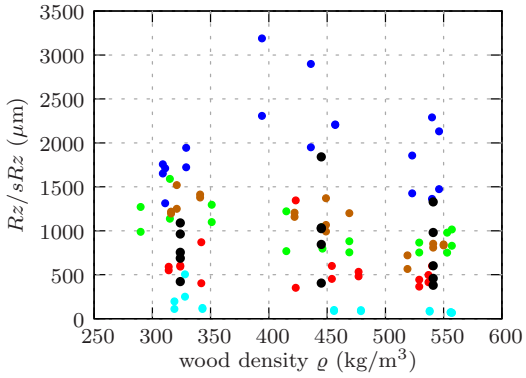


(d) maximum height of profile $Rz/sRz$

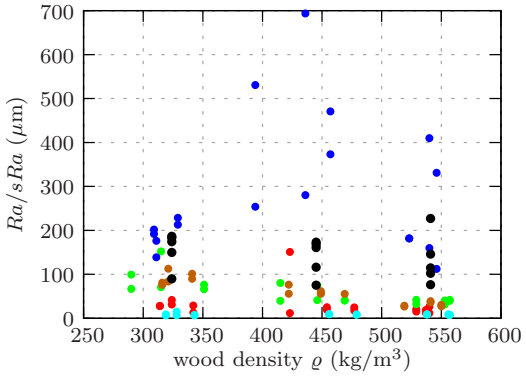


(e) total arithmetic mean deviation $Ra/sRa$

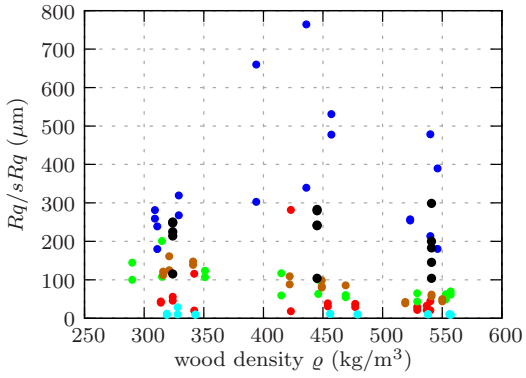


(f) root mean square deviation $Rq/sRq$

Figure B.3: Roughness surface texture parameters for the plane surfaces cut by means of different cutting tools and roughness profile parameters for the bore-hole surfaces: cutting style 1 (red), 2 (green), 3 (blue), 4 (brown), 5 (cyan), and 8 (black)

# Appendix C

# Generalized Lamé curve

A Lamé curve (also called superellipse) is defined by corresponding points $x$ and $y$, which fulfil the equation

$$\left|\frac{x}{a}\right|^n + \left|\frac{y}{b}\right|^n = 1 \ , \tag{C.1}$$

with $a$, $b$, and $n$ positive real numbers. The points describe a closed curve in $\mathbb{R}^2$. The parameters $a$ and $b$ are also called semi-diameters of the curve whereas $n$ describes the curvature. The center of the curve is located at the origin and is symmetric with respect to the principal axes $x = 0$ and $y = 0$, the absolute value guarantees symmetry. Without absolute values, the curve is not closed in the general case but only for even numbers $n = 2, 4, 6, \ldots$. By increasing the exponent, the curve becomes similar to a rectangle of length $2\,a$ and height $2\,b$. A large variety of curves can be drawn using the above equation, which includes circles ($a = b$, $n = 2$) and ellipses ($a \neq b$, $n = 2$) (Figure C.1).

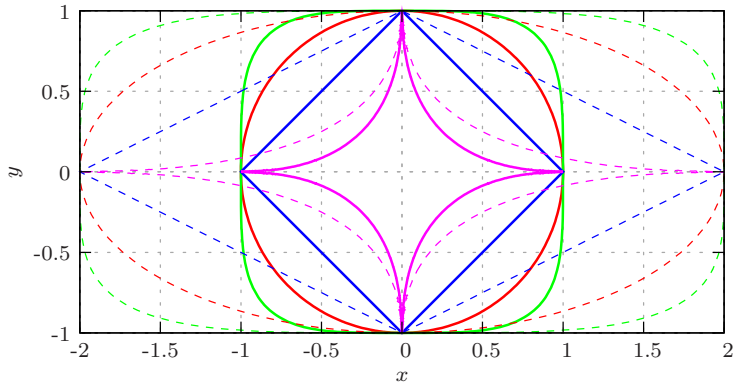


Figure C.1: Lamé curves with varying exponents (green: $n = 4$, red: $n = 2$, blue: $n = 1$, cyan: $n = 1/2$) and semi-diameters (continuous: $a = b = 1$, dashed: $a = 2$, $b = 1$).

By allowing the exponents to be different, the curvature on the ends of both semiaxis

can be controlled separately. Adding correcture terms to the numerators, the center point of the LAMÉ curve along the main axis is shifted. A combination ob both leads to a generalized curve, defined by

$$\left|\frac{x-X}{a}\right|^m + \left|\frac{y-Y}{b}\right|^n = 1 \ . \tag{C.2}$$

Figure C.2 shows typically derived curves.

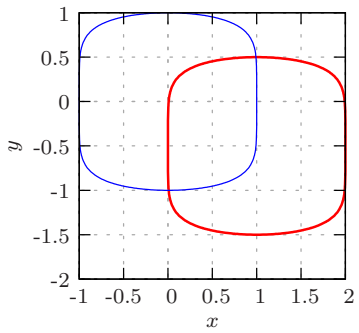


Figure C.2: LAMÉ curves for $a = b = 1$, $m = 2$, and $n = 6$ with varying center points (blue: $X_1 = X_2 = 0$; red: $X_1 = 1$, $X_2 = -0.5$).

# Appendix D

# Lamé-parameters for contact properties

The following tables contain the Lamé parameters obtained by curve fitting for the contact determination of each specimen tested, whereby Table D.1 provides data for the first loading path and Table D.2 for the unloading path.

| Cutting type | Specimen | Density (kg/m$^3$) | $\sigma_0$ (N/mm$^2$) | $n_\sigma$ | $u_0$ (mm) | $n_u$ |
|---|---|---|---|---|---|---|
| 1 | 16B4-10-1 | 324 | 36.5 | 1.10 | 0.101 | 2.59 |
| 1 | 16B4-10-2 | 314 | 35.0 | 1.13 | 0.087 | 3.10 |
| 1 | 16B4-10-3 | 342 | 39.1 | 1.10 | 0.065 | 3.44 |
| 1 | 14_2-9-1 | 477 | 57.9 | 1.10 | 0.085 | 5.36 |
| 1 | 14_2-9-2 | 454 | 52.1 | 1.17 | 0.094 | 4.03 |
| 1 | 14_2-9-3 | 423 | 44.1 | 2.22 | 0.134 | 2.58 |
| 1 | 8A4-8-1 | 529 | 62.5 | 1.24 | 0.088 | 4.95 |
| 1 | 8A4-8-2 | 540 | 63.6 | 1.10 | 0.077 | 5.23 |
| 1 | 8A4-8-3 | 537 | 59.3 | 1.10 | 0.077 | 3.99 |
| 2 | 16B4-2-1 | 315 | 33.9 | 1.18 | 0.294 | 2.35 |
| 2 | 16B4-2-2 | 290 | 28.9 | 1.31 | 0.156 | 2.79 |
| 2 | 16B4-2-3 | 351 | 35.2 | 3.12 | 0.114 | 2.77 |
| 2 | 14_2-1-1 | 469 | 55.3 | 1.10 | 0.225 | 4.30 |
| 2 | 14_2-1-2 | 446 | 55.5 | 1.10 | 0.287 | 3.74 |
| 2 | 14_2-1-3 | 415 | 51.1 | 1.10 | 0.255 | 3.69 |
| 2 | 8A4-1-1 | 529 | 59.8 | 1.10 | 0.176 | 4.98 |
| 2 | 8A4-1-2 | 553 | 63.8 | 1.99 | 0.189 | 4.11 |
| 2 | 8A4-1-3 | 557 | 59.4 | 1.10 | 0.175 | 3.70 |
| 3 | 16B4-4-1 | 311 | 28.7 | 1.35 | 0.975 | 1.98 |
| 3 | 16B4-4-2 | 309 | 30.1 | 1.98 | 0.934 | 1.64 |
| 3 | 16B4-4-3 | 329 | 33.5 | 1.72 | 1.123 | 1.60 |
| 3 | 14_2-5-1 | 457 | 39.1 | 1.45 | 0.612 | 1.89 |
| 3 | 14_2-5-2 | 436 | 46.0 | 1.10 | 0.307 | 2.45 |
| 3 | 14_2-5-3 | 394 | 41.3 | 2.07 | 1.256 | 1.10 |
| 3 | 8A4-3-1 | 523 | 49.2 | 1.22 | 0.222 | 2.91 |
| 3 | 8A4-3-2 | 546 | 54.4 | 1.10 | 0.207 | 2.92 |
| 3 | 8A4-3-3 | 540 | 54.3 | 1.10 | 0.700 | 1.81 |
| 4 | 16B4-5-1 | 316 | 28.1 | 3.28 | 0.165 | 2.53 |
| 4 | 16B4-5-2 | 321 | 29.6 | 1.22 | 0.194 | 3.56 |
| 4 | 16B4-5-3 | 341 | 31.6 | 3.14 | 0.298 | 2.17 |
| 4 | 14_2-4-1 | 469 | 53.0 | 3.80 | 0.169 | 3.71 |
| 4 | 14_2-4-2 | 449 | 52.1 | 1.28 | 0.198 | 4.64 |
| 4 | 14_2-4-3 | 422 | 47.5 | 1.10 | 0.215 | 5.01 |
| 4 | 8A4-4-1 | 519 | 54.8 | 1.25 | 0.136 | 5.70 |
| 4 | 8A4-4-2 | 550 | 58.7 | 2.71 | 0.119 | 5.30 |
| 4 | 8A4-4-3 | 541 | 54.0 | 1.48 | 0.149 | 6.10 |
| 5 | 16B4-6-1 | 328 | 29.3 | 2.36 | 0.105 | 3.97 |
| 5 | 16B4-6-2 | 319 | 29.6 | 1.77 | 0.095 | 3.77 |
| 5 | 16B4-6-3 | 343 | 32.7 | 1.23 | 0.096 | 4.03 |
| 5 | 14_2-6-1 | 479 | 56.5 | 2.21 | 0.075 | 4.05 |
| 5 | 14_2-6-2 | 456 | 52.8 | 1.10 | 0.100 | 4.48 |
| 5 | 14_2-6-3 | 431 | 49.5 | 1.10 | 0.124 | 5.08 |
| 5 | 8A4-6-1 | 538 | 59.3 | 1.46 | 0.069 | 4.24 |
| 5 | 8A4-6-2 | 557 | 63.8 | 1.20 | 0.078 | 3.48 |
| 5 | 8A4-6-3 | 556 | 61.1 | 1.10 | 0.085 | 3.73 |

Table D.1: LAMÉ parameters for the first loading path of all specimens tested.

| Cutting type | Specimen | Density (kg/m$^3$) | $\overline{\sigma}_0$ (N/mm$^2$) | $\overline{n}_\sigma$ | $\overline{u}_0$ (mm) | $\overline{n}_u$ |
|---|---|---|---|---|---|---|
| 1 | 16B4-10-1 | 324 | 36.5 | 1.20 | 0.034 | 3.47 |
| 1 | 16B4-10-2 | 314 | 35.0 | 1.45 | 0.029 | 3.68 |
| 1 | 16B4-10-3 | 342 | 39.1 | 2.18 | 0.026 | 3.49 |
| 1 | 14_2-9-1 | 477 | 57.9 | 5.13 | 0.028 | 3.60 |
| 1 | 14_2-9-2 | 454 | 52.1 | 2.65 | 0.025 | 4.64 |
| 1 | 14_2-9-3 | 423 | 44.1 | 3.07 | 0.056 | 5.48 |
| 1 | 8A4-8-1 | 529 | 62.5 | 1.99 | 0.024 | 3.49 |
| 1 | 8A4-8-2 | 540 | 63.6 | 1.68 | 0.032 | 3.81 |
| 1 | 8A4-8-3 | 537 | 59.3 | 1.76 | 0.034 | 3.32 |
| 2 | 16B4-2-1 | 315 | 33.9 | 2.09 | 0.049 | 4.61 |
| 2 | 16B4-2-2 | 290 | 28.9 | 3.75 | 0.033 | 3.90 |
| 2 | 16B4-2-3 | 351 | 35.2 | 2.98 | 0.038 | 4.05 |
| 2 | 14_2-1-1 | 469 | 55.3 | 8.02 | 0.045 | 4.08 |
| 2 | 14_2-1-2 | 446 | 55.5 | 2.74 | 0.047 | 4.73 |
| 2 | 14_2-1-3 | 415 | 51.1 | 1.96 | 0.043 | 4.64 |
| 2 | 8A4-1-1 | 529 | 59.8 | 2.35 | 0.037 | 3.40 |
| 2 | 8A4-1-2 | 553 | 63.8 | 2.35 | 0.053 | 5.38 |
| 2 | 8A4-1-3 | 557 | 59.4 | 2.39 | 0.054 | 3.34 |
| 3 | 16B4-4-1 | 311 | 28.7 | 1.82 | 0.080 | 4.20 |
| 3 | 16B4-4-2 | 309 | 30.1 | 3.33 | 0.091 | 4.91 |
| 3 | 16B4-4-3 | 329 | 33.5 | 3.19 | 0.101 | 5.18 |
| 3 | 14_2-5-1 | 457 | 39.1 | 2.70 | 0.124 | 6.25 |
| 3 | 14_2-5-2 | 436 | 46.0 | 2.46 | 0.100 | 3.55 |
| 3 | 14_2-5-3 | 394 | 41.3 | 3.86 | 0.066 | 3.45 |
| 3 | 8A4-3-1 | 523 | 49.2 | 8.35 | 0.062 | 2.80 |
| 3 | 8A4-3-2 | 546 | 54.4 | 4.01 | 0.099 | 3.26 |
| 3 | 8A4-3-3 | 540 | 54.3 | 2.95 | 0.157 | 4.75 |
| 4 | 16B4-5-1 | 316 | 28.1 | 1.95 | 0.039 | 3.50 |
| 4 | 16B4-5-2 | 321 | 29.6 | 1.41 | 0.047 | 3.98 |
| 4 | 16B4-5-3 | 341 | 31.6 | 2.79 | 0.067 | 4.89 |
| 4 | 14_2-4-1 | 469 | 53.0 | 4.21 | 0.055 | 6.50 |
| 4 | 14_2-4-2 | 449 | 52.1 | 1.10 | 0.053 | 6.78 |
| 4 | 14_2-4-3 | 422 | 47.5 | 1.10 | 0.056 | 7.07 |
| 4 | 8A4-4-1 | 519 | 54.8 | 3.72 | 0.036 | 5.15 |
| 4 | 8A4-4-2 | 550 | 58.7 | 3.97 | 0.034 | 5.45 |
| 4 | 8A4-4-3 | 541 | 54.0 | 2.16 | 0.034 | 3.79 |
| 5 | 16B4-6-1 | 328 | 29.3 | 1.95 | 0.050 | 4.15 |
| 5 | 16B4-6-2 | 319 | 29.6 | 1.94 | 0.049 | 4.34 |
| 5 | 16B4-6-3 | 343 | 32.7 | 2.44 | 0.052 | 3.70 |
| 5 | 14_2-6-1 | 479 | 56.5 | 6.45 | 0.040 | 3.38 |
| 5 | 14_2-6-2 | 456 | 52.8 | 1.58 | 0.047 | 4.29 |
| 5 | 14_2-6-3 | 431 | 49.5 | 1.10 | 0.055 | 3.35 |
| 5 | 8A4-6-1 | 538 | 59.3 | 6.71 | 0.043 | 3.43 |
| 5 | 8A4-6-2 | 557 | 63.8 | 1.99 | 0.051 | 4.53 |
| 5 | 8A4-6-3 | 556 | 61.1 | 1.54 | 0.046 | 3.62 |

Table D.2: LAMÉ parameters for the unloading path of all specimens tested.

# Bibliography


[1] ABAQUS Manual (2011). *ABAQUS 6.11 Documentation*. 3DS, 2011 edition. 86, 89

[2] Adalian, C. and Morlier, P. (2001). A model for the behaviour of wood under dynamic multiaxial compression. *Composites Science and Technology*, 61(3):403–408. 7

[3] ASTM D5764 97a (2002). Standard Test Method for Evaluating Dowel-Bearing Strength of Wood and Wood-Based Products. 11

[4] Awaludin, A., Smittakorn, W., Hirai, T., and Hayashikawa, T. (2007). Bearing properties of Shorea obtusa beneath a laterally loaded bolt. *Journal of Wood Science*, 53(3):204–210. 11

[5] Bader, T., Hofstetter, K., Hellmich, C., and Eberhardsteiner, J. (2010). Poromechanical scale transitions of failure stresses in wood: From the lignin to the spruce level. *ZAMM Zeitschrift fur Angewandte Mathematik und Mechanik*, 90(10-11):750–767. 7

[6] Bader, T. K. (2011). *Mechanical properties of sound and of deteriorated softwood at different length scales: Poromicromechanical modeling and experimental investigations*. PhD thesis, Vienna University of Technology. 75

[7] Bader, T. K., Hofstetter, K., Alfredsen, G., and Bollmus, S. (2012). Changes in microstructure and stiffness of Scots pine (Pinus sylvestris L) sapwood degraded by Gloeophyllum trabeum and Trametes versicolor – Part II: Anisotropic stiffness properties. *Holzforschung*, 66:199–206. 46

[8] Ballerini, M. and Rizzi, M. (2007). Numerical analyses for the prediction of the splitting strength of beams loaded perpendicular-to-grain by dowel-type connections. *Materials and Structures/Materiaux et Constructions*, 40(1):139–149. 11

[9] Bejtka, I. (2005). *Verstärkung von Bauteilen aus Holz mit Vollgewindeschrauben*. PhD thesis, Versuchsanstalt für Stahl, Holz und Steine Fakultät für Bauingenieur-, Geo- und Umweltwissenschaften Universität Karlsruhe. 10

[10] Bleron, L. and Duchanois, G. (2006). Angle to the grain embedding strength concerning dowel type fasteners. *Forest Products Journal*, 56(3):44–50. 11

[11] Borth, O., Schober, K.-U., and Rautenstrauch, K. (2003). Numerical investigations to the load-carrying capacity of perpendicular to the grain loaded timber joints. Part 1: Fracture mechanical examinations. *Bautechnik*, 80(3):155–161. 11

[12] Bouchair, A. and Vergne, A. (1996). An application of the Tsai criterion as a plastic flow law for timber bolted joint modelling. *Wood Science and Technology*, 30(1):3–19. 12

[13] Byskov, E., Christoffersen, J., Dencker Christensen, C., and Sand Poulsen, J. (2002). Kinkband formation in wood and fiber composites - Morphology and analysis. *International Journal of Solids and Structures*, 39(13-14):3649–3673. 7

[14] Claisse, P. and Davis, T. (1998). High performance jointing systems for timber. *Construction and Building Materials*, 12(8):415–425. 10

[15] Clorius, C., Pedersen, M., Hoffmeyer, P., and Damkilde, L. (2000). Compressive fatigue in wood. *Wood Science and Technology*, 34(1):21–37. 7

[16] Cofer, W., Du, Y., and Hermanson, J. (1999). Development of a simple three dimensional constitutive model for the analysis of wood. *American Society of Mechanical Engineers, Applied Mechanics Division*, 231:107–124. 7

[17] Da Silva, A. and Kyriakides, S. (2007). Compressive response and failure of balsa wood. *International Journal of Solids and Structures*, 44(25-26):8685–8717. 7

[18] Dahl, K. and Malo, K. (2009). Nonlinear shear properties of spruce softwood: Numerical analyses of experimental results. *Composites Science and Technology*, 69(13):2144–2151. 7

[19] Daudeville, L. (1999). Fracture in spruce: Experiment and numerical analysis by linear and non linear fracture mechanics. *Holz als Roh - und Werkstoff*, 57(6):425–432. 7

[20] De Luca, V. and Sabia, D. (2007). Mechanical compression tests to model timber structures behaviour. In *WIT Transactions on Engineering Sciences*, volume 57, pages 273–278. 7

[21] De Magistris, F. and Salmen, L. (2005). Combined shear and compression analysis using a modified Iosipescu shear test device. Experimental studies on dry wood. *Holzforschung*, 59(5):539–545. 7

[22] de Souza Neto, E. A., Peric, D., and Owen, D. R. J. (2008). *Computational Methods for Plasticity: Theory and Applications*. Wiley. 72

[23] DIN 4760 (1982). Gestaltsabweichungen – Begriffe, Ordnungssystem. 35, 36

[24] DIN EN 1995-1-1 (2010). Eurocode 5: Design of timber structures – Part 1-1: General – Common rules and rules for buildings. 3, 5, 17, 137, 142

[25] DIN EN 383 (2007). Timber Structures – Test methods – Determination of embedment strength and foundation value for dowel type fasteners. 8, 11

[26] DIN EN ISO 11562 (1998). Geometrische Produktspezifikationen (GPS) – Oberflächenbeschaffenheit: Tastschnittverfahren – Meßtechnische Eigenschaften von phasenkorrekten Filtern. 35

[27] DIN EN ISO 13565-2 (1998). Geometrische Produktspezifikationen (GPS) – Oberflächenbeschaffenheit: Tastschnittverfahren – Oberflächen mit plateauartigen funktionsrelevanten Eigenschaften – Teil 2: Beschreibung der Höhe mittels linearer Darstellung der Materialanteilkurve. 36, 149

[28] DIN EN ISO 25178-2 (2008). Geometrische Produktspezifikation (GPS) – Oberflächenbeschaffenheit: Flächenhaft – Teil 2: Begriffe und Oberflächen-Kenngrößen (Entwurf). 36

[29] DIN EN ISO 4287 (2010). Geometrical Product Specifications (GPS) – Surface texture: Profile method – Terms, definitions and surface texture parameters. 36, 146, 148, 149

[30] DIN EN ISO 8785 (1999). Oberflächenunvollkommenheiten – Begriffe, Definitionen und Kenngrößen. 35

[31] DIN V 32950 (1997). Geometrische Produktspezifikation (GPS) – Übersicht – ISO/TR 14638:1995. 35

[32] Dorn, M. (2009a). Variation of stiffness properties of wood with growing conditions. Technical report, Institute for Mechanics of Materials and Structures, Vienna University of Technology. 7

[33] Dorn, M. (2009b). Within-tree variation of stiffness properties of softwoods. Technical report, Institute for Mechanics of Materials and Structures, Vienna University of Technology. 7

[34] Eberhardsteiner, J. (2002). *Mechanisches Verhalten von Fichtenholz: Experimentelle Bestimmung der biaxialen Festigkeitseigenschaften.* Springer Wien, New York. 7, 74, 75

[35] Eitelberger, J. (2011). *A multiscale material description for wood below the fiber saturation point with particular emphasis on wood-water interactions.* PhD thesis, Vienna University of Technology. 7

[36] Erchinger, C., Frangi, A., and Fontana, M. (2010). Fire design of steel-to-timber dowelled connections. *Engineering Structures*, 32(2):580–589. 11

[37] Fan, X., Zhang, S., and Qu, W. (2011). Load-carrying behaviour of dowel-type timber connections with multiple slotted-in steel plates. *Applied Mechanics and Materials*, 94-96:43–47. 11

[38] Fleischmann, M. (2005). *Numerische Berechnung von Holzkonstruktionen unter Verwendung eines realitätsnahen orthotropen elasto-plastischen Werkstoffmodells.* PhD thesis, Fakultät für Bauingenieurwesen, Technische Universität Wien. 7, 80

[39] Franke, B. and Quenneville, P. (2010). Numerical Modeling of the Failure Behavior of Dowel Connections in Wood. *Journal of Engineering Mechanics*, 137(3):186–195. 11

[40] FRT (2009a). *Manual FRT Mark III.* Fries Research & Technology GmbH. 44

[41] FRT (2009b). *Operating Manual FRT MicroProf.* Fries Research & Technology GmbH. 41, 42

[42] FRT (2009c). *The Chromatic Sensors FRT CWL and FRT CWL FT.* Fries Research & Technology GmbH. 41

[43] Garab, J., Keunecke, D., Hering, S., Szalai, J., and Niemz, P. (2010). Measurement of standard and off-axis elastic moduli and Poisson's ratios of spruce and yew wood in the transverse plane. *Wood Science and Technology*, 44(3):451–464. 7

[44] Gattesco, N. and Toffolo, I. (2004). Experimental study on multiple-bolt steel-to-timber tension joints. *Materials and Structures/Materiaux et Constructions*, 37(2):129–138. 11

[45] Gnuschke, M., Reyer, E., and Parche, M. (2000). Basis of calculation for load-bearing frame structures made of glued laminated timber with ductile joints under dynamic loads. *Bautechnik*, 77(4):229–245. 11

[46] Good, R. J. (1972). Theory of "Cohesive" vs "Adhesive" Separation in an Adhering System. *The Journal of Adhesion*, 4(2):133–154. 34

[47] Grosse, M. (2005). *Zur numerischen Simulation des physikalisch nichtlinearen Kurzzeittragverhaltens von Nadelholz am Beispiel von Holz-Beton-Verbundkonstruktionen.* PhD thesis, Bauhaus-Universität Weimar. 12

[48] Hackspiel, C. (2010). *A numerical simulation tool for wood grading on the effect of knots on the mechanical behavior of wooden boards.* PhD thesis, Vienna University of Technology. 7

[49] Hammoum, F. and Audebert, P. (1999). Modeling and simulation of (visco)-plastic behavior of wood under moisture change. *Mechanics Research Communications*, 26(2):203–208. 7

[50] HBM (2011). *HBM WI Displacement transducer - Data sheet.* HBM. 48

[51] Hofstetter, K., Hellmich, C., and Eberhardsteiner, J. (2005). Development and experimental validation of a continuum micromechanics model for the elasticity of wood. *European Journal of Mechanics, A/Solids*, 24(6):1030–1053. 7

[52] Hong, J.-P. (2007). *Three-dimensional nonlinear finite element model for single and multiple dowel-type wood connections.* PhD thesis, UNIVERSITY OF BRITISH COLUMBIA. 12

[53] Hwang, K. and Komatsu, K. (2002). Bearing properties of engineered wood products I: Effects of dowel diameter and loading direction. *Jounal of Wood Science*, 48(4):295–301. 11

[54] Jernkvist, L. (2001). Fracture of wood under mixed model loading II. Experimental investigation of Picea abies. *Engineering Fracture Mechanics*, 68(5):565–576. 7

[55] Johansen, K. (1949). Theory of Timber Connections. In *International Association for Bridge and Structural Engineering (IABSE) Pub. 9*, pages 249–262. 8

[56] Ju, S.-H. and Rowlands, R. (2001). A three-dimensional frictional stress analysis of double-shear bolted wood joints. *Wood and Fiber Science*, 33(4):550–563. 12

[57] Kaliske, M. and Resch, E. (2009). Three-Dimensional Numerical Analysis of Dowel-Type Connections in Timber Engineering. In *Computational Structural Engineering Proceedings of the International Symposium on Computational Structural Engineering, held in Shanghai, China, June 22–24, 2009*, pages 619–625. 12

[58] Kohlhauser, C. (2005). A multi-surface plasticity model with strain softening for failure mechanisms of clear spruce wood under plain biaxial stress conditions and stabilization of its numerical implementation for large characteristic lengths. Master's thesis, Technischen Universität Wien Fakultät für Bauingenieurwesen. 74

[59] Kohlhauser, C. (2009). *Elasticity tensor determination by means of ultrasonic pulse transmission*. PhD thesis, Vienna Universitsy of Technology. 45, 51

[60] Laplanche, K., Dhima, D., and Racher, P. (2004). Predicting the behaviour of dowelled connections in fire: Fire tests results and heat transfer modelling. In *Proceedings of the 8th World Conference on Timber Engineering, Lahti, Finland. WCTE 2004. Vol. 2*. 11

[61] Lukacevic, M. (2009). Validation and optimization of a numerical simulation tool for wood grading. Master's thesis, Vienna University of Technology. 7

[62] Mackenzie-Helnwein, P., Eberhardsteiner, J., and Mang, H. (2003). A multi-surface plasticity model for clear wood and its application to the finite element analysis of structural details. *Computational Mechanics*, 31(1-2):204–218. 7

[63] Mackenzie-Helnwein, P., Müllner, H. W., and Eberhardsteiner, J. (2005). Analysis of layered wooden shells using an orthotropic elasto-plastic model for multi-axial loading of clear spruce wood. *Computer methods in applied mechanics and engineering*, 194:2661–2685. 6

[64] Mirianon, F., Fortino, S., and Toratti, T. (2008). A method to model wood by using ABAQUS finite element software Part 1. Constitutive model and computational details. *VTT PUBLICATIONS*, 687:1–58. 7

[65] Moraes, P., Rogaume, Y., Bocquet, J., and Triboulot, P. (2005). Influence of temperature on the embedding strength. *Holz als Roh - und Werkstoff*, 63(4):297–302. 11

[66] Moses, D. (2000). *Constitutive and analytical models for structural composite lumber with applications to bolted connections*. PhD thesis, The University of British Columbia. 11

[67] Murray, Y. D. (2007). Manual for LS-DYNA Wood Material Model 143 – FHWA-HRT-04-097. Technical report, Office of Safety Research and Development Federal Highway Administration. 7

[68] Oudjene, M. and Khelifa, M. (2009). Finite element modelling of wooden structures at large deformations and brittle failure prediction. *Materials and Design*, 30(10):4081–4087. 7

[69] Patton-Mallory, M., Pellicane, P., and Smith, F. (1998a). Experimental Analysis of Bolted Joints in Wood. *Journal of Testing and Evaluation*, 26(1):45–52. 11

[70] Patton-Mallory, M., Pellicane, P., and Smith, F. (1998b). Qualitative Assessment of Failure in Bolted Connections: Maximum Stress Criterion. *Journal of Testing and Evaluation*, 26(5):489–496. 12

[71] Patton-Mallory, M., Pellicane, P., and Smith, F. (1998c). Qualitative Assessment of Failure in Bolted Connections: Tsai-Wu Criterion. *Journal of Testing and Evaluation*, 26(5):497–505. 12

[72] Racher, P. and Bocquet, J. (2005). Non-linear analysis of dowelled timber connections: a new approach for embedding modelling. *Electron J Struct Eng*, 5:1–9. 12

[73] Rammer, D. R. and Winistorfer, S. G. (2001). Effect of moisture content on dowel-bearing strength. *Wood and Fiber Science*, 33(1):126–139. 11

[74] Reid, S. and Peng, C. (1997). Dynamic uniaxial crushing of wood. *International Journal of Impact Engineering*, 19(5-6):531–570. 7

[75] Resch, E. (2010). *Zuverlässige numerische Simulation von Holzverbindungen*. PhD thesis, TU Dresden. 74

[76] Resch, E. and Kaliske, M. (2010). Three-dimensional numerical analyses of load-bearing behavior and failure of multiple double-shear dowel-type connections in timber engineering. *Computers and Structures*, 88(3-4):165–177. 12

[77] Santos, C., De Jesus, A., Morais, J., and Lousada, J. (2009). Quasi-static mechanical behaviour of a double-shear single dowel wood connection. *Construction and Building Materials*, 23(1):171–182. 11, 12

[78] Santos, C., De Jesus, A., Morais, J., and Lousada, J. (2010). A comparison between the EN 383 and ASTM D5764 test methods for dowel-bearing strength assessment of wood: Experimental and numerical investigations. *Strain*, 46(2):159–174. 11

[79] Sawata, K., Sasaki, T., Doi, S., and Iijima, Y. (2008). Effect of decay on shear performance of dowel-type timber joints. *Journal of Wood Science*, 54(5):356–361. 11

[80] Sawata, K. and Yasumura, M. (2002). Determination of embedding strength of wood for dowel-type fasteners. *Journal of Wood Science*, 48(2):138–146. 11

[81] Schmidt, J. (2008). *Modellierung und numerische Analyse hölzerner Strukturen*. PhD thesis, Institut für Statik und Dynamik der Tragwerke, Technische Universität Dresden. 74

[82] Schmidt, J. and Kaliske, M. (2003). Holzverbundkonstruktionen - Modellbildung und Simulation. In *Aktuelle Beiträge aus Baustatik und Comp. Mechanics*. 76

[83] Schmidt, J. and Kaliske, M. (2009). Models for numerical failure analysis of wooden structures. *Engineering Structures*, 31(2):571–579. 7

[84] Schoenmakers, J., Jorissen, A., and Leijten, A. (2009). Evaluation and modelling of perpendicular to grain embedment strength. *Wood Science and Technology*, pages 1–17. 11

[85] Schreyer, A., Lam, F., and Prion, H. (2004). Comparison of Slender Dowel-Type Fasteners for Slotted-in Steel Plate Connections under Monotonic and Cyclic Loading. Technical report. 11

[86] Seweryn, A. and Romanovych, M. (2007). Strength criteria for wood under the conditions of complex stressed state. *Materials Science*, 43(3):343–350. 7

[87] Simo, J. C. and Hughes, T. J. R. (1998). *Computational inelasticity*. Springer. 72

[88] Sjödin, J. and Johansson, C.-J. (2007). Influence of initial moisture induced stresses in multiple steel-to-timber dowel joints. *Holz als Roh - und Werkstoff*, 65(1):71–77. 11

[89] Sjödin, J. and Serrano, E. (2008a). A numerical study of methods to predict the capacity of multiple steel-timber dowel joints. *Holz als Roh - und Werkstoff*, 66:447–454. 11

[90] Sjödin, J. and Serrano, E. (2008b). An experimental study of the effects of moisture variations and gradients in the joint area in steel-timber dowel joints. *Holzforschung*, 62(2):243–247. 11

[91] Sjödin, J., Serrano, E., and Enquist, B. (2008). An experimental and numerical study of the effect of friction in single dowel joints. *Holz als Roh - und Werkstoff*, 66(5):363–372. 12

[92] Smith, I. and Vasic, S. (2003). Fracture behaviour of softwood. *Mechanics of Materials*, 35(8):803–815. 7

[93] Soltis, L. A. (2007). *The Encyclopedia of Wood*, chapter 7: Fastenings, pages 7–1–7–28. Skyhorse Publishing. 29, 34

[94] Stehr, M. and Johansson, I. (2000). Weak boundary layers on wood surfaces. *Journal of Adhesion Science and Technology*, 14(10):1211–1224. 34

[95] Tsai, S. and Wu, E. (1971). A General Theory of Strength for Anisotropic Materials. *Journal of Composite Materials*, 5:58–80. 74

[96] Wehsener, J. and Kasal, B. (2008). Real time radioscopy investigations on ductile dowel-type fastener under dynamic load. *Bautechnik*, 85(10):678–686. 11

[97] Xu, B., Bouchaïr, A., Taazount, M., and Vega, E. (2009a). Numerical and experimental analyses of multiple-dowel steel-to-timber joints in tension perpendicular to grain. *Engineering Structures*, 31(10):2357–2367. 12

[98] Xu, B., Taazount, M., Bouchaïr, A., and Racher, P. (2009b). Numerical 3D finite element modelling and experimental tests for dowel-type timber joints. *Construction and Building Materials*, 23(9):3043–3052. 11

[99] Zienkiewicz, O. C. and Taylor, R. L. (2000). *The Finite Element Method: Solid Mechanics*. Butterworth-Heinemann. 72

# Curriculum Vitae

## Personal Data

| | |
|---|---|
| Name: | **Dipl.-Ing. Michael DORN** |
| Date of Birth: | May 4th 1978 |
| Place of Birth: | Vienna, Austria |
| Nationality: | Austrian |
| Current address: | Plenergasse 10/11, 1180 Vienna, Austria |

## Education

| | |
|---|---|
| since 09/2008 | Doctoral studies at Vienna University of Technology, Vienna, Austria |
| 10/1997 – 11/2004 | Diploma studies in Civil Engineering at Vienna University of Technology, Vienna, Austria |

## Work Experience

| | |
|---|---|
| 09/2008 – present | University Assistant at the Institute for Mechanics of Materials and Structures, Vienna University of Technology, Vienna, Austria |
| 01/2006 – 08/2008 | University Assistant at the Institute for Structural Engineering, Vienna University of Technology, Vienna, Austria |
| 02/2005 – 12/2005 | Structural Steel Engineer at Praher – Schuster Ziviltechniker GmbH, Vienna, Austria |
| 05/2004 – 01/2005 | Structural Engineer at ISP Ziviltechniker GmbH, Vienna, Austria (Part-Time) |

## Activities abroad

| | |
|---|---|
| 09/2001 – 06/2002 | Heriot Watt University, Edinburgh, Scotland, ERASMUS Exchange Student |

## Awards

| | |
|---|---|
| 2010 | 1st Prize, Danubia Adria Symposium 2010, Wrocław, Poland |